Multi-sensor, cooperative autonomous integrity monitoring for Intelligent Transport Systems

by

Jelena Gabela

https://orcid.org/0000-0002-0186-5917

A thesis submitted in total fulfillment for the
degree of Doctor of Philosophy

in the
Department of Electrical and Electronic Engineering
Melbourne School of Engineering
The University of Melbourne

June 2021

Supervisors:
Prof Allison Kealy
Prof William Moran
Dr Mark Hedley

Jelena Gabela: *Multi-sensor, cooperative autonomous integrity monitoring for Intelligent Transport Systems*, © June 2021

Dida, oprosti šta nisan postala "prava" doktorica...

Ne boj se nepovoljnih okolnosti, nemoj na njih misliti, nemoj ih gledati, one donose neuspjeh. Nije važno kako protivnik tebi izgleda. Upri oči u svoj cilj, čvrsto se drži uza nj i uporno misli što ti je još potrebno da bi ga dosegao. Radije vjeruj, privuci uspjeh kao što se privlači zalogaj trave. Uspjeh nije za lijenčine. Trava ti neće sama uletjeti u usta. Moraš joj poći u susret. Tko odustane, taj je unaprijed izgubio bitku.

Božidar Prosenjak, Divlji Konj

Abstract

The integrity of the positioning system solution can be defined as a measure of trust one can put in the value of the estimated position. Some authors have called it "a guarantee of safety". Due to the safety implications, the Global Navigation Satellite Systems (GNSS) position integrity monitoring was first used in civil aviation. Integrity has become a key performance metric for Intelligent Transport Systems (ITS) given the ongoing efforts to develop more robust integrity monitoring algorithms for land-based applications in GNSS-challenged environments.

However, "a guarantee of safety" cannot be given without any risk of misleading information associated with it. This risk exists due to the different error sources that impact the GNSS signals and needs to be up to a specified tolerable level that differs depending on the application.

Any integrity monitoring algorithm proposed for ITS needs to be able to deal with problems specific to the urban environments: reduced measurement availability, satellite/user geometry and presence of large errors such as multipath. The algorithm proposed in this research is based on a robust, multi-sensor and cooperative positioning system with the Particle Filter (PF) as the underlying position estimator.

This research proposes three novel integrity monitoring algorithms built on Bayesian Receiver Autonomous Integrity Monitoring (BRAIM). By using BRAIM, the need for measurement redundancy is mitigated. Although, BRAIM (with the PF as the underlying estimator) tests for different number and different magnitudes of faults through the employment of multiple particles (i.e., hypotheses), Fault Detection and Exclusion (FDE) is added to BRAIM. FDE is added to remove the impact of large biases on the *a posteriori* distribution used to bound the integrity risk estimate. This results in a novel FDE+BRAIM algorithm. In order to decrease the estimated integrity risk, a Spatial Feature Constraint (SFC) algorithm is implemented to constrain solutions to feasible locations within a road feature. By integrating SFC and BRAIM, the second novel algorithm is proposed: SFC+BRAIM. Lastly, a combination of both novel algorithms is proposed: the FDE+SFC+BRAIM algorithm. The performance of the proposed algorithms was evaluated for GPS only, multi-sensor and distributed cooperative data. The best performance is achieved by cooperative SFC+BRAIM. That method achieved the median probability of misleading information of $5.84 \cdot 10^{-9}/epoch$ for the horizontal alarm limit of 5 m and integrity risk of $1 \cdot 10^{-7}/epoch$.

Declaration of Authorship

I, Jelena Gabela, declare that this thesis titled, 'Multi-sensor cooperative autonomous integrity monitoring for Intelligent Transport Systems' and the work presented in it are my own. I confirm that:

- The thesis comprises only my original work towards the degree of Doctor of Philosophy except where indicated in the preface;
- due acknowledgement has been made in the text to all other material used; and
- the thesis is fewer than the maximum word limit in length, exclusive of tables, maps, bibliographies and appendices as approved by the Research Higher Degrees Committee.

Signed: Jelena Gabela

Date: 23.01.2021.

Preface

This thesis is based on my original work. Multi-authored publications or articles included in the thesis are also based on my original work: literature review, methodology, algorithm development, experiment design, data pre-processing, generating results, generating graphs, figures and tables, writing of the thesis.

The co-authors' contribution was made in the capacity of the supervision, editing and mentorship. In the case of a larger contribution to the paper, those parts of the papers have either been omitted from the thesis or if used, the co-authors' contribution was cited and explicitly acknowledged in the thesis manuscript.

It should be noted that none of the work towards this thesis has been carried out prior to enrolment in the degree nor has it been submitted for other qualifications.

No third party editorial assistance was provided in preparation of the thesis.

This research has been funded by Melbourne Research Scholarships (MRS) and CSIRO Data 61 top-up scholarship.

Acknowledgements

First and foremost, I would like to thank my supervisors Mark, Bill and Allison. It has been a great joy and privilege to be accepted and supported by you. Each of you made a significant impact on my research as well as my development as a researcher. Thank you, Mark, for welcoming me at the CSIRO and introducing me to your amazing team. Thank you, Bill, for providing unique insights from the perspective of a mathematician who sold his soul and transitioned to engineering. Most of all thank you for your encouragement, all the Christmases and introducing me to the rhubarb créme brûlée! Thank you, Allison, for being an amazing supervisor and mentor from the start of this journey. Thank you for your valuable guidance that has greatly improved my research skills and my thesis. The first time we spoke on the phone, you told me that you are excited to get another woman into the academia and you really meant it. Thank you for all the emotional and moral support. Thank you for introducing me to so many people from around the world and helping me build connections with so many researchers. Thank you for guiding me to take the right steps at the right time, and look beyond my PhD thesis. Most of all, thank you for accepting Ivan and me into your family and making our time in Australia unforgettable. On that note, thank you, Aidan and Anja, for being my best friends!

I would also like to thank all the amazing people I have met along the way. Thank you, Salil for being my first friend at the uni and for providing much appreciated guidance and help. Big thank you to Yan for being my friend and my conference roommate. I would also like to thank Salil, Yan, Zahra, Surabhi, David, Vero, Ehsan, Aziliz, Thomas, Xavier, Alex, Marko, Johanna and Youjin for all the hours we spent drinking coffee and talking about our research problems. Thank you, Youjin, for all the coffee, food and baby therapy. Special thanks to Liz and Shenghong for collecting the data with me and helping me along the way. Thank you Liz for teaching me the Australian slang and being a great friend and colleague!

Big thank you to my entire family for being the best support. Thank you, mum and dad, for all the sacrifices you made for myself and my siblings. Thank you for being the best parents I could ask for and for having so much (so so much) patience with me. I am not sure, but I may finally be done with school. Thank you to my brother Ante and sister Anika for making my life so much more fun. Thank you for your support and for keeping up with the name-calling when I missed you. Thank you, grandma, for teaching me how to grow plants ("All that school is worthless if you don't know how to grow your own food!"). It helped keep me sane during the COVID-19 lockdowns. Thank you to my friends in Croatia for being a constant support and not losing touch. Thank you for not accounting for the time difference and texting me while I sleep.

Last but not least, thank you to my partner in crime, Ivan. Thank you for understanding my struggles and challenges I went through in the last four years (you going through the same thing probably helped). Thank you for being the best and the most supportive partner I could ever ask for. I have never been more sure that we are made for each other than now when we lived through the lockdown while working full time and writing our theses. I cannot wait to see what is next for us!

List of Publications

Listed publications have been published or submitted for publication during the enrolment in the degree. Emphasised papers (i.e., boldface) are relevant to this thesis and have been used during the production of this manuscript. Where appropriate, this has been noted.

Refereed journal papers

1. **J. Gabela, A. Kealy, W. Moran and M. Hedley. Multi-sensor and cooperative integrity for ITS: A review of literature. Submitted for publication in the *Journal of Navigation* in *January 2021*.**

2. **J. Gabela, A. Kealy, W. Moran and M. Hedley. Integrity risk estimates for multi-sensor and cooperative positioning systems. In revision following peer review in *IEEE Sensors Journal*.**

3. **J. Gabela, A. Kealy, M. Hedley and W. Moran. Case study of Bayesian RAIM algorithm integrated with Spatial Feature Constraint and Fault Detection and Exclusion algorithms for multi-sensor positioning. *Navigation, Journal of Institute of Navigation*, 68(2):333-351, Summer 2021. doi: 10.1002/navi.433.**

4. G. Retscher, A. Kealy, J. Gabela, Y. Li, S. Goel, C. Toth, A. Masiero, W. Błaszczak-Bak, V. Gikas, H. Perakis, Z. Koppányi, and D. Grejner-Brzezinska. A benchmarking measurement campaign in GNSS-denied/challenged indoor/outdoor and transitional environments. *Journal of Applied Geodesy*, 14(2):215-229, February 2020. doi: 10.1515/jag-2019-0031.

5. **J. Gabela, A. Kealy, S. Li, M. Hedley, W. Moran, W. Ni, and S. Williams. The effect of linear approximation and Gaussian noise assumption in multi-sensor positioning through experimental evaluation. *IEEE Sensors Journal*, 19(22):10719-10727, November 2019. doi: 10.1109/JSEN.2019.2930822.**

6. J. Gabela, G. Retscher, S. Goel, H. Perakis, A. Masiero, C. Toth, V. Gikas, A. Kealy, Z. Koppányi, W. Błaszczak-Bak, Y. Li, and D. Grejner-Brzezinska. Experimental evaluation of a UWB-based cooperative positioning system for pedestrians in GNSS-denied environment. *Sensors*, 19(23):5274, November 2019. doi: 10.3390/s19235274.

Refereed conference papers

1. A. Masiero, H. Perakis, J. Gabela, C. Toth, V. Gikas, G. Retscher, S. Goel, A. Kealy, Z. Koppányi, W.Błaszczak-Bak, Y. Li and D. Grejner-Brzezinska. Indoor navigation and mapping: Performance analysis of UWB-based platform positioning. *The International Archives of the Photogrammetry, Remote Sensing and Spatial Information Sciences*, XLIII-B1-2020: 549–555, 2020. doi:10.5194/isprs-archives-XLIII-B1-2020-549-2020.

2. **J. Gabela, I. Majic, A. Kealy, M. Hedley and S. Li. Robust vehicle localization and integrity monitoring based on spatial feature constrained PF. *Proceedings of the 2020 IEEE/ION Position, Location and Navigation Symposium (PLANS)*, Portland, ORE, USA, 661-669, April 2020. doi: 10.1109/PLANS46316.2020.9110189.**

3. **J. Gabela, A. Kealy, X. Bachelet, W. Moran, and M. Hedley. Evaluation of integrity availability based on classic RAIM in different urban environments for stand-alone GPS and multi-sensor solutions. *Proceedings of The International Global Navigation Satellite Systems Association (IGNSS Symposium 2020)*, Sydney, NSW, Australia, February 2020.**

4. **J. Gabela, E. Smith, S. Li, A. Kealy, M. Hedley, W. Ni, A. Dempster, and J. W. Cheong. A measurement campaign for cooperative positioning architecture based on GNSS and local positioning system. *Proceedings of The International Global Navigation Satellite Systems Association (IGNSS Symposium 2020)*, Sydney, NSW, Australia, February 2020.**

5. S. Goel, J. Gabela, G. Retscher, C. Toth, A. Masiero, and A. Kealy. UWB cooperative localization of pedestrians along a constrained building hallway. *Proceedings of The International Global Navigation Satellite Systems Association (IGNSS Symposium 2020)*, Sydney, NSW, Australia, February 2020.

6. A. Kealy, G. Retscher, J. Gabela, Y. Li, S. Goel, C. Toth, A. Masiero, W. Błaszczak-Bak, V. Gikas, H. Perakis, Z. Koppányi, and D. Grejner-Brzezinska. A benchmarking measurement campaign in GNSS-denied/challenged indoor/outdoor and transitional environments. *Proceedings of FIG Working Week*, Hanoi, Vietnam, April 2019. FIG Article of the Month – July/August 2019.

7. A. Kealy, G. Retscher, Y. Li, T. Gonzales, S. Goel, and J. Gabela. Robust positioning performance in indoor environments. *E3S Web of Conferences*, 94:02001, May 2019. doi: 10.1051/e3sconf/20199402001. Presented in International Symposium on Global Navigation Satellite System 2018 (ISGNSS 2018) in Bali, Indonesia, November 2018.

8. G. Retscher, Y. Li, A. Kealy, H. Hofer, J. Gabela, S. Goel, O. Qureshi, E. Smith, and L. Bao. Real-time Wi-Fi RSS variation correction using a network differential positioning approach. *Proceedings of the 2018 International Conference on Indoor Positioning and Indoor Navigation (IPIN)*, Nantes, France, September 2018.

9. **J. Gabela, S. Goel, A. Kealy, M. Hedley, W. Moran, and S. Williams. Cramér Rao Bound analysis for cooperative positioning in Intelligent Transportation Systems. *Proceedings of The International Global Navigation Satellite Systems Association (IGNSS Symposium 2018)*, Sydney, NSW, Australia, February 2018.**

10. S. Goel, J. Gabela, A. Kealy, and G. Retscher. An indoor-outdoor cooperative localization framework for UAVs. *Proceedings of The International Global Navigation Satellite Systems Association (IGNSS Symposium 2018)*, Sydney, NSW, Australia, February 2018.

11. G. Retscher, Y. Li, S. Williams, A. Kealy, W. Moran, S. Goel, and J. Gabela. Wi-Fi positioning using a network differential approach for real-time calibration. *Proceedings of The International Global Navigation Satellite Systems Association (IGNSS Symposium 2018)*, Sydney, NSW, Australia, February 2018.

Contents

Abstract iv

Declaration of Authorship v

Preface vi

Acknowledgements vii

List of Publications ix

List of Figures xiv

List of Tables xvii

Abbreviations xviii

1 Introduction 1
- 1.1 Motivation . . . 2
- 1.2 Need for integrity . . . 5
- 1.3 Urban environment . . . 6
- 1.4 Research aim and questions . . . 8
- 1.5 Outcomes and contributions . . . 9
- 1.6 Thesis structure . . . 11

2 Background 13
- 2.1 Introduction: Definition of integrity . . . 14
  - 2.1.1 Definition of important terms . . . 15
- 2.2 GNSS integrity systems . . . 17
- 2.3 Applications and their requirements . . . 18
  - 2.3.1 Civil aviation . . . 18
  - 2.3.2 Maritime applications . . . 20
  - 2.3.3 Railway . . . 21
  - 2.3.4 Land-based applications . . . 22
- 2.4 Classical integrity algorithms . . . 23
  - 2.4.1 SBAS Protection Level calculation . . . 25
  - 2.4.2 WLSR Protection Level calculation . . . 27
- 2.5 Integrity for Intelligent Transport System . . . 28
  - 2.5.1 Stand-alone GNSS integrity . . . 29
  - 2.5.2 Multi-sensor integrity . . . 33
  - 2.5.3 Cooperative integrity . . . 37
- 2.6 State-of-the-art summary . . . 39
- 2.7 Conclusion . . . 43

3 Vehicle integrity system requirements in urban environment 45
3.1 Introduction . . . 46
3.2 Analysis of multi-sensor and cooperative positioning . . . 47
3.2.1 Loosely coupled centralised cooperative Extended Kalman Filter . . . 48
3.2.2 Posterior Cramér Rao Bound . . . 51
3.2.3 Ad-hoc vehicle and infrastructure network data simulation . . . 52
3.2.4 Results and discussion . . . 53
3.3 Scale of the integrity problem in urban environment . . . 58
3.3.1 Experimental setup . . . 59
3.3.2 Tightly coupled Extended Kalman Filter and SBAS Horizontal Protection calculation . . . 61
3.3.2.1 Multi-sensor Extended Kalman Filter . . . 62
3.3.2.2 SBAS Horizontal Protection Level calculation for multi-sensor system . . . 64
3.3.3 Results and discussion . . . 66
3.3.3.1 GPS integrity in different environments . . . 67
3.3.3.2 Multi-sensor integrity in different environments . . . 72
3.4 Data collection campaign . . . 73
3.4.1 Sensor description . . . 74
3.4.2 Data collection procedure . . . 76
3.4.3 Data availability and quality . . . 78
3.4.4 Use of data for algorithm validation . . . 82
3.5 Conclusions . . . 83

4 Cooperative positioning 85
4.1 Introduction . . . 86
4.2 Terrestrial range error distribution fitting . . . 87
4.3 Analysis of the effect of common assumptions . . . 89
4.3.1 Multi-sensor Particle Filter . . . 91
4.3.2 Results and discussion . . . 93
4.3.2.1 Extended Kalman Filter performance . . . 93
4.3.2.2 Particle Filter performance . . . 95
4.3.2.3 Comparison of Extended Kalman Filter and Particle Filter 95
4.4 Cooperative positioning system . . . 98
4.5 Conclusions . . . 101

5 Position integrity algorithms 103
5.1 Introduction . . . 104
5.2 BRAIM . . . 105
5.3 Comparison of BRAIM and RAIM . . . 108
5.4 Position integrity algorithms . . . 110
5.4.1 BRAIM paired with Fault Detection and Exclusion algorithm . . . 110
5.4.2 BRAIM paired with Spatial Feature Constraint algorithm . . . 113
5.4.3 BRAIM paired with Fault Detection and Exclusion and Spatial Feature Constraint algorithms . . . 117
5.5 Performance evaluation metrics . . . 117
5.6 Conclusions . . . 118

6 Results and discussion 120

6.1 Introduction 121
6.2 Comparison of BRAIM and RAIM 123
6.2.1 Positioning and integrity performance 125
6.2.2 Discussion on availability 127
6.3 Performance of the three novel algorithms 130
6.3.1 Positioning performance 130
6.3.2 Integrity performance 132
6.3.3 Discussion on availability 137
6.4 Utility of proposed SFC approach 140
6.4.1 Experimental setup 141
6.4.2 Results and discussion 142
6.5 Conclusions 148

7 Conclusions **150**
7.1 Future work 154

Bibliography **157**

List of Figures

1.1 Share of cumulative GNSS revenue from 2019 to 2029 (as in [6]). 3
1.2 Toll charging example. 5
1.3 Anti-collision example. 6
1.4 Challenging environment. 7

2.1 Chapter 2 structure. 15
2.2 Graphical representation of AL and PL definitions under the perfect scenario (i.e., $PE < PL < AL$). 16
2.3 System-level integrity monitoring (as shown in [25]). a) SBAS. b) GBAS. . 18
2.4 Flowchart of classical integrity algorithms consisting of three modules: Fault Detection (FD), Fault Exclusion (FE) and HPL modules tasked with integrity availability determination. 24

3.1 Chapter 3 structure. 46
3.2 Simulated trajectories with starting positions for a) Car 1. b) Car 2. 53
3.3 P2I positioning with 15 nodes. a) Position estimation. b) PCRB. 54
3.4 P2I positioning with six nodes. a) Position estimation. b) PCRB. 55
3.5 P2I positioning with four nodes. a) Position estimation. b) PCRB. 56
3.6 P2I positioning with three nodes. a) Position estimation. b) PCRB. 56
3.7 P2P positioning for Car 1. a) Position estimation. b) Position accuracy. c) Relative positions of vehicles at time 10480. d) Relative positions of vehicles at time 11110. 57
3.8 P2I+P2P positioning for Car 1. a) Position estimation. b) PCRB. 58
3.9 a) The trajectory of the vehicle on the highway (Citylink) with Google Earth satellite image as a base map. b) The velocities reached by the vehicle. 60
3.10 a) The trajectory of the vehicle in the open-sky environment (Albert Park) with Google Earth satellite image as a base map. b) The velocities reached by the vehicle. 60
3.11 a) The trajectory of the vehicle in the urban/suburban environment (South Melbourne) with Google Earth satellite image as a base map. b) The velocities reached by the vehicle. 61
3.12 a) The trajectory of the vehicle in the urban canyon (Melbourne Central Business District) with Google Earth satellite image as a base map. b) The velocities reached by the vehicle. 61
3.13 Integrity results for a static vehicle in an open-sky environment. a) Stanford diagram with integrity assessment. b) Timeline of HPL and 2D error estimation compared to HAL. 68
3.14 Integrity results for a vehicle on a highway. a) Stanford diagram with integrity assessment. b) Timeline of HPL and 2D error estimation compared to HAL. 68

3.15 Integrity results for a vehicle in an open-sky environment. a) Stanford diagram with integrity assessment. b) Timeline of HPL and 2D error estimation compared to HAL. 69
3.16 Integrity results for a vehicle in a suburban environment. a) Stanford diagram with integrity assessment. b) Timeline of HPL and 2D error estimation compared to HAL. 70
3.17 Integrity results for a vehicle in an urban canyon. a) Stanford diagram with integrity assessment. b) Timeline of HPL and 2D error estimation compared to HAL. 71
3.18 Availability of GPS satellites in different environments. 71
3.19 Comparison of the integrity availability estimates for positioning systems based on GPS only (top row) and GPS+P2I (bottom row) data. Integrity estimate is compared for all four different environments: highway, open sky, suburb and urban canyon environment. 72
3.20 During the measurement campaign three types of sensors were used: a) GNSS receiver. b) WASP unit. c) UWB unit. 75
3.21 Data collection area with anchors. An example of the trajectory is shown in red. 76
3.22 Sensor set-up for a) an example of the infrastructure node. b) Master user. 77
3.23 The measurement campaign was divided into three different experiments. a) Experiment 1: static. b) Experiment 2: Master user. c) Experiment 2: Dynamic. d) Experiment 3: Dynamic+multipath. 78
3.24 Dynamics of the master user during the dynamic experiment. This figure was originally published in [92]. 78
3.25 Availability of WASP P2I measurements for all users and all experiments. . 79
3.26 Availability of WASP P2P measurements for all users and all experiments. . 79
3.27 The overall measurement availability during all experiments for User 2 (i.e., master user). 80
3.28 The average error of WASP P2I measurements for all anchors (x-axis). The average error is shown for all users as well as all experiments. 81
3.29 The average error of WASP P2P measurements for all users (x-axis). The average error is shown for all users as well as all experiments. 82

4.1 Ranging combinations between the static nodes. 88
4.2 Actual error distribution with the fitted three-component GMM and fitted Normal distribution. 88
4.3 Examples of the EKF and the PF performance. 2D EKF trajectories are shown in the local coordinate system. a) The EKF estimation based on GPS data only. b) The EKF estimation based on the WASP data. c) The PF estimation based on the GPS+WASP data with the assumption of Gaussianity. d) The PF estimation based on the GPS+WASP data with GMM distribution for relative ranging errors. 94
4.4 CDF plot for comparison of the EKF and PF performances based on the used data sets and measurement error assumptions. As per the graph legend, different data sets are shown in different colours. PF performance is shown with higher line width. The solid line is used when Gaussian assumptions are made and dashed lines when Gaussianity is not assumed for WASP data. PF performance of all 15 runs is shown here. 95
4.5 Average accuracy improvement from the EKF to the PF with GMM as a WASP measurement error distribution. The graph presents improvement for WASP and GPS+WASP data set calculated based on the data in Table 4.2. 97

5.1 Side-by-side flowcharts of classical RAIM and BRAIM. 109
5.2 Example of how BRAIM works. Weights of particles within AL (green) are summarised. 115
5.3 Example of how SFC+BRAIM works. Weights of particles within AL and the road feature are summarised. 116

6.1 Chapter 6 structure. 121
6.2 Multi-sensor solution using P2I terrestrial ranges to the LPS and GNSS pseudoranges for position and integrity estimation. 124
6.3 Cooperative solution using the P2I terrestrial ranges to the LPS, P2P terrestrial ranges between all the vehicles, shared positions of all the vehicles in the network and GNSS pseudoranges for position and integrity estimation. 124
6.4 Improvement of the median BRAIM integrity estimate through the employment of a more advanced positioning solution. The Gaussian assumption is made for WASP error distribution. 127
6.5 Improvement of the median BRAIM integrity estimate through the employment of a more advanced positioning solution. WASP error distribution is approximated by the GMM. 128
6.6 Comparison of RAIM and BRAIM integrity availability rates for road-level applications. Gaussian assumption is made for WASP error distribution. . . 129
6.7 Comparison of RAIM and BRAIM integrity availability rates for road-level applications. WASP error distribution is approximated by the GMM. . . . 129
6.8 Integrity estimation for GPS+WASP data depending on the applied integrity algorithm. 134
6.9 Integrity estimation for GPS+WASP(GMM) data for road-level positioning depending on the applied algorithm. 135
6.10 Integrity availability assessment for GPS+WASP data set for road-level positioning depending on the applied IM algorithm. 138
6.11 Integrity availability assessment for GPS+WASP(GMM) data for road-level positioning depending on the applied algorithm. 139
6.12 Trajectory and the road polygon for the highway environment [118]. 143
6.13 Trajectory and the road polygon for the: a) open-sky environment, b) urban canyon. [118] 143
6.14 Average integrity estimates for each point of the trajectory in the highway environment for: a) BRAIM, b) SFC+BRAIM. 144
6.15 An example of the error in map data due to incompleteness of attribute data. Only one lane is assumed on a road where three lanes exist. 145
6.16 Average integrity estimates for each point of the trajectory of open-sky data for: a) BRAIM, b) SFC+BRAIM. 146
6.17 Average integrity estimates for each point of the trajectory of urban canyon data for: a) BRAIM, b) SFC+BRAIM. 146
6.18 Examples of the estimated trajectory in urban environment estimated using: a) PF, b) SFC+PF when SFC has taken the vehicle into the wrong direction, and c) SFC+PF when SFC has correctly identified that vehicle is driving in W-E direction. 147

List of Tables

2.1 GNSS integrity requirements for civil aviation [3]. 19
2.2 GNSS maritime integrity requirements for general navigation [31]. 20
2.3 GNSS maritime integrity requirements for positioning [31]. 20
2.4 GNSS railway integrity requirements [34]. 22
2.5 GNSS integrity requirements for road applications as defined in [4]. 23

3.1 Accuracy of P2I and P2I+P2P in horizontal sense. 54
3.2 Performance of WLS RAIM in different environments based on GPS. 67
3.3 Performance of WLS RAIM in different environments based on GPS+P2I data. 73

4.1 Three-component Gaussian Mixture Model (GMM) 89
4.2 Statistical Information about HPEs. 96

5.1 Comparison of the classical RAIM and BRAIM characteristics. 110

6.1 Experiment parameters used in different analyses. 123
6.2 Comparison of the estimated integrity for GPS data. 125
6.3 Comparison of the estimated integrity for multi-sensor data. 126
6.4 Estimated integrity parameters for CP BRAIM. 127
6.5 Positioning performance results 131
6.6 Estimated integrity for $AL = 5\ m$ 133
6.7 Estimated integrity for $AL = 1.1\ m$ 137
6.8 Values of the *lanes* and *oneway* attributes of OSM road features, and the implied numbers of lanes and road widths [118]. 142
6.9 Positioning and integrity results for the highway environment 144
6.10 Positioning and integrity results for open-sky environment 146
6.11 Positioning and integrity results for urban canyon environment 147

Abbreviations

2D	**T**wo **D**imensional
3D	**T**hree **D**imensional
AAIM	**A**ircraft **A**utonomous **I**ntegrity **M**onitoring
ABAS	**A**ircraft-**B**ased **A**ugmentation **S**ystem
ADAS	**A**dvanced **D**river **A**ssistance **S**ystem
AL	**A**larm **L**imit
ARAIM	**A**dvanced **R**eceiver **A**utonomous **I**ntegrity **M**onitoring
ARGN	**A**ustralian **R**egional **G**NSS **N**etwork
AUD	**AU**stralian **D**olar
BDSBAS	**B**ei**D**ou **S**atellite **B**ased **A**ugmentation **S**ystem
BRAIM	**B**ayesian **R**eceiver **A**utonomous **I**ntegrity **M**onitoring
CDF	**C**umulative **D**istribution **F**unction
CIM	**C**ooperative **I**ntegrity **M**onitoring
CORS	**C**ontinuously **O**perating and **R**eference **S**tation
CP	**C**ooperative **P**ositioning
CR	**C**ontinuity **R**isk
CRAIM	**C**arrier based **R**eceiver **A**utonomous **I**ntegrity **M**onitoring
CSIRO	**C**ommonwealth **S**cientific and **I**ndustrial **R**esearch **O**rganisation
DOF	**D**egrees **o**f **f**reedom
DOLPHIN	**D**edicated **O**mni-purpose Inter-vehicle Communication **L**inkage **P**rotocol for **Hi**ghway **N**avigation
DR	**D**ead **R**eckoning
DSRC	**D**edicated **S**hort **R**ange **C**ommunication
ECEF	**E**arth-**C**entred, **E**arth-**F**ixed
EGNOS	**E**uropean **G**eostationary **N**avigation **O**verlay **S**ervice
EGSA	**E**uropean **G**lobal Navigation **S**atellite System **A**gency

EKF	**E**xtended **K**alman **F**ilter
ERAIM	**E**xtended **R**eceiver **A**utonomous **I**ntegrity **M**onitoring
ERTMS	**E**uropean **R**ail **T**raffic **M**anagement **S**ystem
ETC	**E**lectronic **T**oll **C**harging
EUR	**EUR**o - European Monetary Unit
FA	**F**alse **A**larm
FB	**F**orward-**B**ackward test
FD	**F**ault **D**etection
FE	**F**ault **E**xclusion
FDE	**F**ault **D**etection and **E**xclusion
FIS	**F**uzzy **I**nference **S**yste,
GAGAN	**G**PS-**A**ided **G**eo **A**ugmented **N**avigation
GBAS	**G**round **B**ased **A**ugmentation **S**ystem
GLONASS	**Glo**bal'naya **Na**vigatsionnaya **S**putnikovaya **S**istema
GMM	**G**aussian **M**ixture **M**odel
GNSS	**G**lobal **N**avigation **S**atellite **S**ystem
GPS	**G**lobal **P**ositioning **S**ystem
HAL	**H**orizontal **A**larm **L**imit
HPE	**H**orizontal **P**osition **E**rror
HPL	**H**orizontal **P**rotection **L**evel
I2I	**I**nfrastructure to **I**nfrastructure
ICAO	**I**nternational **C**ivil **A**viation **O**rganization
INS	**I**nertial **N**avigation **S**ystem
IM	**I**ntegrity **M**onitoring
IMO	**I**nternational **M**aritime **O**rganization
IMU	**I**nertial **M**easurement **U**nit
IR	**I**ntegrity **R**isk
IRNSS	**I**ndian **R**egional **N**avigational **S**atellite **S**ystem
ITS	**I**ntelligent **T**ransport **S**ystem
IVHS	**I**ntelligent **V**ehicle **H**ighway **S**ociety
IVS	**I**n-**V**ehicle **S**ystems
KDE	**K**ernel **D**ensity **E**stimation
KF	**K**alman **F**ilter
LCA	**L**iability-**C**ritical **A**pplication

LIDAR	**LI**ght **D**etection and **R**anging
LMS	**L**east **M**edian **S**quares
LOS	**L**ine-**o**f-**S**ight
LPPL	**L**ane **P**ositioning **P**rotection **L**evel
LPS	**L**ocal **P**ositioning **S**ystem
LTE	**L**ong-**T**erm **E**volution
LTS	**L**east **T**rimmed **S**quares
MASPS	**M**inimum **A**viation **S**ystem **P**erformance **S**tandards
MD	**M**issed **D**etection
MHSS	**M**ultiple **H**ypothesis **S**olution **S**eparation
MM	**M**ap **M**atching
MOPS	**M**inimum **O**perational **P**erformance **S**tandards
MSAS	**M**TSAT **S**atellite **A**ugmentation **S**ystem
MTSAT	**M**ultifunctional **T**ransport **Sat**ellites
NLOS	**N**on-**L**ine-**o**f-**S**ight
NRTK	**N**etwork **R**eal **T**ime **K**inematic
OCDR	**O**verall **C**orrect **D**etection **R**ate
P2I	**P**eer to **I**nfrastructure
P2P	**P**eer to **P**eer
PCA	**P**ayment-**C**ritical **A**pplication
PCRB	**P**osterior **C**ramér **R**ao **B**ound
PDF	**P**robability **D**ensity **F**unction
PE	**P**osition **E**rror
PF	**P**article **F**ilter
PL	**P**rotection **L**evel
PNT	**P**ositioning, **N**avigation and **T**iming
PPP	**P**recise **P**oint **P**ositioning
QZSS	**Q**uasi-**Z**enith **S**atellite **S**ystem
RADAR	**RA**dio **D**etection and **R**anging
RAIM	**R**eceiver **A**utonomous **I**ntegrity **M**onitoring
RMIT	**R**oyal **M**elbourne **I**nstitute of **T**echnology
RRAIM	**R**elative **R**eceiver **A**utonomous **I**ntegrity **M**onitoring
RTCA	**R**adio **T**echnical **C**ommission for **A**eronautics
RTK	**R**eal **T**ime **K**inematic

SAIM	**S**atellite **A**utonomous **I**ntegrity **M**onitoring
SBAS	**S**atellite **B**ased **A**ugmentation **S**ystem
SC-159	**S**pecial **C**ommittee**-159**
SCA	**S**afety-**C**ritical **A**pplication
SDCM	**S**ystem for **D**ifferential **C**orrections and **M**onitoring
SFC	**S**patial **F**eature **C**onstraint
SLAM	**S**imultaneous **L**ocalisation **a**nd **M**apping
SLT	**S**equential **L**ocal **T**est
SN	**S**outh**N**orth
SouthPAN	**South**ern **P**ositioning **A**ugmentation **N**etwork
ST	**S**ubset **T**esting
TOA	**T**ime-**O**f-**A**rrival
TRAIM	**T**ime **R**eceiver **A**utonomous **I**ntegrity **M**onitoring
TTA	**T**ime **t**o **A**larm
UAV	**U**nmanned **A**erial **V**ehicle
UERE	**U**ser **E**quivalent **R**ange **E**rror
UNSW	**U**niversity of **N**ew **S**outh **W**ales
UMM	**U**rban **M**ultipath **M**odel
URL	**U**niform **R**esource **L**ocator
UWB	**U**ltra-**W**ide **B**and
USA	**U**nited **S**tates of **A**merika
VAIM	**V**ehicle **A**utonomous **I**ntegrity **M**onitoring
VAL	**V**ertical **A**larm **L**imit
VA-RAIM	**V**ision **A**ided **R**eceiver **A**utonomous **I**ntegrity **M**onitoring
VPL	**V**ertical **P**rotection **L**evel
WAAS	**W**ide **A**rea **A**ugmentation **S**ystem
WASP	**W**ireless **A**d hoc **S**ystem for **P**ositioning
Wi-Fi	**Wi**reless **Fi**delity
WLS	**W**eighted **L**east **S**quare
WLSR	**W**eighted **L**east **S**quare **R**esidual

1

Introduction

This chapter motivates the research presented in this doctoral thesis. Firstly, Intelligent Transportation Systems (ITS) are defined and how the meaning of ITS evolved in recent years is explored. Special focus is put on today's understanding of ITS and technologies it can rely on. These include Global Navigation Satellite Systems (GNSS), multi-sensor and cooperative solutions. Given that ITS typically rely on a position estimate, the concept of position integrity, as the main metric of safety, is introduced. Challenges for position integrity in urban environments and its importance are presented in the following section using two representative examples: toll charging and anti-collision systems. Outcomes and contributions are formalised following the definition of research aims and questions.

1.1 Motivation

For over 100 years, people have been trying to use intelligence to improve the safety of transportation systems. In the early 20th century, the first electric traffic signal was deployed in 1914 in United States of America (USA), and the first parking meter was deployed in 1935 [1]. These events marked the beginning of the modern Intelligent Transportation Systems (ITS). However, the actual term ITS was not used before the early 1990s when it replaced the USA's Intelligent Vehicle Highway Society (IVHS) to de-emphasise the focus on vehicle guidance technologies [1]. With the economic downturn in the 2000s, the focus of ITS development turned to increasing efficiency of the highway systems and vehicle fleets. The full timeline of ITS development throughout history is available at the United States Department of Transportation website[1]. Given this brief historical overview, it can generally be said that the main goal of the ITS has been to make transportation safer and more efficient. Thus, ITS can be defined as "operational systems of various technologies that, when combined and managed, improve the operating capabilities of the overall system" [1].

When talking about ITS today, we mainly focus on applications involving automated vehicles. Automated vehicles include all vehicles where input from drivers is not necessary for certain safety-critical and payment-critical functions such as anti-collision systems and toll charging. They may also be autonomous, meaning that they operate solely based on vehicle sensors, or connected, meaning they operate in a distributed network with other vehicles, participants in the traffic or the infrastructure [1]. Six levels of driving automation have been defined in [2]. The levels range from Level 0 which refers to no driving automation, through Level 2 which means partial driving automation, all the way to Level 5 — full driving automation, which entails no expectation that a user will have to intervene.

With the current understanding of ITS, in addition to developing robust positioning systems capable of achieving required accuracy levels, the focus of researchers has moved to position integrity. From the safety point of view, it is the most important metric of performance [3]. Position integrity can be defined as a measure of trust one can put into the correctness of the position their positioning system is reporting [4]. The position integrity answers a question — "How much trust can I put into the reported position and what is

[1] https://www.its.dot.gov/about/HistoryITS_Timeline.pdf (accessed 22.01.2021.)

the probability of my system failing?" The answer to that question has become increasingly important as the stakes of different liability- and safety-critical applications became higher. Hence, integrity monitoring algorithms are being developed in order to alert the user based on the processes of fault detection and exclusion and integrity estimation [5].

Before going into position integrity and its challenges, we must mention the state of the positioning technologies that are the basis of any integrity algorithm. The majority of today's ITS applications are supported by a multitude of technologies, among which Global Navigation Satellite System (GNSS) makes one of the essential parts of existing and future technologies. According to the European GNSS Agency's (EGSA) report from 2019 (see [6]), GNSS technology will grow from €150 billion in 2019 to €325 billion in 2029. Figure 1.1 shows the percentage of revenue attributed to each of the applications. 55% of revenue will be generated from the road sector, which mainly includes In-Vehicle Systems (IVS), applications regarding automated vehicles and fleet management. The other large portion of the revenue is attributed to the consumer solutions including GNSS receivers used by smartphone and tablet devices. This figure indicates the potential GNSS technology has in terms of market growth, especially in terms of the development of automotive applications.

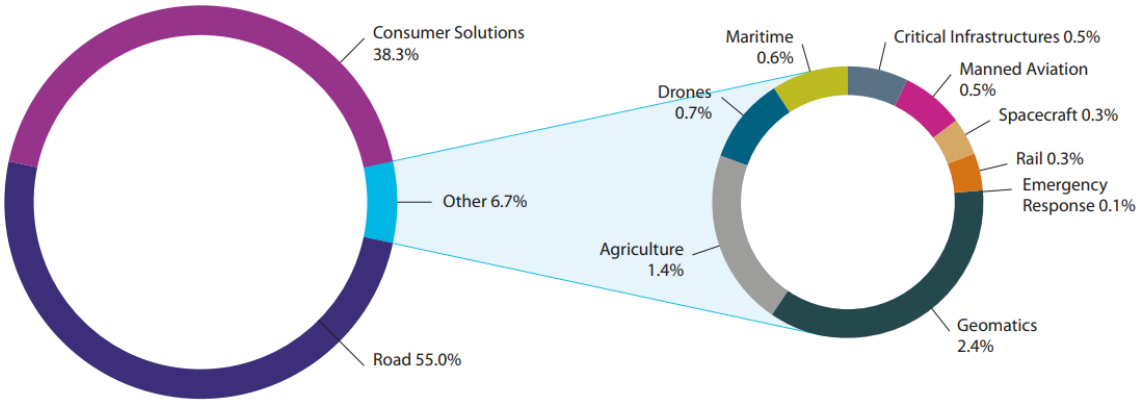


FIGURE 1.1: Share of cumulative GNSS revenue from 2019 to 2029 (as in [6]).

Another study showing the potential of GNSS technologies such as Satellite Based Augmentation Systems (SBAS) was conducted in Australia.[1] This study started in late 2016 and demonstrated the potential financial and performance benefits for Australia and New Zealand in ten industry sectors, including the road sector. The same study cites 1.1 billion AUD in economic benefits for the road sector over 30 years as a result of the deployment of SBAS for Australia and New Zealand. This amount takes into account an estimate of the

[1] https://frontiersi.com.au/wp-content/uploads/2018/08/SBAS-Test-bed-Overview-Report.pdf (accessed 22.01.2021.)

economic benefits resulting from a reduction in fatalities and serious injuries arising from enhanced cooperative ITS.[1] However, the road sector test-bed has shown that a fusion of different positioning technologies is necessary for connected and automated vehicles. This need results from rapid changes in the road environment, which impacts any satellite-based solution, including the SBAS.

Given the challenges of the road environment, the majority of today's solutions are based on multi-sensor fusion. Traditionally, the fusion of GNSS and Inertial Navigation System (INS) has been implemented to solve the problem of position estimate availability during periods of GNSS outages. In urban environments, the prolonged period over which GNSS is unavailable means that the algorithms cannot cope with the accumulation of errors typical in low-cost INS [7, 8]. Given that some of the ITS applications require at least 0.7 m accuracy at 95% confidence level to position a vehicle within the lane, INS/GNSS integration may not be sufficiently accurate [9, 10]. Therefore, an alternative approach for estimating position in complex urban environments is needed. Multi-sensor solutions can be built on the fusion of GNSS with different sensors such as Radio Detection and Ranging (RADAR), Light Detection and Ranging (LIDAR), visual sensors (i.e., camera) and ranging sensors like Ultra Wide-Band (UWB) radios or Dedicated Short Range Communication (DSRC) devices [11–13].

While INS/GNSS integration was sufficiently good for improving position availability and accuracy, constant position estimation availability is now not the only relevant issue for ITS applications. The problem of integrity came to the forefront with the appearance of applications that require a certain degree of automation. Technologically, we are at the point where a system capable of achieving any required accuracy levels (although, at a cost) is easily designed. When it comes to applications such as automated vehicles, it is not enough to have a system capable of achieving required levels of accuracy with 99% confidence. As accuracy cannot be estimated for real-time applications, an additional measure is needed. Consequently, a measure of position integrity became relevant for road applications as it did previously for the civil aviation in the 1980s due to its safety implications. This thesis will tackle the development of robust positioning and integrity algorithms more appropriate for challenging road/urban environments. As a result, I will focus on three performance parameters — integrity accuracy, and availability.

[1] https://frontiersi.com.au/wp-content/uploads/2018/08/SBAS-Economic-Benefits-Report.pdf (accessed 22.01.2021.)

1.2 Need for integrity

This section aims to explain the practical importance of integrity monitoring on two examples representative of liability-critical and safety-critical ITS applications.

As their name suggests, Liability-Critical Applications (LCA) are those where a failure to correctly position a vehicle or a user can lead to economic and legal repercussions [14]. Some of the examples include fleet management, pay as you drive insurance and toll charging [4, 14]. In the case of toll charging, failure to correctly position a vehicle can lead to undercharging or overcharging. The former means loss of revenue and the latter affects the user [15]. Figure 1.2 is an example of overcharging where the vehicle is inaccurately placed on a more expensive road. The road authorities do not want to overcharge the users and be liable for that, but also, they do not want to charge less than they are entitled to. One of the ways to alert the user or the authority that the reported positions are not to be trusted is through integrity monitoring algorithms that bound the maximum acceptable rates of undercharging and overcharging.



FIGURE 1.2: Toll charging example.

Safety-Critical Applications (SCA) are those where a failure to correctly position a vehicle can cause harm to humans, cause loss of human life or damage the environment [14]. Examples of those applications are autonomous driving, Advanced Driver Assistance Systems (ADAS) such as automated lighting, adaptive cruise control, lane-keeping, automate braking or anti-collision systems [4, 14]. Anti-collision systems are clearly an SCA that

can lead to more serious consequences such as injury. Since positioning accuracy is unknown, position integrity estimate is necessary. In this example, due to undetected faulty positions, the user can either unnecessarily brake (i.e., false alarm) or not brake when it is necessary (i.e., missed detection) as shown in Figure 1.3. With the former case being less dangerous, neither one of these cases is desirable. As in the previous example, position integrity is needed to bound the rates of misleading information and warn the user when the system is not to be trusted.

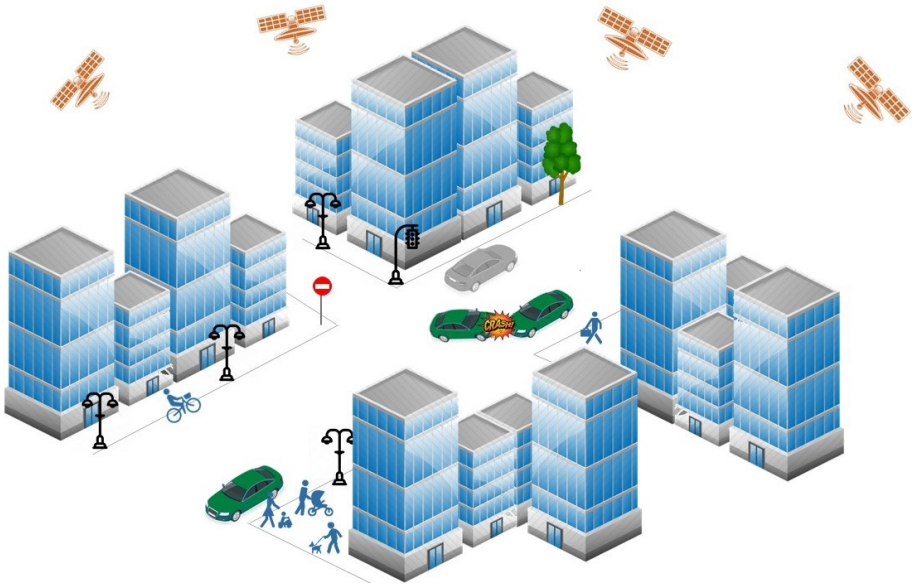


FIGURE 1.3: Anti-collision example.

1.3 Urban environment

The urban environment is commonly addressed as a GNSS challenging environment when it comes to the performance of GNSS. This section discusses why the urban environment is considered a GNSS challenging environment. As mentioned, robust positioning systems capable of achieving high position accuracy in an urban environment are available and no longer remain the main focus of researchers. Furthermore, estimation availability in urban environments has been resolved by fusing INS and GNSS. However, position integrity estimation and integrity monitoring remain problematic for road applications, especially the urban environments such as urban canyons.

This is important for integrity since classical GNSS integrity methods were first developed for civil aviation. In an urban environment, GNSS error sources are different from those

of civil aviation. Consequently, there are associated difficulties of directly implementing such algorithms for urban environments.

Four main problems of using GNSS in urban environment are [16]:

1. Reduced satellite availability,
2. Deteriorated satellite/user geometry,
3. Multipath, and
4. Non-Line-Of-Sight (NLOS) signal reception.

Figure 1.4 illustrates these problems. Due to the inability of satellite signals to propagate through obstacles such as trees and buildings, the number of available satellite measurements is affected and in some cases, to the point that no satellites are available. However, this is rarely the case since multi-GNSS (more than one satellite constellation) receivers are available. If the number of satellites is reduced, by default, satellite/user geometry deteriorates (denoted as (1) and (2) in the figure). For example, in an urban canyon, only a small number of satellites with high elevation angles will be available. Multipath happens when a satellite signal arrives at the receiver via more than one path because of the reflections from surfaces such as buildings and other vehicles [16]. Multipath usually refers to the satellites that are in direct Line-Of-Sight (LOS) of the user (denoted as (3) in the figure). If the satellite signal is received from a satellite that is not visible to the user, an NLOS signal reflected from surfaces such as buildings can be received (denoted as (4) in the figure).

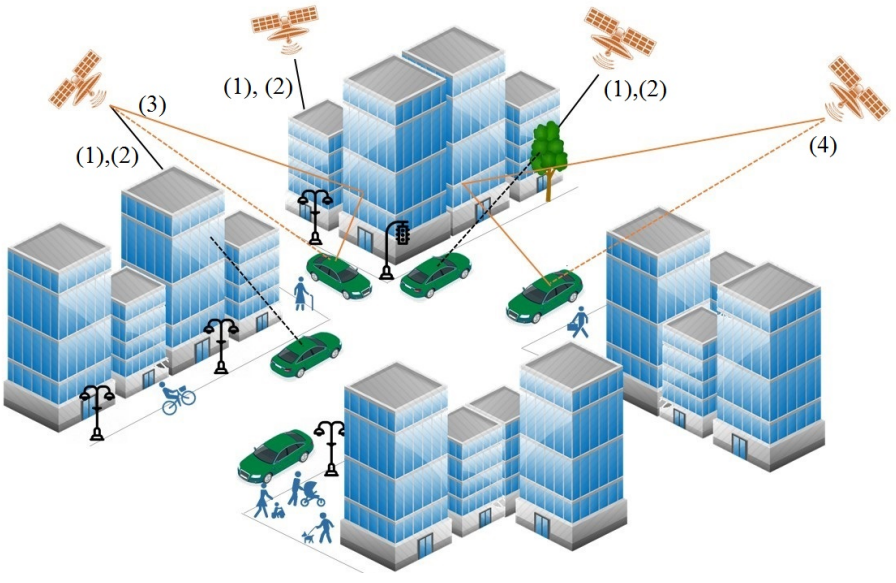


FIGURE 1.4: Challenging environment.

The majority of integrity methods designed for urban environments try to address one or more problems. Usually, to improve measurement availability, multi-sensor systems are used instead of stand-alone GNSS. In addition to integrity estimation, as part of the integrity monitoring process, different fault detection and exclusion techniques are deployed to deal with large biases such as multipath. Because of the complexity of the environment where error sources are rarely stationary, it is difficult to model the errors [17]. A solution that addresses all listed issues has not been proposed yet. Examples of this can be found in the existing literature and will be further discussed in Chapter 2.

1.4 Research aim and questions

This research aims to develop an integrity algorithm able to deal with problems specific to the urban environment: reduced measurement availability, satellite/user geometry and presence of large errors such as multipath. The proposed algorithm will be based on a robust positioning system as a prerequisite to integrity. Furthermore, this research aims to provide a generalised solution independent of the application and its requirements.

The main research question of this thesis is — *How can the positioning and integrity solution for ITS applications in the urban environment be improved?*

To answer this question, more specific questions were defined in order to build upon each other. Each of these research questions has been answered in the thesis in specific chapters and sections.

1. *What positioning system and algorithm will be the basis of the proposed integrity algorithm?* — Chapter 3 and Chapter 4.

2. *What level of integrity is achievable with an existing integrity method for stand-alone GNSS and multi-sensor solution?* — Chapter 3.

3. *Given the identified problems of the existing integrity algorithm in the urban environment, what algorithm can be proposed?* — Chapter 5.

4. *What is the best achievable integrity for multi-sensor and cooperative systems based on a Particle Filter?* — Chapter 6.

1.5 Outcomes and contributions

In line with the previously listed research questions, outcomes and four major contributions of this research can be articulated.

Because of the challenges of the urban environment, before proposing the integrity algorithm, a positioning algorithm capable of achieving the required positioning performance had to be designed. Theoretically best achievable performance was determined for simulated stand-alone GNSS, multi-sensor and Cooperative Positioning (CP) system, through analysis via the Posterior Cramér Rao Bound (PCRB). This analysis was done for a commonly used algorithm for sensor fusion — the Extended Kalman Filter (EKF). Having fused GNSS measurements and terrestrial range data for multi-sensor and CP, appropriateness of linear approximation came into question. When it comes to GNSS measurements, a linear approximation is a good approximation because of the distance from the receiver to the GNSS satellites. This approximation may not be appropriate and may impact the positioning and integrity performance when it comes to terrestrial ranges. Furthermore, the problem of making Gaussian assumptions had to be addressed. Although common, this assumption may not be appropriate for systems that are expected to provide high accuracy and high integrity results. Before this, the impact of the linear approximation and Gaussian assumption was unknown in the context of positioning with terrestrial ranges. To encompass all of these challenges, the performance of the multi-sensor EKF and the Particle Filter (PF) positioning algorithms is analysed on real-world data. Based on those results, a decision is made to use the multi-sensor and cooperative PF as the underlying position estimator to the proposed integrity algorithm.

The first major contribution of this research is the experimental analysis of positioning systems and algorithms and consequently, the proposed distributed cooperative PF based on the fusion of terrestrial range measurements, GNSS raw measurements and shared positions between vehicles.

Before going into the design of the integrity algorithm, the performance of the classical integrity method from aviation is tested on real-world GPS data. This is done to experimentally demonstrate the problems of implementing such algorithms in different urban environments: highway, urban canyon, suburban area and open-sky environment. The results confirmed the hypothesis that the algorithms designed for aviation are not suitable

for critical road applications due to the reduced measurement availability, reduced satellite/user geometry, and the presence of large errors. Furthermore, problems of implementing Receiver Autonomous Integrity Monitoring (RAIM) methods in the urban environment are identified. Firstly, having an algorithm that depends on having sufficient measurement redundancy in the urban environment is not ideal as measurement redundancy cannot be guaranteed. A proportional increase in the estimated integrity bound arising from a deterioration in satellite/user geometry is not ideal in an environment where satellite/user geometry rapidly changes. The drawbacks of implementing classical integrity algorithms in the urban environment have been described and the future integrity algorithm will need to mitigate some of these.

The second major contribution of this research is the use of multi-sensor fusion and CP to mitigate the environmental impact on integrity estimation.

The previous two contributions have served as a starting point in the process of designing a novel integrity algorithm. As mentioned, because of the non-linearity of the proposed positioning system, the PF was chosen as the underlying position estimator of the integrity algorithm. PCRB results and analysis of the classical integrity techniques lead to the proposal of multi-sensor and CP solutions. Given this, Bayesian Receiver Autonomous Integrity Monitoring (BRAIM) from [18] was identified as a potential algorithm to be the basis of the novel integrity algorithms. BRAIM was originally defined for standalone GNSS and tested on simulated data. In this research, the expansion to the multi-sensor system and CP system is proposed. The main benefits of BRAIM are the fact that sufficient measurement redundancy is not a requirement for integrity estimate availability, the integrity estimate does not depend on the unstable network geometry nor the number of measurements. Consequently, an integrity estimate is always available (good or bad) unlike for classical RAIM methods where integrity estimate cannot be available if a sufficient measurement redundancy requirement is not met. Implementation of multi-sensor and CP BRAIM addresses the first two problems of using GNSS in the urban environment from Section 1.3. To mitigate the impact of large biases on the *a posteriori* distribution used to estimate the integrity, Fault Detection and Exclusion (FDE) is added to BRAIM. This is done, even though BRAIM and PF test for a different number and different magnitudes of faults through the employment of multiple particles (i.e., hypotheses). With this, a novel FDE+BRAIM was proposed. BRAIM algorithm does not assume any prior knowledge of the environment (e.g., 2D or 3D maps). Since vehicles are driving on roads, it is common to use such knowledge to improve the positioning and integrity performance by

employing methods such as Map Matching (MM). Similarly, Spatial Feature Constraint (SFC) algorithm is proposed to eliminate the particles (i.e., hypotheses) that are not within the spatial feature (i.e., road), and re-weight the particles bounded by the spatial feature. This resulted in a novel SFC+BRAIM algorithm. Lastly, a combination of both novel algorithms is proposed — FDE+SFC+BRAIM algorithm. All three algorithms partially solve the problem of large biases present in the measurements but do not specifically solve the last two problems of using GNSS in the urban environment from Section 1.3. Unlike any other method found in literature, the performance of BRAIM and three novel algorithms are tested for both the Gaussian and non-Gaussian distribution assumptions. The results will indicate the key role of a better approximation of the terrestrial range error distribution and how it affects the integrity estimate.

The third major contribution of this research are the three novel integrity algorithms implemented and validated on real-world data — FDE+BRAIM, SFC+ BRAIM, and FDE+SFC+BRAIM. It is to be noted that these algorithms are not specific to certain sensors as the integrity is bounded by the *a posteriori* distribution. As a result, there is potential to add additional sensors to the solution without having to adapt the integrity method. The proposed algorithms are not tailored to a specific ITS application. The proof-of-concept of combining FDE and SFC with BRAIM was shown for specific methods. However, any FDE or SFC method can be used. In that sense, the proposed algorithms are customisable.

Finally, **the fourth major contribution of this research** is the first distributed, fully connected cooperative position integrity method where the integrity measure is simultaneously estimated based on all the measurements involved in the measurement model.

1.6 Thesis structure

This thesis is structured as follows. Chapter 2 provides a background of integrity monitoring from its start in civil aviation to ITS applications. Special consideration is given to different autonomous integrity algorithms and their application in the urban environment. This chapter provides the necessary state-of-the-art of integrity for automotive applications and lays out the necessary steps to address the identified problems.

Integrity systems requirements in the urban environment will be defined in Chapter 3. This includes the analysis of the positioning and position integrity capabilities of the proposed multi-sensor and cooperative positioning systems. The theoretically best achievable performance of multi-sensor and cooperative positioning is tested. Furthermore, position integrity is tested in different urban environments with a demonstration of multi-sensor integrity capabilities. As part of the analysis of integrity system requirements, this chapter proposes and presents data collection campaign necessary for the initial algorithm validation.

It is important to address the chosen positioning system before the actual position integrity algorithm. In this thesis, the positioning system is treated as a prerequisite. It is important to have a positioning system that can achieve accuracy levels superior to the required levels of position integrity. Chapter 4 presents the chosen multi-sensor and cooperative positioning system based on the PF. Before that, a comparison of EKF and PF performance is done for the multi-sensor system where the assumption of Gaussianity and linear approximation are tested.

Chapter 5 introduces the BRAIM algorithm and three novel position integrity algorithms. Each of the novel algorithms is built upon BRAIM and addresses a certain problem. BRAIM is chosen as the underlying integrity algorithm as it does not require sufficient measurement redundancy to estimate integrity. The first novel algorithm fuses BRAIM with FDE to eliminate the effect of faulty measurements. Furthermore, FDE's exclusion is not constrained by a sufficient measurement redundancy requirement. The second proposed algorithm fuses BRAIM and SFC to further remove the effect of faulty measurements and to decrease the integrity risk. Finally, the third novel algorithm combines SFC and FDE.

The performance of the proposed algorithms is tested and presented in Chapter 6. Firstly, a comparison of different positioning systems (i.e., stand-alone GPS, multi-sensor, CP) for classical RAIM and BRAIM is provided. The following section presents the performance of the novel algorithms applied for different positioning systems, different integrity requirements and for different error distributions. The chapter is concluded with the utility study of the SFC approach.

Chapter 7 summarises and discusses the major findings of this thesis. The discussion also includes the analysis of limitations and the plans for future work.

2

Background

In addition to providing the literature overview of the integrity algorithms for ITS applications, this chapter provides a brief background overview of GNSS integrity monitoring. The theme of the chapter is built up from the formation of the Integrity Working Group in 1986 which defined integrity in a context of GPS in civil aviation, through the existing integrity methods and how integrity became relevant in other applications, all the way to the state-of-the-art of integrity monitoring in the urban environment. Three different GNSS integrity systems are introduced: Satellite-, Ground- and Aircraft-Based Augmentation Systems. Furthermore, integrity monitoring in different environments/applications is described: civil aviation, maritime, railway and land-based applications. Finally, going from a high-level definition of integrity monitoring in different environments, the main focus is on integrity for ITS applications in the urban environment from the point of view of used technologies — stand-alone GNSS, multi-sensor and cooperative positioning.

2.1 Introduction: Definition of integrity

The Integrity Working Group, formed in April 1986 by the Radio Technical Commission for Aeronautics' (RTCA's) Special Committee-159 (SC-159[2]), defined integrity monitoring as "the ability of a system to provide timely warnings to users when the system should not be used for navigation" [19]. Similarly, [5], defined integrity monitoring (IM) as a capability to detect faults, exclude faults, and raise a timely alarm if the positioning system is deemed unsafe.

In a report by the European GNSS Agency [4], integrity was defined as a "general performance feature referring to the level of trust a user can have in the value of a given position or velocity as provided by a location system."

It is important to differentiate IM and integrity. As defined, IM is a capability to alert the user based on the processes of fault detection and exclusion, and integrity estimation. Integrity is a performance metric used to inform the IM about the level of trust.

The author of [20] writes that, practically, integrity means "a guarantee of safety". As such, GNSS position integrity was first used in civil aviation [3, 19, 21]. Integrity has now become a key performance metric for ITS [5] given the ongoing efforts to develop more robust IM algorithms for road-based applications in GNSS-challenged environments [17]. However, a "guarantee of safety" cannot be given without any risk of misleading information associated with it. This risk exists due to the different error sources that impact the GNSS signal and needs to be up to a specified tolerable level that differs depending on the application.[3]

With that in mind, this chapter provides the background to the problem of GNSS IM and integrity estimation. Firstly, the definition of commonly used terms in the IM algorithms is given. Then, a brief overview of different GNSS integrity systems is provided, followed by the overview of different applications and their requirements. This is done for civil aviation, maritime, railway and land-based application. The fourth section presents two classical integrity algorithms and introduces how IM algorithms usually work. The fifth

This chapter (other than Section 2.1.1) is the extended version of a paper entitled *Multi-sensor and cooperative integrity for ITS: A review of literature*. It has been submitted for publication to *The Journal of Navigation* in *January 2021*.

[2]https://www.rtca.org/content/sc-159

[3]This paragraph has been adapted from a paper entitled *Case study of Bayesian RAIM algorithm integrated with Spatial Feature Constraint and Fault Detection and Exclusion algorithms for multi-sensor positioning* ([22] in the bibliography) first published in *Navigation, Journal of Institute of Navigation* in *Summer 2021*.

section is the main contribution of this chapter. It provides the literature review of the state-of-the-art of different implementations of the IM algorithms for ITS applications with a focus on urban environments. The structure of this chapter is graphically represented in Figure 2.1.

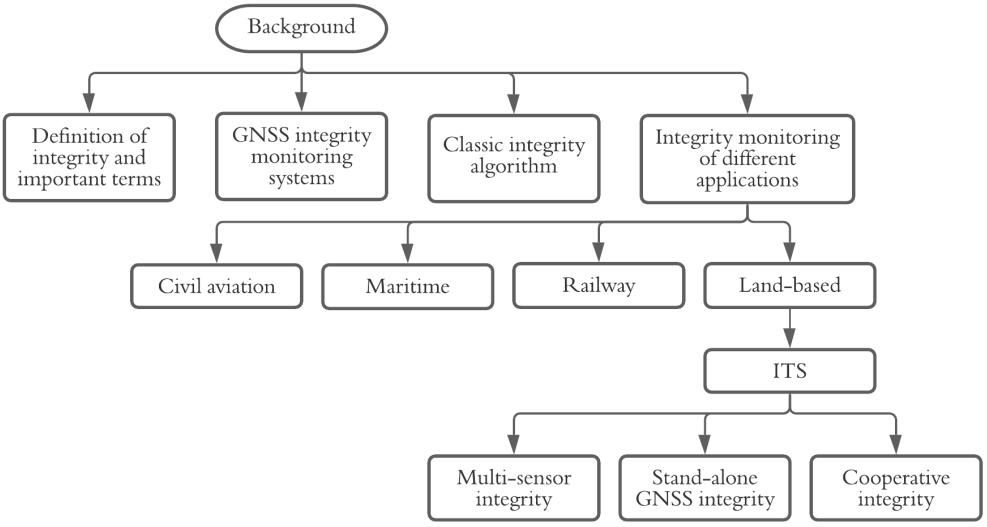


FIGURE 2.1: Chapter 2 structure.

It should be noted that, in the context of this thesis, "integrity" means position integrity. Themes such as spoofing, jamming or protecting against adversaries are out of the scope of this thesis.

2.1.1 Definition of important terms

This section defines some commonly used terms related to the IM. Used definitions are taken from [4]. According to [4], for each application, five key performance metrics need to be defined: integrity risk, protection level, alarm limit, time to alarm and continuity risk.

Integrity Risk (IR) or p_{IR} can be defined as a "probability that, at any moment in a certain reference time interval, the position error (PE) exceeds a confidence interval" [4]. IR is the inverse of integrity and is often used to specify the integrity [23].

That confidence interval can be called **Protection Level** (PL). The PL can be defined as in [18] as a " radius of an interval (of a circle in a plane), with its centre being at the true position, which describes the region which is *assured* to contain the estimated

Details of Section 2.1.1 are part of the paper *Integrity risk estimates for multi-sensor and cooperative positioning systems*. It is in a process of revision following peer review by *IEEE Sensors Journal*.

quantity" with probability $1 - p_{IR}$. It can be said that the estimated position solution (by the positioning system) is bounded by the PL (estimated by the integrity algorithm) with the probability of $1 - p_{IR}$.

According to [4], the **Alarm Limit** (AL) can be defined as "a radius of an interval (of a circle in a plane), with its centre being at the true position, which describes the region which is *required* to contain the indicated position with a probability $1 - p_{IR}$." Definition of the AL is similar to the one of the PL, with a key difference. While the PL is estimated by an algorithm like RAIM and represents a confidence interval that assures the user that the position is within a certain value, AL requires user's position to be within a certain value.Given that the user's PE is unknown in real-time, the integrity algorithm estimates the PL with the probability of containing the estimated position $1 - p_{IR}$. If the estimated PL exceeds AL, an alarm should be raised. Hence, the name alarm limit. The difference between AL and PL is graphically shown in Figure 2.2 for an ideal case where PL successfully assures the user that the PE is bounded by it. Given that the PL is bounded by the AL, the alarm is not raised. While the other parameters defined in this section are key performance requirements, PL is commonly estimated by algorithms such as RAIM.

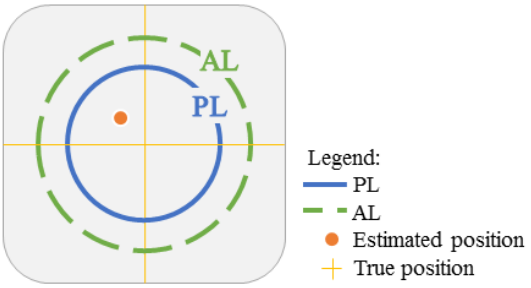


FIGURE 2.2: Graphical representation of AL and PL definitions under the perfect scenario (i.e., $PE < PL < AL$).

The **Time To Alarm** (TTA) is the "maximum allowable time elapsed from the onset of the estimation system being out of tolerance until the equipment enunciates the alarm" [4]. In the context of integrity, "out of tolerance" means that estimated PL exceeds the minimum required AL.

The **Continuity Risk** (CR) can be defined as the "probability that, at any moment and over a specified time interval, the integrity of the estimation system is compromised and an alarm is raised" [18]. As such, CR is connected with the probability of false alarm (FA) which is the probability of failure detection when there are none [4].

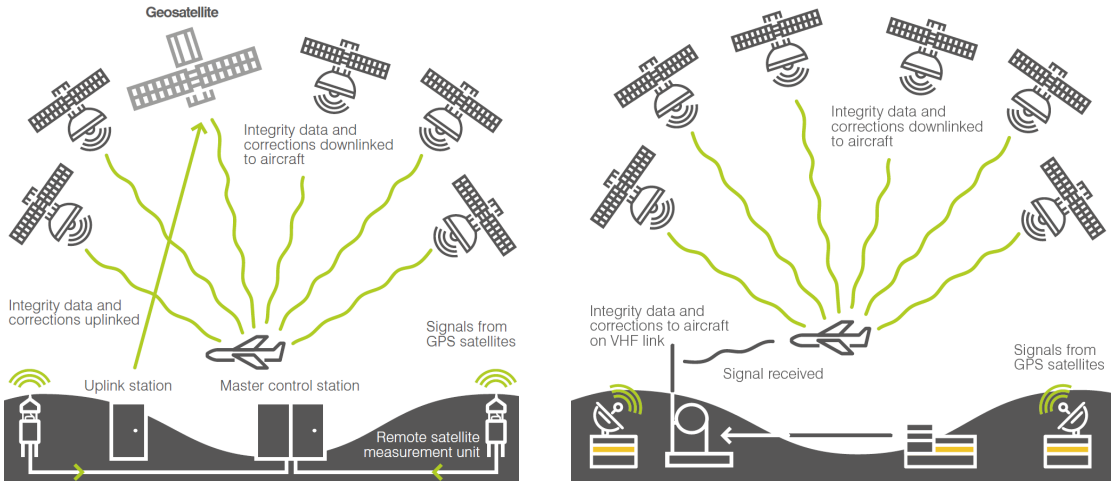
As previously stated, IM was defined in [19] as "the ability of a system to provide timely warnings...". It could be said that the IM algorithms consist of two main functions: detecting a problem and timely reporting of a problem. The latter (i.e., TTA) will not be considered in this research. The main focus of this research will be put on the former, which leads to the use of AL, IR, CR and PL.

2.2 GNSS integrity systems

The IM service can be provided at a system-level or a user-level [5]. A system-level IM includes two systems: Satellite-Based Augmentation System (SBAS) and Ground-Based Augmentation System (GBAS) which rely on satellites, respectively ground based reference stations. A user-level IM can be called Aircraft-Based Augmentation System (ABAS) [23, 24]. Some literature such as [17] also denotes ABAS as Airborne-Based Augmentation System. According to [24], ABAS includes a class of algorithms based on consistency checking of redundant measurements.

SBASs are regional systems that improve the accuracy of the GNSS measurements and generate real-time integrity estimates [5]. The space segment is made out of geostationary satellites that are timed with Earth's rotation and because of that, appear to be stationary with respect to a point on Earth [25]. The geostationary satellites provide ranging data, integrity data and corrections that are downlinked to the aircraft [16]. The control segment consists of a ground network of reference stations that monitor satellite signals and of the master station that processes that data and generates the SBAS message that is then uplinked to the geostationary satellite [16, 25]. The principle of SBAS is shown in Figure 2.3a. Some examples of existing SBAS systems are American Wide Area Augmentation System (WAAS), European Geostationary Navigation Overlay Service (EGNOS), Australian Southern Positioning Augmentation Network (SouthPAN) and Indian GPS-Aided GEO Augmented Navigation (GAGAN).

GBASs are set up in local areas (e.g., in the vicinity of the airports to support precision approach service) and like SBASs, they also provide the integrity information. They consist of ground pseudolites transmitting GNSS-like signals and a reference station that transmits corrections and integrity data to the aircraft [16, 25]. The principle of GBAS is shown in Figure 2.3b.



(A) (B)

FIGURE 2.3: System-level integrity monitoring (as shown in [25]). a) SBAS. b) GBAS.

The biggest drawback of system-level integrity monitoring is a need for complex and costly infrastructure [5]. On the other hand, ABAS does not require infrastructure. There are two ABAS systems: Receiver Autonomous Integrity Monitoring (RAIM) and Aircraft Autonomous Integrity Monitoring (AAIM) [17, 25]. The most commonly used ABAS is RAIM. Within the GNSS receiver, the measurement consistency is checked using the redundancy of GNSS signals [5]. The AAIM makes use of redundant position estimates from other on-board sensors (e.g., IMU) in addition to GNSS [17].

2.3 Applications and their requirements

All of the systems described in the previous section can also be used for other applications. As other safety- and payment-critical applications developed to use GNSS for navigation and positioning, integrity became necessary as one of the performance metrics. This section will focus on four applications: aviation, maritime, railway and land-based applications (e.g., automotive), and their integrity requirements.

2.3.1 Civil aviation

Every integrity algorithm developed for civil aviation must adhere to certain predefined integrity requirements. Defining the performance parameters for civil aviation is supported by the International Civil Aviation Organisation (ICAO) [3], which has defined minimum required integrity levels for specific flight phases. As in [3], Table 2.1 shows the integrity requirements for civil aviation.

TABLE 2.1: GNSS integrity requirements for civil aviation [3].

Operation	**IR** p_{IR}	**AL**	**TTA** $[s]$
Oceanic	$1 \cdot 10^{-7}/hr$	22.96 km	120
En-route	$1 \cdot 10^{-7}/hr$	3.70 km	60
Terminal	$1 \cdot 10^{-7}/hr$	1.85 km	30
NPA*	$1 \cdot 10^{-7}/hr$	0.56 km	10
APV* I	$2 \cdot 10^{-7}/approach$	0.56 km (H)/ 50 m (V)	10
APV II	$2 \cdot 10^{-7}/approach$	40 m (H) / 20 m (V)	6
Cat.* I	$2 \cdot 10^{-7}/approach$	40 m (H) / $10-15$ m (V)	6
Cat. II	$1 \cdot 10^{-9}/15$ s	17.3 m (H) / 5.3 m (V)	1
Cat. III	$1 \cdot 10^{-9}/15$ s	15.5 m (H) / 5.3 m (V)	1

* NPA - Non-Precision Approach; APV - Approach Procedure with Vertical guidance;

* Cat. - Category

Vertical approaches have been a subject of more intensive research as the majority of operations are not problematic in a sense of the availability of a method that satisfies integrity requirement [26, 27].

In addition to the development of methods for vertical approaches, availability of multiple GNSS constellations has introduced a need for new developments. Although multi-GNSS data can be utilised to produce a result of better accuracy and greater measurement redundancy, there is also a higher probability of satellite failure than for GPS only [28]. The availability of multi-GNSS led to the development of Advanced RAIM (ARAIM).

In addition to the existing algorithms and systems, Satellite Autonomous Integrity Monitoring (SAIM) algorithms have been proposed [29, 30]. One of the main benefits of SAIM argued by [29] is the capability of the "reduction of probability of latent space-segment failures being present in user measurements". When a failure is detected, SBAS and GBAS need to determine if it is a result of a satellite failure or there is a different source. SAIM would enable transmission of immediate warnings to the users when a satellite failure occurred. A further benefit of SAIM over SBAS/GBAS is the distribution of the monitoring since SAIM would monitor only the integrity of the satellite it is attached to. SAIMs are designed to be built into or added onto the navigation satellites to monitor the signal as it is being generated. In terms of RAIM, the SAIM aims to improve user integrity by providing information about satellite failures before faulty satellites affect the user [29].

In this section, I have highlighted some parts of the civil aviation integrity challenges. There are many more, and a lot of research effort is still put into this. Nevertheless, the IM of GNSS data in civil aviation has paved the way for the IM in different environments and for different applications.

2.3.2 Maritime applications

Another application that has to comply with the strict integrity requirements are maritime applications. Those requirements are given in a resolution made by the International Maritime Organization (IMO). Unlike civil aviation, where requirements for nine different flight operations are defined, IMO defines requirements for general navigation and specific positioning applications. Integrity requirements for general navigation are given in Table 2.2.

TABLE 2.2: GNSS maritime integrity requirements for general navigation [31].

Operation	**IR** $p_{IR}/3hr$	**AL** $[m]$	**TTA*** $[s]$
Ocean	$1 \cdot 10^{-5}$	25	10
Coastal	$1 \cdot 10^{-5}$	25	10
Port approach and restricted waters	$1 \cdot 10^{-5}$	25	10
Port	$1 \cdot 10^{-5}$	2.5	10
Inland waterways	$1 \cdot 10^{-5}$	25	10

* More stringent required for ships operating above 30 nm/h

TABLE 2.3: GNSS maritime integrity requirements for positioning [31].

AL	**Application**
25 m	Traffic management, track control, automatic collision avoidance, search and rescue, oceanography, casualty analysis, fisheries, recreation and leisure
$2.5 - 5$ m	Hydrography
2.5 m	Tugs and pushers, icebreakers, cable and pipeline laying, aids to navigation management, port operations, casualty analysis in port approach and restricted waters, offshore exploration and exploitation
0.25 m	Automatic docking, dredging, construction works, cargo handling*

* $TTA = 1$ s

Table 2.3 shows the ALs defined for different applications ranging from less stringent applications such as traffic management and search and rescue, to the more stringent applications such as automatic docking. IR and TTA are not shown as they remain $10^{-5}/3h$ and 10 s, respectively, for all applications.

Clear definition of these requirements is necessary as maritime applications highly rely on GNSS and GNSS augmentation technologies. A report commissioned by the Australian Department of Industry, Innovation, Climate Change, Science, Research and Tertiary Education [32], has presented both the economic and the ecological benefits of using augmented GNSS for maritime applications. For example, GNSS plays a key role in petroleum transport through the Great Barrier Reef region, which brings Australia AUD $17B$. A significant oil spill would cost in salvage and clean-up around AUD $30M$ and would have a damaging impact on industries such as fishing and tourism that bring in AUD $5B$ per year. Hence, augmented GNSS can improve the safety of maritime operations and having a clear definition of the minimum required GNSS performance is key in ensuring all vessels adhere to the same standards.

2.3.3 Railway

A list of reasons why GNSS has become important in railway has been provided in [33]. There, the authors list cost-driven reasons such as the introduction of intelligent and communicating trains and wagons, which improves the service. They also note the technological reasons. Europe is currently developing the European Rail Traffic Management System (ERTMS) which is intended to standardise the technology used and the signalling rules, which have historically been different for different countries. GNSS is the technology that will ensure interoperability and increase the capacity of railway lines [33]. Autonomous positioning of trains will then be enabled, which will have an impact on the safety functions of the train. Some examples of these functions include controlling the speed limit, controlling the direction, controlling that each train stays within its zone, controlling that points of different switches on rails are blocked, checking if an object or a person is on the track, etc. As in civil aviation and maritime applications, the use of GNSS in these safety functions requires the IM.

According to [34], unlike civil aviation and maritime applications, there are no standardised integrity requirements that all railway users need to adhere to. They cite examples of requirements that can be found in the literature. Those requirements are shown in

Table 2.4. Similar ALs have been defined in [33]. There 2 or 5 m, 20 m and 50 m have been defined for high density, middle density and low density lines, respectively. Similar ALs have been defined in [35] for corridor/station, non-corridor and regional lines. IRs of $3.5 \cdot 10^{-7}/150s$ and $2 \cdot 10^{-7}/hr$ for safety-of-life service have been defined in [35]. This is less stringent than the ones shown in Table 2.4. However, they also define the IR for local safety-of-life service as $2 \cdot 10^{-9}/150s$, which is more in line with requirements given in the table. The European Union funded project: ASTRail project[1] proposed GNSS minimum performance requirements in [36]. According to [36], IR of $1 \cdot 10^{-9}/hr$ is required for all operations in railway.

TABLE 2.4: GNSS railway integrity requirements [34].

Operation	**IR** p_{IR}/hr	**HAL** $[m]$	**TTA*** $[s]$
Main corridor lines, stations	$1 \cdot 10^{-9}$ or $1 \cdot 10^{-11}$	Along: 25 Lateral: 2.5	1
Main and secondary lines	$1 \cdot 10^{-9}$ or $1 \cdot 10^{-11}$	$25 - 125$	1
Regional and industrial lines	$1 \cdot 10^{-9}$ or $1 \cdot 10^{-11}$	$50 - 125$	1

The railway seems to require more stringent integrity requirements than civil aviation and maritime applications. The railway also faces similar issues of GNSS-challenged environment (as discussed in Chapter 1), which has resulted in the same need for hybridised solutions such as the ones proposed in [33] and [34].

2.3.4 Land-based applications

Land-based applications include agriculture, mapping and surveying, location based services and road applications. However, when writing about the IM for land-based applications, the literature refers to the road or ITS applications (e.g., [5]). This is because other applications do not use GNSS augmentation systems for the IM but for improving the positioning quality of the GNSS solution.

Similar to the railway, land-based applications do not have an internationally mandated set of minimum integrity performance requirements. This has resulted in a wide variety of integrity requirements in the literature (to be demonstrated in Section 2.5).

[1] https://cordis.europa.eu/project/id/777561

EGSA report [4] on the performance and level of integrity for ITS applications has provided a list of integrity requirements depending on the class of ITS applications: safety-critical (SCA), liability-critical (LCA) and regulatory-critical (RCA) applications. Some examples of SCA given in the previous chapter include autonomous driving and ADAS, such as anti-collision systems. The previous chapter also provided some examples of LCA, such as fleet management and toll charging. Lastly, the examples of RCA are eCall and navigation of emergency vehicles [4]. The requirements have also been specified for different categories of applications: stringent and loose. Although each specific application may require a different integrity level as seen in maritime applications, the requirements defined in [4] may help researchers determine the requirements appropriate for their applications. Table 2.5 shows the minimum required integrity levels as shown in [4]. It is to be noted that some values in Table 2.5 will be used in Chapters 3 and 6 for algorithm validation.

TABLE 2.5: GNSS integrity requirements for road applications as defined in [4].

	IR		**HAL**		**TTA**	
Operation category	Stringent (every 5 to 150s)	Loose (every 10min to 1h)	Stringent $[m]$	Loose $[m]$	Stringent $[s]$	Loose $[s]$
SCA	$1 \cdot 10^{-8}$ to $1 \cdot 10^{-7}$	$1 \cdot 10^{-7}$ to $1 \cdot 10^{-5}$	$5 - 10$	$10 - 25$	$1 - 6$	$6 - 10$
PCA	$1 \cdot 10^{-6}$ to $1 \cdot 10^{-5}$	$1 \cdot 10^{-4}$ to $1 \cdot 10^{-3}$	$10 - 20$	$20 - 40$	6	≥ 60
RCA	$1 \cdot 10^{-5}$ to $1 \cdot 10^{-4}$	$1 \cdot 10^{-4}$ to $1 \cdot 10^{-3}$	$10 - 25$	$25 - 50$	6	≥ 60

As defined in Chapter 1, this research focuses on integrity and IM for road applications. The literature review of the state-of-the-art in road applications will be provided in Section 2.5. However, to facilitate a better understanding of the described algorithms, Section 2.4 will firstly present two existing classical integrity algorithms used for PL calculation.

2.4 Classical integrity algorithms

According to the reviewed literature (e.g., [37, 38]) and inspired by [17], a high-level flowchart common to most IM algorithms has been created in Figure 2.4. The figure

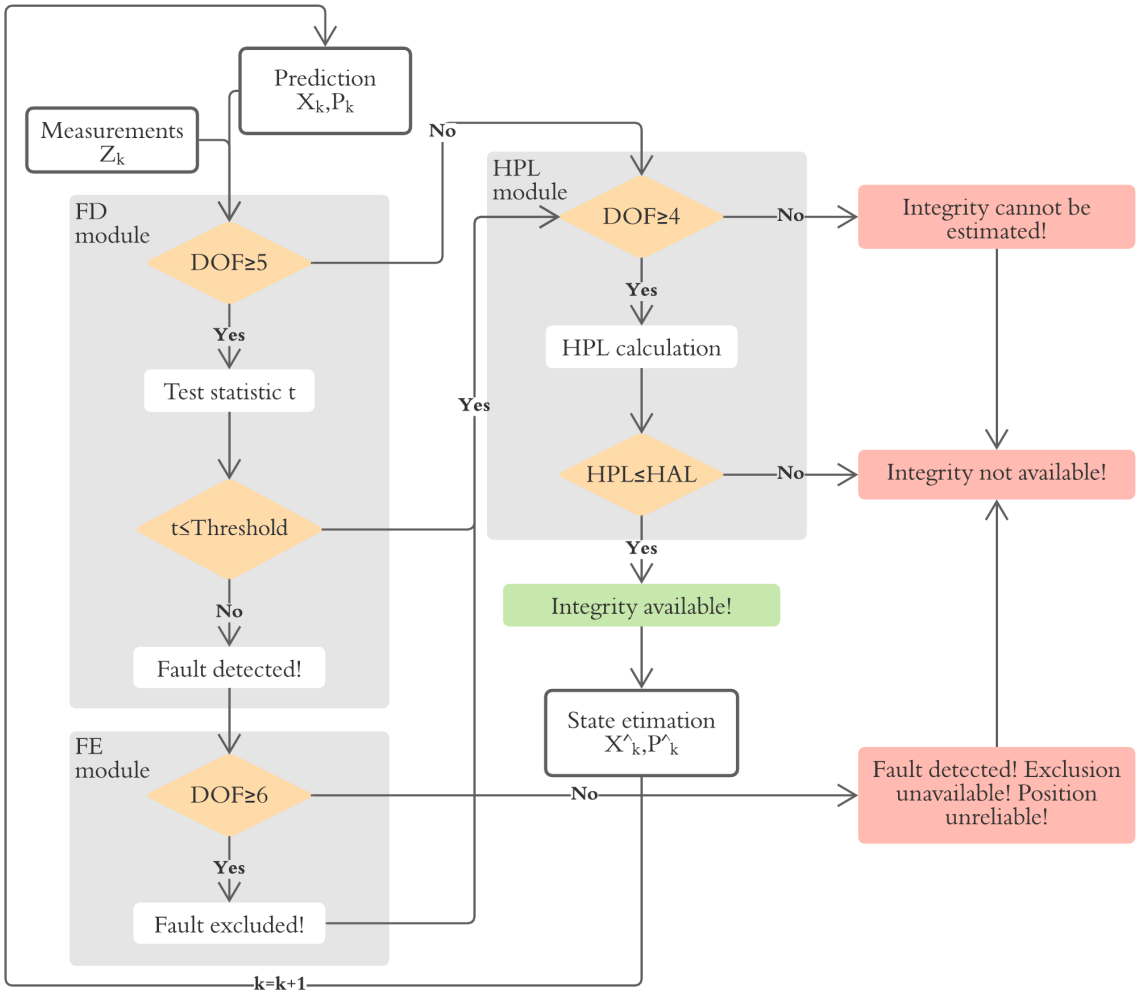


FIGURE 2.4: Flowchart of classical integrity algorithms consisting of three modules: Fault Detection (FD), Fault Exclusion (FE) and HPL modules tasked with integrity availability determination.

shows the process of IM as a three step process consisting of fault detection (FD), fault exclusion (FE) and Horizontal PL (HPL) calculation, given the sufficient measurement redundancy. The Fault Detection and Exclusion (FDE) algorithms are intrinsic to the IM algorithms. They work on a principle of using the measurement residuals to calculate the test statistic used to determine if faults are present and by eliminating the measurement with the largest residual. FD and FE will not be explained here, as they will be the focus of a later chapter.

This section presents two classical integrity algorithms for HPL estimation, designed for GNSS integrity in civil aviation applications. The first algorithm is formulated in essentially the same way as SBAS and can be found in [37]. The second presented algorithm is Weighted Least Square Residual (WLSR) RAIM and can be found in [38] and [39]. It should be noted that all presented algorithms refer to HPL since this research focuses on the horizontal component of the position. A formulation for calculating Vertical PL (VPL)

is shown in respective references. Some other classical algorithms are range-comparison method and solution separation RAIM [21]. [21] shows the equivalence of these two methods and the Least Squares Residual method given the Gaussian assumption and if equal alarm rates are chosen.

2.4.1 SBAS Protection Level calculation

The underlying algorithm for position estimation is Weighted Least Squares (WLS). Since the equations of WLS are well known, the basic equations and their derivations will not be explained here in detail. More on WLS can be found in [40]. The starting point of the HPL calculation is setting up the measurement model for WLS position estimation.

$$\Delta Z = H\Delta X + E. \tag{2.1}$$

ΔZ denotes the measurement deviation between the measurements and predicted measurements. ΔX is a state vector (consists receiver's 3D position and clock bias estimates). H denotes the measurement matrix generated by linearisation of the non-linear measurement model around predicted (i.e., initial) state vector. H is determined by the geometry between satellites and the user. E is the measurement error vector. The WLS estimate $\Delta\hat{X}$ of ΔX can then be calculated using

$$\Delta\hat{X} = \left[H^T W H\right]^{-1} H^T W \Delta Z. \tag{2.2}$$

W is a measurement weight matrix often calculated as the inverse of the covariance matrix Σ (i.e., $W = \Sigma^{-1}$). In this case, the covariance matrix is a diagonal matrix with diagonal elements being the variances of each of the available satellites σ_j^2 where $j \in 1, \ldots, N_S$. Finally, the estimated position can be calculated as $\hat{X} = X^o + \Delta\hat{X}$.

Given that the ground truth is unavailable during the position estimation process, the RAIM methods usually depend on the measurement residual which can be expressed as a deviation between measurements and calculated measurements based on the estimated $\Delta\hat{X}$ as

$$res = \Delta Z - H\Delta\hat{X}. \tag{2.3}$$

After derivation using Equation 2.2, as shown in [39], measurement residual can be expressed as

$$\begin{aligned} res &= \left(I - H\left[H^T W H\right]^{-1} H^T W\right)\Delta Z, \\ res &= \left(I - H \cdot S\right)\Delta Z, \end{aligned} \tag{2.4}$$

where $S = \left[H^T W H\right]^{-1} H^T W$. Calculated residuals can be used for implementation of FDE algorithms. However, the focus of this section is HPL calculation where S matrix becomes a central part. As shown in [37], HPL can be calculated using the following equation

$$HPL = K_{\text{ffmd}} d_{\text{major}}. \tag{2.5}$$

K_{ffmd} is a missed detection multiplier which is defined using the required IR p_{IR}.

$$K_{\text{ffmd}} = -\sqrt{2} \cdot \text{erfcinv}\left(2 \cdot \left(1 - \frac{1 - p_{IR}}{2}\right)\right). \tag{2.6}$$

erfcinv denotes the inverse complementary error function. This parameter stays constant for the duration of the experiment. d_{major} denotes the 1σ standard deviation of the position that is to be estimated in the direction of the major axis of the error ellipse. This means that HPL is estimated for the worst-case horizontal error. d_{major} is calculated as follows

$$d_{\text{major}} = \sqrt{\frac{d_x^2 + d_y^2}{2} + \sqrt{\left(\frac{d_x^2 - d_y^2}{2}\right)^2 + d_{xy}^2}}. \tag{2.7}$$

x and y are horizontal coordinates and can refer to any local coordinate system or grid reference system. d_x^2, d_y^2 and d_{xy} are the error variances in the direction of the x and y axis, and covariance between the x and y, respectively. They are estimated by propagating the measurement variances through the measurement model as shown,

$$\begin{aligned} d_x^2 &= \sum_{m=1}^{N_S} S_{x,m}^2 \sigma_m^2, \\ d_y^2 &= \sum_{m=1}^{N_S} S_{y,m}^2 \sigma_m^2, \\ d_{xy}^2 &= \sum_{m=1}^{N_S} S_{x,m} S_{y,m} \sigma_m^2. \end{aligned} \tag{2.8}$$

S_x and S_y are the x and y elements of the S matrix for satellite m from Equation 2.4.

It should be mentioned, the estimated HPL is proportional to the Horizontal Dilution Of Precision (HDOP) which is often used in geomatics to quantify the network geometry quality. In case of GNSS data, network geometry refers to the observed satellite geometry. HDOP is calculated as,

$$R = \left(H^T H\right)^{-1}, \tag{2.9}$$

$$HDOP = \sqrt{\sigma^2_{R,x} + \sigma^2_{R,y}}. \tag{2.10}$$

$\sigma^2_{R,x}$ and $\sigma^2_{R,y}$ denote the diagonal elements of R matrix referring to the x and y coordinates.

Given that the measurement model is linearised, the user/satellite geometry is known, and the measurement errors are assumed to be Gaussian, measurement errors can be propagated through the measurement model without knowledge of the estimated position. Consequently, this algorithm and the following one can be used for predicting achievable integrity levels for different applications with different requirements (i.e., p_{IR} and HAL), different user/satellite geometry and assumed GNSS availability.

2.4.2 WLSR Protection Level calculation

According to [38], WLSR RAIM's HPL is "derived from the smallest bias the algorithm is able to detect satisfying the false alarm and missed detection requirement." According to [38] and [39] HPL can be calculated as a product of p_{bias} and the maximum horizontal slope function $HSLOPE_{max}$ that refers to the worst satellite,

$$HPL = HSLOPE_{max} \cdot p_{bias}, \tag{2.11}$$

where, as in [38],

$$p_{bias} = \sigma_m \sqrt{\lambda}. \tag{2.12}$$

λ is the non-centrality parameter that does not depend on measurements. It is a function of probability of missed detection p_{MD}, degrees of freedom DOF and fault detection threshold Th which, as shown in 2.13, depends on the probability of false alarm p_{FA} and DOF [39]. Th achieves fault detection at p_{FA} rate under the fault free conditions.

$$p_{FA} = 1 - cdf_{\chi^2_{DOF}}\{Th\}. \tag{2.13}$$

Then, λ can be defined as the non-centrality parameter "of the test distribution in a faulty case that results in a missed detection rate p_{MD}" [39],

$$p_{MD} = cdf_{\chi^2_{DOF,\lambda}}\{Th\}. \tag{2.14}$$

The non-centrality parameter is the smallest detectable, with the probability equal or lower p_{MD}. [38] and [39] provide a relationship between λ and the minimum detectable bias magnitude for each satellite. With further derivation, a relationship between λ and bias projection in the horizontal error $|b_H|$ can be expressed as,

$$|b_H| = HSLOPE_m \cdot \sigma_m \sqrt{\lambda}, \tag{2.15}$$

where

$$HSLOPE_m = \frac{\sqrt{S^2_{x,m} + S^2_{y,m}}}{\sqrt{1 - HS_{m,m}}}, \tag{2.16}$$

and

$$\begin{aligned} \underset{4\times N_S}{S} &= \left[H^T W H\right]^{-1} H^T W, \\ \underset{N_S \times N_S}{HS} &= H \left[H^T W H\right]^{-1} H^T W. \end{aligned} \tag{2.17}$$

Each satellite m has its own slope where $S_{x,m}$ and $S_{y,m}$, denote x and y elements of the S matrix and $HS_{m,m}$ denotes the element of matrix HS. The highest slope indicates which satellite is the most difficult to detect [39].

$$HSLOPE_{max} = \underset{m}{max}(HSLOPE_m), \tag{2.18}$$

2.5 Integrity for Intelligent Transport System

In recent years, a couple of literature review papers has been published on the IM of GNSS in urban environments [17, 41]. Stand-alone GNSS approaches and reporting on different proposed methods for stand-alone GNSS are the focus of [17]. [41] presents different FDE methods, as well as the different integrity methods such as Advanced RAIM (ARAIM), Relative RAIM (RRAIM), Extended RAIM (ERAIM), Carrier-based RAIM (CRAIM), Time RAIM (TRAIM) and Vision-Aided RAIM (VA-RAIM).

However, a comprehensive literature review of the state-of-the-art in the integrity estimation techniques applied and validated for urban environments is not yet available. In this thesis, a review of the literature from the perspective of road applications (i.e., ITS) is provided. Specifically, implemented integrity and positioning algorithms will be looked into, what integrity requirements were used, what level of integrity was achieved, what sensor technology was used and were the algorithms validated on real or simulated data. An additional aim of this section is to highlight the way existing algorithms have been adapted to the urban environment.

To do this, this review has been divided into sections depending on the used technology relevant to the urban environment. The three sections will review available implementations of the integrity algorithms for stand-alone GNSS, multi-sensor systems and lastly, for the cooperative systems. Within each of these sections, a variety of integrity algorithms and used technologies for integrity estimation will be covered.

2.5.1 Stand-alone GNSS integrity

The simplest positioning system that can underlie an IM algorithm for an urban environment can be based on stand-alone GNSS. As mentioned, given the reduced satellite availability in urban environments, this can prove to be a challenge. Nevertheless, there are many examples of research done on stand-alone GNSS integrity where the algorithms have been adapted to the environment.

In [15], a modified WLSR RAIM is proposed for the Electronic Toll Collection (ETC) in the urban and rural environment. The biggest issue of employing the classical WLSR RAIM (Section 2.4.2) in urban environments is the reduction of the number of valid positions reported by the IM due to the increase of the HPL. This happens because of the satellite/user geometry degradation and reduction of satellite visibility. To mitigate this problem, [15] proposes a trade-off between the RAIM availability and restriction on maximum p_{FA}, which modifies the WLSR RAIM to constant-probability-of-detection RAIM. This means that p_{FA} is not limited by the integrity requirement (i.e., it changes). By doing this, the WLSR RAIM is always available since the HPL is equalised with HAL, which makes it constant. As pointed out in [15], this leads to high FA probabilities for satellites with high slopes. The performance of this algorithm has been evaluated on the GPS and Galileo LOS pseudoranges simulated in rural and urban data through the generation of buildings of varying heights. HAL values of 25 m and 50 m have been used as

the integrity requirements. According to [4] those values are not stringent enough for ETC for which they cite $10 - 20$ m for stringent and $20 - 40$ m for loose PCA (Table 2.5). In addition to said HAL values, p_{MD} of $5 \cdot 10^{-5}$ and two values for p_{FA} of $5 \cdot 10^{-3}$ and $5 \cdot 10^{-5}$ have been used. [15] has demonstrated that the gain of RAIM availability compensated for the increase of FA rate. The expected benefit of dual constellation receivers was also demonstrated with the undercharging rates of several orders of magnitude lower than for the GPS only.

Another algorithm based on the stand-alone GNSS and WLS is presented in [42]. The authors present a complete IM scheme for road applications and test it on the real-world data collected in the urban environment of Nantes, France. One of the adaptations to the urban environment has been made through the use of the hybrid pseudorange weighting model based on the satellite elevation, signal-to-noise-ratio and LOS/NLOS indicator. This indicator is defined by utilising the Urban Multipath Model (UMM) which identifies the NLOS signals based on the 3D map, which ensures higher weighting of the LOS pseudoranges. The HPL is calculated by summarising the SBAS HPL and WLSR HPL. The main motivation behind this is the fact that the former method provides HPL estimate based on the impact of the measurement noise on the user position, and the latter one provides HPL estimate based on the impact of the measurement bias on the user position [42]. The results show the best median HPL of 12.4 m is achieved for values of $p_{FA} = p_{MD} = 10^{-2}$. Chosen probabilities may not be stringent enough for most applications in the urban environment.

An IM algorithm that consists of three phases of integrity checks: positioning integrity, speed integrity and Map Matching (MM) integrity is proposed in [43]. Even though GPS and wheel speed data are used, the proposed algorithm is not an example of multi-sensor IM. Wheel speed information is used to validate the reliability of the GPS Doppler speed data, which is actually used for speed integrity module. Three separate phases of integrity checks happen in sequence and not simultaneously. Firstly, WLSR RAIM (from Section 2.4.2) and FD are used for the position integrity module. Values $p_{FA} = 10^{-3}$, $p_{MD} = 10^{-5}$ and $HAL = 15$ m are chosen as position integrity requirements. If a fault is not detected, the algorithm moves on to the speed integrity module. If an error is not detected there, MM integrity phase can start. This includes topological MM and a Fuzzy Inference System (FIS) to reason about the uncertainty of MM results. The main issue of this algorithm is that each module's conditions need to be satisfied to move on to the next one. This may be problematic in terms of implementation in urban environments

where the first module could run into the issues of availability as demonstrated in [15]. The Overall Correct Detection Rate (OCDR) (Equation 2.19) for experimental GPS data collected in an urban environment is 98.24%, 99.23% in a rural environment and 97.20% in a mixed environment [43, 44]. However, these numbers include the correct detection of availability and unavailability. Integrity was correctly classified as available 72.93%, 89.30% and 71.49% of the time, respectively. That is consistent with reduced availability of satellites in the urban environment, using the civil aviation algorithm implementation.

$$OCDR = 1 - FA\ rate - MD\ rate. \tag{2.19}$$

Similar to [44], sequential map-aided IM for GPS is proposed in [45]. Firstly, HPL is calculated by employing a WLSR HPL like method, characteristic of the operational environment is checked (urban or rural?) and the integrity of MM is determined. [45] also used OCDR as a measure of success rate. For real-world data collected in mostly urban and suburban environments, success rates of 98.2% and 99.4% were achieved, respectively. However, it was not possible to calculate the integrity availability and unavailability (correctly classified) as it was for [44]. [45] used the same integrity requirements as [44].

Some methods implement a combination of GPS and SBAS. For example, [46] calculates SBAS HPL for GPS/EGNOS combination. However, SBAS satellites have the same satellite visibility issue in the urban environment as the GNSS satellites. This is addressed in [46]. They propose an architecture where, during NLOS of EGNOS, the system switches to broadcasting SBAS messages via the internet. During the satellite visibility, HPL values range from $5 - 15\ m$. When EGNOS satellite is not visible, 12% of HPL values grow to $\sim 20\ m$ and peaks ranging from $200 - 450\ m$ occur. These peaks occur due to the major identified issue of latency of SBAS messages communicated via the internet. Although certain application requirements would be satisfied by this performance (e.g., biohazard goods hauliers tracking [46]), the majority of urban environment applications would not.

Many other algorithms that are not based on WLSR and SBAS methods are proposed. For example, an IM method applying Non-Linear Information Filter (expressed as another form of an Extended Kalman Filter (EKF)) and a Log-likelihood ratio test is proposed in [47]. However, the authors do not test their proposed algorithm in terms of determining the PLs. Another example is the Bayesian RAIM (BRAIM) algorithm proposed in [18], which is based on the Particle Filter (PF) as the underlying position estimator. The integrity metric is calculated based on the *a posteriori* distribution, which means that the integrity

is estimated directly in the position domain. So far, all the presented examples have estimated the integrity in the measurement domain since they were based on the analytical estimators (i.e., closed-form expressions for error propagation are available). Unlike all the previous algorithms where the estimated integrity metric was expressed by the HPL, BRAIM estimates the probability of misleading information. The BRAIM was tested on the simulated random 100 trajectories with the constellation of six satellites where a large error was injected for two satellites of lower elevation. The presented algorithm in [18] has multiple benefits such as simplicity, no restrictions on geometry, number of satellites and number of faulty measurements. As such, it seems to fit well with the complexity of the urban environment where many of the listed items cannot be guaranteed. However, [18] tests BRAIM on loose integrity requirements of 50 m and 150 m for HAL. For such requirements, 8% of cases of insufficient integrity were false alarms, and 56% of cases of sufficient integrity classification were misleading information (i.e., missed detection MD). [48] propose a RAIM method for GPS only using the improved PF based on the genetic algorithm for detecting satellite failures. In addition to that, a bank of auxiliary PFs is used to aid failure detection. Unlike other methods, [48] simulates a Gaussian core-Laplacian tail Probability of Density function (PDF) as the pseudorange distribution for six satellites. This is explained by the fact that the tail part of the distribution can be heavier due to errors such as multipath. However, as observed before, the proposed algorithm is not validated in terms of integrity but in terms of PE improvement.

At the start of this chapter, IM was defined as a capability to detect and exclude faults and raise an alarm if the positioning system is deemed unsafe. However, it should be noted that a lot of available literature, when talking about the IM refers to the development of FDE as an important part of the IM. Hence, a lot of literature does not estimate the integrity but looks at the effectiveness of the FDE through the positioning performance. For example, both [49] and [50] propose multi-GNSS WLSR-based IM methods for GPS and GLONASS data, and GPS and BeiDou data, respectively. However, they never estimate the integrity. Nevertheless, the fact that so much research is being done on improving FDE as the essential part of the IM, shows how significant the problem of FDE for ITS applications is, and that it requires attention.

The majority of the presented algorithms would not satisfy stringent integrity requirements nor some of the loose requirements shown in Table 2.5. As previously stated, the way this issue can be approached is through the employment of multi-sensor IM methods.

2.5.2 Multi-sensor integrity

When it comes to the IM of land-based applications, the solution is most commonly based on the multi-sensor positioning system. By fusing the multi-sensor data, measurement redundancy can be achieved even in urban environments. Inertial measurement unit (IMU) and dead-reckoning (DR) sensors are the most commonly combined sensors with GNSS. [11] and [12] list different technologies used in the context of multi-sensor IM. Some of the mentioned methods are — Radio Detection and Ranging (RADAR) such as Ultra-Wide Band (UWB) radios, Light Detection and Ranging (LIDAR), visual sensors such as cameras, sensors that enable inter-vehicular communications and communication with infrastructure such as Dedicated Short Range Communication (DSRC), UWB and Dedicated Omni-purpose inter-vehicle communication Linkage Protocol for Highway Navigation (DOLPHIN).

One of the more prominent ways of fusing multi-sensor data is through the EKF estimator. As a result, it is understandable that the EKF is commonly used as the underlying position estimator for multi-sensor integrity.

An example of this is given in [51] where an integrity algorithm based on the fusion of GPS, EGNOS and IMU data using the EKF is proposed. In their framework, the SBAS HPL algorithm is used to calculate GPS and EGNOS HPL values. When GPS data and EGNOS data are not available, SBAS HPL cannot be calculated. [51] proposes the usage of Horizontal Trust Level (HTL) which is calculated as a 6-sigma value of the maximum horizontal standard deviation. The HTL values ranged from 6 to 7 m and as expected, the HTL values deteriorate as the satellite visibility gets reduced. The authors did not provide HPL values for the periods of satellite visibility. Nevertheless, they have demonstrated that even when satellite visibility is reduced, integrity estimate can still be provided due to the use of IMU data.

Another example of multi-sensor IM based on EKF can be found in [52]. The proposed framework is based on cellular long-term evolution (LTE) signals (modelled as pseudoranges) and IMU. The absence of GNSS in their system is valid in terms of applicability of the system in the complex urban environment where GNSS signals are sparse. However, when it comes to remote areas where it is fair to assume that cellular signals weaken and that the network density of the cellular transmitters decreases, the fusion with GNSS is necessary since it will probably become a primary source of reliable measurements. HPLs are estimated in a way similar to the WLSR HPL method shown in Section 2.4.2. The

performance of the IM algorithm proposed in [52] was tested on real-world data collected in an urban environment with five cellular transmitters in the vicinity. The results indicate that HPLs range from 15 m to 30 m. A HAL of 35 m was used as a requirement. However, it is unclear what were the required probabilities of FA and MD. The same authors conducted further experiments in [53] where they used $p_{FA} = 1 \cdot 10^{-3}$ and $p_{MD} = 5 \cdot 10^{-4}$. Then, the observed HPL was ranging from 5 m to 15 m due to the proposed algorithm accounting for multipath and unmodelled biases in cellular pseudoranges.

Multi-sensor IM can also utilise the visual data to estimate integrity. A Simultaneous Localisation and Mapping (SLAM)-based IM algorithm is proposed in [54]. Vehicles and a landmark are being localised by means of graph optimisation. GPS data, vehicle dynamics and pixel intensities from fish-eye cameras are used. The proposed algorithm is validated on real-world data collected in the semi-urban environment. HPLs of 10 to 15 m are achieved. However, it is not clear what FA and MD probabilities were used as integrity requirements. A similar concept has also been shown in [55] where an IM of an integrated GPS/Galileo receiver, IMU and Fish-eye camera is proposed.

Classical RAIM algorithms view integrity as a separate issue to the state estimation. They estimate the integrity based on the assumption of correctness of the state estimate and based on the associated measurements [56]. This effectively makes integrity estimate biased given the one tested the hypothesis with respect to faulty measurements (e.g., single state estimate for WLS or EKF). Similar to [18], [56] proposes Particle RAIM where integrity monitoring is jointly estimated with the state estimation. The proposed Particle RAIM uses multiple hypotheses (i.e., particles) related to different measurements and their faults to estimate the joint integrity based on the *a posteriori* state distribution. The Particle RAIM proposed in [56] is validated for 50 simulated trajectories with assumed five visible satellites and available odometer and heading measurements. AL of 20 m was used. The authors have concluded that the Particle RAIM fails to bound the IR with a small AL.

Another IM solution for multi-sensor PF and for MM is proposed in [57]. The multi-sensor system is based on the fusion of GNSS, gyroscope and odometer data. These data are used in addition to the enhanced maps for lane-level IM. The proposed algorithm provides a common solution for position and MM integrity. The MM confidence is calculated as a sum of normalised weights of particles (i.e., position hypotheses) that are within the lane. This confidence is compared with the threshold probability of 0.86. Then the position integrity is estimated by calculating Lane Positioning Protection Level (LPPL) based on

the constant $p_{MD} = 10^{-2}$ and position covariance. Calculated LPPL is compared with the required $HAL = 1.5\ m$. The chosen p_{MD} value may be too loose for ITS applications that may require lane-level integrity. The algorithm was validated on experimental data collected in Nantes, France and Berlin, Germany in a semi-urban environment. OCDR ranges from 85.22% in cases when GPS masks were simulated to 99.21% under normal conditions. The rates of correctly classified integrity availability and correctly classified integrity unavailability are unclear. This algorithm proposes an interesting way of fusing multiple sensors, implementing MM and estimating integrity for both. Unlike, classical RAIM algorithms where position does not have to be estimated for integrity to be evaluated, here, position estimation is necessary as in previously discussed BRAIM [18]. This happens due to the underlying positioning algorithm, i.e., PF, for which closed-form expression for error propagation is not possible due to its non-linearity and possible non-Gaussianity.

So far, all the mentioned algorithms have been implemented for code-based GNSS pseudoranges. If lane-level integrity is required for a given ITS application, the literature indicates that phase-based GNSS measurements or Real-Time Kinematic (RTK) GNSS have to be used.

[58] presents an integrity monitoring algorithm for tightly-coupled Precise Point Positioning (PPP) and IMU integration. A bank of EKFs is used as the underlying positioning algorithm for the algorithm originally developed for ARAIM and is based on the solution separation RAIM. The proposed method is validated on data collected on a highway and in a suburban environment in Calgary, Alberta, Canada. Their multi-sensor solution results in HPL of $1 - 2\ m$ and $3 - 4\ m$ in the suburban environment and on the highway, respectively. When only PPP is used, during signal outages, it takes time until the HPL values converge due to carrier phase ambiguities having to be re-estimated. However, as expected, once the IMU is introduced, these jumps in HPL value do not happen. It is unclear what integrity requirements were used in [58].

[59] compares the performance of Multiple-Hypothesis Solution Separation (MHSS) (bank of KFs) and Innovation Sequence (IS) (single KF) integrity techniques for automotive IMU/GNSS system. In addition to that, the dynamics of the vehicle are constrained. For example, restricted lateral movement of the vehicle can be used to reduce the drift due to yaw gyroscope and lateral accelerometer biases. The integrity requirements used in [59] are $p_{FA} = 10^{-6}$, a prior fault probability for hypotheses of 10^{-5}, and $HAL =$

0.5, 1, 2, *and* 3 m. Both algorithms have been tested for four, five and six visible satellites. Differential GPS data with PPP accuracy was simulated to test and validate these algorithms. To somewhat realistically model the effect of multipath in an urban canyon, stochastic models obtained from data collected on a highway were used. The results indicate that dynamic constraints have helped to bound the IR and HPL. Without dynamic constraints, MHSS outperforms IS and achieves IR of 10^{-18} to 10^{-17} and 10^{-9} to 10^{-5} for $HAL = 1$ m for six and four visible satellites over a period of one hour, respectively. Despite the use of IMU data, when geometry quality and the number of satellites reduces, the IR reduces significantly as well. Once the dynamics are constrained, MHSS is able to achieve IR levels of 10^{-7} for four satellites (no GNSS redundancy). The authors have demonstrated that tightly-coupled IMU/GNSS integration can achieve sub-metre HPLs for different values of IR. They have also shown that tightly-coupled architecture can reduce IMU instrumental drift with only a few satellites available. However, integrity performance is not preserved in that case.

Some available research uses RAIM algorithms implemented in commercially available software such as Hexagon Positioning Intelligence's [1] PPP filter using TerraStar X corrections [60]. The achieved HPL for stand-alone automotive-grade GNSS receiver and IMU/GNSS system is presented in [60]. They test the integrity in three different environments: an open-sky environment in Canada; highway/rural environment in the USA and highway/-suburban environment Germany. For stand-alone GNSS, for integrity risk of $10^{-7}/hr$ and $HAL = 3$ m, 95% of HPL are within 1.04 m, 5.63 m and 21.66 m, respectively. As expected, as the environment becomes more complex, the HPL values deteriorate. Since the PPP measurements are used, when outages happen, especially in a highway/suburban environment, the initialisation of GNSS significantly impacts the integrity performance as was shown in [58]. Once automotive-grade IMU is integrated with PPP GNSS, 95% of HPL values are within 14.12 m for highway/suburban environment.

Lane-level integrity levels have been achieved in [61] and [62]. To achieve this, [61] combines RTK, Doppler-based positioning and IMU with the vehicle speedometer. Similarly, [62] combines the same sensors except the vehicle's odometer is used instead of the speedometer. During RTK outages, the proposed system uses Doppler-based velocity to estimate the position. If this is also unavailable, the position can be determined based on the vehicle's speedometer or odometer, and the IMU data [61, 62]. Furthermore, both of the

[1] https://hexagonpositioning.com/ and https://hexagondownloads.blob.core.windows.net/public/Novatel/assets/Documents/Papers/RAIM/RAIM.pdf

papers provide the formulation used to calculate RTK HPL and Doppler/IMU HPL. The algorithms were tested on the same experimental data collected in Tokyo, Japan. Different values of IR were used to test the algorithm presented in [61]. Those ranged from $1 \cdot 10^{-3}$ to $1 \cdot 10^{-7}$. $p_{FA} = 1 \cdot 10^{-2}$ was chosen. The authors tested the integrity performance of the proposed IM algorithm on four GNSS constellation combinations — GPS only, GPS and BeiDou, GPS and GLONASS, and a combination of all three. Similar median HPL was observed no matter what IR is used and is in all cases smaller than 0.3 m. This would mean that for, correct ambiguity fixing, HAL can be between 0.5 and 1 m, and the availability will be larger than 99%. Furthermore, RTK was available from 88% to 96% of the time (depending on the used GNSS combination). A different point of view was taken when testing the proposed algorithm in [62], where RTK, Doppler positioning, IMU and odometer data were used. The algorithm was tested for IR ranging from $1 \cdot 10^{-3}$ to $1 \cdot 10^{-6}$. The same p_{FA} was used. In these experiments, RTK (GPS, GLONASS, BeiDou) was available 72.2% of the time. Doppler-based positioning was then employed 25.8% of the time and finally, the IMU/odometer the remaining 2% of the time. RTK HPL remained as in the previous results (lower than 0.3 m). However, the median Doppler-based HPL exceeded 2 m, and IMU/odometer HPL stayed under 2 m. These results refer to the IR of $1 \cdot 10^{-6}$. The results do not show how these values changed once $1 \cdot 10^{-7}$ IR was chosen.

2.5.3 Cooperative integrity

With the development of inter-vehicular networks and communication technologies, the integrity monitoring of cooperative positioning systems has recently become an area of interest. To the author's best knowledge, not a lot of research has been carried out in the field of cooperative IM, and there are a lot of opportunities to contribute. Only a few recent papers have been found that discuss the integrity of cooperative positioning systems.

A Cooperative IM (CIM) algorithm is proposed in [63] and [64]. However, the proposed algorithm does not estimate the integrity. CIM exploits the GNSS and inter-vehicle UWB measurements for FDE only based on the decentralised EKF via the innovation decomposition method and cooperative innovation estimation. Furthermore, CIM is validated on simulated GNSS and UWB data.

Cooperative integrity has been researched throughout the years by Liu et al. [65–70]. Their CP framework is based on the GNSS and DSRC inter-vehicle ranging. In [66], a method of bounding the cooperative localisation estimate is proposed. One of the components of the proposed bound is calculated as the SBAS HPL shown in Section 2.4.1. [68] employs method presented in Section 2.4.2 under the cooperative environments. However, cooperative IM is not demonstrated, and both of the proposed methods are validated on simulated data. An improved RAIM method using vehicle-to-vehicle communication (i.e., DSRC) with the Cubature KF as the underlying position estimator was proposed in [65, 67, 69, 70]. The HPL in [67] is calculated based on the method presented in Section 2.4.2. However, the presented method does not demonstrate the cooperative IM algorithm as it uses DSRC ranges only to simulate virtual satellites. The authors achieve HPL of $\sim 25\ m$ for $p_{FA} = 1 \cdot 10^{-5}$ and $p_{MD} = 1 \cdot 10^{-3}$ under the simulated scenario of four BeiDou satellites and one virtual satellite. Additional work on the IM algorithm using the cooperative DSRC measurements is presented in [65]. However, the focus of that paper is on the FDE capability of the proposed algorithm. In both [67] and [65], cooperative DSRC ranges are used to generate the forward estimate of the vehicle's position. Using that position, virtual pseudoranges are calculated based on the known position of the NLOS satellites. Then LOS pseudoranges and virtual pseudoranges are used for IM. Similar is done in [69] where solution separation RAIM method was used instead of previously used WLSR HPL calculation. [70] presents a conservative HPL calculation method where HPL is calculated as a combination of the WLSR HPL method using the residuals, a similar method using the Kalman gain matrix and HPL component based on estimated error covariance. Although the cooperative DSRC ranges have been utilised to rebuild pseudoranges from the NLOS satellites, this proposed method does not represent a true cooperative IM algorithm as cooperative measurements were not part of the integrity estimation. Authors have also identified several problems concerning the forward estimation, some of which are clock synchronisation error between all the cooperating vehicles and the position error of the neighbouring vehicles. As before, due to the complexity of the algorithm validation for cooperative vehicular networks, data were simulated. It is important to note that, although not cooperative, methods presented in [65, 67, 69, 70] have successfully mitigated the issue of reduced GNSS availability in GNSS-challenged environments.

[71] presents an algorithm for FDE and integrity for GNSS-based CP. The importance of FDE in cooperative networks is emphasised as the fault in one user can influence the other

users and result in large PEs. Centralised CP EKF is chosen as the underlying positioning algorithm for the fusion of GNSS data and terrestrial range measurements. The solution separation ARAIM method is implemented to detect and exclude faults in the simulated data, and the performance is evaluated on the effect of fault exclusion on the PE. The integrity (i.e., PL) is not estimated.

A distributed cooperative SLAM-based IM algorithm is proposed in [72]. Like in [63], UWB data were used for inter-vehicle ranging in addition to the GPS data. Unlike other presented methods, [72] estimates the PLs while accounting for faults in the GPS and the UWB data. The PLs are calculated using the worst-case failure slope method. The algorithm is validated on a sparsely connected network of six simulated vehicles where some of them are driving in an open-sky area, one of them is static in the open-sky area, and some of them are driving in a semi-urban area. Each vehicle processes data received from other vehicles which includes their positions and inter-vehicle ranges. The results indicate that the distributed cooperative solution performs better than the stand-alone SLAM IM. The average estimated PLs range from 1.8 m for a vehicle in the open-sky to 5.4 m for the vehicle in the semi-urban area. However, it is unclear what integrity requirements (e.g., p_{IR}, p_{FA} or p_{MD}) were used to achieve these PLs.

One of the major points that all of these papers have in common is the emphasis that they put on the FDE of cooperative/hybrid solutions. Effective FDE methods need to be found as the cooperative networks introduce new fault modes which can be distributed across the vehicle network. These papers propose interesting methods for improvement of the cooperative IM. However, only [72] proposes and validates an integrity method which estimates integrity while accounting for faults for multiple sensors that are part of the cooperative solution.

2.6 State-of-the-art summary

This chapter has presented an extensive literature review of the state-of-the-art of the IM and the integrity algorithms for road applications. Based on the presented literature review, the following summary can be made:

1. There are no defined integrity requirements that every algorithm has to aim for depending on the application (as seen in maritime applications) or a phase of an application (as seen for civil aviation). Except being a relatively novel field of research

and having a large diversity of algorithms with different integrity metrics, one of the major factors may be the lack of international organisational involvement. As shown, ICAO and IMO have regulated navigation performance requirements for every civil plane and every vessel, respectively. Such an organisation does not exist for road applications as the technology, traffic regulations, and signage are not standardised internationally. Consequently, integrity requirements are not standardised as well. A similar inference has already been made for railways (see Section 2.3.3).

2. Some additional points can be made about integrity requirements:

   (a) Time reference (e.g., $1 \cdot 10^{-7}/hr$ or $1 \cdot 10^{-7}/150\ s$) is often not specified in the literature. However, it is clear in all the tables in Section 2.3 that a time reference for the IR should always be provided.

   (b) Integrity requirements used to produce results and validate proposed algorithms are often not specified in the literature. Without this, it is not possible to compare the performances of different algorithms presented in different papers.

   (c) When integrity requirements are specified, they often seem too loose and/or arbitrary. Using too loose requirements may result in misleading results and ignore larger problems that may need to be looked at. Furthermore, using arbitrary requirements will not lead to the "standardisation" of requirements or an agreement amongst the scientific community.

3. Assumptions of Gaussianity of measurement error distributions are made across the board. Only one publication [48] has been found where this assumption has not been made. However, they validated the proposed algorithm in terms of PE and not integrity. It is important to find better approximations of the actual measurement error distributions as that will give us more trustworthy integrity results. As emphasised in [70], any significant deviation of the error distribution may increase FA and MD rates.

4. Many of the proposed IM algorithms do not analyse those algorithms in terms of their integrity performance. The emphasis is still put on the PE. Moreover, a lot of proposed IM algorithms are validated solely based on their FDE performance. The effectiveness of the FDE is often evaluated through its impact on positioning performance and not the integrity itself. Although this is an important part of the IM as a whole, it does not provide any information on integrity on its own.

5. This brings up another important point. Integrity and IM (algorithms) are often used interchangeably and as synonyms. However, a distinction needs to be made. As defined in Section 2.1 and in [61], IM involves two tasks. Those are the FDE and computation of an integrity measure. In the case of the majority of the integrity algorithms, that measure is the PL. That integrity measure effectively guarantees to bound the true position with a certain probability. An integrity algorithm only involves the calculation of that integrity measure, and the IM algorithm is a complete framework that involves both the FDE and the integrity algorithm, in addition to any other algorithms.

6. An interesting observation can be made in terms of the usage of term RAIM. By definition presented in Section 2.2, RAIM is supposed to be Receiver Autonomous IM, and it monitors the integrity based on the redundant GNSS measurements. Hence, such an IM algorithm is receiver-based. However, as other sensors are introduced to aid the GNSS measurements, the integrity is no longer autonomously monitored within the GNSS receiver but within the aircraft system. That is why such algorithms are called AAIM in civil aviation. By extending that logic to road applications, any IM algorithm proposed for ITS that relies on more than GNSS should be called VAIM - Vehicle Autonomous Integrity Monitoring (or a similar variation). However, this is not the case in the literature where the term RAIM has become synonymous with autonomous integrity monitoring.

7. Limitations of classical IM techniques from civil aviation related to the application in urban environments are highlighted in [73]. For example, classical algorithms do not account for issues such as reduced satellite visibility (including the SBAS), deteriorated satellite/user geometry, LOS and NLOS multipath. Almost every algorithm proposed for urban environments tackles one or more of these issues. For example, [46] proposes a framework where EGNOS, when LOS is unavailable, switches to broadcasting the messages. Reduced satellite visibility has often been mitigated by either using multi-GNSS, IMU or some other type of sensor. Dependence on the satellite/user geometry has often been mitigated through sensor fusion or in some cases by implementing algorithms independent of geometry such as [18]. In addition to the FDE and the integrity algorithm, IM algorithms proposed for the urban environment may use 3D map data to eliminate NLOS signals [42] or to produce virtual pseudoranges as in [70].

8. In order to satisfy more stringent integrity requirements for safety-of-life applications requiring metre-level AL, GNSS code-based measurements cannot be used. Either PPP or RTK measurements have to be used [58, 59, 61, 62].

9. When it comes to implementing IM algorithms for the urban environment, stand-alone GNSS and/or SBAS solutions cannot be the only sensor technology the algorithms are relying on. Even with using NLOS virtual measurements, it is unfeasible to have an IM algorithm that does not rely on any other sensor technology. By the sheer amount of available literature employing multi-sensor systems for positioning and IM, it is fair to say that there is a consensus in the research community with researchers proposing and/or implementing these systems.

10. Multi-sensor integrity methods based on the code-based GNSS measurements cannot achieve metre-level PL. For example, [52] achieved HPL of 15 m to 30 m for HAL of 35 m. It is unknown what the required probabilities were used. However, in their further work they achieved HPL of 5 m to 15 m for $p_{FA} = 1 \cdot 10^{-3}$ and $p_{MD} = 5 \cdot 10^{-4}$ [53]. According to [4], those probabilities and HAL would be too loose for SCA applications and more in line with the PCA applications. [57] achieves 85% OCDR success rate for the requirements of $HAL = 1.5$ m and $p_{MD} = 10^{-2}$. As before, $p_{MD} = 10^{-2}$ is a large probability of missed detection and too loose for SCA applications. Some difficulties exist in comparing different algorithms and their performances, given that the integrity requirements are often not specified. A significant contribution can be made in developing methods capable of achieving integrity levels appropriate for SCA applications as defined in Table 2.5.

11. Similar problem of the integrity requirement definition exists for cooperative integrity methods. [67] achieves HPL of ~ 25 m for $p_{FA} = 1 \cdot 10^{-5}$ and $p_{MD} = 1 \cdot 10^{-3}$. As in the previous point, these integrity levels and probabilities are not stringent enough for SCA. [72] proposes a distributed cooperative IM method and achieves HPL of 1.8 m for a vehicle in the open-sky to 5.4 m for a vehicle in the semi-urban area. However, they do not specify the integrity requirements used to achieve these HPLs, which would satisfy the SCA if they were estimated based on the stringent integrity requirements.

12. In addition to the points already made, some other areas where significant contributions can be made have been identified based on the literature review:

(a) There are a lot of opportunities to contribute in terms of the cooperative IM. Only one of the reviewed papers has implemented a cooperative IM and presented the integrity results (estimated HPL values with unknown integrity requirements).

(b) Given that a vehicle is limited to the road network, not a lot of proposed methods used this to improve their integrity estimates.

(c) The majority of methods estimate integrity in the measurements domain (number of measurements and the satellite/user geometry are important factors).

(d) Only a few examples of multi-sensor systems where terrestrial ranges are used have been found in the literature (e.g., [53, 63]).

(e) All cooperative IM algorithms and a lot of the multi-sensor and stand-alone GNSS IM algorithms have been validated on simulated data. This suggests the complexity of collecting such data.

2.7 Conclusion

The points made in the previous section indicate areas where significant contributions can be made. When designing the three novel algorithms proposed in this research, the majority of these points have been considered as guidelines pointing towards the issues that need to be addressed.

In response to points 1 and 2 from Section 2.6, some of the requirements defined in Table 2.5 will be used. Since the solution will be based on the GNSS pseudoranges, it is expected that lane-level integrity will not be achieved (as noted in point 8). Achieving road-level or an SCA integrity level will be the aim of this thesis (points 10 and 11). More on the integrity requirements will be given in Chapter 6.

As showcased in this literature review, the problem of IM in the urban environment is very complex and a difficult one to solve. This thesis will aim to mitigate problems of satellite visibility, deteriorated satellite/user geometry and the effect of large biases (point 7). This will be done through a multi-sensor approach and CP, and implementation of integrity algorithms in the position domain independent of the number of measurements and the geometry. Both the multi-sensor and the CP solution will be based on the integration of GNSS and terrestrial ranges. Terrestrial ranging methods are chosen because of identified research gaps in the previous sections and their increasing availability as signals

of opportunity. Furthermore, a version of the MM algorithm will be integrated into the IM algorithm. The proposed algorithm will not assume Gaussianity for terrestrial ranges. A better approximation of the actual terrestrial range error distribution will be used and its effect on positioning, integrity and IM performance will be tested as well (Chapters 4 and 6). More details on all the proposed algorithms will be given in Chapter 5.

3

Vehicle integrity system requirements in urban environment

The three main sections of this chapter have originally been published in three separate peer-reviewed papers (specified later). They form a unit of work that provides background knowledge mixed with the original work used to set up the integrity system requirements. Firstly, the theoretically best achievable performance of multi-sensor and cooperative positioning is quantified. As a first system requirement, underlying positioning systems of the proposed integrity method are chosen. The second system requirement is defined based on the analysis of the scale of the position integrity problem in urban environments such as highway, urban canyon, suburban and open-sky areas. As part of the last integrity system requirement, data sets necessary for multi-sensor and cooperative integrity implementation and validation are chosen and analysed.

3.1 Introduction

The goal of this chapter is to experimentally demonstrate and document the analysis of the integrity system requirements, which will be defined here. The structure of the chapter is shown in Figure 3.1 and described in the following paragraphs.

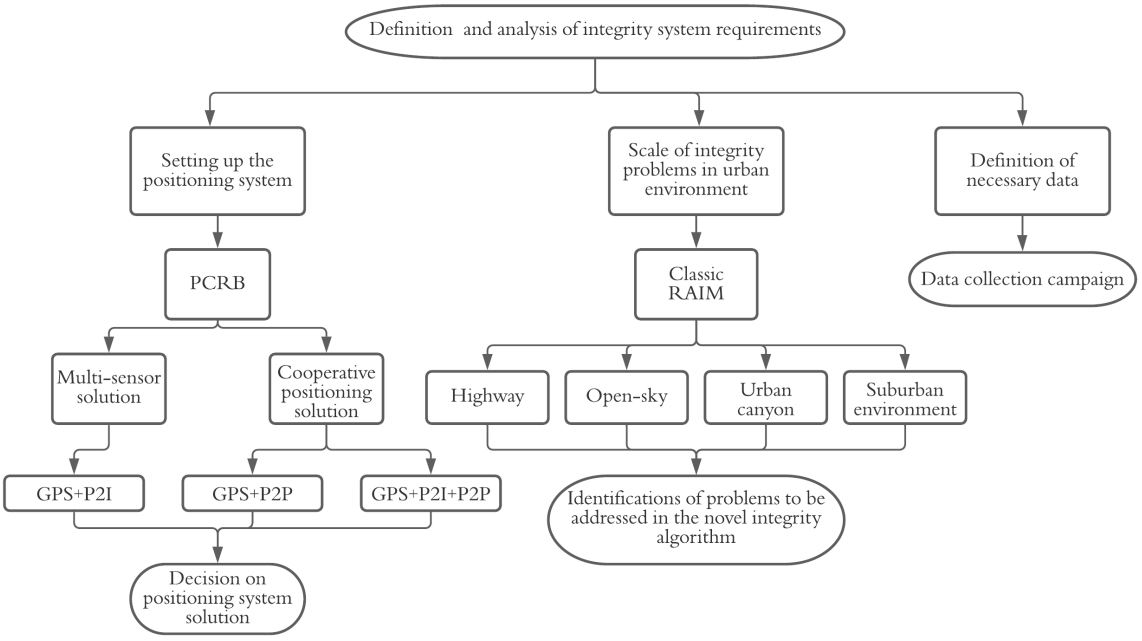


FIGURE 3.1: Chapter 3 structure.

For any integrity algorithm, it is necessary to build up a discussion on the positioning system to be used. Hence, the first considered integrity system requirement is the set up of the positioning system. Based on the literature review in Chapter 2, it is clear that the researchers are turning towards developing cooperative integrity techniques. This section will quantify the expected performance of multi-sensor and cooperative positioning (CP) based on the terrestrial ranges between users and infrastructure (Peer-to-Infrastructure P2I) and between users themselves (Peer-to-Peer P2P). The theoretical capabilities of such positioning systems will be determined by calculating the theoretically best achievable performance by analysing the Posterior Cramér Rao Bounds (PCRB) in Section 3.2.

Having defined the first integrity system requirement, the goal of Section 3.3 is to demonstrate the scale of the position integrity problem in the urban environment. Position integrity is estimated for one of the classical integrity methods from Section 2.4 based on real-world GPS data collected in different urban environments — highway, urban canyon,

suburban area and open-sky area. This answered the question of the magnitude of integrity problem in the urban environment. Furthermore, to mitigate part of the environmental effect connected to satellite visibility, satellite/user geometry and the requirement of sufficient measurement redundancy, GPS position integrity is expanded to multi-sensor integrity by fusing GPS and simulated P2I terrestrial ranges. This demonstrated the capability of multi-sensor integrity, and indirectly, CP integrity. By doing this, a set of integrity system requirements determined based on the problems specific to integrity in urban environments was defined and used to design the novel integrity methods proposed in Chapter 5. An analysis like this, and with the aim of integrity system requirement definition, was previously unavailable in the literature and is considered one of the major contributions of this research.

Defining system requirements is not just about algorithms. It is also about determining the data necessary to collect for development and validation of the multi-sensor and the cooperative integrity algorithms. The last integrity system requirement is presented in Section 3.4, and it defines and describes the collected data.

3.2 Analysis of multi-sensor and cooperative positioning

This section presents the positioning system to be used as the basis of the position estimator that underlies the proposed integrity method. Thus, the benefits of multi-sensor and CP are demonstrated.

In this research, the multi-sensor positioning system relies on the vehicle's GNSS data and terrestrial ranges measured to the infrastructure (i.e., P2I). CP systems were defined in [9] as "data fusion methods for combining position-related data among a group of participating entities, which can communicate with each other." This section will define the centralised CP method based on GNSS data available for vehicles and terrestrial ranges measured between them (i.e., P2P). In addition to that, the centralised CP method where vehicles measure terrestrial ranges to other vehicles and to the infrastructure will be analysed (i.e., P2I+P2P).

The content of Section 3.2 was first published in a conference paper entitled *Cramér Rao Bound analysis for cooperative positioning in Intelligent Transportation Systems* in the *IGNSS 2018 Symposium* in *February 2018* ([74] in the bibliography). The contents of the paper is not fully reproduced here. Only a portion of the results and discussion are demonstrated.

These systems will be tested for a simulated ad-hoc network of four vehicles and 15 infrastructure nodes. During the entire simulation, GNSS data are not available for one out of four vehicles. The performance of P2I, P2P and combination of P2I and P2P (i.e., P2I+P2P) positioning is assessed using the PCRB and estimated position accuracy.

The main goal is to calculate the theoretically best achievable performance of proposed positioning systems by means of PCRB and to make conclusions on the capability of achieving the accuracy levels required by ITS applications. The desired level of accuracy for lane-level applications can range from 0.5 m [9, 75] to 1.5 m [10]. For road-level applications, 5 m accuracy is required [10]. The following subsections present the EKF as a standard algorithm used for sensor fusion, define the PCRB, describe the data simulation process and present the results.

3.2.1 Loosely coupled centralised cooperative Extended Kalman Filter

It should be noted that the notations used in the original paper have been changed here to adapt to the remainder of the thesis. The EKF algorithm is further generalised.

A network of N_M mobile nodes (i.e. vehicles) and N_{IN} infrastructure nodes is considered. It is assumed that positions of infrastructure nodes have been precisely determined in a global coordinate reference system. Positions of N_M mobile nodes are not known, and they are to be determined using the P2I+P2P measurements. All mobile nodes cooperatively share their positions and terrestrial ranges between each other (i.e., P2P). The terrestrial ranges from N_M mobile nodes and N_{IN} infrastructure nodes are measured, which enables multi-sensor positioning (i.e., P2I). Infrastructure nodes form a Local Positioning System (LPS).

A mathematical model for the centralised EKF used here is a variation of the model developed in [76]. There, a detailed mathematical model for centralised and distributed CP can be found. [76] demonstrates the benefits of CP on the example of Unmanned Aerial Vehicles (UAVs). This section extends their centralised mathematical model and demonstrates its performance for ITS applications.

In a centralised CP system, the joint state vector X_k at time epoch k for N_M users is given as:

$$X_k = \left[(x_1)^T \quad \dots \quad (x_{N_M})^T \right]^T , \tag{3.1}$$

where x_i denotes a state vector for $i \in 1, \ldots, N_M$ as

$$x_i = \begin{bmatrix} r_i & v_i \\ 1\times3 & 1\times3 \end{bmatrix}^T. \tag{3.2}$$

The state vector x_i estimated for a single node at time k consists of six states where r_i denotes 3D position estimate, and v_i denotes 3D velocity estimate. The evolution of joint state vector can be expressed as follows,

$$\begin{aligned} X_k &= f(X_{k-1}, \omega_k), \\ \omega_k &\sim \mathcal{N}(0, Q_k). \end{aligned} \tag{3.3}$$

Equation 3.3 represents the evolution of the joint state vector. X_{k-1} denotes the joint state vector estimated at the previous time epoch $k-1$. ω_k denotes the Gaussian process noise with zero-mean and variance matrix Q_k that consists of velocity noise. The equation of motion governing the state transition (i.e., dynamic model) function $f(\cdot)$ is given as,

$$\dot{r} = v, \tag{3.4}$$

where $\dot{r}$ stands for a change of position which equals to velocity v. In this particular model, a constant velocity model is used.

According to [77], the evolution of the joint state vector can be expressed as,

$$X_k = F_k X_{k-1} + \omega_k, \tag{3.5}$$

where F_k denotes the joint transition matrix. The time increment between the two states is denoted by δt and I is an identity matrix. In that case, the state transition matrix for a single mobile node F_k^i and for all nodes F_k, respectively, can be defined as,

$$\underset{6\times6}{F_k^i} = \begin{bmatrix} \underset{3\times3}{I} & \underset{3\times3}{I} \cdot \delta t \\ \underset{3\times3}{0} & \underset{3\times3}{I} \end{bmatrix}, \tag{3.6}$$

$$\underset{N_M\times N_M}{F_k} = \begin{bmatrix} F_k^1 & \cdots & \underset{6\times6}{0} \\ \vdots & \ddots & \vdots \\ \underset{6\times6}{0} & \cdots & F_k^{N_M} \end{bmatrix}. \tag{3.7}$$

As stated before, in this framework, all mobile nodes are measuring terrestrial ranges between themselves (i.e., P2P) and with infrastructure nodes (i.e., P2I). Additionally, all mobile nodes with available GNSS measurements are sharing their GNSS positions. Because position measurements from GNSS are assumed instead of pseudoranges, this implementation of EKF is loosely coupled.

The measurement vector Z_k, for time epoch k, is defined by

$$Z_k = \begin{bmatrix} (d_{M,M})^T & (d_{M,IN})^T & (r_M^{GNSS})^T \end{bmatrix}^T, \tag{3.8}$$

where $d_{M,M}$ denotes the P2P ranges measured between mobile nodes, and $d_{M,IN}$ denotes the P2I ranges measured between mobile nodes. Available GNSS positions are denoted with r_M^{GNSS}. With that in mind, the measurement matrix for the overall network can be obtained by linearising measurement equations with respect to the mobile nodes involved. The measurement model for terrestrial ranges between any two nodes q and w with coordinates (x_q, y_q, z_q) and (x_w, y_w, z_w), respectively, can be given as

$$d_{q,w} = \sqrt{(x_q - x_w)^2 + (y_q - y_w)^2 + (z_q - z_w)^2} + \zeta_{d_{q,w}}, \tag{3.9}$$

where $\zeta_{d_{q,w}}$ denotes the terrestrial range measurement noise vector that is assumed to be Gaussian with zero-mean and variance R_k. The generalised joint measurement matrix H_k can be written as

$$\underset{N_{meas} \times 6N_M}{H_k} = \begin{bmatrix} H^{M_1}_{d_{M_1,M_2}} & H^{M_2}_{d_{M_1,M_2}} & \dots & H^{M_{N_M}}_{d_{M_1,M_2}} \\ \vdots & \vdots & \dots & \vdots \\ H^{M_1}_{d_{M_{N_M-1},M_{N_M}}} & H^{M_2}_{d_{M_{N_M-1},M_{N_M}}} & \dots & H^{M_{N_M}}_{d_{M_{N_M-1},M_{N_M}}} \\ H^{M_1}_{d_{M_1,IN_1}} & H^{M_2}_{d_{M_1,IN_1}} & \dots & H^{M_{N_M}}_{d_{M_1,IN_1}} \\ \vdots & \vdots & \dots & \vdots \\ H^{M_1}_{d_{M_{N_M},IN_{N_{IN}}}} & H^{M_2}_{d_{M_{N_M},IN_{N_{IN}}}} & \dots & H^{M_{N_M}}_{d_{M_{N_M},IN_{N_{IN}}}} \\ \underset{3\times3}{I} \,|\, \underset{3\times3}{0} & \underset{3\times6}{0} & \dots & \underset{3\times6}{0} \\ \vdots & \vdots & \ddots & \vdots \\ \underset{3\times6}{0} & \underset{3\times6}{0} & \dots & \underset{3\times3}{I} \,|\, \underset{3\times3}{0} \end{bmatrix}. \tag{3.10}$$

$H^w_{d_{q,w}}$ denotes the Jacobian matrix for any measured range $d_{q,w}$ between nodes q and w, with respect to any mobile or infrastructure node w. In case of mobile nodes (i.e., P2P

ranges) $q, w \in M_1, M_2, \ldots, M_{N_M-1}, M_{N_M}$. In case of P2I ranges, $w \in IN_1, IN_2, \ldots, IN_{N_{IN}}$.

$$H^w_{d_{q,w}} = \begin{bmatrix} \frac{\partial d_{q,w}}{\partial x_w} & \frac{\partial d_{q,w}}{\partial y_w} & \frac{\partial d_{q,w}}{\partial z_w} & 0 & 0 & 0 \end{bmatrix}^T. \tag{3.11}$$

Many of these matrices are going to be equal to zero. For example, the first row of the joint measurement matrix in Equation 3.10, refers to the P2P range between the first mobile node M_1 and the second mobile node M_2: d_{M_1,M_2}. The Jacobian matrices for this range calculated for nodes other than M_1 and M_2 will be 0.

Rows of the matrix denote all available measurements $N_{meas} = N_{d_{M,M}} + N_{d_{M,IN}} + 3 \cdot N_{r_M^{GNSS}}$ and columns of the joint measurement matrix denote the number of states in the joint state vector $6 \cdot N_M$. Rows of the H_k matrix must have the structure as the measurement vector in Equation 3.8. Firstly, Jacobian matrices for P2P ranges between mobile nodes are calculated. Following that, Jacobians for P2I ranges between mobile nodes and infrastructure nodes are derived. Lastly, Jacobian matrices for GNSS positions are derived. Since the EKF is loosely-coupled, Jacobians of a certain position measured by GNSS (x,y,z) are going to be equal to the identity matrix. The presented form of the H_k matrix is for the general P2I+P2P case. However, in case of P2I only or P2P only, rows in Z_k and H_k corresponding to the missing terrestrial ranges would be left out.

Having defined the joint transition and measurement matrices, the standard EKF equations can be used for estimating the positions of all mobile nodes [40].

3.2.2 Posterior Cramér Rao Bound

The PCRB can be used to find the best theoretically achievable performance of any positioning system including the proposed CP as well. Although [78], [79] and [80] derive expressions for CRB CP, they are derived for static CP systems and cannot be used for proposed dynamic CP system.

The expression for PCRB used in this thesis was firstly derived by Taylor in [81]. In order to derive the PCRB for a dynamic non-linear positioning system, an estimator needs to be used. [81] has shown that Fisher information matrix "propagates according to the same equations as the filter covariance matrix for an EKF linearised about the true (unknown) trajectory". Since the EKF is used as the estimator in this chapter, Taylor's method of calculating PCRB could be applied. It is important to note that, based on Taylor's

definition of PCRB, it can only be calculated for the positions where the ground truth is known (i.e., simulations). Therefore, it is a useful tool to estimate if the EKF or any other estimator is adequate for the proposed non-linear dynamic system. Furthermore, it is useful to determine if the effort should be put in developing an appropriate mathematical model or if the positioning system itself needs to be modified. Although Taylor's expression for PCRB has been derived without assuming process noise, it has been shown in [82] that process noise can be added to one of the summands in Taylor's original expression. Consequently, propagation of the posterior Fisher information matrix and PCRB matrix are given as,

$$J_k = \left(F_{k-1} J_{k-1} F_{k-1}^T + Q_{k-1}\right)^{-1} + H_k^T R_k^{-1} H_k, \tag{3.12}$$

$$PCRB = J_k^{-1}, \tag{3.13}$$

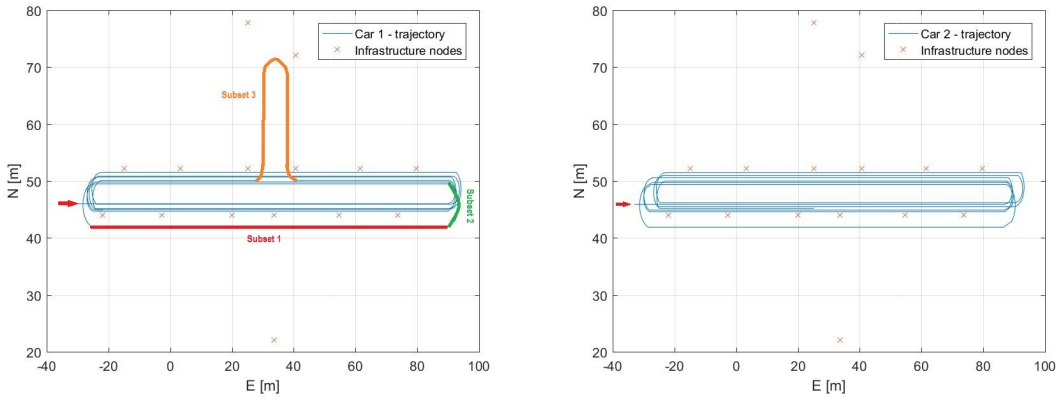
where F_{k-1} denotes state transition matrix, J_{k-1} denotes Fisher information matrix for time instant $k-1$, Q_{k-1} denotes process noise, H_k denotes measurement matrix, and R_k denotes measurement noise. The PCRB is then calculated by finding an inverse to the Fisher information matrix.

3.2.3 Ad-hoc vehicle and infrastructure network data simulation

To test the performance of the proposed multi-sensor and centralised cooperative EKF, a network of four vehicles and 15 LPS anchor (i.e., infrastructure) nodes is simulated. All vehicles are able to communicate amongst themselves. The presented EKF is in the generalised form for N_M vehicles and N_{IN} infrastructure nodes. In the simulation, it is assumed that one vehicle (Car 1 from now on) out of four is not able to receive GNSS signal, terrestrial ranges from LPS network of 15 anchors are available to it, and terrestrial ranges from other vehicles in addition to their GNSS positions.

The standard deviation of the measured GNSS positions is assumed to be 2 *cm* horizontally and 4 *cm* vertically. This level of precision for GNSS measurements can be achieved by using Network Real Time Kinematic (NRTK) GNSS [83]. Terrestrial ranges could be measured with any type of device capable of dynamically measuring the terrestrial ranges (e.g., UWB radios). It is assumed that the standard deviation of simulated ranges is 1 m. The simulated road is assumed to be 10.5 m wide, and the positions of infrastructure nodes are simulated to follow the road network with approximate relative distances of 19 m.

Vehicles are driving in a loop along the road with a constant velocity of 5 m/s on the straight parts of trajectory and 1 rad/s in turns, for approximately 5 min. The trajectory of Car 1 is more complicated than for the other vehicles, as it turns right into the South-North (SN) loop at some point (Figure 3.2a). Car 2 is simulated to follow Car 1 until it turns into the SN loop at which point Car 2 overtakes it. As shown in Figure 3.2b, Car 2 always drives on the main part of the trajectory. Unlike Cars 1 and 2, Cars 3 and 4 are starting from the east side of the road while constantly following each other. Based on these trajectories, synthetic measurements are generated. Measurement errors are assumed to follow Gaussian distribution with 2 cm standard deviation for 2D GNSS, 4 cm standard deviation for GNSS heights, and 1 m standard deviation for all terrestrial range measurements. The inverse of the initial state covariance matrix has been used as the initial Fisher information matrix. Different process noise is used for straight parts of the trajectory and turns because of the different dynamics of driving straight and turning. It is assumed that the data rate is 50 Hz, i.e., measurements are available at every 0.02 s.



(A) (B)

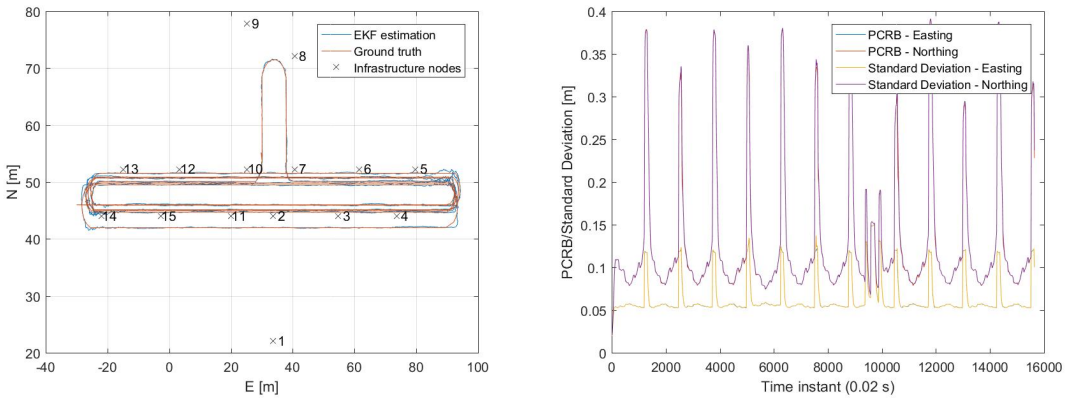
FIGURE 3.2: Simulated trajectories with starting positions for a) Car 1. b) Car 2.

3.2.4 Results and discussion

This section presents results of multi-sensor positioning (i.e., P2I) and CP (i.e., P2P and P2I+P2P). Principal performance metrics are PCRB and Position Errors (PE).

The first experiment tests the theoretically best performance for multi-sensor positioning. In this experiment, Car 1 estimates its position based on available terrestrial range measurements to all infrastructure nodes (i.e., P2I ranges).

The P2I performance is tested for different LPS network geometries and a different number of LPS nodes. Firstly, a fully available network of 15 infrastructure nodes is assumed (Figure 3.3a). The positions (blue colour) seem to be well estimated, except when the vehicle is turning. It is to be noted that different process noises are used for straight parts of the trajectory and in turns, which resulted in an improvement in the overall performance. In addition to the estimated PCRB, Figure 3.3b shows the standard deviation of the estimated position solution. Easting and Northing PCRB increase in value every time the vehicle turns. Easting PCRB is ~ 5 *cm* when the vehicle is driving straight and grows to ~ 12 *cm* in turns. The Northing PCRB varies from ~ 7 *cm* to ~ 11 *cm* when the vehicle is driving straight and grows up to ~ 38 *cm* in turns. It is to be noted that standard deviations of estimated trajectories are mostly equal or larger than PCRB. This is expected since the PCRB represents the theoretically best achievable performance.



(A) (B)

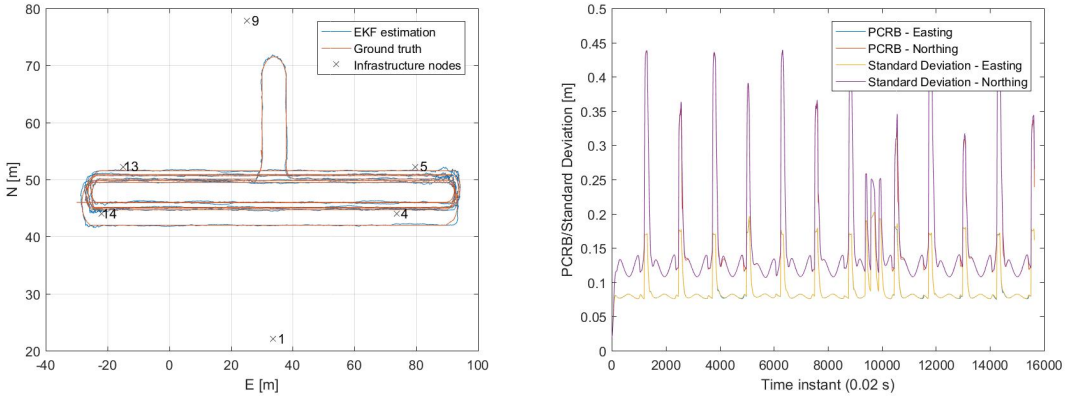
FIGURE 3.3: P2I positioning with 15 nodes. a) Position estimation. b) PCRB.

Average and maximum positioning errors, as well as their standard deviation, are shown in Table 3.1. Only 2D PEs are shown here. PEs associated with the height can be found in the original paper. The average horizontal PE (HPE) is 13.4 *cm*.

TABLE 3.1: Accuracy of P2I and P2I+P2P in horizontal sense.

	P2I				P2I+P2P
[m]	15 nodes	6 nodes	4 nodes	3 nodes	15 nodes
Average	0.134	0.176	0.313	0.244	0.131
Max	2.539	2.528	2.661	2.613	2.508
St. dev.	0.177	0.201	0.269	0.242	0.175

In the second instance, a network of six infrastructure nodes was used. The geometry of those nodes is shown in Figure 3.4a. The chosen geometry can be described as good as a decrease of 60% in the number of static nodes did not cause a significant increase of PCRB. Easting and Northing PCRB values have increased for ~ 3 *cm* when the car driving straight and ~ 5.5 *cm* in turns (Figure 3.4b). Table 3.1 shows an increase of average HPE for ~ 4 *cm*.



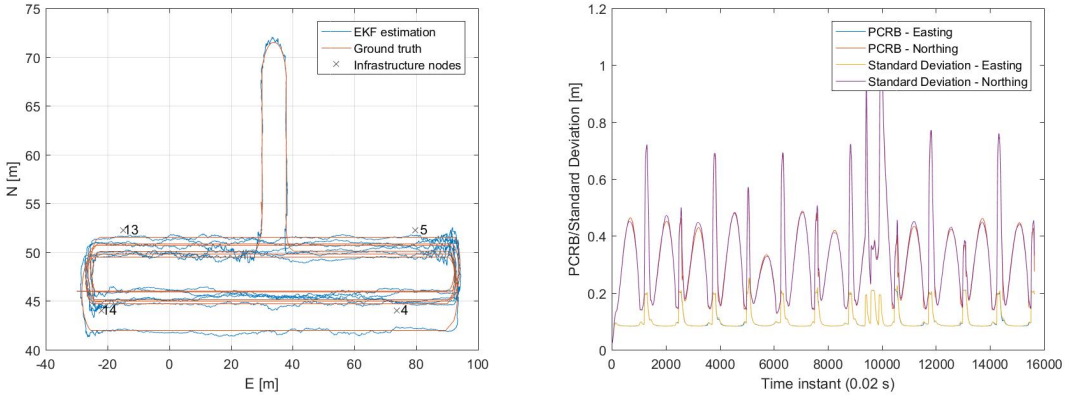
(A) (B)

FIGURE 3.4: P2I positioning with six nodes. a) Position estimation. b) PCRB.

In the third instance, a network of four LPS nodes is chosen (Figure 3.5a). In this network, the separation distance between LPS nodes is greater in the east-west (EW) direction (~ 100 *m*) than in SN direction (~ 10 *m*). As a result, it is expected that PE deteriorates more in SN direction. The impact of such LPS network geometry on position estimation is visible in Figure 3.5b and Table 3.1. Furthermore, Northing PCRB values are almost doubled in comparison to the previous Northing PCRB values. Easting PCRB is not affected as much. The average HPE shows increase of ~ 18 *cm* from previous 13.4 *cm* (for 15 nodes) to 31.3 *cm* (see Table 3.1).

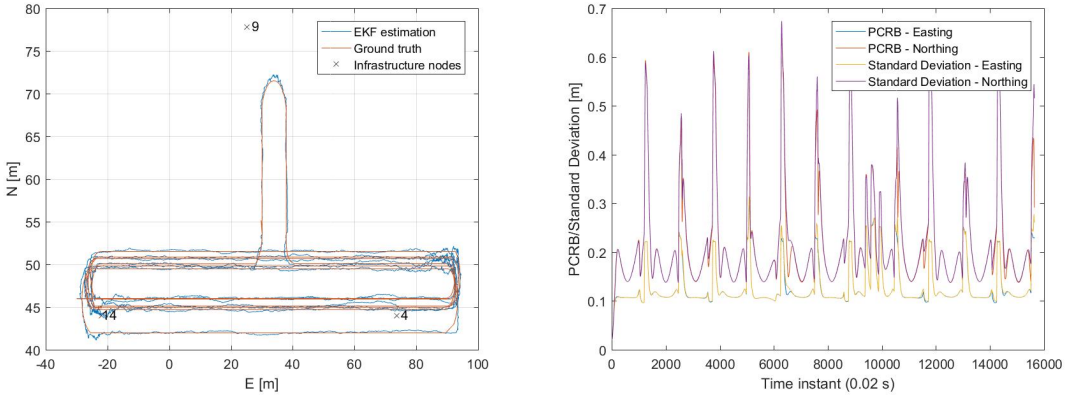
Finally, the number of LPS nodes is further decreased to a network of three LPS nodes (Figure 3.6a). Despite the decrease of the number of LPS nodes, improvement of average HPE is observed in Table 3.1 (compared to a network of four LPS nodes). The geometry quality is more important in this case. Figure 3.6b shows that Easting PCRB remains similar to that one of the four node LPS. However, Northing PCRB is improved for ~ 20 *cm* and ~ 10 *cm* for straight parts of the trajectory and for turns, respectively.

As expected, P2I results show that the geometry of infrastructure nodes can deteriorate the overall system's performance. Since roads have linear geometry and ITS infrastructure must follow the roads, the geometry of infrastructure nodes will always have to follow the



(A) (B)

FIGURE 3.5: P2I positioning with four nodes. a) Position estimation. b) PCRB.



(A) (B)

FIGURE 3.6: P2I positioning with three nodes. a) Position estimation. b) PCRB.

linear geometry of roads. As shown in the third and fourth instances in this section, linear geometry reduces the system's performance. In that case, better network geometry outperformed despite having a smaller number of nodes within the network.

In **the second experiment**, positions of Car 1 are estimated based on the P2P ranges to other vehicles and their GNSS positions.

P2P simulation does not show good results. Firstly, in a system like this, where only GNSS of three other vehicles and ranges between Car 1 and them are available, there is a lack of measurements. Secondly, the solution depends on the dynamic ever changing relative geometry of all vehicles. Since only four vehicles are considered and since the road is 10.5 m wide, a good geometry could rarely be achieved. The position estimation for the SN loop is good (Figure 3.7a), probably due to the improvement of inter-vehicle geometry when Car 1 drives through it (similar to three node P2I results). Figure 3.7b shows the PE plotted against the time. Certain peaks in the PE graph for Northing coordinate can

be noticed. Those are the peaks corresponding to the peaks of estimated trajectory in Figure 3.7a. The positions of the vehicles in those two moments are shown in Figures 3.7c and 3.7d. Both figures show similar geometry where all vehicles with available GNSS are positioned on one side (west or east) of the Car 1 at distances bigger than $\sim 35\ m$. This geometry is inadequate, especially when a 10.5 m wide road is in question.

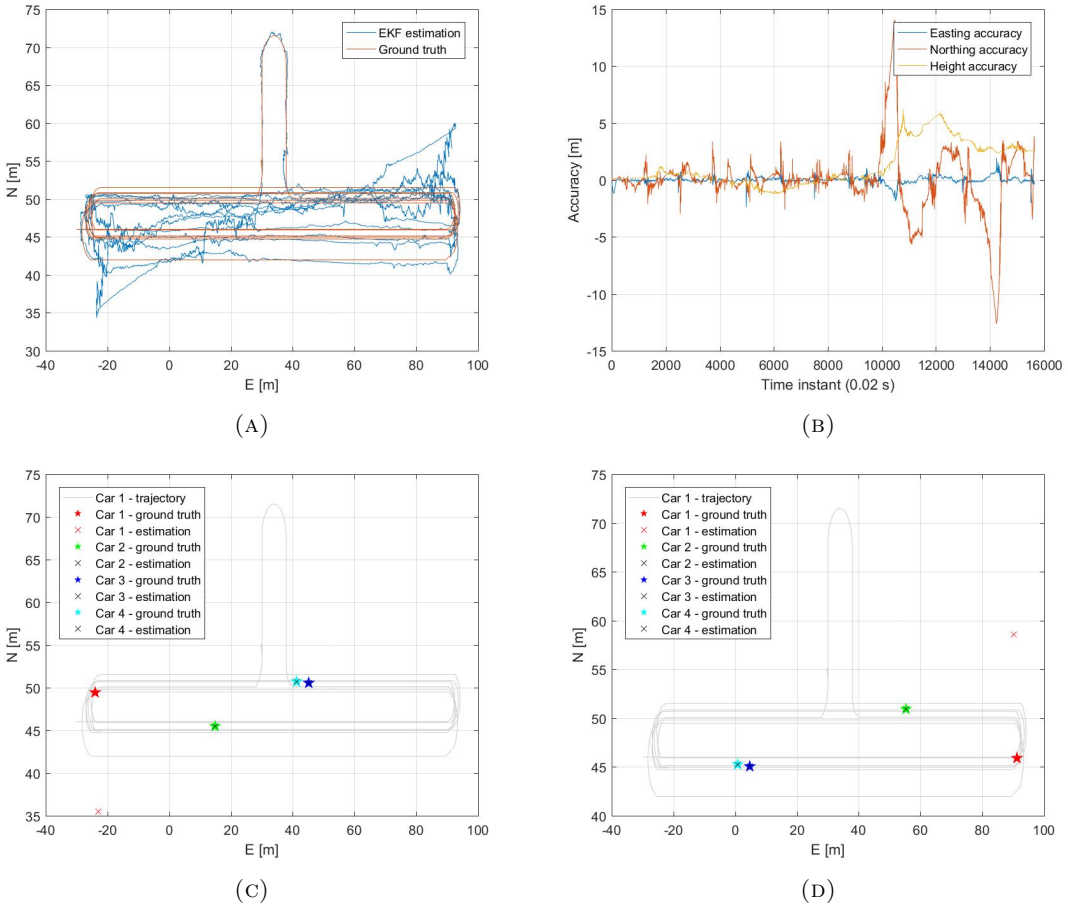
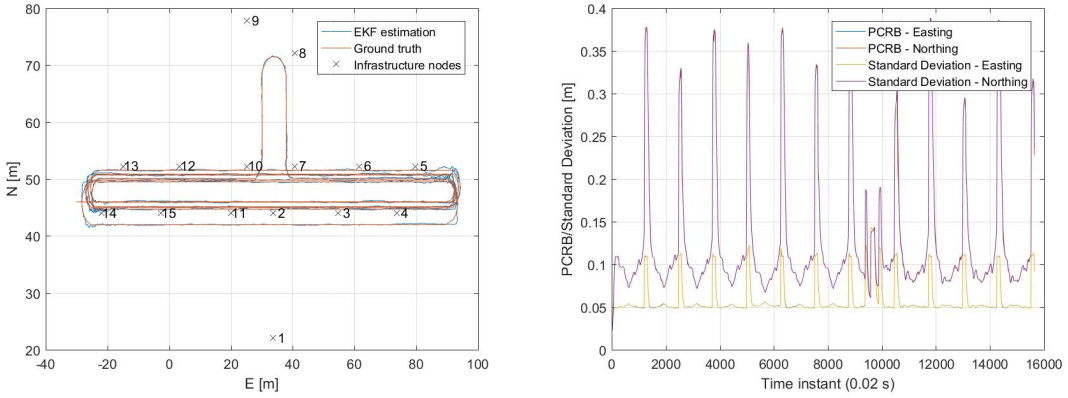


FIGURE 3.7: P2P positioning for Car 1. a) Position estimation. b) Position accuracy. c) Relative positions of vehicles at time 10480. d) Relative positions of vehicles at time 11110.

Lastly, **the third experiment** tests the performance of P2I+P2P (i.e., cooperative) positioning. In these experiments, it is assumed that Car 1 measures terrestrial ranges to 15 LPS nodes and all the other vehicles in addition to receiving GNSS positions from them. Because it is a combined solution, an increase in accuracy is expected.

Figure 3.8a shows the position estimation of the Car 1 in the system described above. Calculated PCRBs are presented in Figure 3.8b. The values of Northing and Easting PCRB are similar to those of the P2I positioning with the network of 15 infrastructure nodes. Table 3.1 provides information about the average HPE where a decrease of average HPE



(A) (B)

FIGURE 3.8: P2I+P2P positioning for Car 1. a) Position estimation. b) PCRB.

is observed when compared to the corresponding P2I solution. Although the improvement is minor, it shows the potential of using the combined system. This is especially true for urban environment navigation where measurements can be sparse, and the final estimate can benefit from all measurements. In this case, because so many infrastructure nodes are available, compared to the number of vehicles, it can be seen that poor inter-vehicle geometry does not impact the final positioning solution. The overall accuracy of the system and the theoretically best achievable performance results are promising for further development. The previously defined requirements (the most stringent one was 0.5 m) have been satisfied in all examples except in case of P2P positioning where inter-vehicle geometry could not be constrained with LPS.

3.3 Scale of the integrity problem in urban environment

The main goal of this section is to demonstrate the scale of the integrity problem in the urban environment. By doing this, additional integrity system requirements will be defined and used to design a novel integrity algorithm.

To experimentally demonstrate the scale of the integrity problem, this section analyses the effects of different types of the environment on position integrity for real-world GPS data. Integrity will be estimated using the classical SBAS RAIM presented in Section 2.4.1 with the EKF as the underlying position estimator in an open-sky environment, on a highway, in a suburban area and in the urban canyon area. Given the results in [15] and [85] where

The content of Section 3.3 was first published in a conference paper *Evaluation of integrity availability based on classical RAIM in different urban environments for stand-alone GPS and multi-sensor solutions* published as part of the *IGNSS 2020 Symposium* in *February 2020* ([84] in the bibliography).

different RAIM algorithms have been tested in different environments on GNSS data, the hypothesis of this section is that integrity availability will decrease as the environment types are becoming more complex and challenging. Unlike [85] where a change of HPL has been studied, the integrity will also be analysed in terms of availability for a specific application class. A case study will be carried out on multiple environments, and detailed analysis of the environment effects will be made.

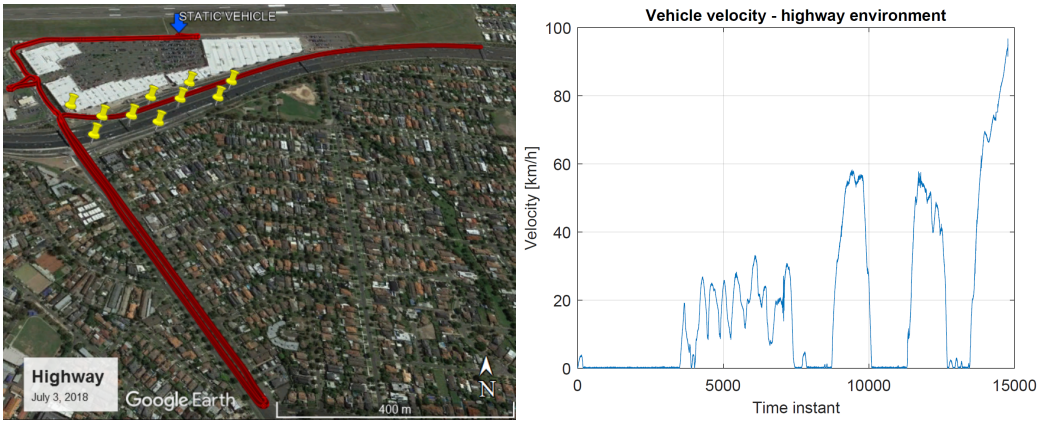
Finally, to mitigate the effect of the urban environment on the integrity, possible improvements of position estimation and integrity will be tested for a multi-sensor system with simulated terrestrial P2I ranges. It is expected that LPS data will be able to improve overall measurement availability and integrity availability.

The contribution of this section is the analysis of the effect of different environments on integrity availability, identification of some of the biggest drawbacks of implementing RAIM-like methods for ITS applications and reduction of the effect of the environment on integrity estimate by employing the multi-sensor positioning system.

3.3.1 Experimental setup

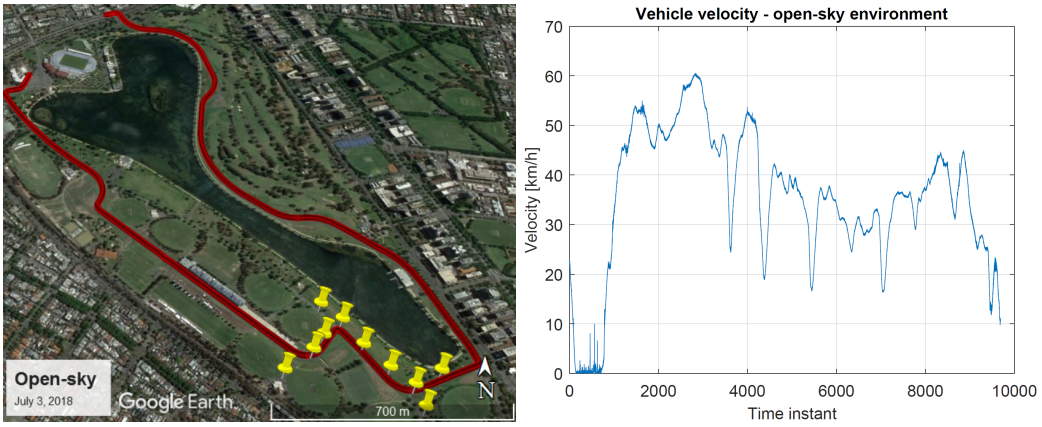
Experiments in this section have been performed on real-world GPS data collected in Melbourne, Australia in July 2018. As one of the aims is to demonstrate the possible effects of different types of the environment on the performance of the SBAS RAIM algorithm, the data used in the experiments were collected in four different environments — highway, open-sky, urban/suburban and urban canyon. In addition to this, the integrity performance is tested for a static vehicle in open-sky conditions. Open-sky, suburb and urban canyon areas were chosen due to different satellite visibility. The highway was chosen so that the performance of EKF and RAIM could be tested when the vehicle is moving with high speed. Figures 3.9a to 3.12a are showing the trajectories of the vehicles in all four environments. It should be noted that Figure 3.9a also shows the location where the static vehicle data were collected in the open-sky environment (blue mark). The highest achieved velocity was just under 100 km/h (Figure 3.9b). Velocities of the vehicle in all environments are shown in Figures 3.9b to 3.12b.

To test the potential capabilities of the integration of GPS and LPS (i.e., multi-sensor), terrestrial ranges are simulated on subsets of the shown trajectories. Anchor nodes (yellow pins in Figures 3.9a to 3.12a) are set up around the road segments. As before, the terrestrial



(A) (B)

FIGURE 3.9: a) The trajectory of the vehicle on the highway (Citylink) with Google Earth satellite image as a base map. b) The velocities reached by the vehicle.

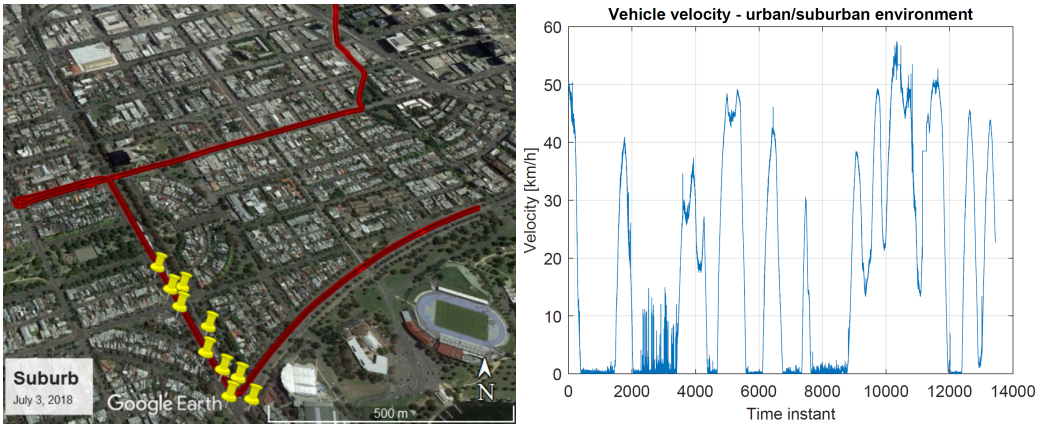


(A) (B)

FIGURE 3.10: a) The trajectory of the vehicle in the open-sky environment (Albert Park) with Google Earth satellite image as a base map. b) The velocities reached by the vehicle.

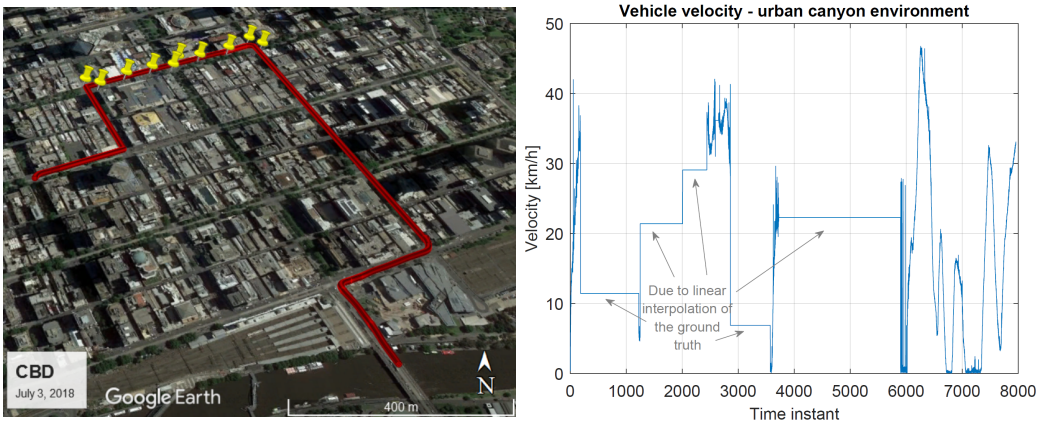
ranging data between the vehicle and the anchors are simulated with added zero-mean Gaussian noise with a standard deviation of 1 m.

GNSS data were collected using the surveying grade Leica GNSS receiver. The receiver was mounted on the vehicle using a magnetic mount. More information about the used receiver can be found in Leica Geosystems AG data sheet [86]. Only GPS code pseudoranges, uncorrected for atmospheric effects, were used as the measurements. Post-processed dual-frequency GPS data in addition to the data from Continuously Operating Reference Station (CORS) in Melbourne (i.e., MOBS) were used as the ground truth for integrity and accuracy assessment. The RTKLib open-source software package was used to determine the ground truth with the precision at a sub-centimetre level. It should be noted, that during a big portion of the data collection in the urban canyon and at some instances in the suburban environment, when less than four measurements were available, it was not



(A) (B)

FIGURE 3.11: a) The trajectory of the vehicle in the urban/suburban environment (South Melbourne) with Google Earth satellite image as a base map. b) The velocities reached by the vehicle.



(A) (B)

FIGURE 3.12: a) The trajectory of the vehicle in the urban canyon (Melbourne Central Business District) with Google Earth satellite image as a base map. b) The velocities reached by the vehicle.

possible to determine the ground truth with sub-centimetre precision. Given the linearity of the road segments where this occurs, linear interpolation was used to derive the ground truth positions. Further, when interpolating the positions, constant velocity was assumed (as shown in Figure 3.12b).

3.3.2 Tightly coupled Extended Kalman Filter and SBAS Horizontal Protection calculation

The position estimator presented here is based on the general CP EKF presented in Section 3.2.1 and [76]. Furthermore, the SBAS RAIM method used in this section is based on [37] and has previously been presented in Section 2.4.1.

3.3.2.1 Multi-sensor Extended Kalman Filter

This section presents a modified multi-sensor positioning framework based on the EKF. In comparison to the one presented in Section 3.2.1, this EKF (and for the remainder of this thesis) will be constant acceleration, tightly-coupled EKF. Please note that the symbols used in this framework will be consistently used for the remainder of the thesis.

Pseudorange (i.e., GNSS satellite measurements) and terrestrial range (i.e., LPS range) measurements are being fused. A network of N_{IN} LPS anchors (i.e., infrastructure nodes) and a network of N_S GNSS satellites are considered. Since only multi-sensor EKF is defined, a number of mobile nodes is $N_M = 1$. The positions of the GNSS satellites are predicted using the ephemeris data and are determined in ECEF (Earth-Centred, Earth-Fixed) frame. The positions of the infrastructure nodes (i.e., LPS nodes or anchors) are assumed to have been precisely determined in the ECEF frame as well. The position r_k of the vehicle or a different type of road user is estimated within the state vector X_k at a time instant k. In addition to the 3D position, 3D velocity v_k, 3D acceleration a_k and user clock bias c_b^k in units of length (obtained by multiplying clock bias with the speed of light) are all estimated within the X_k. The presented algorithm is for a single GNSS constellation. Making it multi-GNSS algorithm would require an additional clock bias or incorporating satellite constellation time offset as shown in [87].

$$X_k = \begin{bmatrix} r_k & v_k & a_k & c_b^k \\ 1\times3 & 1\times3 & 1\times3 & 1\times1 \end{bmatrix}^T. \tag{3.14}$$

Although the presented framework estimates the 3D positions of the user, by removing the third dimension of the position, velocity, and acceleration in the state vector, the algorithm can be altered to estimate 2D positions, 2D velocity, and 2D acceleration. However, it should be noted that in the case of the fusion of pseudoranges and terrestrial ranges, 3D ranges are usually measured and without angle measurements, it is not possible to reduce them to 2D ranges. The measurement vector Z_k consists of pseudorange measurements vector ρ_k and terrestrial range measurement vector d_k.

$$\underset{(N_{IN}+N_S)\times1}{Z_k} = \begin{bmatrix} d_k & \rho_k \\ 1\times N_{IN} & 1\times N_S \end{bmatrix}^T. \tag{3.15}$$

The user's state evolution is expressed with

$$\begin{aligned} X_k &= F_k X_{k-1} + \omega_k, \\ \omega_k &\sim \mathcal{N}(0, Q_k), \end{aligned} \tag{3.16}$$

where X_{k-1} denotes previously estimated state at time instant $k-1$. ω_k is the process noise which is normally distributed with zero mean and covariance matrix $Q_k = \begin{bmatrix} 0 & 0 & \omega_a & \omega_{c_b} \\ 1\times3 & 1\times3 & 1\times3 & 1\times1 \end{bmatrix}^T$. The covariance matrix consists of the acceleration noise with variance ω_a and GNSS receiver clock bias noise with variance ω_{c_b}. Now, the variance matrix consists of the acceleration and GNSS receiver clock bias process noise. The state transition functions governing the state evolution are given as,

$$\begin{aligned} \dot{r} &= v, \\ \dot{v} &= a. \end{aligned} \tag{3.17}$$

$\dot{r}$ denotes the rate of change of position which equals velocity v, and $\dot{v}$ denotes the rate of change of velocity that equals acceleration a. In this case, the state evolution model is a constant acceleration model. The transition matrix F_k is defined as

$$F_k = \begin{bmatrix} \underset{3\times3}{I} & \underset{3\times3}{I} \cdot \delta t & \frac{1}{2}\underset{3\times3}{I} \cdot \delta t^2 & \underset{3\times1}{0} \\ \underset{3\times3}{0} & \underset{3\times3}{I} & \underset{3\times3}{I} \cdot \delta t & \underset{3\times1}{0} \\ \underset{3\times3}{0} & \underset{3\times3}{0} & \underset{3\times3}{I} & \underset{3\times1}{0} \\ \underset{1\times3}{0} & \underset{1\times3}{0} & \underset{1\times3}{0} & 1 \end{bmatrix}, \tag{3.18}$$

where I is an identity matrix with dimensions specified under the symbol and δt is the time increment between two states. The measurement model is expressed as

$$Z_k = h(X_k) + u_k, \tag{3.19}$$

$$u_k = \begin{bmatrix} \zeta_k & \xi_k \end{bmatrix}^T, \tag{3.20}$$

$$\zeta \sim \mathcal{N}(0, \sigma_{IN}^2), \tag{3.21}$$

$$\xi \sim \mathcal{N}(0, \sigma_S^2). \tag{3.22}$$

u_k is a measurement noise vector which consists of terrestrial range measurement noise ζ_k and pseudorange measurement noise ξ_k. Both are assumed to be zero-mean Gaussian

with standard deviations σ_{IN}^2 and σ_S^2, respectively. $h(\cdot)$ denotes a general non-linear measurement function. In this case, the measurement model consists of two non-linear functions

$$d_k^i = \sqrt{(x_{IN}^i - x_k)^2 + (y_{IN}^i - y_k)^2 + (z_{IN}^i - z_k)^2} + \zeta_k^i, \tag{3.23}$$

$$\rho_k^m = \sqrt{(x_S^m - x_k)^2 + (y_S^m - y_k)^2 + (z_S^m - z_k)^2} + c_b^k + \xi_k^m, \tag{3.24}$$

where ρ_k^m and d_k^i denote the pseudorange and terrestrial range measurements, respectively. (x_k, y_k, z_k) denotes the predicted user's position. $(x_{IN}^i, y_{IN}^i, z_{IN}^i)$ is the ECEF position of the i^{th} anchor node where $i \in 1, 2, \ldots, N_{IN}$ at time instant k. (x_S^m, y_S^m, z_S^m) is the ECEF position of the m^{th} satellite where $m \in 1, 2, \ldots, N_S$ at time instant k. The first-order Taylor series expansion is used to approximate the non-linear measurement model. Jacobian matrices for the i^{th} anchor and the m^{th} satellite are given below, as well as the measurement matrix H_k which consists of all the individual Jacobian matrices.

$$H_k^{d_i} = \begin{bmatrix} \frac{\partial d_k^i}{\partial r_k} & 0 & 0 & 0 \\ 1\times3 & 1\times3 & 1\times3 & 1\times1 \end{bmatrix}. \tag{3.25}$$

$$H_k^{\rho_m} = \begin{bmatrix} \frac{\partial \rho_k^m}{\partial r_k} & 0 & 0 & 1 \\ 1\times3 & 1\times3 & 1\times3 & 1\times1 \end{bmatrix}. \tag{3.26}$$

$$\underset{(N_{IN}+N_S)\times10}{H_k} = \begin{bmatrix} H_k^{d_1} & \ldots & H_k^{d_{N_{IN}}} & H_k^{\rho_1} & \ldots & H_k^{\rho_{N_S}} \end{bmatrix}^T. \tag{3.27}$$

Presented matrices are defined for a multi-sensor solution where GNSS data and LPS data are fused. However, in the case of stand-alone GNSS EKF, rows in Z_k, U_k and H_k related to terrestrial ranges would be removed. For stand-alone LPS data, all rows in the same matrices relating to the GNSS measurements would be removed. The standard EKF equations can be used to estimate the user's state [40]. Please note that this EKF will be used for the comparison purposes in the rest of the thesis.

3.3.2.2 SBAS Horizontal Protection Level calculation for multi-sensor system

SBAS HPL method has previously been explained in Section 2.4.1 where it has been implemented with WLS algorithm. In this case, variables used to calculate HPL are

provided by the EKF. The HPL can be calculated (same as Equation 2.5) as follows

$$HPL = K_{\text{ffmd}} d_{\text{major}}. \tag{3.28}$$

The definition of the missed detection multiplier K_{ffmd} is given in Equation 2.6. As before, d_{major} denotes the 1σ standard deviation of the position that is to be estimated in the direction of the major axis of the error ellipse. d_{major} is calculated as in Equation 2.7. The elements used to calculate d_{major} differ given the change of the positioning system to the multi-sensor system. d_x^2, d_y^2 and d_{xy} are still the error variances in the direction of the x and y axis, and covariance between the x and y, respectively. They are calculated by propagating the measurement variances through the measurement model as shown in Equation 3.29. Given that the measurement model is linearised, the geometry between the user and the GNSS/LPS is known, and the measurement errors are assumed to be Gaussian, errors can be propagated without knowledge of the estimated position.

$$\begin{aligned} d_x^2 &= \sum_{i=1}^{N_{IN}} S_{x,i}^2 \sigma_{IN}^2 + \sum_{m=1}^{N_S} S_{x,m}^2 \sigma_S^2, \\ d_y^2 &= \sum_{i=1}^{N_{IN}} S_{y,i}^2 \sigma_{IN}^2 + \sum_{m=1}^{N_S} S_{y,m}^2 \sigma_S^2, \\ d_{xy}^2 &= \sum_{i=1}^{N_{IN}} S_{x,i} S_{y,i} \sigma_{IN}^2 + \sum_{m=1}^{N_S} S_{x,m} S_{y,m} \sigma_S^2. \end{aligned} \tag{3.29}$$

$S_{x,i}$ and $S_{y,i}$ are the x and y elements of the S matrix for the infrastructure node i. $S_{x,m}$ and $S_{y,m}$ are the x and y elements of the S matrix for the satellite m. S matrix calculated as $S = \left[H^T W H\right]^{-1} H^T W$. All the matrices used to determine S have been defined as part of the EKF. W is defined as

$$\underset{(N_{IN}+N_S)\times(N_{IN}+N_S)}{W} = \begin{bmatrix} \sigma_{IN,i}^2 & \dots & 0 & 0 & \dots & 0 \\ 0 & \ddots & 0 & 0 & \dots & 0 \\ 0 & \dots & \sigma_{IN,N_{IN}}^2 & 0 & \dots & 0 \\ 0 & \dots & 0 & \sigma_{S,m}^2 & \dots & 0 \\ 0 & \dots & 0 & 0 & \ddots & 0 \\ 0 & \dots & 0 & 0 & \dots & \sigma_{S,N_S}^2 \end{bmatrix}. \tag{3.30}$$

The presented algorithm is tailored for multi-sensor fusion. In case of HPL estimation for stand-alone GNSS solution, terms in Equation 3.29 relating to the LPS become equal to

zero, and rows in matrices H_k and W are removed. The same applies to LPS only solution. As mentioned in Section 2.4.1, the estimated HPL is proportional to the HDOP (i.e., the network geometry quality measure) (Equations 2.9 and 2.10).

According to [42], HPL calculated as shown is only part of the HPL in the urban environment. Complete HPL is composed of two terms [42]: "impact of the measurement noise on the user position and the impact of measurement bias on user position." SBAS HPL (Section 2.4.1) is the former and WLSR HPL (Section 2.4.2) is the latter. By summarising both of these, complete HPL can be determined. If that is taken into account, all the results presented in the next subsection should be larger due to the added bias portion of the HPL. Given that the calculated SBAS HPL will prove to be large for loose integrity requirements, these results and the conclusion made based on them would not change. Because of that, WLSR HPL was not added to SBAS HPL in this instance.

3.3.3 Results and discussion

This section presents the results of the experiments carried out using the data collected in different environments for the EKF and RAIM algorithms. Firstly, the performance of stand-alone GPS data is tested. Then, the simulated terrestrial ranges measured to the simulated LPS are used for producing the multi-sensor fusion results. The performance for both data sets is tested when the vehicle is static in the open-sky environment, and dynamic in four types of environment — highway, open-sky area, suburban area and urban canyon.

Process noise and measurement noise are assumed to be Gaussian with zero-mean. The standard deviation of the acceleration noise is 1 ms^{-2}. The clock bias noise is assumed to have a standard deviation of 1 m. GPS pseudorange standard deviation is 5.1 m and for simulated terrestrial ranges is 1 m. Based on the requirements for payment-critical applications specified in Table 2.5, HAL of 20 m is chosen with the required integrity risk of $1 \cdot 10^{-5}$. Note that these requirements are less stringent when compared to the ones later used. However, these requirements were sufficiently stringent to demonstrate the performance of classical RAIM in different environments for stand-alone GPS and multi-sensor positioning. Position and integrity estimates are available every 0.05 s (i.e., 20 Hz).

3.3.3.1 GPS integrity in different environments

The integrity performance results are shown on a Stanford diagram (more about them in [17]). Stanford diagrams classify the integrity assessment in five different groups: nominal operations, misleading operations, hazardously misleading operations, system unavailable and misleading information, and system unavailable. These classifications are based on the fulfilment of the requirements that the estimated Horizontal Positioning Error (HPE) needs to be within the HPL, which cannot be larger than the HAL.

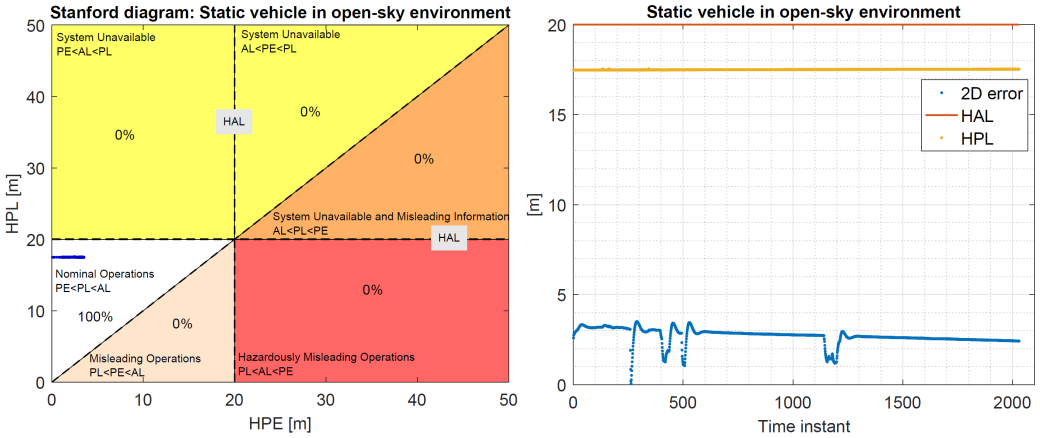
Table 3.2 shows the simple statistics calculated (average, standard deviation, minimum and maximum) for the estimated HPL and HPE values for stand-alone GPS RAIM in every type of urban environment.

TABLE 3.2: Performance of WLS RAIM in different environments based on GPS.

[m]	Static vehicle	Highway	Open sky	Suburbs	Urban canyon
Average HPL	17.5	19.3	25.1	32.7	43.1
Stand. deviation	0.01	2.7	3.3	15.9	22.2
Min HPL	17.5	17.5	23.8	23.1	19.6
Max HPL	17.6	35.6	51.5	129.7	133.4
Average HPE	2.7	2.6	2.6	3.1	39.1
Stand. deviation	0.4	3.3	0.3	1.5	59.5
Max HPE	3.5	18.2	5.0	34.1	366.9

Firstly, the performance of the static vehicle GPS data is shown (see Figure 3.13). Figure 3.13a shows that 100% of the time, integrity has been correctly classified as available (i.e., nominal operations). As said in the previous section, HPL is proportional to the network geometry. Given that the vehicle was static for a short period (under 2 min), the geometry of satellites was not changing, which has resulted in a stable HPL assessment. Figure 3.13b shows the HAL and HPE (i.e., 2D error) along the timeline of the experiment. On average, HPL was estimated to be 17.5 m with a probability of failure $1 \cdot 10^{-5}$ (see Table 3.2).

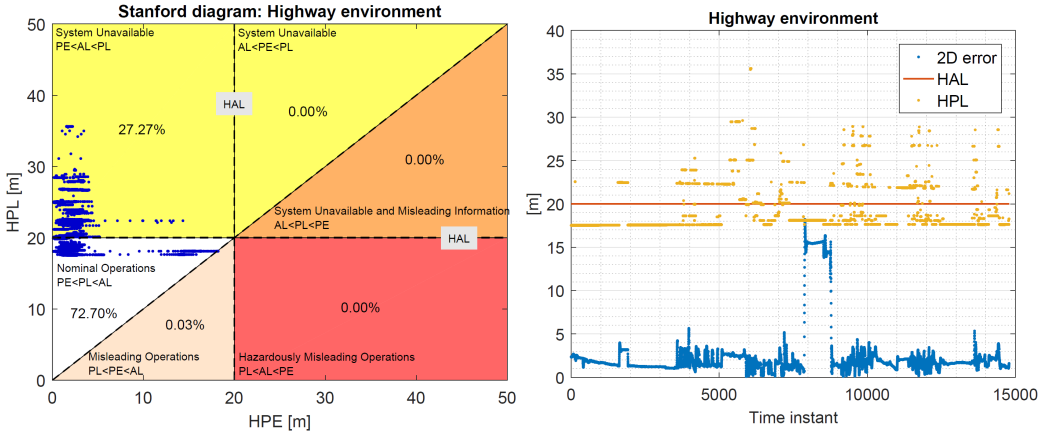
Data collection on the highway lasted for around 12 min. During the data collection, the HPE has never exceeded the HAL. However, HPL did exceed the HAL 27% of the time, which has resulted in integrity unavailability. 73% of the time, integrity was correctly classified as available (see Figure 3.14a). Figure 3.14b shows the variation in estimated HPL from 17.5 m to about 30 m. As shown in the graph, the majority of the estimated



(A) (B)

FIGURE 3.13: Integrity results for a static vehicle in an open-sky environment. a) Stanford diagram with integrity assessment. b) Timeline of HPL and 2D error estimation compared to HAL.

HPL values for highway environment are similar to the average HPL of static data. This is probably because geometry and number of satellites could not change much since highway data were collected right after the collection of static data (see Figure 3.9a). However, the visible variations in estimated HPL happened as a result of the variations of satellite geometry due to temporary satellite signal outages. These temporary outages could happen for a number of reasons, such as driving under an overpass or driving under a tree line. Table 3.2 shows that the maximum estimated HPL was around 36 m with the average HPL of 19 m. The average HPE remained similar to the ones in the static experiment.



(A) (B)

FIGURE 3.14: Integrity results for a vehicle on a highway. a) Stanford diagram with integrity assessment. b) Timeline of HPL and 2D error estimation compared to HAL.

Figure 3.15a shows the Stanford diagram for the open-sky environment where the vehicle's position integrity was unavailable 100% of the time. Although the average HPE was the same as for the static or highway data, the estimated HPL was always larger than the

required HAL. The average estimated HPL is 25 m with the standard deviation of 3 m due to the presence of the large HPL estimates from 30 m to 50 m (see Table 3.2). Figure 3.15b shows the change of HPL and HPE along the timeline (about 8 min of data). In comparison to the highway data, it seems that although worse, the geometry in the open-sky environment was more stable. Better stability of HPL in the open-sky environment was expected due to the reduced number of obstacles (e.g., there were no overpasses). However, the values of HPL were not expected as it was expected that the performance and measurement availability in the open-sky environment would be the best. Further explanation of these results is given at the end of this section where satellite visibility was analysed.

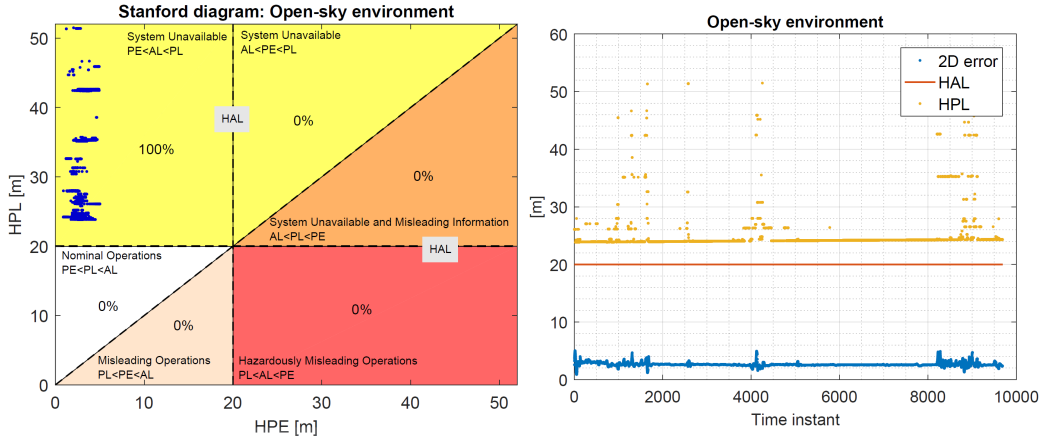


FIGURE 3.15: Integrity results for a vehicle in an open-sky environment. a) Stanford diagram with integrity assessment. b) Timeline of HPL and 2D error estimation compared to HAL.

Figure 3.16a shows the integrity availability for the suburban environment. Here, integrity was unavailable 99.4% of the time. It should be noted that in 11.5 min of data collection with the frequency of 20 Hz, five time instances occurred where less than five measurements were available. Because of that, in 0.60% cases, the integrity estimate was unavailable. Figure 3.16b shows the HPL and HPE along the timeline of the data collection. A differentiation is made between the positions estimated when less than five measurements are available and when five or more are available in this graph. The same is done for the HPL estimate. Yellow dots show the missing HPL estimations (when the number of measurements is less than five). Note that the value of 140 m for their HPL estimates is purely nominal; an estimate is unavailable in these cases. Table 3.2 shows that the average HPL is 33 m with the standard deviation of 16 m. Maximum estimated HPL is 130 m. However, looking at the Figure 3.16b, the results seem to be similar to

the results in the open-sky environment where a clear limit below which there are no HPL estimates is visible, and the increases occur when the geometry changes.

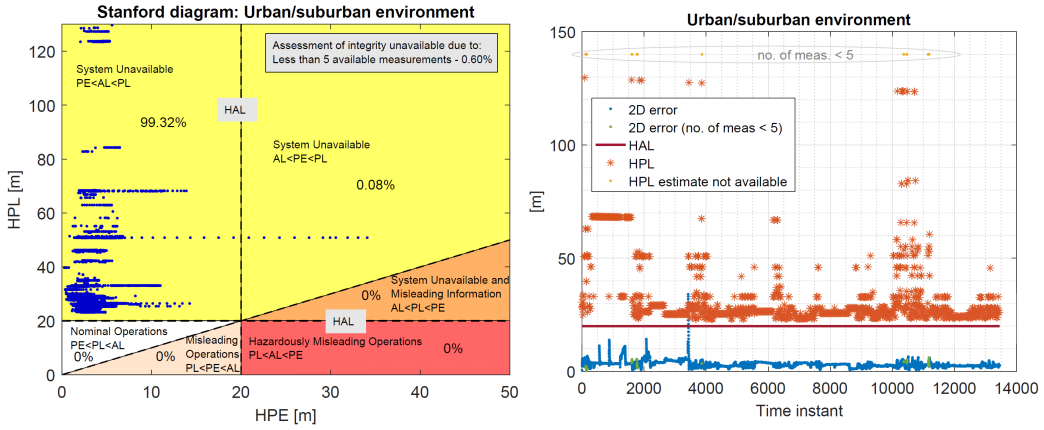
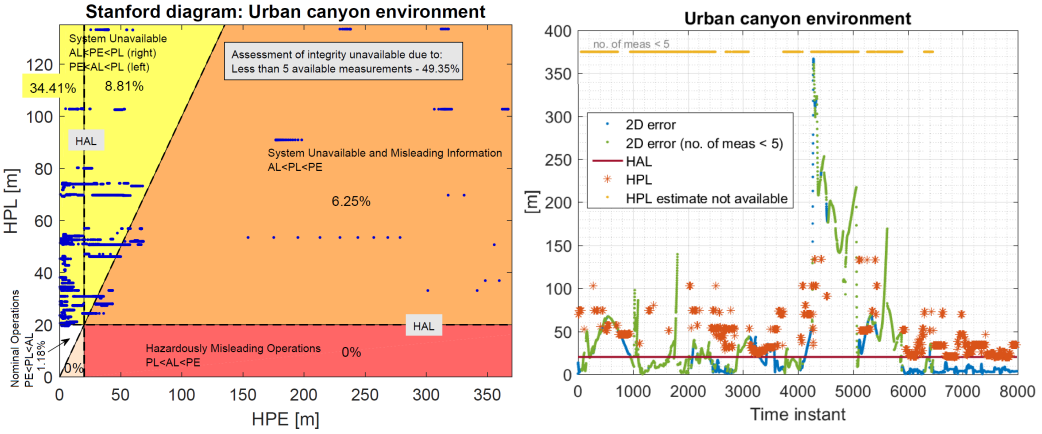


FIGURE 3.16: Integrity results for a vehicle in a suburban environment. a) Stanford diagram with integrity assessment. b) Timeline of HPL and 2D error estimation compared to HAL.

Finally, the results for data collected in the urban canyon are shown in Figure 3.17. Here, 49% of the time, the integrity estimate was not available due to lack of measurements for HPL calculation. Even before the integrity is calculated, 49% of positions automatically do not have an integrity assessment available. As shown in Figure 3.17a, an additional 43% of positions do not have integrity available due to HPL exceeding HAL. 1% of the time, integrity is correctly classified as available. Figure 3.17b shows that this occurs at the end of the 7 *min* data collection. When the HPL assessment is available, it is on average equal to 43 m with the standard deviation of 22 m. The maximum estimated HPL is similar to the one in the suburban environment. Unlike all the other environments where the HPE is similar, in an urban canyon average HPE is around 39 m. This is probably due to the impact of error sources like multipath and due to measurement unavailability.

Figure 3.18 shows the GPS pseudorange availability for all experiments. It can be seen that when the vehicle is static, the geometry between the vehicle and the GPS satellites is stable, not only due to the short data collection but more importantly because the number of pseudoranges does not change very often.

When the vehicle is on the highway, it was shown that the HPL estimate changes, which implies that the geometry between the vehicle and the satellites changes repeatedly. This can be explained with the changing number of available measurements, which affects the geometry. As noted before, these changes could occur due to numerous trees and viaducts on the route where the vehicle was driving (Figure 3.9). The integrity was unavailable



(A) (B)

FIGURE 3.17: Integrity results for a vehicle in an urban canyon. a) Stanford diagram with integrity assessment. b) Timeline of HPL and 2D error estimation compared to HAL.

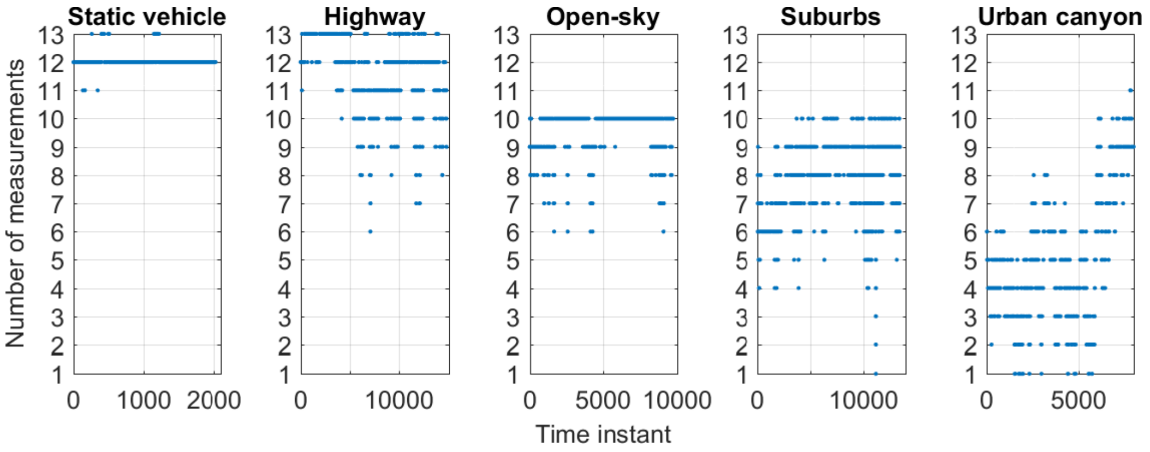


FIGURE 3.18: Availability of GPS satellites in different environments.

100% of the time in the open-sky environment. It was expected that the performance and measurement availability in the open-sky environment would be the best. However, the maximum number of terrestrial ranges measured in open-sky was 10 in comparison to the highway where it was 13. After the sky plots and satellite elevations were checked for highway data collection, three satellites with a low elevation (about 5°) that was dropping were identified. By the time the vehicle arrived to the open-sky environment, those three satellites were no longer visible. Consequently, the minimum HPL estimate probably shifted up due to lower number of visible satellites. The changes in the number of measurements coincide with the temporary changes of the HPL in Figure 3.15b. The same can be said for the suburban environment where the number of visible satellites changes more often. This was expected since the suburban environment consists of obstacles such as trees avenues, low-rise buildings and houses, traffic constructions. Finally, the biggest changes of both the measurements and the HPL happen in the urban canyon. As expected, the most

probable cause of this is the local environment causing the measurement unavailability and presence of more error sources (i.e., multipath from buildings). The reason why integrity is available 1% of the time at the end of the urban canyon experiment can be seen in the highest number of available measurements in the experiment which occurs because the vehicle at that point gets out of the urban canyon (see Figure 3.12a, the south portion of the trajectory).

3.3.3.2 Multi-sensor integrity in different environments

The previous section has shown the dependence of the RAIM algorithm on the environment of the user when it is based solely on the GPS data. Here, simulated terrestrial ranges are fused with GPS data, and the effect of that fusion is discussed.

It should be noted that this comparison was only made on the portions of the data where LPS anchors were simulated (see Figures 3.9a to 3.12a). Therefore, for comparison purposes, availability of integrity for stand-alone GPS data was estimated for those subsets of data. Consequently, the percentages in Figure 3.19 for GPS will be slightly different from the integrity levels shown in the previous section.

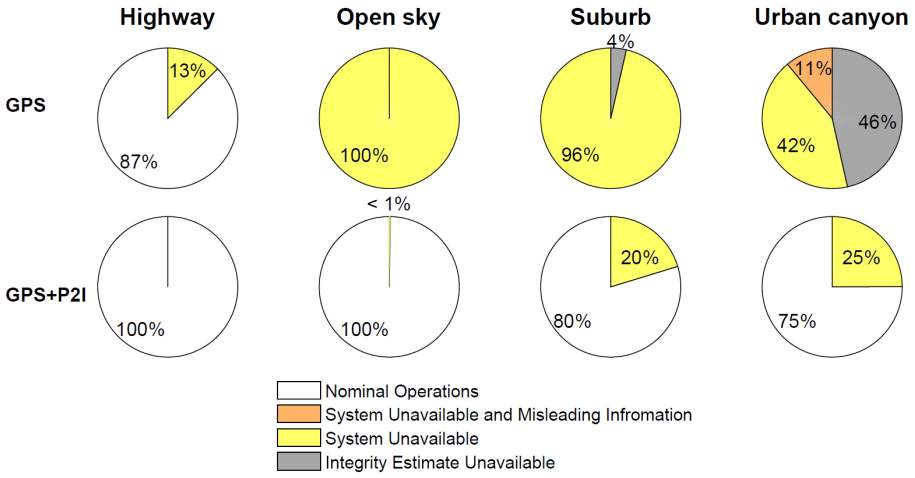


FIGURE 3.19: Comparison of the integrity availability estimates for positioning systems based on GPS only (top row) and GPS+P2I (bottom row) data. Integrity estimate is compared for all four different environments: highway, open sky, suburb and urban canyon environment.

As hypothesised, the LPS has significantly improved the rate of integrity availability. The rates of integrity availability are similar and seem to depend on the environment less than they used to. Figure 3.19 compares the integrity availability assessments for four environments where the vehicle was dynamic. The performance of GPS data is shown in the

first row, and the GPS+P2I data is shown in the second row (V2I refers to Vehicle-to-Infrastructure). As shown, for the highway and the open-sky environment, the availability grows to the same level of 100%. Unavailability of integrity estimate (due to lack of measurements) is completely removed for both the suburban and urban canyon environments because of the fusion of GPS with LPS measurements. Now, integrity is available 80% and 75% of the time in the suburban and urban canyon environment, respectively. Levels of integrity unavailability are probably still present in the suburban and urban canyon environment because of the bad GPS data. The improvement in HPL and HPE for all environment types is numerically shown in Table 3.3.

TABLE 3.3: Performance of WLS RAIM in different environments based on GPS+P2I data.

	Highway		Open-sky		Suburb		Urban canyon	
[m]	GPS	GPS+P2I	GPS	GPS+P2I	GPS	GPS+P2I	GPS	GPS+P2I
HPL	18.4	9.7	24.2	7.7	42.8	14.8	45.0	16.7
HPE	1.8	0.5	2.6	0.3	3.0	0.7	16.6	1.0

3.4 Data collection campaign

The last integrity system requirement to be defined in this chapter is not about the algorithms. It is about determining what data are necessary, collecting that data and analysing them. After that, the requirement of having data for integrity algorithm validation will be fulfilled. One of the reasons for collecting real-world data was to avoid optimistic results where random outages or large random outliers were not introduced into the systems.

A lot of literature today in multi-sensor and cooperative positioning uses simulated data to verify and validate their positioning and integrity algorithms as it limits the number of errors introduced into the system [65]. This approach has its benefits, such as high rate of simulation runs to create statistically significant results and capability of creating large data sets. The biggest disadvantage of using simulated data for algorithm validation is the lack of realistic random error sources. The algorithms tested only using simulated data may not be able to perform correctly when exposed to real-world data. As described in Chapter 2 there are multiple examples of researchers using real-world data.

The content of Section 3.4 was first published in a conference paper *A measurement campaign for cooperative positioning architecture based on GNSS and local positioning system* published as part of the *IGNSS 2020 Symposium* in *February 2020* ([88] in the bibliography).

The European GNSS Agency report from 2015 [4] lists model validation as one of the open issues that need to be addressed in terms of integrity algorithms. As mentioned before, algorithms validated using only the simulated data may not be able to perform correctly when exposed to the specific error sources of the local environments. To fully validate a framework one of the objectives needs to be an extensive data collection campaign "aiming to characterise error sources, magnitudes and probabilities for two important GNSS terrestrial application areas: automotive and pedestrian users". This is one of the objectives of the European Commission funded project The Integrity GNSS Receiver (IGNSSRX) [89]. However, extensive data collections for multi-sensor and CP systems can be costly, logistically demanding, time-consuming to plan and hard to organise due to a lot of variables (e.g., number of participants, sensors, organising vehicles, organising data collection area). This research proposes a smaller scale data collection with smaller costs, less complicated and less demanding organisation, as a means of initial algorithm validation. The data sets collected like this cannot fully capture the benefits of an extensive measurement campaign. Still, they will introduce the realistic random errors which will not result in the over-optimistic performance estimates for the proposed algorithms.

A data collection campaign, where real-world CP data are collected and processed to establish the effect of realistic errors on current CP techniques, is detailed in this section. The experiment was a joint undertaking between the University of Melbourne, University of New South Wales (UNSW), Royal Melbourne Institute of Technology (RMIT) University and the Commonwealth Scientific and Industrial Research Organisation (CSIRO). The focus of this section is the description of the measurement campaign, which includes a description of the commercial sensors used, data collection process and the analysis of data availability and quality. Lastly, the data used in this research as well as the process of determining the ground truth are defined.

3.4.1 Sensor description

A GNSS receiver, a WASP system and a UWB system were used for data collection (see Figure 3.20). This section provides a short description of each of those sensors.

Four Leica Viva GS15 receivers were used during the measurement campaign (e.g., Figure 3.20a). They were used for positioning of the mobile users as well as for determining their ground truth trajectories. The precise positions of the LPS anchors were determined using GNSS measurements. Leica's datasheet in [86] provides technical details about the



(A) (B) (C)

FIGURE 3.20: During the measurement campaign three types of sensors were used: a) GNSS receiver. b) WASP unit. c) UWB unit.

used receivers. Although the receivers are multi-GNSS receivers, only GPS data are used in this research. However, it should be noted that all the algorithms are applicable for multi-GNSS solutions. More on the used GPS measurements is in Section 3.4.4.

As described in [90], WASP or Wireless Ad hoc System for Positioning, has been developed by CSIRO. Figure 3.20b shows one of the used WASP units. The terrestrial range between the WASP units is computed from the measured Time-Of-Arrival (TOA). WASP is a wireless sensor network platform that can provide sub-metre positioning and ranging accuracy by using low-cost electronics. Testing in [90] has shown that 85% of ranging errors are within 0.15 m in an outdoor environment, 82% are within 0.50 m in a LOS indoor environment, and only 65% of ranging errors are within 0.50 m in an NLOS indoor environment. These tests were conducted in a network of around 12 nodes with ranges up to 200 m outdoors and 30 m indoors. For static localisation, positioning errors have been shown to range from 0.11 m for KF in the outdoor environment to 0.66 m for KF in the indoor NLOS environment [90]. Additional details about WASP's hardware and software can be found in [90]. In this data collection campaign, WASP was used to measure terrestrial ranges between dynamic nodes (i.e., P2P), between dynamic and anchor nodes (i.e., P2I) and between anchor nodes (i.e., I2I).

In this campaign, Decawave's MDEK1001 Development Kit (Figure 3.20c) was used for terrestrial ranging, as well as WASP. However, unlike WASP, Decawave's UWB units were used for ranging between only one dynamic node and anchor nodes (i.e., P2I). According to the Decawave's product brief [91], 2D accuracy is typically better than 0.10 m with

the maximum frequency of position estimation of 10 Hz. In LOS conditions, up to 60 m range can be expected. More details about this UWB system can be found in [91].

Due to the use of different measurement systems with different clocks that are independent of each other, time synchronisation was performed. By calculating and compensating the relative clock offsets between each system, the time synchronisation was achieved. More details on how this was achieved are given in [88].

3.4.2 Data collection procedure

As the experiment uses terrestrial ranging devices, the UWB and WASP units required setting up a Local Positioning System (LPS). A network of 15 anchor nodes (i.e., infrastructure nodes) was set up as shown in Figure 3.21. This was done to mimic the geometry of available infrastructure on the actual roads, given that geometry proved to be important in [74]. Out of 15 anchors that were equipped with WASP units, seven anchors were also equipped with the UWB units. Given the idea of collecting real-world data on a smaller scale, the anchor nodes were set up on an open-sky area of about 30 $m \times 60$ m with the largest distance between the infrastructure nodes ~ 62 m. An example of the infrastructure node is shown in Figure 3.22a. The road polygon (i.e., map feature) used later for SFC method was created by vectorising the satellite image around the improvised road (polygon shown in Figure 3.21).



FIGURE 3.21: Data collection area with anchors. An example of the trajectory is shown in red.

In this measurement campaign, there were four users collecting data. All users collected GNSS data, WASP terrestrial ranges to the infrastructure (i.e., P2I) and WASP terrestrial ranges to other users (i.e., P2P). In addition to this, the master user (User 2 during the campaign) measured UWB terrestrial ranges to the infrastructure nodes (i.e., UWB P2I). All users were equipped with one GNSS receiver and one WASP unit. The master user shown in Figure 3.22b was also equipped with UWB radio.



(A) (B)

FIGURE 3.22: Sensor set-up for a) an example of the infrastructure node. b) Master user.

A measurement campaign consisted of three different experiments — static, dynamic and dynamic+multipath. During the static experiment, all users were stationary in the area between anchors 5-10 for almost 3 *min* (see Figure 3.23a). The static experiment was followed by the dynamic experiment where the users walked along the improvised road segment with an average speed of 1 ms^{-1} for 6.5 *min* (see Figures 3.23b and 3.23c). The speed of the master user during the dynamic experiment is plotted in Figure 3.24. The final executed experiment involved inducing the multipath in an otherwise open area without big sources of multipath. This experiment is named dynamic+multipath. During this experiment, possible multipath sources were installed along one part of the trajectory. As shown in Figure 3.23d, big reflective panels and vehicles were used. The users again walked with an average speed of $1ms^{-1}$ for a little over 6 *min*.



(A) (B)

(C) (D)

FIGURE 3.23: The measurement campaign was divided into three different experiments. a) Experiment 1: static. b) Experiment 2: Master user. c) Experiment 2: Dynamic. d) Experiment 3: Dynamic+multipath.

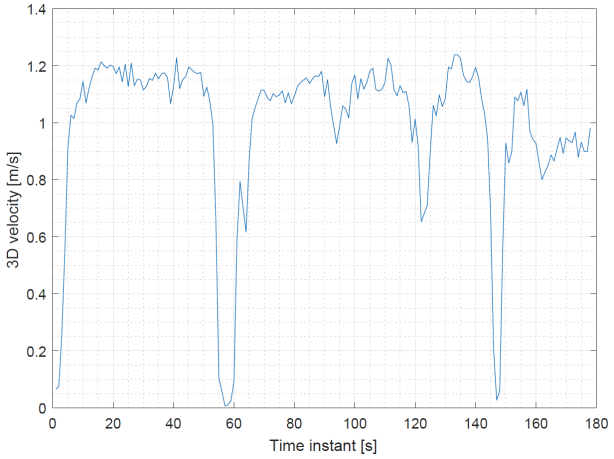


FIGURE 3.24: Dynamics of the master user during the dynamic experiment. This figure was originally published in [92].

3.4.3 Data availability and quality

This section provides an overview of the data availability and quality of ranging data for all LPS P2I and P2P measurements. WASP ranging measurements to 14 anchor nodes (during

the data collection one anchor stopped working which reduced the number of anchors from 15) and three users from master user were made at a frequency of approximately 10 Hz. The frequency of the UWB ranging measurements from the master user (referred to as User 2 in this section) to all seven infrastructure nodes was around 9.8 Hz. GNSS data were collected with a frequency of 1 Hz. Data availability and quality are shown for 1 Hz frequency.

Figure 3.25 shows the availability of the WASP P2I measurements for all users across all experiments. User 1 and 3 experience more outages during the dynamic experiment (orange colour in the graph) than in the dynamic+multipath experiment (yellow colour in the graph). It is unknown why this occurs and what will be the effect of this on the positioning/integrity performance. In terms of measurement availability, WASP P2I measurements seem to be stable as the number of available ranges rarely goes under 12. The availability of the WASP P2P ranges is shown in Figure 3.26. Similarly, to the WASP P2I ranges, in terms of availability, WASP measurements seem to be stable as the number of P2P measurements rarely goes under 2.

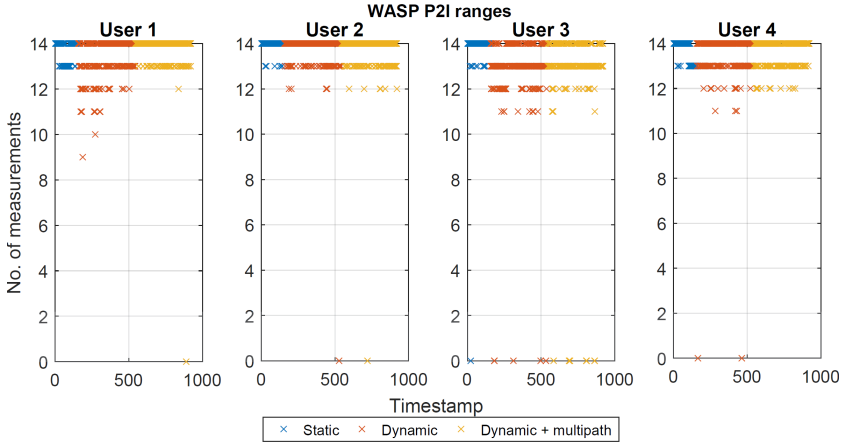


FIGURE 3.25: Availability of WASP P2I measurements for all users and all experiments.

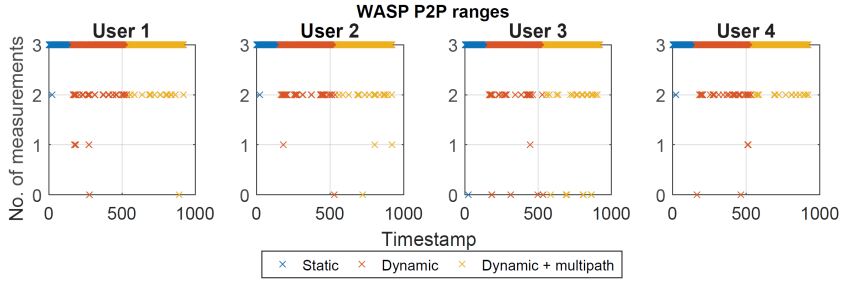


FIGURE 3.26: Availability of WASP P2P measurements for all users and all experiments.

User 2 was the only one equipped with a UWB radio. The availability of the UWB P2I terrestrial ranges is shown in Figure 3.27 (green colour). Although there were seven anchors equipped with UWB units, User 2 communicated with the maximum of four UWB units at each epoch. The rate of data outage is little under 50% of the time. Furthermore, Figure 3.27 shows the availability of all used sensors for User 2, including GPS measurements, across all the experiments. As expected, the number of measurements seems to be the most stable during the static experiments. GPS data is also stable in terms of availability, where more outages are experienced when multipath is provoked.

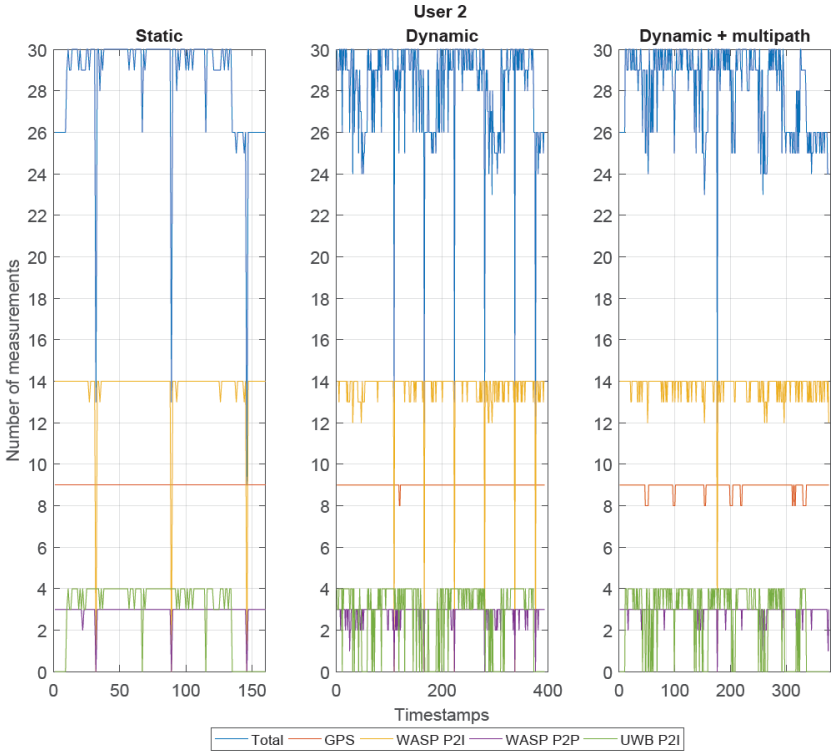


FIGURE 3.27: The overall measurement availability during all experiments for User 2 (i.e., master user).

The analysis of the LPS ranging errors for all users and all anchor nodes across all the experiments is presented as well. The range errors are estimated by comparing the measured ranges and range measurements calculated from the ground truth.

Firstly, WASP P2I ranges are analysed (see Figure 3.28). The x-axis of the graph represents every infrastructure node. Generally, the best ranging accuracy was achieved for all anchors during the static experiment. It was expected that the ranging accuracy will decrease when multipath is provoked in comparison to the dynamic experiment. However, this was not the case. Only User 2 and 3 show the expected accuracy deterioration. User 1 shows that the ranging accuracy improves during the dynamic+multipath experiment (in

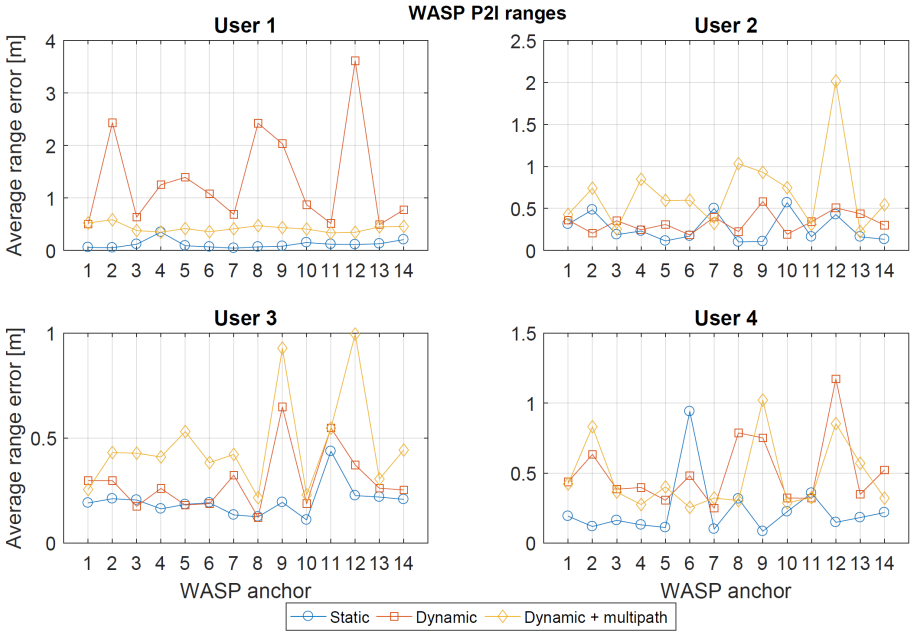


FIGURE 3.28: The average error of WASP P2I measurements for all anchors (x-axis). The average error is shown for all users as well as all experiments.

comparison to the dynamic experiment). The average accuracy of WASP P2I ranging for the static experiment is 0.2 m. The average accuracy for the dynamic experiment is 0.6 m. However, it should be mentioned that the average ranging accuracy for User 1 is 1.3 m, Users 2 and 3 is around 0.3 m, and for User 4 is 0.5 m. That difference is caused by the larger outliers recorded by Users 1 and 4 (maximum around 90 m in comparison to the maximum 60 m for User 2 and 3). However, it is unknown why this happened. It may be due to some device-specific reasons or due to an error made during the data collection. The average error for dynamic+multipath experiment is 0.5 m. On average, User 1's ranging error is 0.4 m, 0.7 m for User 2 and 0.5 m for Users 3 and 4. Average errors confirm the results shown in Figure 3.28: User 1 performs better during dynamic+multipath experiment, User 2 and 3 perform as expected, and User 4 performs similarly during both the experiments.

Figure 3.29 shows the average accuracies of WASP P2P ranges (i.e., ranges between users). If the average ranging error is equal to 0 m, this indicates it is the communicating node (i.e., if the communicating node is User 1, measurement to User 1 does not exist it is shown with 0 m average error). The average accuracy of WASP P2P for all users is around 0.2 m (same as P2I). During the dynamic experiments, the average ranging error is estimated to be 1.5 m, and for the dynamic+multipath experiments, it is 1.1 m. Again, the overall average accuracy is probably affected by the larger outliers present in the dynamic experiment data (maximum outlier is 104 m compared to maximum dynamic+multipath outlier of 66 m).

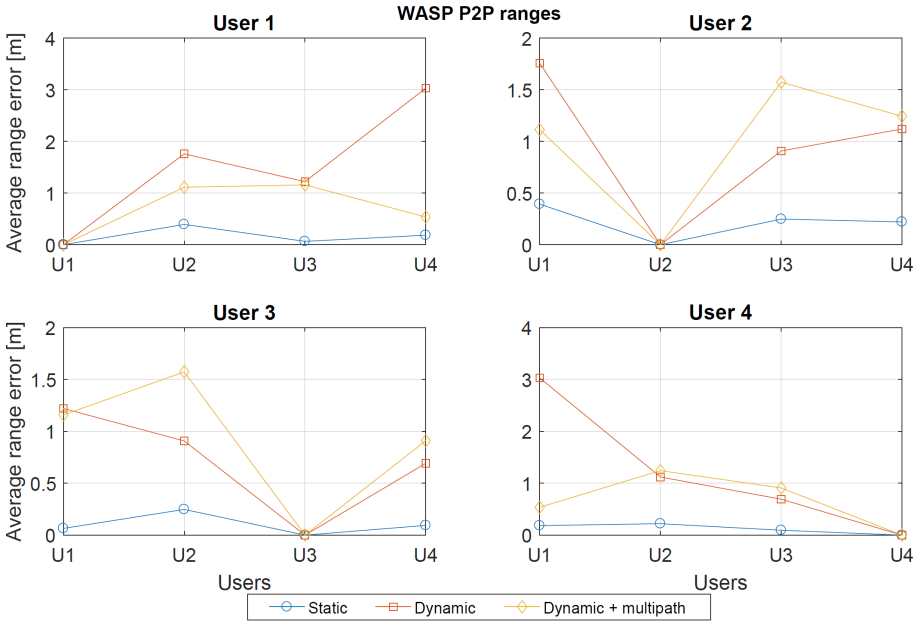


FIGURE 3.29: The average error of WASP P2P measurements for all users (x-axis). The average error is shown for all users as well as all experiments.

3.4.4 Use of data for algorithm validation

WASP and UWB units provide terrestrial range measurements between users and/or infrastructure nodes. As such, they can be used for positioning and IM directly without the need for preprocessing. However, that is not the case for GNSS pseudoranges. This section specifies GNSS measurements used for positioning, IM, and determining of ground truth and infrastructure nodes position.

In this research, proposed algorithms are not designed for a specific device. They can work with any and multiple systems that can provide terrestrial ranges. Although WASP and UWB data were available, WASP terrestrial ranges were chosen for performance analysis in Chapter 6 due to availability of P2I ranges for all users as well as the P2P ranges. Whereas UWB data were available for P2I ranging only for the master user. Furthermore, WASP was able to measure I2I ranges which enabled the error distribution characterisation as shown in Chapter 3.

Although a multi-GNSS receiver was used to collect GNSS data, only GPS data were used in this research. However, it should be noted that the presented algorithms are not specific to GPS and are capable of working with multi-GNSS data. In this research, the use of only GPS was considered enough for a proof of concept.

The content of Section 3.4.4 has not been previously published in [88] or any other publication.

GPS code pseudoranges L1 C/A (C1) were used as the satellite pseudorange measurements for the positioning and integrity algorithms. Pseudorange measurements are equivalent to the time difference between the time of signal reception and its time of emission from a satellite [16]. Due to the one-way concept, the time of signal reception is a reading of the receiver clock, and the time of emission is a reading from the satellite clock. Hence, clock biases need to be considered. Because of the receiver and satellite clock biases as well as the other biases such as atmospheric effects, measured ranges are denoted as pseudoranges [16]. In this research, GPS pseudoranges used for positioning and integrity estimation are not corrected for the atmospheric effects. The ranges were not corrected for atmospheric effects because of the assumed availability of affordable single frequency GPS receiver. However, the proposed algorithms could be applied to corrected pseudoranges. Pseudoranges are corrected for a satellite clock bias which is available in the navigation message that provides the broadcast ephemeris data necessary to calculate the positions of the satellites in ECEF. Furthermore, receiver clock bias is estimated as a part of the state vector as previously shown in Equation 3.14.

When it comes to algorithm validation, the key prerequisite for quantifying the performance quality is having ground truth data. In this research ground truth data implies the positions of each of the users determined with higher accuracy and precision than the estimated positions (e.g., trajectory shown in Figure 3.21). Furthermore, precise positions of anchor nodes had to be known as well. These data were determined by post-processing the multi-frequency GPS L1+L2+L5 carrier-phase measurements using the RTKLib software package. The coordinates were determined relative to the Australian Regional GNSS Network's (ARGN) base station SYDN in Sydney with known coordinates. Instead of broadcast ephemeris data that are available in real-time, precise ephemeris data, published two weeks later, were used for satellite ephemeris and clock. Broadcast ionospheric and Saastamoinen models were applied for correction of ionospheric and tropospheric effects, respectively. The information about these atmospheric models can be found in [16]. This process provided the ground truth data with precision at a sub-centimetre level.

3.5 Conclusions

Determination of the integrity system requirements as shown in this chapter is important in the process of designing novel integrity algorithms. Based on all the results from the Sections 3.2 and 3.3 (in addition to the literature review), an informed decision on the

positioning system can be made. The positioning system underlying any of the proposed integrity methods will be based on multi-sensor and CP systems.

The results shown in Section 3.3 have helped to generate a set of integrity system requirements (in addition to the positioning system). Any proposed integrity algorithm should address all of the following system requirements.

1. Multi-sensor or CP systems need to be used to ensure sufficient measurement redundancy in all urban environments. This issue has been highlighted during the urban canyon experiment where integrity was unavailable almost 50% of the time, by default, due to insufficient measurement redundancy.

2. An integrity method where its bounding of integrity does not depend on the quality of the satellite/user or LPS/user geometry is necessary for the urban environment.This is visible in the algorithm for HPL calculation where proportionality to the satellite/user geometry is clear.

3. An integrity method where its bounding of the integrity does not depend on the number of measurements is necessary. This is important since a change in the number of measurements effectively changes the geometry.

In addition to these three requirements, the new method should be capable of estimating integrity under more stringent requirements than shown in this chapter and Chapter 2. Furthermore, as with classical integrity methods, an FDE algorithm is needed to exclude large biases.

Lastly, it is necessary to collect real-world data to validate the novel integrity method that will be proposed in this research. Although the proposed algorithms can be applied for multi-GNSS and for any type of available terrestrial ranging device, GPS and WASP data will be used for their validation in this research.

4

Cooperative positioning

With the EKF being the most commonly implemented sensor fusion technique, assumptions of Gaussianity in describing the errors of data are commonly made, and the measurement models are commonly linearised. However, these assumptions and approximations may negatively affect the positioning performance and possibly the integrity performance if the Gaussian distribution is far from the actual distributions and the measurement models are highly non-linear. The main contribution of this chapter is the empirical study on the effect of these assumptions on the positioning accuracy of the previously defined multi-sensor positioning system. Based on the conclusions of this analysis, cooperative Particle Filter is presented as the underlying positioning algorithm of the proposed integrity algorithms.

4.1 Introduction

As the literature review (Chapter 2) demonstrates, it is a common practice to make a Gaussian assumption for measurement error because of the availability of a closed-form linear estimator. Those estimators also rely on a linear approximation of the non-linear measurement models. In case of a larger non-linearity, it is unknown how big the effect of the linear approximation would be on the positioning performance. When it comes to integrity, the effect of these assumptions may be crucial. For example, integrity estimate may be too optimistic and hazardously misleading information may occur as a result.

Although these assumptions hold and produce good results in the majority of cases, that may not be true in the case of the multi-sensor system as defined in this research. In this chapter, given the use of non-traditional signals such as WASP, it is unknown if the Gaussian assumption is appropriate. In the case of WASP measurements collected as explained in Section 3.4, a better approximation of the actual error distribution was found to be three-component Gaussian Mixture Model (GMM) (to be shown in the following section). Furthermore, it was hypothesised that the terrestrial ranges measured from LPS may be highly non-linear due to the proximity of LPS nodes. This is unlike GNSS, where the linear approximation is good, despite the non-linear measurement model, due to the large distance between the user and the satellite.

Motivated by this, the effect of linear approximation and the Gaussian noise assumption in multi-sensor positioning through experimental evaluation is studied. Specifically, the performance of multi-sensor EKF and PF is quantified by using a real-world experimental platform. It should be noted that the effects of common assumptions will not be tested on both the multi-sensor and the CP data. However, the impact of making such assumptions on CP will be deduced from the multi-sensor results. The contributions of this chapter are summarised as follows: An experimental multi-sensor tracking system which fuses GNSS data with ranges measured against local reference nodes is deployed. The performances of EKF and PF algorithms are evaluated experimentally using the collected data. The effect of linearisation on positioning accuracy is quantified. A Gaussian Mixture Model (GMM) based ranging error model is proposed, which accurately captures the statistical

Part of Section 4.1 and whole of Sections 4.2 and 4.3 were first published in *IEEE Sensors Journal* in *November 2019* a paper entitled *The effect of linear approximation and Gaussian noise assumption in multi-sensor positioning through experimental evaluation* ([92] in the bibliography). Minor changes have been made to terminology.

distribution of ranging errors in the system. The model is used in the PF, and the performance improvement over using Gaussian ranging error models is quantified. Lastly, motivated by the results of the study of the said effects, cooperative PF is proposed. Both multi-sensor and cooperative PF will be used to implement the integrity method proposed in this research.

4.2 Terrestrial range error distribution fitting

According to [93], modelling a distribution as a Gaussian when it is not, can underestimate the probability of a random error (e.g., tails of Gaussian distribution are not 'fat' enough). If that assumption is not made, this random error can provide useful information for the system. [93] also states that if error distributions of the measurements are a better approximation of the actual error distribution, measurements and models will be used in a better way.

Given the results in [94] where an empirical ranging error model was fitted for the WASP ranges in an indoor environment, an assumption of Gaussianity of the WASP error distribution is not valid. The fitted ranging error distribution was non-Gaussian, and the model showed a long tail on the right side. Therefore, here, an error distribution of the WASP ranges in an outdoor environment is fitted. Given that the ranges were measured outdoors with no obstacles and with the largest distance between the infrastructure nodes being $\sim 62\ m$, it is assumed that the distribution of the ranging error is independent of the distance between nodes. In the case of longer distances between nodes, this statement would have to be reconsidered. In general, the error distribution needs to be characterised in different environments and for different distances. This would be used as *a priori* knowledge for real-time applications.

The infrastructure network of 14 nodes was set up (details in Section 3.4). While the user measured the ranges to the nodes, the inter-node distances were also taken (see Figure 4.1). Based on more than half a million measured distances between the static nodes, and the ground truth distances calculated from the infrastructure node coordinates, the errors were calculated. Those errors were used to fit the terrestrial range error distribution (see Figure 4.2). Only the significant part of the curve is shown. 99.83% of measurement errors fall into the $[-2m, 2m]$ interval shown in Figure 4.2.

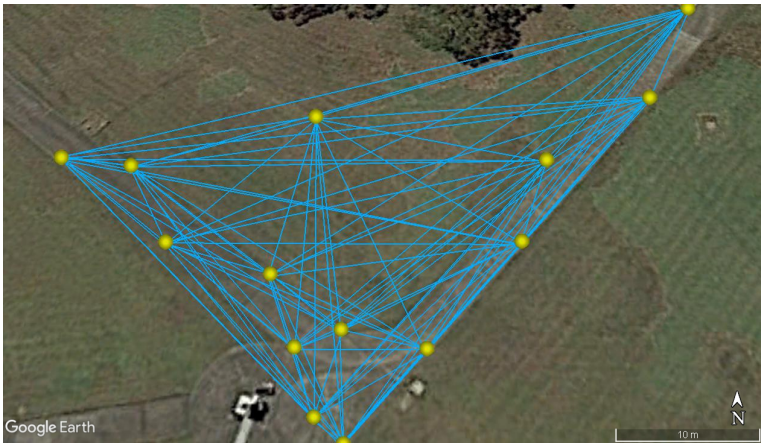


FIGURE 4.1: Ranging combinations between the static nodes.

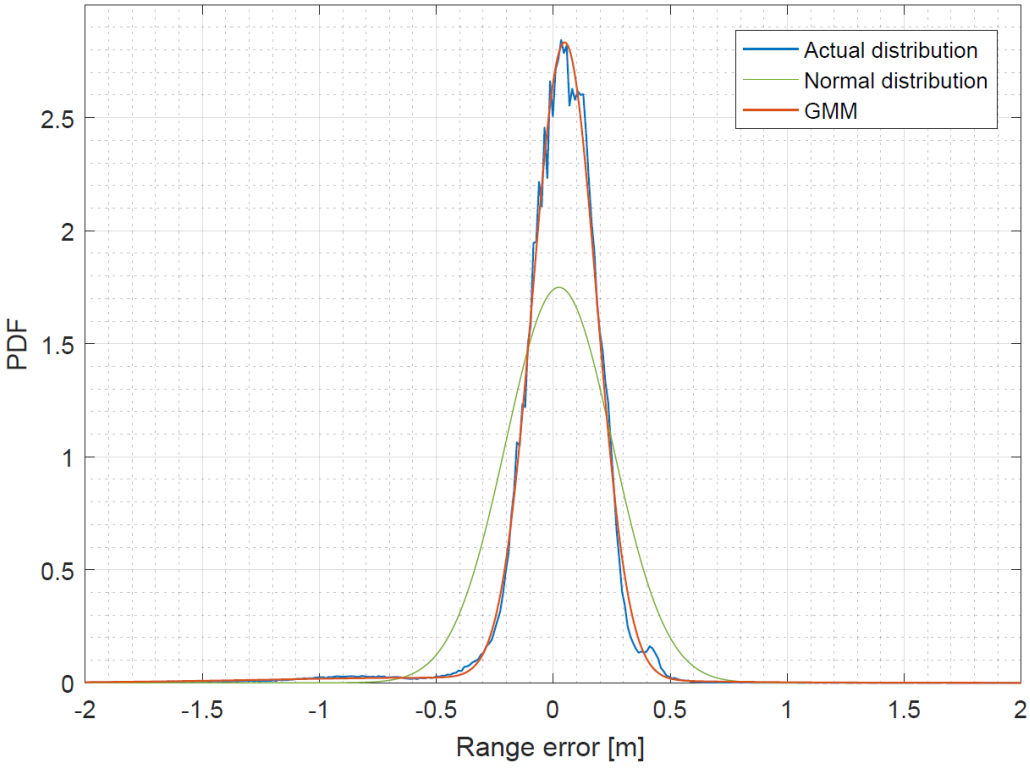


FIGURE 4.2: Actual error distribution with the fitted three-component GMM and fitted Normal distribution.

It is visible in Figure 4.2, that Gaussian distribution (green) is not a good approximation of the actual error distribution (blue) of the terrestrial ranges. As one of the aims of this chapter is to test the impact of assuming Gaussianity, a better approximation is found. A three-component Gaussian Mixture Model (GMM) is fitted to the measurement errors. It can be seen in Figure 4.2, an empirically fitted GMM (orange) closely approximates the actual distribution (blue) of the terrestrial ranges. In future developments of the proposed integrity method, Kernel Density Estimation (KDE) could be used as a non-parametric way to estimate the measurement error distribution.

The PDF of the GMM for a scalar continuous random variable e can be written as in [95],

$$p(e) = \sum_{c=1}^{N_C} w_c \cdot \mathcal{N}(e; \mu_c, \sigma_c^2), \tag{4.1}$$

where $c \in 1 \dots N_C$ denotes the number of components of the GMM. Each component c is attributed with component weight w_c and is normally distributed with corresponding mean μ_c and variance σ_c^2. When implementing the PF, Equation 4.1 is used as a PDF of terrestrial range measurement p_i from Equation 4.3. Parameters for the three-component GMM fitted in this chapter are given in Table 4.1.

TABLE 4.1: Three-component Gaussian Mixture Model (GMM)

Parameters\Component number	1	2	3
$\mu[m]$	0.0111	-0.5085	0.0776
$\sigma^2[m^2]$	0.0176	0.5335	0.0171
w	0.4321	0.0414	0.5265

4.3 Analysis of the effect of common assumptions

To test the effect of a Gaussian assumption and linear approximation, a multi-sensor fusion architecture where a node determines its position using GNSS and terrestrial range measurements to the static anchor nodes (i.e., LPS) is deployed.

One of the most prominent ways of fusing multi-sensor data is through the EKF (Kalman Filter's non-linear counterpart). The KF is known as a linear Gaussian optimal filter [96]. When dealing with non-linear system dynamics and non-linear measurement models, linearisation can be performed by using one of the linear approximation techniques. Although there are many, the first-order Taylor series expansion used in the EKF [97] was used here as well. More details about this method can be found in [98]. The first-order Taylor series expansion can provide a good approximation of a non-linear dynamic and measurement model, but the more non-linear those models are, the less appropriate the EKF becomes and the position solution will diverge [99, 100]. Even though the first-order Taylor series expansion is a good approximation of non-linearities for the GNSS measurement model, this is unknown in the case of the LPS measurement model. Furthermore, the more non-Gaussian the measurement error distribution is, the further away the EKF is from the

optimal filter. This can cause large errors, as well as divergence of the solution [100]. Since the performance of the KF based solutions depends on the nature of non-linearities and non-Gaussianity, their applicability needs to be determined [101].

Considering both the effect of linearisation and the Gaussian assumption on the accuracy of the position estimation, Monte Carlo filters were chosen, known as Particle Filters (PF) to be used as sub-optimal estimators [99–102] for comparison with the EKF. The PF solution is not an analytically tractable solution [100, 103]. In the PF, the *a posteriori* error distribution is represented by a set of random particles with associated weights, that are numerically propagated through the non-linear dynamic and measurement model. Larger populations of particles improve the approximation of this discretised *a posteriori* distribution to the functional form of the *a posteriori* used in other filters, and the PF approaches an optimal estimator [103].

The theoretical background of the estimators indicates that the PF will outperform the EKF as the system dynamics and distributions diverge from being linear and Gaussian. However, the level of accuracy degradation is unknown since it depends on the specific dynamics, measurement model, sensors, etc. When designing a multi-sensor positioning system, it is important to know what is the impact of the assumptions that are being made and if that impact is significant in regards to the positioning requirements (accuracy, integrity, availability). This section will elucidate to the positioning system designers whether their linear and Gaussian approximations are sufficient or their system requires better approximations of non-linear dynamic and measurement models and measurement error distribution.

Whether first-order Taylor series expansion is a good approximation of the non-linear LPS measurement model will be tested by comparing the EKF and the PF performance. Furthermore, to quantify the effect of the Gaussian assumption in case of the LPS ranging measurements, the performance of two PFs will be compared, one that assumes Gaussianity and one that does not assume Gaussianity for the LPS measurements.

Most of the literature comparing the performance of the KF based algorithms and the PF algorithms show that the non-linear estimator (e.g., PF) performs better when dealing with non-linear measurement models [77, 99, 101–104]. A small number of papers was found where error distributions of ranging errors were modelled to the actual error distribution [94, 105, 106]. These papers mostly refer to indoor environment positioning systems that are not based on multi-sensor integration. However, they do show that there is a need

for measurement error distribution modelling due to complexity and error sources of the indoor environment which is similar to the conditions of the urban environment. In [100], accuracy improvement is shown when PF is used for non-linear dynamic and non-linear non-Gaussian measurement model. However, the models in question are not similar to the models of the proposed multi-sensor positioning system.

Much of the available research on multi-sensor positioning systems has been done in a simulated environment with well-established assumptions of the Gaussianity of measurement errors and linearisation of measurement models [77, 104, 107, 108]. However, due to the fusion of the traditionally used data (e.g., GNSS) and non-traditional ranging data (e.g., Wi-Fi, UWB), there is a need to investigate traditional assumptions and how they hold up for the terrestrial ranging data. In this case, where GNSS data are fused with terrestrial ranging information from LPS, understanding the error distribution for non-traditional ranging signals remains the problem. Further, it is unknown if linearisation for the LPS measurements is a good approximation of the non-linear LPS measurement model.

4.3.1 Multi-sensor Particle Filter

The implemented multi-sensor EKF has already been presented in Section 3.3.2.1. The PF implementation is a modified version of the mathematical model described in [77].

Unlike the EKF, the PF is a non-linear non-Gaussian filter. "For non-linear or non-Gaussian problems there is no general analytic (closed-form) expression for the *a posteriori* distribution [100]." PF approximates *a posteriori* distribution of a state vector at the time k by employing the random particles (i.e., hypotheses h) $X_k^h = \begin{bmatrix} r_k & v_k & a_k & c_b^k \end{bmatrix}^T$, which are propagated through a dynamic model (Equation 3.17), and the associated weights w_k^h [77, 102, 103]. Thus, making a set $\left\{X_k^h, w_k^h\right\}_{h=1}^{N_h}$ where $h \in 1, 2, \ldots, N_h$. The larger the number of particles N_h is, the closer PF characterisation comes to the analytical description of the *a posteriori* probability density function (PDF) [103].

As in [77], the importance density is chosen to be the *a priori* density $p(X_k, X_{k-1}^h)$ which is drawn from the system model. In practice, this means that a set of particles X_k^h is propagated through the dynamic model using Equations 3.16 and 3.18 or N_h particles. Initially, the particles are weighted the same. Furthermore, the initial particles are drawn from the random Normal distribution around the initial state vector.

Particle weights are then updated based on the measurement likelihood as shown in the Equation 4.2. To each particle in the sample, a weight w_k^h is attributed based on the likelihood of observations $Z_k = \begin{bmatrix} d_{IN(k)} & \rho_{S(k)} \end{bmatrix}^T$. According to [77], the associated weight is given as follows,

$$w_k^h = w_{k-1}^h \cdot p(Z_k|X_k^h), \tag{4.2}$$

where $p(Z_k|X_k^h)$ stands for a likelihood function of the measurements Z_k. The likelihood function for the case of integrated terrestrial range measurements $d_{IN(k)}$ and pseudoranges $\rho_{S(k)}$ can be calculated as a product of the PDF associated with each measurement [77]. As in [77] and as shown in Equation 4.3, it is assumed that LPS and GNSS ranges are statistically independent of each other (within and across each measurement type).

$$\underset{multi-sensor}{p(Z_k|X_k^h)} = \prod_{i=1}^{N_{IN}} p_i \left(\underset{measured}{d^i_{IN(k)}} - \underset{predicted}{d^{i(h)}_{IN(k)}} \right) \cdot \prod_{m=1}^{N_S} p_m \left(\underset{measured}{\rho^m_{S(k)}} - \underset{predicted}{\rho^{m(h)}_{S(k)}} \right). \tag{4.3}$$

where $d^i_{IN(measured)}$ and $\rho^m_{S(measured)}$ are the i^{th} terrestrial range and the m^{th} pseudorange, respectively. $d^{i(h)}_{IN(predicted)}$ is a terrestrial range calculated based on Equation 3.23 using the i^{th} infrastructure node coordinates and a sample X_k^h of N_h particles. $\rho^{m(h)}_{S(predicted)}$ denotes a pseudorange calculated based on Equation 3.24 using the m^{th} satellite coordinates and a sample X_k^h of N_h particles. In Equation 4.3, the probability of terrestrial range measurement is denoted by p_i and it is calculated as a difference between every terrestrial range measurement and the predicted ranges for particle h where $h \in 1 \dots N_h$. p_m is the pseudorange probability and it is calculated as a difference between every pseudorange and the predicted pseudoranges for particle h. This is where either Gaussian assumption is made, or a better approximation of the actual error distribution can be used. $p_i \sim \mathcal{N}(0, \sigma^2_{IN})$ (as in Equation 3.21) or Equation 4.1 with parameters from Table 4.1 can be used as a better approximation. For GNSS measurements, a Gaussian assumption will be made $p_m \sim \mathcal{N}(0, \sigma^2_S)$ (as in Equation 3.22).

Associated weights w_k^h, calculated using Equation 4.2, are then normalised so that $\sum_{h=1}^{N_h} w_k^h = 1$ is true. The estimated user's state $\hat{X}_k$ is calculated based on normalised weights and particles X_k^h [102, 103].

$$\hat{X}_k = \sum_{h=1}^{N_h} w_k^h \cdot X_k^h. \tag{4.4}$$

After estimating the user's state, the particles are resampled to avoid the "degeneracy of the weight" [99]. In this research, the method described in [100] is used for resampling.

4.3.2 Results and discussion

As the aim is to test the impact of the Gaussian error distribution assumption and the impact of linearisation of the measurement model on the positioning solution, a set of experiments is performed for three different sets of data: GPS, WASP data, and a combination of the GPS and the WASP data (further: GPS+WASP).

The effect of linearisation is tested by comparing the EKF and the PF performance under the assumption of Gaussianity for all measurements. The effect of Gaussian error distribution model is tested by comparing two different implementations of the PF where one uses the fitted GMM for terrestrial range error distribution, and the other assumes Gaussianity. Lastly, the overall effect of both the Gaussian assumption and linearisation is tested by comparing the EKF performance and the performance of the PF that does not make any of those assumptions.

A zero-mean Gaussian error distribution with a standard deviation of 7.1 m is assumed for GPS measurements. That value is chosen based on the User Equivalent Range Error (UERE) for single frequency C/A code pseudoranges from [109]. Further, when Gaussian error distribution is assumed for terrestrial ranges, a standard deviation of 1 m is used. When Gaussianity is not assumed, parameters of the three-component GMM from Table 4.1 are used. The process noise that consists of acceleration noise and receiver clock bias noise are also assumed to be normally distributed with zero mean and variances that are randomly drawn from the standard normal distribution at every timestamp for all particles. All the PFs were run 15 times for half a million particles.

4.3.2.1 Extended Kalman Filter performance

The EKF performance for GPS data is shown in Figure 4.3a. Given the offset of the trajectory from the ground truth, a bias is present in the positioning solution. As can be seen in Figure 4.4, HPE is mostly between 2.5 and 3 m. This bias is present since none of the systematic GPS error sources are modelled out as described in [16] (e.g., atmosphere effects, satellite clock error, multipath). When initialising the EKF, the user is assumed to be static, and the initial position is assumed to be adequate ground truth position. As a

result, due to the biased pseudorange measurements, the estimated positions diverge from the ground truth at the beginning of the estimation process (Figure 4.3a). Figure 4.3b shows the user trajectory when only the WASP data are used. The trajectory of the GPS+WASP data is not shown, however, Figure 4.4 shows that the performance is similar to the WASP data performance. As visible in the majority of the estimated positions, the WASP system is not under any obvious systematic biases. Further, when combined with the GPS pseudoranges, it is shown that the WASP data affects the whole system's performance since the solution converges closer to the ground truth (see Figure 4.4). That greater effect of the WASP data is expected due to the weighting of the data (i.e., chosen variances for the pseudoranges and terrestrial ranges). Large position errors can be noticed in Figure 4.3b. The most likely explanation is the presence of the unmodelled outliers in the WASP terrestrial ranges. As shown in Figure 4.4, when the WASP data are used, $\sim 90\%$ of the position estimates are within 1 m from the ground truth.

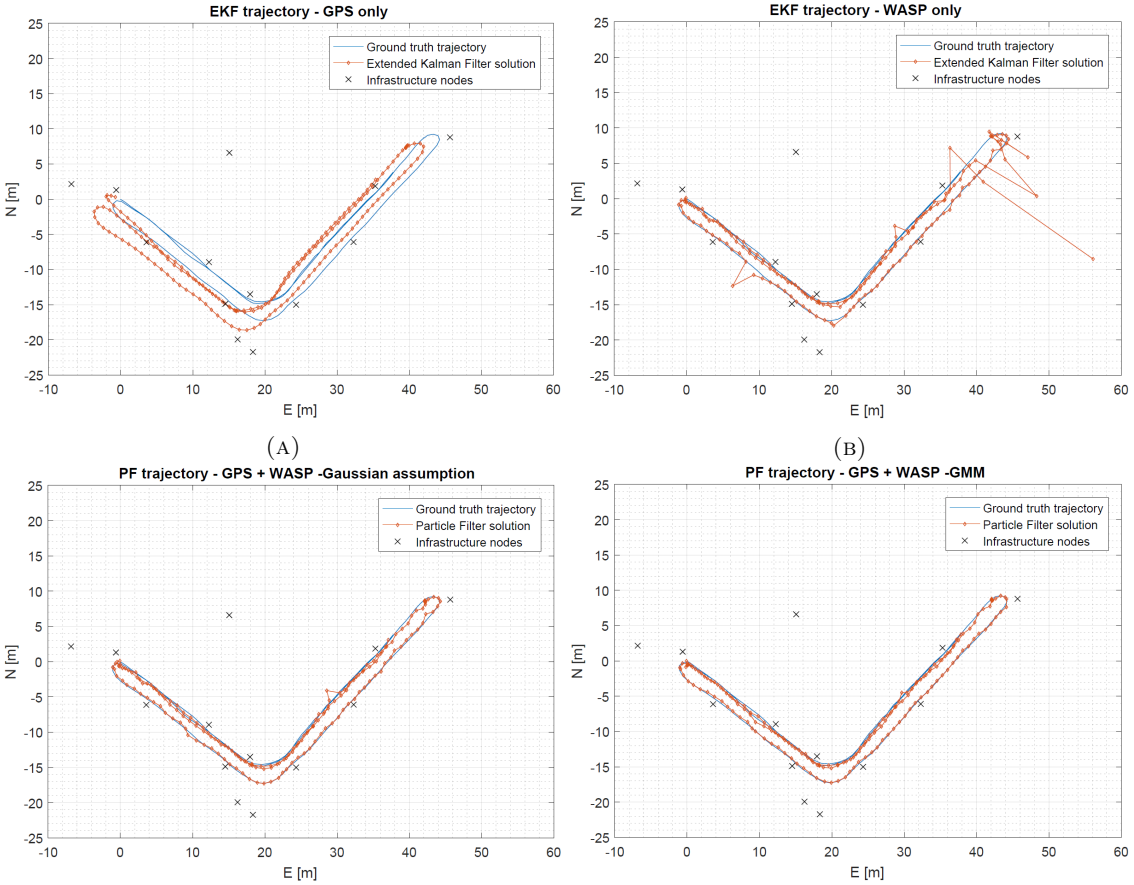


FIGURE 4.3: Examples of the EKF and the PF performance. 2D EKF trajectories are shown in the local coordinate system. a) The EKF estimation based on GPS data only. b) The EKF estimation based on the WASP data. c) The PF estimation based on the GPS+WASP data with the assumption of Gaussianity. d) The PF estimation based on the GPS+WASP data with GMM distribution for relative ranging errors.

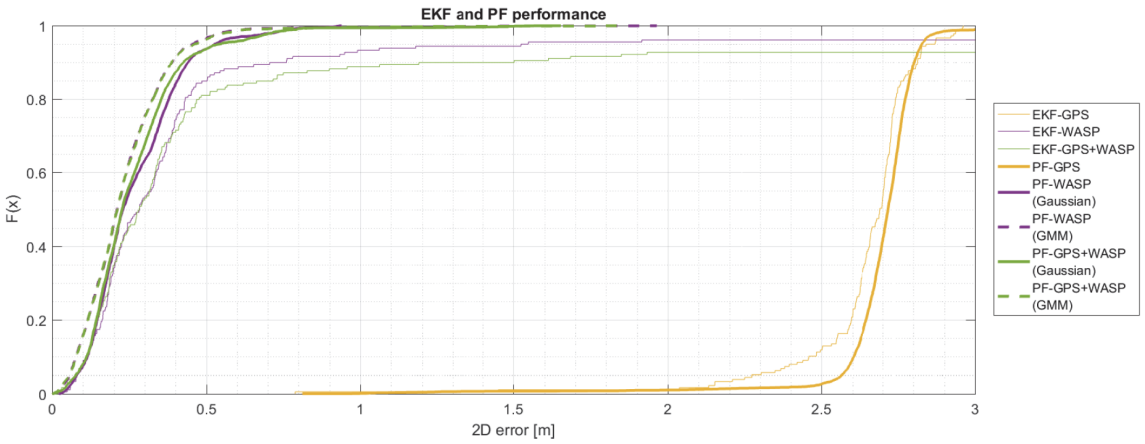


FIGURE 4.4: CDF plot for comparison of the EKF and PF performances based on the used data sets and measurement error assumptions. As per the graph legend, different data sets are shown in different colours. PF performance is shown with higher line width. The solid line is used when Gaussian assumptions are made and dashed lines when Gaussianity is not assumed for WASP data. PF performance of all 15 runs is shown here.

4.3.2.2 Particle Filter performance

The PF performance of the GPS data is similar to the EKF performance with HPE $\sim 2.7\ m$. The trajectory shown in Figure 4.3c is estimated based on the Gaussian error distribution assumption, and the trajectory in Figure 4.3d is estimated based on the fitted GMM (both are examples of one PF run for GPS+WASP data). As can be seen in Figure 4.4 (dashed lines), when the Gaussianity is not assumed (i.e., GMM used) better accuracy is achieved (for $3 - 4\ cm$) for both data sets. As shown in Figure 4.4, the performance of the WASP data and the GPS+WASP data is similar. Two larger divergences from the ground truth are visible in Figure 4.3c. This happens when only GPS data are available at those time instants, because of which, the estimated positions diverge due to the biased GPS measurements. In Figure 4.3d, when the distribution of terrestrial ranges is not assumed to be Gaussian, those divergences are not visible.

4.3.2.3 Comparison of Extended Kalman Filter and Particle Filter

The performance of the EKF and the PF is compared in Figure 4.4 to test the impact of Gaussian assumptions and measurement model linearisation. As is shown in the Cumulative Distribution Function (CDF) plot, the PF generally performs better than the EKF. The performance of the PFs for the WASP and the GPS+WASP data are similar (see Figure 4.4 and Table 4.2).

Table 4.2 shows the descriptive statistics calculated for the performance of the EKF and all the PF runs. Averages, standard deviations, maximum and minimum 2D errors were calculated.

TABLE 4.2: Statistical Information about HPEs.

Estimator	Data type$^{\diamond}$	Distribution*	Avg $[m]$	St Dev $[m]$	Max $[m]$	Min $[m]$	90%* $[m]$
EKF	GPS	G	2.644	0.223	2.962	0.789	2.813
	WASP	G	0.617	1.921	22.109	0.031	0.761
	G+W	G	0.933	2.636	21.844	0.010	1.501
PF	GPS	G	2.704	0.207	5.799	0.812	2.802
	WASP	G	0.268	0.148	0.939	0.023	0.441
	WASP	GMM	0.231	0.148	1.965	0.003	0.389
	G+W	G	0.263	0.167	1.653	0.003	0.427
	G+W	GMM	0.232	0.149	1.837	0.001	0.388

$^{\diamond}$ Used data set is specified. 'G+W' denotes the GPS+WASP data. * G denotes Gaussian distribution assumption.* '90%' column gives information about the range within which 90% of 2D errors are contained.

Firstly, the performance of the EKF and the PF under the Gaussian assumption is compared to test the effect of measurement model linearisation. On average, the PF filter outperforms the EKF for ~ 36 cm and ~ 67 cm for the WASP and the GPS+WASP data, respectively (see Table 4.2). The standard deviation is significantly smaller for the PF due to large range errors caused by the outliers in the data that the EKF is unable to deal with. 90% of the EKF errors are smaller than 76 cm and 1.5 m depending on the data set, however, for the PF with assumed Gaussianity, that value falls to $43 - 44$ cm for both the WASP and the GPS+WASP data. Figure 4.5 graphically presents the accuracy improvement of 57% and 72% when the PF is used, depending on the used data set. As expected, this shows that the first-order Taylor expansion is not a good approximation of the non-linear measurement model presented in Section 4.3 and that the PF, as a non-linear estimator, is more appropriate for this positioning system.

Secondly, the performance of the PF under the Gaussian assumption and the PF where the GMM is used as the terrestrial range error distribution is compared. The results in Table 4.2 show accuracy improvement when a better approximation of the actual error distribution (i.e., GMM) is used. On average, accuracy is improved by $3 - 4$ cm for both the WASP and the GPS+WASP data, and the standard deviation of the errors is similar. When the GMM is used, 90% of errors are smaller than 39 cm for both data sets. However, 90% of the position estimates for the PF with the Gaussian assumption are within 44 cm

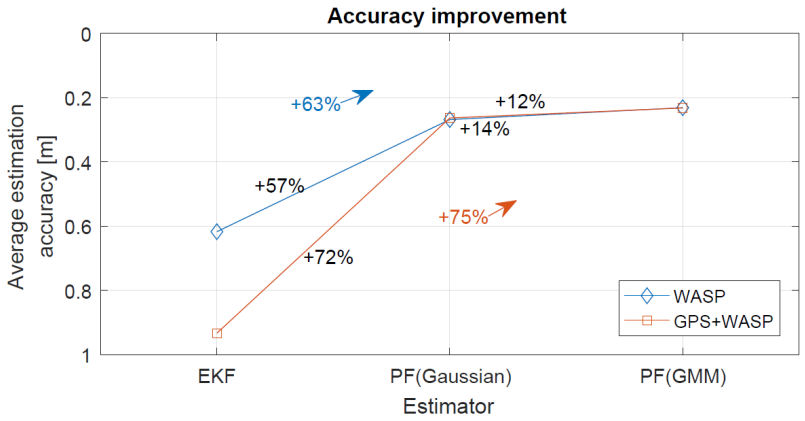


FIGURE 4.5: Average accuracy improvement from the EKF to the PF with GMM as a WASP measurement error distribution. The graph presents improvement for WASP and GPS+WASP data set calculated based on the data in Table 4.2.

and 43 *cm* of the ground truth, for the WASP and the GPS+WASP data, respectively. This confirms that using the distribution fitted on the empirical data, and not assuming Gaussianity, on average, reduces the effect of the outliers. As shown in Figure 4.5, using the better WASP measurement error distribution approximation (i.e., GMM), on average improved accuracy by 14% and 12% for WASP and GPS+WASP data, respectively.

Lastly, the EKF performance is compared with the PF that uses GMM for terrestrial range error distribution. An overall improvement in accuracy can be observed when the measurement model is not linearised and Gaussianity not assumed. On average, 39 *cm* and 70 *cm* accuracy improvement is achieved for the WASP and the GPS+WASP data, respectively (see Table 4.2). This means that on average, accuracy improved $63-75\%$ (as seen in Figure 4.5).

Although this work aims to explore the effects of linearisation and the Gaussian assumption on estimation accuracy, the practicality of implementing these algorithms in real-time applications cannot be ignored. As expected, the resampling and a large number of particles used in the computation makes the computational cost of the PF, significantly higher than that of the EKF. To run 3 *min* of 1 *s* frequency measurements, the cost of the EKF is in order of seconds and the PF under 3 *min* on average. In the case of 1 *s* measurement frequency, the PF would generally be practical in real-time applications. The algorithm could still run in real-time but would need to be coded for speed and/or use higher performance processing hardware. As the main goal of this research is to develop an integrity algorithm capable of achieving desired levels of integrity, this issue was not further considered.

The benefits of fusing two independent absolute positioning systems are shown for both algorithms, the EKF and the PF. It is demonstrated in the case of biased GPS data that having an additional positioning system, can improve accuracy significantly. It is also demonstrated, that in case of unavailability of the GPS (i.e., only WASP), good performance is achievable. The PF based positioning framework has an advantage over the EKF based positioning framework since it deals better with the non-linearities of the measurement model and outliers in the WASP data.

4.4 Cooperative positioning system

Based on the previous analysis, multi-sensor PF and consequently, the cooperative PF is chosen as the underlying position estimator for the integrity algorithm to be proposed in the next chapter. In this section, the chosen position estimator will be presented.

The PF mathematical model used in this research is based on the one from [77]. A user is being positioned using the distributed CP system. As before, the state vector is denoted by $X_k = \begin{bmatrix} r_k & v_k & a_k & c_{b(k)} \\ 1\times3 & 1\times3 & 1\times3 & 1\times1 \end{bmatrix}^T$ (Equation 3.14) and it consists of 3D position r_k, 3D velocity v_k, 3D acceleration a_k and the GNSS receiver clock bias $c_{b(k)}$. The state is being estimated over time where the current time instant is denoted by k. The GNSS receiver clock bias is given in units of length (i.e., metre in this case) which is calculated by multiplying the clock bias with the speed of light.

The position of a dynamic node is being updated with terrestrial range measurements from the LPS and GNSS pseudoranges. Equation 4.5 shows the measurement vector Z_k. It can consist of N_{IN} terrestrial ranges measured from the dynamic node to the infrastructure nodes denoted by d_{IN}, terrestrial ranges d_{CP} measured to N_{CP} other dynamic nodes (i.e., users) in the cooperative network, and N_S GNSS satellite pseudoranges ρ_S received by the dynamic node at a time instant k. In the case of the CP, a measurement vector Z_k will consist of all types of measurements. However, in the case of multi-sensor positioning, it will consist of d_{IN} and ρ_S only. The total number of available measurements is equal to $N_{IN} + N_{CP} + N_S$ in case of CP.

$$\underset{(N_{IN}+N_{CP}+N_S)\times1}{Z_k} = \begin{bmatrix} d^k_{IN} & d^k_{CP} & \rho^k_S \\ 1\times N_{IN} & 1\times N_{CP} & 1\times N_S \end{bmatrix}^T. \tag{4.5}$$

Section 4.4 is part of the paper *Integrity risk estimates for multi-sensor and cooperative positioning systems*. It is in a process of revision following peer review by *IEEE Sensors Journal*.

In addition to the measurements, positions of GNSS satellites over time are necessary, as well as the static positions of the LPS anchor nodes. All coordinates are given in the ECEF frame which is Cartesian global reference coordinate system. The system model (i.e., state evolution) $X_k = F_k X_{k-1} + \omega_k$ as in Equation 3.16, is a constant acceleration model and equations of motion governing this model are: $\dot{r} = v$ and $\dot{v} = a$ (Equation 3.17). ω_k is the process noise which is normally distributed with zero mean and covariance matrix $Q_k = \begin{bmatrix} 0 & 0 & \omega_a & \omega_{c_b} \\ 1\times3 & 1\times3 & 1\times3 & 1\times1 \end{bmatrix}^T$. The covariance matrix consists of the acceleration noise with variance ω_a and GNSS receiver clock bias noise with variance ω_{c_b}. Since the system model is the constant acceleration model, the transition matrix F_k is the same as in Equation 3.18.

As before, due to PF not having a general closed-form expression for the *a posteriori* distribution of the state, it is approximated by propagating a set of N_h particles through the dynamic model. Each particle h with the state X_k^h is assigned a weight w_k^h. Thus, a set $\{X_k^h, w_k^h\}_{h=1}^{N_h}$ of particles is formed. For every k, a new set of particles is propagated through the dynamic model and the particle weights are updated based on the likelihood of the measurements Z_k as in Equation 4.2: $w_k^h = w_{k-1}^h \cdot p(Z_k|X_k^h)$.

Because of the cooperative nature of the proposed positioning system where LPS terrestrial ranges and GNSS pseudoranges are fused, the likelihood function $p(Z_k|X_k^h)$ of the measurements Z_k is calculated for every particle h as a product of the PDF of each measurement type [77]. The probability of each particle h for CP is

$$\begin{aligned} \underset{cooperative}{p(Z_k|X_k^h)} = &\prod_i^{N_{IN}} p_i \left(\underset{measured}{d^i_{IN(k)}} - \underset{predicted}{d^{i(h)}_{IN(k)}} \right) \cdot \prod_j^{N_{CP}} p_j \left(\underset{measured}{d^j_{CP(k)}} - \underset{predicted}{d^{j(h)}_{CP(k)}} \right) \\ &\cdot \prod_m^{N_S} p_m \left(\underset{measured}{\rho^m_{S(k)}} - \underset{predicted}{\rho^{m(h)}_{S(k)}} \right) . \end{aligned} \tag{4.6}$$

PDFs for LPS terrestrial ranges to the infrastructure nodes, to other dynamic nodes, and GNSS pseudoranges are denoted by p_i, p_j and p_m, respectively, where $i \in 1, 2, \ldots, N_{IN}$, $j \in 1, 2, \ldots, N_{CP}$ and $m \in 1, 2, \ldots, N_S$. p_i is calculated for the difference between every available terrestrial range measurement $d^i_{IN(measured)}$ to infrastructure node i, and the predicted measurement for particle h denoted by $d^{i(h)}_{IN(predicted)}$. p_j is calculated for the difference between every available terrestrial range measurement $d^j_{CP(measured)}$ to dynamic node j, and the predicted measurement for particle h denoted by $d^{j(h)}_{CP(predicted)}$. p_m is calculated for the difference between every available GNSS pseudorange $\rho^m_{S(measured)}$ for

GNSS satellite m and the predicted pseudorange $\rho^{m(h)}_{S(predicted)}$. Predicted LPS terrestrial ranges and GNSS pseudorange are calculated for each particle h, where $h \in 1, 2, \ldots, N_h$, using the following equations,

$$d^{i(h)}_{IN(k)} = \sqrt{(x^i_{IN} - x^h_k)^2 + (y^i_{IN} - y^h_k)^2 + (z^i_{IN} - z^h_k)^2}, \tag{4.7}$$

$$d^{j(h)}_{CP(k)} = \sqrt{(x^{j(k)}_{CP} - x^h_k)^2 + (y^{j(k)}_{CP} - y^h_k)^2 + (z^{j(k)}_{CP} - z^h_k)^2}, \tag{4.8}$$

$$\rho^{m(h)}_{S(k)} = \sqrt{(x^m_S - x^h_k)^2 + (y^m_S - y^h_k)^2 + (z^m_S - z^h_k)^2} + c^h_{b(k)}. \tag{4.9}$$

The coordinates of the particle h are given as $(x^h, y^h, z^h)_k$. The coordinates of the infrastructure node i are denoted by $(x^i_{IN}, y^i_{IN}, z^i_{IN})$. The coordinates of the dynamic node j cooperating with the user at time k are $(x^j_{CP}, y^j_{CP}, z^j_{CP})_k$. GNSS satellite m coordinates at time k are given as $(x^m_S, y^m_S, z^m_S)_k$ and the GNSS receiver clock bias is denoted by $c^h_{b(k)}$ for particle h.

In case of the Gaussian assumption, error distributions of all measurement types can be given as,

$$p_i \sim \mathcal{N}(0, \sigma^2_{IN}), \tag{4.10}$$

$$p_j \sim \mathcal{N}(0, \sigma^2_{CP}), \tag{4.11}$$

$$p_m \sim \mathcal{N}(0, \sigma^2_S). \tag{4.12}$$

The standard deviations are denoted by σ_{IN}, σ_{CP}, and σ_S for LPS ranges to infrastructure, LPS ranges to other users and GNSS pseudoranges, respectively. For the GMM, Equation 4.1 and parameters from Table 4.1 can be used to calculate p_i and p_j.

After the weight update and their normalisation, the state of the user is estimated as shown in Equation 4.4. For multi-sensor positioning, state estimation is performed in one iteration. However, in the case of the CP, two iterations are necessary. All users first perform multi-sensor positioning as the first iteration. Then, in addition to the measured distances between each other, users share their own positions $\hat{r}^j_k = \hat{X}^j_{k,1:3}$ (estimated in the first iteration as a part of the state vector) and the trace of the corresponding covariance sub-matrix $trace(\hat{R}^j_k)$. As in [77], the estimated covariance matrix $\hat{P}^j_k$ for the dynamic

node j (where $\hat{R}_k^j$ is the sub-matrix corresponding to the position) is calculated as follows,

$$\hat{P}_k^j = \frac{\sum_{h=1}^{N_h} w_k^{j(h)} \left(X_k^{j(h)} - \hat{X}_k^j\right) \left(X_k^{j(h)} - \hat{X}_k^j\right)^T}{1 - \sum_{h=1}^{N_h} \left(w_k^{j(h)}\right)^2}. \tag{4.13}$$

Once data from N_{CP} dynamic nodes is received, the user is able to update the particle weights using Equations 4.2 and 4.6 where p_j for dynamic node j is normally distributed with zero-mean and variance that is now equal to the intrinsic LPS range variance σ_{IN}^2 added to the uncertainty of dynamic node's position at time instant k, $trace(\hat{R}_k^j)$ [77].

$$\left(\sigma_{CP(k)}^j\right)^2 = \sigma_{IN}^2 + trace(\hat{R}_k^j). \tag{4.14}$$

The second iteration is finalised once the weights are updated and CP state vector is estimated using Equation 4.4. Lastly, to avoid "degeneracy of the weight", after position and integrity estimation, particles weights are resampled according to the method described in [100] and the process of estimating user's position and integrity for the following timestamp is started.

4.5 Conclusions

This chapter has demonstrated that using the non-linear filter instead of measurement model linearisation on average results in 57% and 72% position estimate improvement depending on the used data set. In that case (i.e., when the non-linear model is used), the accuracy of the proposed positioning system is on average ~ 26 *cm*.

Additional accuracy improvement of 14% and 12% has been shown when fitted three-component GMM is used, rather than a Gaussian distribution approximation, for the terrestrial ranging data error distribution. This improvement was in the order of a couple of centimetres. For some applications this may be enough to assume Gaussianity but, it is unclear how that would impact the integrity performance since the description of the tail ends of the *a posteriori* distribution is important for integrity.

Overall, for the WASP and the GPS+WASP data sets, 63% and 75% average accuracy improvements have been observed when the non-linear non-Gaussian filter is used. An average accuracy of ~ 23 *cm* for both data sets (i.e., WASP and GPS+WASP) was achieved.

Significance of these improvements depends on the designed algorithm, its application and positioning requirements. These results indicate significant improvement when the linear approximation is not made. The same cannot be said for the Gaussian assumption and the GMM. Although an improvement was shown, it is not clear if the Gaussian assumption significantly impacted the performance.

Nevertheless, this work has demonstrated the performance benefits of better error modelling and non-linear filtering. Based on the results of the previous chapters, multi-sensor and CP solutions with the PF algorithm are chosen as underlying positioning systems of the integrity algorithm that is to be proposed in the next chapter.

5

Position integrity algorithms

This chapter proposes three novel integrity algorithms based on Bayesian Receiver Autonomous Integrity Monitoring (BRAIM). Three problems of position integrity algorithms and IM in general for land-based applications for GNSS challenging environment are explored: measurement availability, requirements for sufficient measurement redundancy and the presence of large biases. The need for measurement redundancy was mitigated by using BRAIM. This enabled the employment of a Fault Detection and Exclusion (FDE) algorithm without the required minimum availability of six measurements. A Spatial Feature Constraint (SFC) algorithm is implemented to constrain solutions to feasible locations within a road feature in order to increase the estimated integrity. Three algorithms are proposed — FDE+BRAIM, SFC+BRAIM, FDE+SFC+BRAIM.

5.1 Introduction

Chapters 2 and 3 demonstrated the need for a more appropriate integrity algorithm for the urban environment. Through the literature review and experimental evaluation of the integrity requirements, I have decided to focus on three major factors — measurement availability, the requirement of the sufficient measurement redundancy and large biases. In addition to that, Chapter 4 demonstrated the need for a position estimator that does not rely on linear approximation due to the non-linearity of LPS, and that does not rely on Gaussian assumptions of LPS measurements.

As demonstrated, solutions based on GNSS data only and/or RAIM cannot be relied on when it comes to the urban environments. The biggest disadvantages of applying the classical RAIM algorithms in the urban environment are a result of the determination of the integrity in the measurement domain based on sufficient measurement redundancy. Consequently, integrity estimate is often unavailable as the measurement unavailability often occurs in such challenging environments [84]. As a possible solution to this problem, multi-sensor and cooperative positioning were proposed to assure measurement availability in urban environments and to improve positioning accuracy.

Chapter 4 experimentally demonstrated that linear approximations made in EKF (commonly used method of fusing data) are not appropriate for multi-sensor and CP systems where GNSS data and LPS ranges are fused. It was also demonstrated that positioning accuracy can be improved if the Gaussian assumption is not made for LPS ranges. To further improve positioning accuracy, the PF was chosen as an underlying positioning algorithm.

Given all these integrity requirements, a RAIM method with the PF as the underlying position estimator is chosen. That method is called Bayesian RAIM (BRAIM). To deal with large measurement biases and to improve the integrity estimate, FDE and SFC algorithms will be implemented with BRAIM. As discussed in Chapter 2, FDE is a method commonly paired with RAIM algorithms, and it is used to isolate large biases. Furthermore, when it comes to the ITS applications, SFC can constrain the vehicle to the road and further reduce the faults.

With all of that in mind, in this chapter, BRAIM as a method of estimating integrity in the position domain is presented, and three novel solutions aimed at improving integrity performance are proposed.

5.2 BRAIM

Unlike civil aviation, land-based operations are more affected by biases such as multipath due to the presence of reflective surfaces like buildings, vehicles and trees [16, 110]. Furthermore, due to the inability of GNSS signals to propagate through obstacles, the availability of GNSS data is reduced in urban environments. Algorithms like RAIM developed for civil aviation may not be appropriate for such challenging environments. A review of the literature has been carried out in [17] where different classical RAIM algorithms have been discussed from a perspective of land-based applications. One of the main highlighted problems of classical RAIM algorithms is that they require sufficient measurement redundancy to estimate integrity. When it comes to GNSS data, a minimum of four measurements are required for position estimation, five for integrity estimation and fault detection, and a minimum of six for single fault exclusion in order to be able to still estimate integrity in case a fault is excluded [16, 17]. The effect of this problem has been experimentally shown in Section 3.3 where integrity availability could not be estimated due to insufficient GPS measurement redundancy almost 50% of the time in downtown Melbourne, Australia. When the measurement redundancy requirement was satisfied, integrity was available $\sim 2\%$ of the time. In this case, the use of multi-GNSS would probably reduce the occurrence of insufficient measurement redundancy. However, the problems of using a GNSS only solution in the urban canyon would remain.

The BRAIM algorithm, as shown in [18], has been adapted here with the PF as an underlying position estimator to mitigate the problem of insufficient measurement redundancy. Unlike the classical RAIM algorithms where integrity is estimated in the measurement domain, BRAIM estimates integrity in the position domain by solving "the state-space estimation problem by finding the *a posteriori* distribution of the state $\hat{X}_k$"[18]. This is relevant since the integrity is estimated based on an *a posteriori* error distribution which is always available, as opposed to the indirect estimation through observations as in classical RAIM algorithms [18]. Because of that, integrity estimate will be available even if the measurements are not. However, without any measurements, the *a posteriori* distribution, and by default, the integrity estimate, would mainly be based on the *a priori* state distribution. This will affect the trustworthiness of such a result.

Sections 5.2, 5.4 and 5.5 were first published in *Navigation, Journal of Institute of Navigation* in *Summer 2021* paper entitled *Case study of Bayesian RAIM algorithm integrated with Spatial Feature Constraint and Fault Detection and Exclusion algorithms for multi-sensor positioning* ([22] in the bibliography).

Although BRAIM does not require measurement redundancy, the fusion of GNSS pseudoranges and terrestrial ranges should positively affect the *a posteriori* distribution [92] and consequently the integrity. The fusion of GNSS and terrestrial ranges (as defined and used in this research) is not commonly used in integrity and IM algorithms for ITS applications. Only two studies that have done this have been found [70] [63]. It is also worth mentioning that similar efforts of ensuring sufficient measurement redundancy have been previously made in civil aviation. For example, [27] and [111] demonstrate navigation integrity method for aircraft precision landing using the GNSS and ground-based pseudolites which ensure sufficient measurement redundancy.

Given that the positioning system used in this thesis is capable of achieving positioning accuracy well under the required AL that will be used as one of the requirements, it is expected that the frequency of misleading information will be reduced.

Unlike the classical RAIM methods where PL is estimated, the BRAIM algorithm estimates the probability of misleading information p_{MI}. p_{MI} is the probability of the position error being out of bounds of the required AL. It can be estimated by performing integration of the *a posteriori* distribution over a set $\Omega_{AL}\hat{X}_k$ (as shown in Equations 5.1 and 5.2) [18]. The BRAIM algorithm and equations below have been first presented in [18].

$$1 - p_{MI} = \int_{\Omega_{AL}\hat{X}_k} \sum_{h=1}^{N_h} w_k^h \delta(X_k^h - \hat{X}_k) dX_k \tag{5.1}$$

where

$$\Omega_{AL}\hat{X}_k = \{X_{k,1:3}^{1:N_h} | \|X_{k,1:3}^{1:N_h} - \hat{X}_{k,1:3}\| \leq AL\}. \tag{5.2}$$

Equation 5.2 shows that $\Omega_{AL}\hat{X}_k$ is a subset of a set of all N_h particles for which the distance from the particles $X_{k,1:3}^{1:N_h}$ and estimated position $\hat{X}_{k,1:3}$ is smaller than the required AL. Hence, if a particle h is part of the $\Omega_{AL}\hat{X}_k$ subset, its position is within the bounds of AL from the estimated position and its weight is summarised towards the p_{MI}. δ denotes a Dirac delta function. Indices $1:3$ indicated that the first three states corresponding to the 3D position as shown in Equation 3.14 are used to calculate the distance.

Equation 5.1 can be simplified as shown in Equation 5.3. There, it is clear that the p_{MI} is directly calculated as a sum of particle weights for those particles in a subset of particles J, where J is $\{h : X_{k,1:3}^h \in \Omega_{AL}\hat{X}_k\}$. Unless all the particles are within AL from the

estimated position, $1 - p_{MI}$ will never be equal to one.

$$1 - p_{MI} = \sum_{h \in J} w_k^h \tag{5.3}$$

In addition to AL, IR is another integrity requirement. Once the p_{MI} is estimated, it is compared with the required IR probability p_{IR}. More on this in the Section 5.5. The pseudocode for multi-sensor BRAIM is given in Algorithm 1. For CP BRAIM, p_{MI} is estimated during the second iteration of CP PF position estimate.

Algorithm 1 Pseudocode for BRAIM

```
p_IR, AL
Initialise X_k and w_k for N_h particles
for time epoch k do
    Propagate particles through dynamic model
    Measurement likelihood: p(Z_k|X_k^h)
    Update particle weight: w_k^h = w_{k-1}^h · p(Z_k|X_k^h)
    State estimate X̂_k
    if ||X_{k,1:3}^h − X̂_{k,1:3}|| ≤ AL where h ∈ 1, 2, ..., N_h then
        1 − p_MI = Σ_{h∈J} w_k^h
    end if
    if p_MI ≤ p_IR then
        "Integrity is available!"
    else
        "Integrity is not available!"
    end if
    Particle weight resampling
end for
```

Algorithm 1 currently keeps running even after integrity becomes unavailable. If this algorithm was to be implemented for a real-world ITS application, the user would either stop the operation and reinitialise, or it would switch to an alternative positioning system, if available. However, in this thesis, this was not done as one of the main goals was to demonstrate how p_{MI} changes with the new incoming measurements.

The presented BRAIM is similar to the multiple hypotheses approach presented in [112]. In this research, every particle represents a hypothesis with the assigned weight given the measurement likelihoods. The approach in [112] is "founded on the direct evaluation of IR under the unified consideration of all single-element failure hypotheses and the no-failure hypothesis". As here, p_{MI} (or in their case p_{IR}) is defined as the likelihood that the unknown position error exceeds AL. As in this thesis, [112] determines integrity unavailability when p_{MI} exceeds the required IR.

A RAIM method based on PF is presented in [56] where each particle is considered a hypothesis as well. Because PF is not analytically tractable and the particles are numerically propagated, each particle can 'hypothesise' about the correctness of different measurement subsets through the process of weighting them. As explained in [56], BRAIM can test multiple hypotheses and their likelihoods by distributing IR or as used in this thesis, p_{MI}, among all possible hypotheses. This, in turn, provides a robust estimation of p_{MI} since multiple hypotheses are considered and not just one with respect to the presence of faulty measurements (as it is done in the classical RAIM methods) [56]. Hence, it could be said that the BRAIM method will be able to deal with the presence of faulty measurements robustly due to multiple hypotheses.

An additional difference from the classical RAIM methods is the fact that p_{MI} is estimated and not the protection level PL. However, there are classical RAIM methods such as the one presented in [15], which have been adapted to the urban environment by equating PL and AL. With that, the probability of false alarm was no longer a requirement, and because of that it was not constant (see Section 2.5.1). Although different, a parallel could be drawn with the BRAIM method where p_{MI} is adaptable depending on robust multiple hypotheses and PL can, for practical purposes, be considered to be equal to AL.

5.3 Comparison of BRAIM and RAIM

Following the performance analysis of the classical RAIM algorithm in Section 3.3, this section aims to introduce some main characteristics of BRAIM through comparison with the classical RAIM methods detailed in Section 2.4.

Figure 5.1 shows side-by-side flowcharts of classical RAIM (from now on — RAIM) and BRAIM. In addition to representing the RAIM and BRAIM algorithms, these flowcharts demonstrate some of the key differences between the two. As mentioned before, the biggest difference is the fact that BRAIM estimates integrity in the position domain and RAIM estimates it in a measurement domain [18]. This reflects on the integrity assessment which has been shown in Section 3.3 where the estimate of integrity availability was unavailable 50% of the time in an urban canyon due to lack of sufficient redundant measurements. Because the position estimate is always available, BRAIM will always be able to estimate integrity. But, if the integrity is estimated in the measurement domain as it is in RAIM,

The content of Section 5.3 has not been previously published.

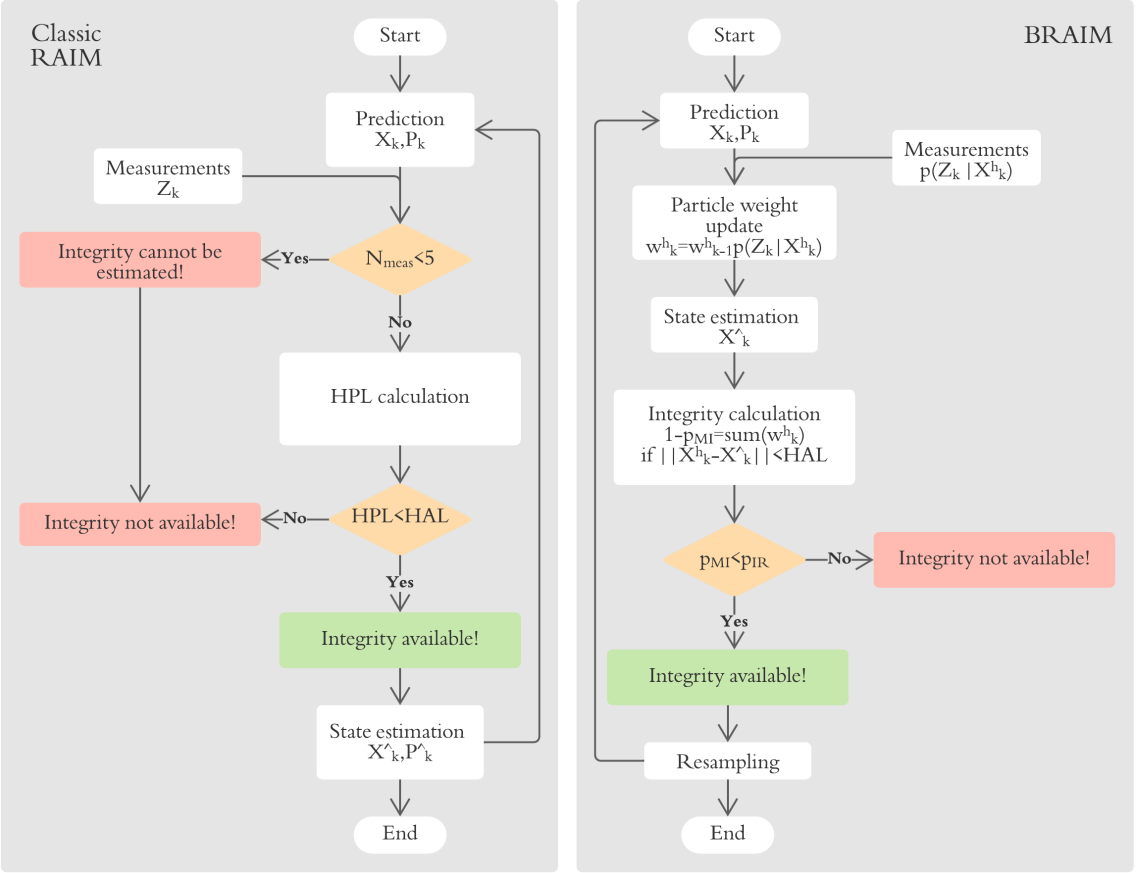


FIGURE 5.1: Side-by-side flowcharts of classical RAIM and BRAIM.

it will not be possible to estimate it if no measurements or not enough redundant measurements are available. In terms of IM in urban environments, this is problematic as such environments often experience low satellite availability or no satellite availability at all, which could result in large unavailability of integrity estimate by default. Because of the way integrity is estimated in RAIM, it is directly dependent on the geometry quality [84]. In open-sky environments, this may not present a problem as the satellite/network geometry tends to be good. In urban environments, such characteristics may cause bad integrity estimates, as the geometry always changes and is generally not good due to the low measurement availability and complexities of the environment [84]. It could be concluded that algorithm such as BRAIM is more appropriate for the urban environment. Characteristics of RAIM and BRAIM are further compared in Table 5.1.

Although it is not the focus of this research, the computational cost of running algorithms like BRAIM needs to be mentioned. Given the results from [92] it is expected that the cost of running BRAIM with the PF as the position estimator is higher than that of the RAIM. Compared to a couple of seconds run-time of the EKF, PF+BRAIM run-time is expected to be over 2 minutes for stand-alone GPS and just over 3 minutes for multi-sensor

TABLE 5.1: Comparison of the classical RAIM and BRAIM characteristics.

WLS RAIM	**BRAIM**
Measurement domain estimation	Position domain estimation
Requires at least 5 measurements	Does not require measurements
Integrity est. not always available	Integrity est. always available
Proportional to DOP	Not proportional to DOP
Not computationally costly	Computationally costly
"Assumes correctness of a single state estimate" [56]	"Assumes likelihood over a state estimate in the form of particles" [56]
"Retains a single measurement -fault hypothesis" [56]	"Retains a particle distribution over different measurement-fault hypotheses" [56]

data. The algorithm could run in real-time but would need to be coded for speed and/or use higher performance processing hardware. As this is not one of the main aims of this thesis, this problem was not considered.

5.4 Position integrity algorithms

When designing novel integrity algorithms proposed in this research, factors like measurement availability, measurement redundancy and the effect of biased measurements were considered. So far, the first two factors have been addressed. In this section, the latter factor will be considered and three novel integrity algorithms will be proposed.

5.4.1 BRAIM paired with Fault Detection and Exclusion algorithm

By using the multi-sensor/CP system and by implementing the BRAIM as the integrity method, the challenges of measurement availability and insufficient redundancy in the urban environment have been mitigated. The effect of large biases created by multipath needs to be addressed.

Despite BRAIM's advantage of robust p_{MI} estimate, the estimate may benefit from integrating the BRAIM and a simple FDE algorithm. FDE algorithms are always paired with the integrity methods as part of the pre-screening process aimed at removing faulty measurements before integrity availability estimate is made. Although BRAIM estimates integrity no matter the number of measurements, the *a posteriori* distribution is still negatively affected by large biases [110]. Error sources like multipath can cause outliers in

available measurements that are then introduced into the particle weight update process and consequently, the position and integrity estimation. It was shown in Chapter 4 that the implemented PF deals with larger errors better than the EKF. However, they still affect the positioning performance and therefore, integrity. To minimise the instances of misleading information that can happen due to larger positioning errors, before estimating p_{MI}, an FDE is performed in the measurement domain.

It is expected that the overall integrity estimate will improve and rate of false positives and negatives will decrease by employing a Fault Detection and Exclusion (FDE) algorithm in addition to multi-sensor BRAIM (i.e., FDE+BRAIM algorithm).

The FDE algorithm would, as in some RAIM methods [17], use measurement residuals to detect and exclude multiple faulty measurements. A comparison of different FDE methods is provided in [41] and [113] (e.g., subset testing, sequential local test, forward-backwards test, Danish method). Papers [52, 63, 70, 114] and [115] propose and implement different FDE methods for the purpose of IM. However, a lot of available literature requires measurement redundancy of at least six measurements to remove one fault [114, 115] or is only able to consider one fault at each time-stamp [52, 70]. In [70], an FDE method capable of excluding a single fault even if RAIM is not possible is proposed. This is necessary for the urban environment where measurement redundancy cannot be expected [84]. Cooperative Integrity Monitoring is proposed in [63] in addition to the FDE algorithm that is capable of better detection of GNSS faults than RAIM, and of detecting multiple faulty cooperative measurements.

In this thesis, multiple fault FDE is possible without a limitation on the number of measurements that can be removed. Because RAIM depends on sufficient redundant measurements, the exclusion of faulty measurements usually stops when there are less than six measurements left. However, when the FDE and BRAIM algorithms are used, the exclusion of faulty measurements can proceed past this point since the problem of having sufficient measurements is addressed by using the BRAIM algorithm.

The chosen FDE algorithm is a simple outlier test described in [38] and [116]. However, some small modifications have been made here to adapt to the PF framework presented in Chapter 4. Instead of using the least-squares estimated position, the PF estimated position $\hat{X}_k$ is used. The difference between the vector of measurements $Z_{measured}$ and

predicted measurements $Z_{predicted}$ is given as,

$$\Delta Z = Z_{measured} - Z_{predicted}. \tag{5.4}$$

$Z_{predicted}$ is calculated using the Euclidean formula for 3D distance between user's estimated position (from state vector $\hat{X}_k$) and appropriate infrastructure node or a satellite. The residual vector res can be calculated as follows,

$$res = \left[I - H\left(H^T H\right)^{-1} H^T\right] \Delta Z \tag{5.5}$$

where I denotes the identity matrix and H denotes a measurement matrix.

$$\underset{(N_{IN}+N_S)\times 10}{H_k} = \left[H_k^{d_1} \quad \dots \quad H_k^{d_{N_{IN}}} \quad H_k^{\rho_1} \quad \dots \quad H_k^{\rho_{N_S}}\right]^T, \tag{5.6}$$

$$H_k^{d_i} = \begin{bmatrix} \frac{\partial d_k^i}{\partial r_k} & \underset{1\times 3}{0} & \underset{1\times 3}{0} & \underset{1\times 1}{0} \end{bmatrix}, \tag{5.7}$$

$$H_k^{\rho_m} = \begin{bmatrix} \frac{\partial \rho_k^m}{\partial r_k} & \underset{1\times 3}{0} & \underset{1\times 3}{0} & \underset{1\times 1}{1} \end{bmatrix}. \tag{5.8}$$

As in [92], the measurement matrix H describes the linear relation between the measurements (i.e., the LPS ranges and GNSS satellite pseudoranges) and the state estimate $\hat{X}_k$. Due to the non-linearity of the measurement model (as shown in Equations 3.23 and 3.24), the measurement matrix H consists of Jacobian matrices derived for every range (Equation 5.7) and pseudorange measurement (Equation 5.8). The Jacobians are the first-order partial derivatives of Equations 3.23 and 3.24 with respect to estimated state $\hat{X}_k$. Equation 5.9 shows the test statistic for fault detection calculated based on the measurement residual res and degrees of freedom DOF.

$$teststat = \sqrt{\frac{res^T res}{DOF}}. \tag{5.9}$$

$DOF = n - n_{unknowns}$ for $n = N_{IN} + N_S$ measurements and $n_{unknowns}$ states (i.e., in this case it is a part of the state vector: 3D position and receiver clock bias).

The threshold is calculated as,

$$Th = \sigma_o \sqrt{\frac{T_{chi}}{DOF}} \tag{5.10}$$

where T_{chi} denotes a normalised chi-squared distribution threshold calculated using the DOF and the probability of false alarm p_{FA} as the probability of exceeding the threshold under normal conditions, which would falsely alert the user. Since p_{FA} is related to the continuity risk, value $p_{FA} = 10^{-5}$ as defined in [4] was chosen. σ_o is the *a priori* standard deviation of the measurements.

In case teststat $\leq Th$ the fault has not been detected. Otherwise, the fault has been detected. Once the fault has been detected, the measurement with the highest residual res is removed, and residuals, the test statistic and the threshold are recalculated. This process is repeated as long as the $DOF > 0$ and teststat $> Th$. Due to the use of multiple measurement systems (i.e., LPS and GNSS), choosing a common value of Th and comparing it with the test statistic calculated based on the joint H matrix will result in FDE being either too loose or too stringent for one or both measurement types. To avoid this issue, separate test statistics and threshold values have been determined for satellite and LPS measurements. For both types, $\sigma_o = 1$ was used. DOF values were also determined separately. Then, the fault presence was detected separately for each type as explained above.

If any faults are detected and faulty measurements excluded, the PF *a posteriori* state $\hat{X}_k$ is re-estimated since the measurement likelihood function $p(Z_k|X_k^h)$ and consequently, particle weights change. Now, p_{MI} is calculated and integrity availability assessment is made. The pseudocode for FDE+BRAIM is given in Algorithm 2. As previously for BRAIM, CP FDE is performed during the second iteration of CP PF position estimate.

The chosen method of FDE is the simplest method of fault detection and exclusion. It should be noted that this thesis aims to demonstrate the proof-of-concept for the proposed ideas and algorithm combinations, and not to propose a robust FDE method for two types of measurements. The proposed concept of combining FDE with BRAIM can work with any FDE algorithm. FDE methods designed for a PF would be ideal since linear approximations and Gaussian assumptions would not be made. For example, [117] uses a bank of auxiliary PFs to detect faults.

5.4.2 BRAIM paired with Spatial Feature Constraint algorithm

Given that the vehicles are constrained to roads, a Spatial Feature Constraint (SFC) [118] algorithm was implemented to further remove the effect of faulty measurements

Algorithm 2 Pseudocode for FDE+BRAIM

p_{IR}, AL
Initialise X_k and w_k for N_h particles
for time epoch k **do**
  Propagate particles through dynamic model
  Measurement likelihood: $p(Z_k|X_k^h)$
  Update particle weight: $w_k^h = w_{k-1}^h \cdot p(Z_k|X_k^h)$
  State estimate $\hat{X}_k$
  Initialise FDE: ΔZ, res, $teststat$ and Th
  if $teststat \leq Th$ **then**
    "The fault has not been detected!"
    BRAIM integrity assessment as in Algorithm 1
    Particle weight resampling
  else
    "The fault has been detected!"
    Exclude measurement where $max(res)$
    while $teststat > Th$ and $DOF > 0$ **do**
      Re-calculate ΔZ, res, $teststat$ and Th
      Exclude measurement where $max(res)$
    end while
    Re-estimate particle weights and $\hat{X}_k$
    BRAIM integrity assessment as in Algorithm 1
    Particle weight resampling
  end if
end for

and to decrease the IR. Unlike the classical Map Matching (MM) algorithm where a position solution is snapped back to the spatial feature, SFC eliminates the particles (i.e., hypotheses) of the PF that are not within the spatial feature. The particles bounded by the spatial feature are re-weighted. Usually, the GNSS integrity and the integrity of MM are considered separately as in [119]. On the contrary, [57] proposes a method where both positioning and MM are performed simultaneously by the PF, which includes both processes in the integrity estimate. In addition to MM where 2D maps are usually used, recently, 3D maps have been used for characterising/detecting GNSS errors in the urban environment in order to aid the IM [115, 120]. This research will use a 2D map to represent spatial features, and the position integrity estimated by the proposed algorithms will also include the integrity of the SFC algorithm.

The previous algorithm, FDE+BRAIM, in addition to not being dependent on measurement availability/redundancy as a result of the nature of BRAIM, also attempts to mitigate the problem of measurement outliers in the measurement domain (FDE). However, there is a third component that needs to be considered: the implementation of the BRAIM algorithm (the effect of summarising the particle weights as shown in Figure 5.2). Because

the integrity is assessed based on the sum of weights for the particle subset determined as in Equation 5.2, the integrity is going to directly depend on the measurement likelihood of those particles. In theory, looking at Equation 5.3, correct classification of integrity availability depends on having as many particles as possible within the AL from the estimated position. Otherwise, those particles that are bounded by AL and closer to the true position need to be assigned a higher weight. Additional information necessary for the increase of particle weights is derived from the SFC method.

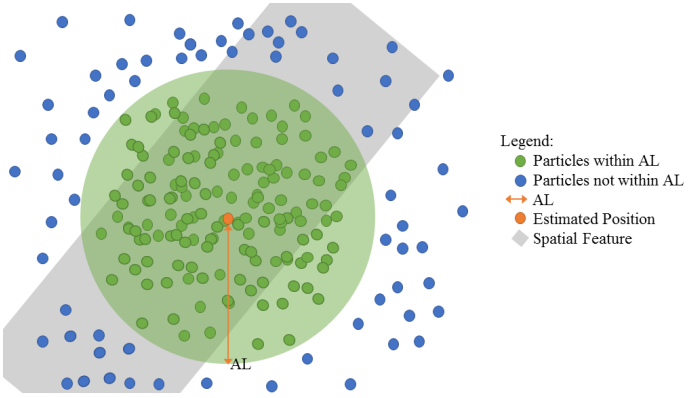


FIGURE 5.2: Example of how BRAIM works. Weights of particles within AL (green) are summarised.

To achieve this, the fact that most vehicles drive on the roads was used. A simple SFC algorithm as presented in [118] was applied by utilising the map of the road network. As in [121], the measurement likelihood can now be redefined with a binary weighting scheme,

$$p(Z_k|X_k^h) = \begin{cases} \epsilon, & h \text{ outside of road polygon} \\ p(Z_k|X_k^h), & h \text{ inside of road polygon} \end{cases} \tag{5.11}$$

where particles that are outside of the predefined road polygon get assigned a very small or zero likelihood ϵ and the particles that are within the road polygon get assigned the likelihood calculated according to Equations 4.3 and 4.6 for multi-sensor and cooperative positioning, respectively. In this thesis $\epsilon = 0$. Having defined measurement likelihood for each particle, particle weights can be updated as shown in Equation 4.2 and consequently normalised to sum up to 1.

The example of how SFC works is shown in Figure 5.3. It is expected that by effectively eliminating the particles outside of the road network ($\epsilon = 0$) and increasing the weights of the particles within the road network, the weight of some particles bounded by AL will also increase. Hence, the integrity estimate is expected to be improved. Algorithm 3

presents the pseudocode for SFC+BRAIM. As before, SFC for CP is performed during the second iteration of position estimation.

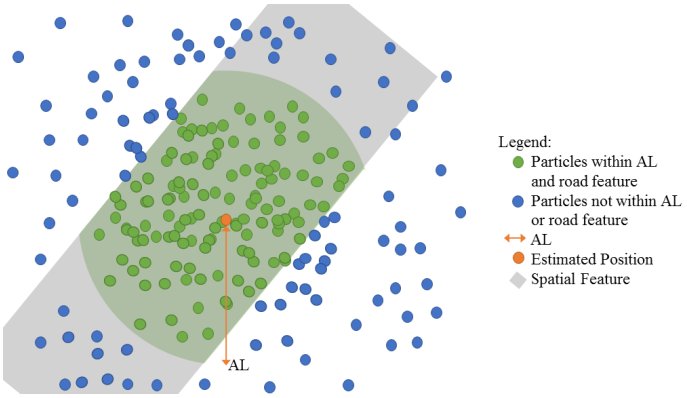


FIGURE 5.3: Example of how SFC+BRAIM works. Weights of particles within AL and the road feature are summarised.

Algorithm 3 Pseudocode for SFC+BRAIM

p_{IR}, AL
Initialise X_k and w_k for N_h particles
for time epoch k **do**
  Propagate particles through dynamic model
  for particle h **do**
    if particle $\in$ polygon **then**
      Measurement likelihood: $p(Z_k|X_k^h)$
    else
      Measurement likelihood: 0
    end if
  end for
  Update particle weight: $w_k^h = w_{k-1}^h \cdot p(Z_k|X_k^h)$
  State estimate $\hat{X}_k$
  BRAIM integrity assessment as in Algorithm 1
  Particle weight resampling
end for

The quality of map data is a problem to be considered for the purpose of global scalability of an MM or SFC integrity algorithm [57]. In [118], the effect of using real maps, that are often affected by problems such as missing attribute data or mapping errors, on the positioning and integrity estimation is shown. By utilising the OpenStreetMap data in [118] as an example of globally available map data, the capabilities of utilising currently available maps for globally applicable integrity estimation has been experimentally demonstrated (this will be shown in the next chapter).

To avoid problems such as the one shown in [118], in this thesis, a map created specifically for the test area is used (see Section 3.4 and Figure 3.21). Furthermore, in order to not

base the proposed method on the assumption of the "perfect map", a buffer area was created around the map to account for the assumed accuracy of the map. To validate the algorithms, the accuracy of 1 m will be assumed. By doing this, the p_{MI} of the SFC process will decrease because more particles will be within the map feature. Theoretically, this will increase p_{MI} (it will get worse) since particles and their weights (i.e., hypotheses) will be dispersed further than the ones when "perfect map" is used. This should provide a more realistic position integrity estimate, i.e., p_{MI} estimate. In results, the SFC method implemented with the added buffer will be denoted with 'map+1m'.

5.4.3 BRAIM paired with Fault Detection and Exclusion and Spatial Feature Constraint algorithms

Finally, to mitigate the problems addressed previously, FDE, SFC and BRAIM are combined into the FDE+SFC+BRAIM algorithm. SFC binary weighting scheme is implemented (see Algorithm 3) during the re-estimation of particle weights w_k and user's state $\hat{X}_k$ in Algorithm 2. It is expected that the results of this implementation will provide the best results since both the measurement outlier mitigation (FDE) and increase of particle weights that are within the road feature (SFC) will be implemented in addition to the BRAIM algorithm.

5.5 Performance evaluation metrics

BRAIM, FDE+BRAIM, SFC+BRAIM and FDE+SFC+BRAIM provide binary results: "Integrity is available!" and "Integrity is not available!" (as shown in Figure 5.1). In the proposed algorithms, AL and IR are the integrity requirements, where AL is used to bound the particles for integrity estimation, and IR is used to "decide" if the integrity is available or not. The IR probability p_{IR} can be defined as a maximum allowed probability that the estimated position will exceed the required AL. If the estimated probability of misleading information p_{MI} is smaller than the required p_{IR}, the integrity is estimated to be available. Otherwise, integrity is unavailable.

The integrity value and its availability are estimated in real-time. To evaluate the capability and performance of presented algorithms, the integrity and position estimate will be compared to the otherwise unavailable ground truth (i.e., position error PE).

Given the binary output of the integrity algorithm in real-time, when compared to PE, there are four possible outcomes:

- *Integrity is available.* Integrity is correctly classified as available when $PE \leq AL$ and $p_{MI} \leq p_{IR}$ are true.
- *Integrity is not available.* Integrity is correctly classified as unavailable when $PE > AL$ and $p_{MI} > p_{IR}$ are true.
- *False negative* (i.e., false alarm). Integrity is incorrectly classified as unavailable when $PE \leq AL$ and $p_{MI} > p_{IR}$ are true. The user is alerted when it should not have been.
- *False positive.* Integrity is incorrectly classified as available when $PE > AL$ and $p_{MI} \leq p_{IR}$ are true. The user is not alerted when it should have been.

The example of false negative and false positive can be given on an anti-collision system. In the case of the false negative, the user is informed that the integrity is not available when it should be, which causes the vehicle to brake or stop unnecessarily. In the case of the false positive, the user is not alerted about the unavailability of integrity, which could result in a collision.

In this thesis, one of the ways the performance will be evaluated is through the comparison of different estimated values of probability of misleading information. In addition to this, the rate of integrity availability will be estimated, as described in this section, with four different outcomes in mind — integrity available, integrity unavailable, false alarm, false positive. It is common to use Overall Correct Detection Rate (OCDR) as in [44]. However, this rate includes both the correct identification of availability and the unavailability of integrity. In this thesis, the rate of availability and unavailability will be presented separately as the aim is not just to increase OCDR but also to increase the availability. In addition to reducing p_{MI} and improving integrity availability, the aim of the implementation of algorithms like the FDE and SFC, is to reduce false negative and false positive rates.

5.6 Conclusions

Three novel integrity algorithms are proposed in this chapter — FDE+ BRAIM (a combination of FDE and BRAIM), SFC+BRAIM (a combination of SFC and BRAIM) and

FDE+SFC+BRAIM (a combination of FDE, SFC and BRAIM). The capabilities of these algorithms will be compared to the existing BRAIM, which was also presented in this chapter. Compared to [18] which used simulated stand-alone GNSS test data, in this research the proposed algorithms and the BRAIM will be evaluated using the real-world data fusion of GPS data and P2I and P2P terrestrial range data.

The performance of these algorithms will be analysed in Chapter 6 where the results will be presented. It should be noted that the implementation of the presented algorithms will be used as a proof-of-concept. All of the algorithms are easily customisable by implementing more sophisticated FDE and SFC algorithms. Furthermore, current algorithms are not curated for a specific bias present in the urban environment. More customisation is possible in that area.

6

Results and discussion

This chapter analyses the performance of the proposed integrity algorithms for the multi-sensor and the cooperative solution. Firstly, RAIM performance is compared to the proposed BRAIM for three different positioning solutions — stand-alone GPS, multi-sensor and cooperative positioning. This is followed by the analysis of the same three positioning solutions for the BRAIM, BRAIM paired with FDE, BRAIM paired with SFC, and finally, BRAIM paired with both the FDE and the SFC. The performance of these novel algorithms is analysed based on integrity metric improvement (i.e., reduction of probability of misleading information) and the integrity availability for the generalised road-level application. Lastly, the utility of the proposed SFC approach is tested on real-world data using the existing open-source map data.

6.1 Introduction

The goal of this chapter is to present the performance of the proposed integrity algorithms in terms of improvement in integrity metric estimation (i.e., probability of misleading information) and in terms of the availability of integrity for road-level application. Although it is not the focus of this thesis, the positioning accuracy is presented and discussed for better understanding of algorithms and their effects on the positioning. Some of the research questions that this chapter will answer are — What is the best achievable probability of misleading information for the multi-sensor and cooperative positioning system based on PF? What is the rate of success of the proposed methods? How does the probability of misleading information and integrity availability change depending on the algorithm conditions? Are the proposed algorithms sufficient for road-level or lane-level applications? The structure of the chapter is graphically represented in Figure 6.1.

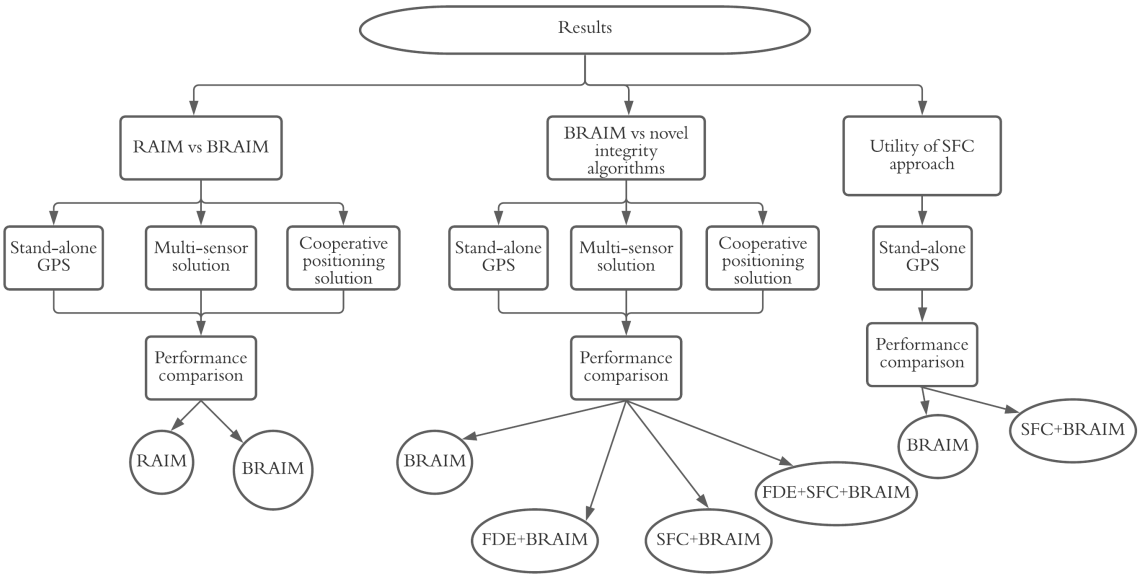


FIGURE 6.1: Chapter 6 structure.

Firstly, the performance of the BRAIM algorithm will be compared with the performance of the RAIM method in Section 6.2. As mentioned previously, the performance of the BRAIM presented in [18] has been evaluated on simulated GNSS data for six satellites. In this analysis, the performance of the BRAIM will be evaluated on the real-world GPS, multi-sensor and cooperative data described in Section 3.4. The main contribution of this section is the results for the first distributed, fully connected cooperative position

Parameter specifications detailed in Section 6.1 were first published in *Navigation, Journal of Institute of Navigation* in *Summer 2021* paper entitled *Case study of Bayesian RAIM algorithm integrated with Spatial Feature Constraint and Fault Detection and Exclusion algorithms for multi-sensor positioning* ([22] in the bibliography).

integrity method where the integrity measure is simultaneously estimated based on all the measurements involved in the measurement model.

Section 6.3 shows the second analysis, which compares GPS only, multi-sensor and cooperative BRAIMs with the performance of the three proposed integrity algorithms for the same three solutions. Those three novel algorithms are a combination of BRAIM and FDE, BRAIM and SFC and BRAIM, FDE and SFC. They are proposed as one of the major contributions of this thesis. As such, the contribution of this section is the analysis of the performance of those novel algorithms, including the integrity results for the cooperative solution.

The third and final analysis, presented in Section 6.4, looks further into the utility and limits of the SFC approach. Unlike the previous two analyses, this will be done on GPS data collected in Melbourne as described in Section 3.3. The main contribution of this section is the analysis of the SFC approach in addition to the BRAIM, where globally available map data are used.

When estimating the performance of the proposed algorithms, the following requirements will be used in the first two analyses. A required IR of $1 \cdot 10^{-7}/per\ epoch$ and $p_{FA} = 1 \cdot 10^{-5}$ based on [4] and [122] will be used. A HAL of 5 m is chosen according to [10] which is a requirement for road-level application accuracy and is a stringent SCA requirement in Table 2.5.

The error distribution of GPS measurements is assumed to be Gaussian with zero mean and a standard deviation of 5.7 m [123]. The error distribution of WASP measurements is either assumed to be Gaussian with zero mean and standard deviation of 0.9 m, or the three-component GMM defined in Section 4.2, Table 4.1 is used as a better approximation of the measurement error distribution. Acceleration noise and GNSS receiver clock bias noise were both assumed to be Gaussian with zero mean and variances randomly drawn from the standard normal distribution $\mathcal{N}(0, 1)$ at every time epoch for all particles. Every PF was run ten times for 300000 particles. The proposed algorithms were validated offline and not in real-time with the incoming stream of data. This also means that there was no need to have a system in place to relay the predetermined global coordinates of LPS nodes to the user. In a real-time system, this would have to be done through internet access to a database containing information about infrastructure nodes or using protocols such as the Dedicated Short Range Communication (DSRC) [124].

Table 6.1 specifies different parameters used in different analyses. It is to be noted that all of these will be further specified in the respective sections.

TABLE 6.1: Experiment parameters used in different analyses.

Analysis	Integrity requirements	Particle number	Error distribution GPS	Error distribution WASP	Injected errors	Data
1 Sec. 6.2	$p_{IR} = 1 \cdot 10^{-7}$ $HAL = 5m$	300 000	$\sigma = 5.7m$	Gaussian: $\sigma = 0.9m$ GMM: Table 4.1	$\emptyset$	Sydney Sec. 3.4
2 Sec. 6.3	$p_{IR} = 1 \cdot 10^{-7}$ $HAL = 5m$	300 000	$\sigma = 5.7m$	Gaussian: $\sigma = 0.9m$ GMM: Table 4.1	GPS: 80-120s $3\sigma - 6\sigma$ WASP: 1-90s $+25m$ or$+10m$	Sydney Sec. 3.4
3 Sec. 6.4	$HAL = 5m$	300 000	Sat. elev. based variance	$\emptyset$	$\emptyset$	Melbourne Sec. 3.3.1

It should also be noted, although Chapters 4 and 5 present algorithms capable of estimating 3D PE and p_{MI}, in this research, results are presented for the horizontal domain as that component of the position is more important for land-based applications. Thus, HPE, HPL and HAL are considered.

6.2 Comparison of BRAIM and RAIM

This section builds upon the work done in Section 3.3 and Chapter 4 by analysing the performance capabilities of two different RAIM algorithms: classical RAIM (Section 2.4.1), which is based on EKF, and BRAIM (Section 5.2), which is an algorithm with the PF as an underlying estimator. This section aims to analyse capabilities of BRAIM only for GPS, multi-sensor and CP systems and compare the performance with the RAIM method.

Results presented in Section 6.2 are part of the paper *Integrity risk estimates for multi-sensor and cooperative positioning systems*. It is in a process of revision following peer review by *IEEE Sensors Journal*.

Multi-sensor and CP positioning solutions are set up as explained in Chapter 4. The multi-sensor solution is based on GPS pseudoranges and P2I ranges (Figure 6.2). This will be denoted with GPS+WASP. Further notation can be added depending on the error distribution used for WASP measurements. In addition to the GPS pseudoranges and P2I ranges, the CP solution is based on the P2P WASP ranges and the shared positions of the collaborating vehicles (Figure 6.3). This will simply be denoted with CP with the added notation of error distribution used for all WASP ranges.

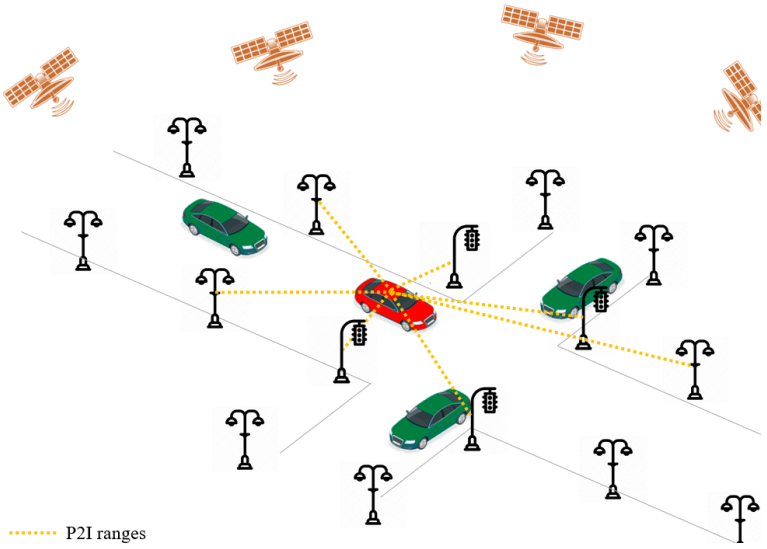


FIGURE 6.2: Multi-sensor solution using P2I terrestrial ranges to the LPS and GNSS pseudoranges for position and integrity estimation.

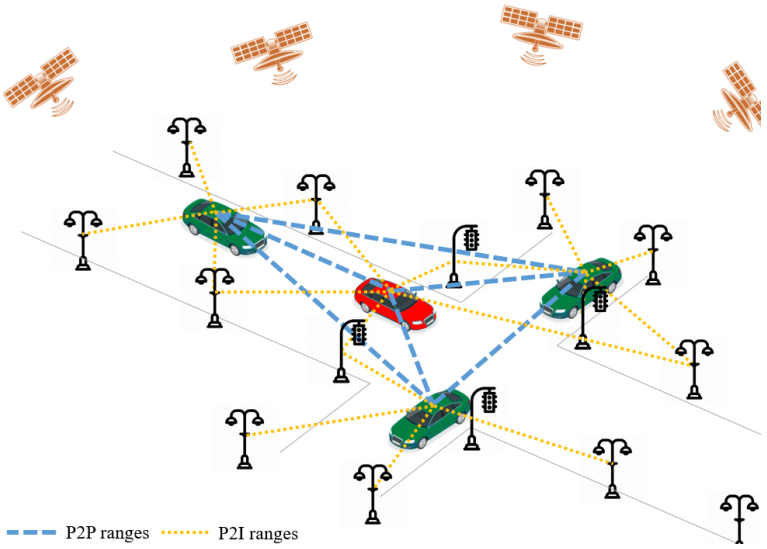


FIGURE 6.3: Cooperative solution using the P2I terrestrial ranges to the LPS, P2P terrestrial ranges between all the vehicles, shared positions of all the vehicles in the network and GNSS pseudoranges for position and integrity estimation.

The results are presented based on the used position solution (just like Section 2.5). Firstly,

the performance is analysed for stand-alone GPS data where both RAIM and BRAIM have been implemented. This is followed by the results for multi-sensor data where the same algorithms have been implemented. Lastly, the performance for CP between two, three and four users are presented for the BRAIM algorithm only. Integrity is analysed in terms of an improvement of the estimated integrity values and later discussed in terms of the integrity availability, for road-level application. The improvement of estimated integrity is observed through the improvement of HPL for RAIM and p_{MI} for BRAIM. The experiment parameters used to produce the results are specified in Table 6.1.

6.2.1 Positioning and integrity performance

In terms of the position accuracy, the EKF and the PF performances are similar for **GPS data**. As concluded in Chapter 4, this happens because the EKF's first-order Taylor series approximation of the non-linear measurement model is a good approximation for GPS data. Because of that. Using a non-linear estimator like the PF does not have a significant impact on the position estimation. Average HPE for both the EKF and PF is around 2.7 m with a standard deviation of around 0.2 m.

Table 6.2 shows the estimated integrity parameters which depend on the implemented algorithm. Both algorithms have the same requirements — IR p_{IR} and HAL. However, HPL is estimated in RAIM and probability of misleading information p_{MI} is estimated in BRAIM. The results show that for the required IR of $1 \cdot 10^{-7}$, RAIM is able to achieve a median HPL of 32.83 m. Implementation of BRAIM results in median p_{MI} of $2.56 \cdot 10^{-1}$ integrity which is significantly larger than the required IR. In both cases, the estimated integrity values indicate that the integrity estimates based on GPS only are not satisfactory for given integrity requirements. It could be concluded that stand-alone GPS in not adequate for integrity monitoring in urban environments. To mitigate this problem, in line with the review of the literature and the analysis in Chapter 3, GPS is integrated with P2I LPS ranges.

TABLE 6.2: Comparison of the estimated integrity for GPS data.

Req. HAL	**Req. IR**	**Alg.**	**Med. est. integrity**	
5 m	$1 \cdot 10^{-7}$	RAIM	HPL	32.83 m
		BRAIM	p_{MI}	$2.56 \cdot 10^{-1}$

The positioning performance for GPS+WASP data is consistent with the positioning results presented in Section 4.3.2. For the RAIM that is based on EKF position estimator, an average HPE is 0.95 m. This is reduced to 0.26 m and 0.34 m when PF is used and Gaussianity is assumed for WASP range error distribution, or GMM approximation is used, respectively. Table 6.3 shows the estimated integrity values for multi-sensor RAIM and BRAIM. The median estimated HPL has decreased to 5.36 m. GPS and WASP data fusion has resulted in median estimated integrity of $1.33 \cdot 10^{-10}$ and $3.04 \cdot 10^{-7}$, for Gaussian assumption and GMM approximation for WASP error distribution, respectively. In case of the Gaussian assumption, that is three orders of magnitude better than the required IR of $1 \cdot 10^{-7}$, and for the GMM it is close to the required IR. The results of this section indicate the potential of the multi-sensor system for road-level applications. When GMM is used, the estimated integrity should be improved to increase integrity availability rates. To potentially further improve the availability of road-level integrity, CP is implemented.

TABLE 6.3: Comparison of the estimated integrity for multi-sensor data.

Req. HAL	**Req. IR**	**Alg.**	**GPS+WASP**	**Med. est. integrity**	
5 m	$1 \cdot 10^{-7}$	RAIM		HPL	5.36 m
		BRAIM	Gaussian	p_{MI}	$1.33 \cdot 10^{-10}$
			GMM	p_{MI}	$3.04 \cdot 10^{-7}$

CP has been tested on the BRAIM algorithm only, for two, three and four users collaborating in the network. Average positioning accuracy remained around 0.26 m for both the Gaussian and the GMM error distributions of WASP.

It can be observed in Table 6.4 that the median integrity estimate for road-level applications keeps improving as the number of nodes cooperating increased. Compared to the initial integrity for multi-sensor BRAIM, an improvement of one order of magnitude has occurred for a network of four users in CP BRAIM.

Figures 6.4 and 6.5 summarise the above results for BRAIM and show how median p_{MI} improved with the different positioning solutions as well as the number of users in cooperation.

TABLE 6.4: Estimated integrity parameters for CP BRAIM.

Req. HAL	Req. IR	CP	No. of users	*Med. est.* p_{MI}
5 m	$1 \cdot 10^{-7}$	Gaussian	2	$5.75 \cdot 10^{-11}$
			3	$2.63 \cdot 10^{-11}$
			4	$1.75 \cdot 10^{-11}$
		GMM	2	$1.27 \cdot 10^{-7}$
			3	$8.33 \cdot 10^{-8}$
			4	$3.24 \cdot 10^{-8}$

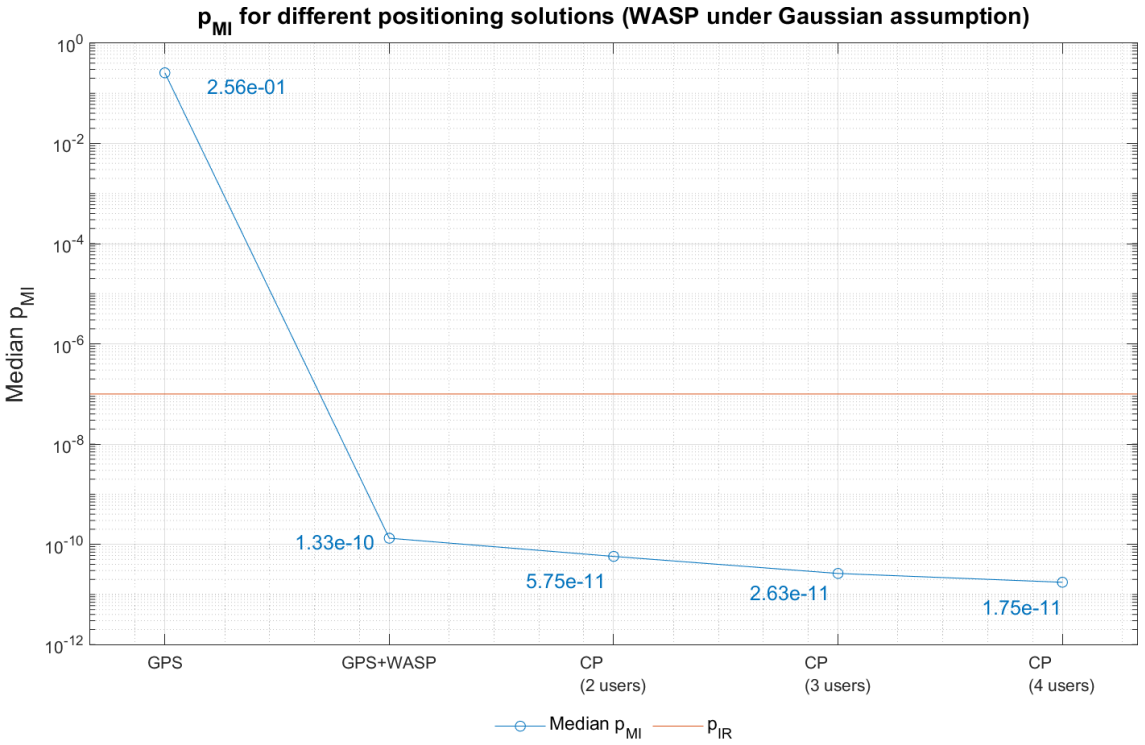


FIGURE 6.4: Improvement of the median BRAIM integrity estimate through the employment of a more advanced positioning solution. The Gaussian assumption is made for WASP error distribution.

6.2.2 Discussion on availability

The availability of integrity can be calculated as shown in Section 5.5 for the estimated integrity values and calculated HPE.

Given the estimated values of HPL and p_{MI} for GPS only data in Table 6.2, and the average HPE of 2.7 m, it is clear that FA rates will be high. In both the RAIM's and the BRAIM's case, the FA rate of 100% was observed. This is true for the road-level application requirements defined at the beginning of this chapter. Both of these solutions may be satisfactory for less stringent applications, as shown in Table 2.5. For example,

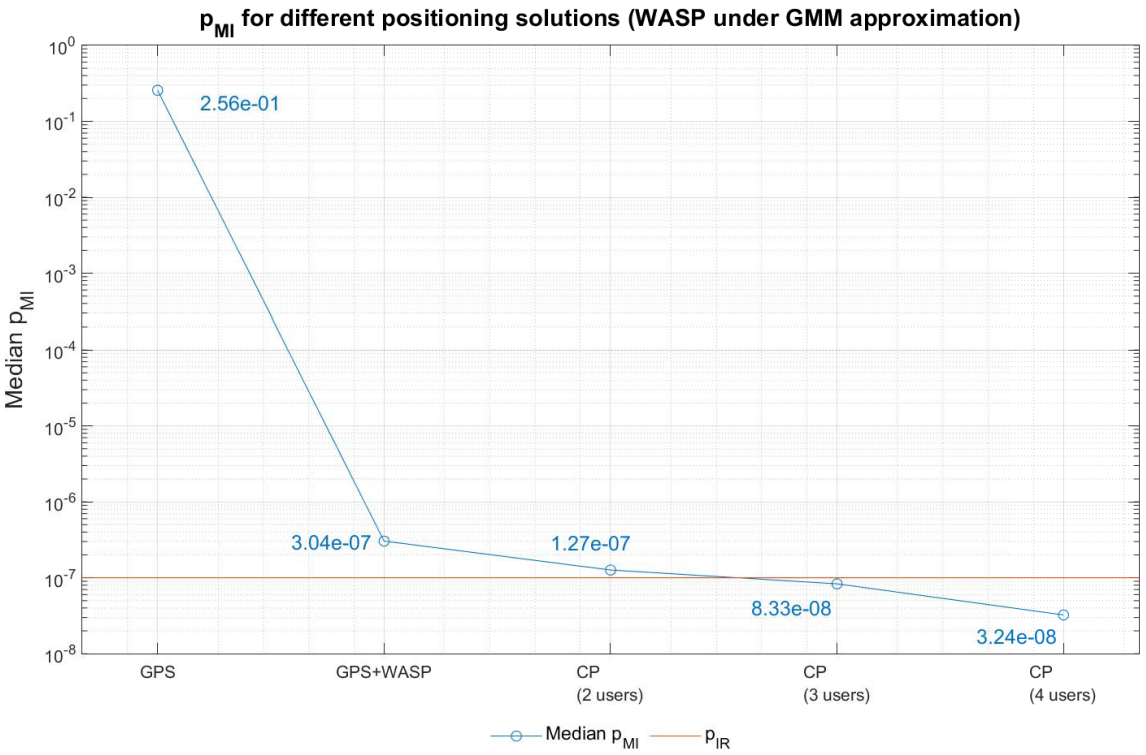


FIGURE 6.5: Improvement of the median BRAIM integrity estimate through the employment of a more advanced positioning solution. WASP error distribution is approximated by the GMM.

those can be PCA where required IR can range from $1 \cdot 10^{-4}$ to $1 \cdot 10^{-3}$ and HAL from 20 m to 40 m.

The results shown in Figures 6.6 and 6.7 indicate that the approach to mitigate problems of integrity unavailability for stand-alone GPS by implementing multi-sensor and CP integrity was successful.

Integrity availability for RAIM method increased from previously 0% to 40.22%. In Section 3.3 real GPS data was integrated with the simulated terrestrial ranging data, and the results have shown that availability increased to almost 100% in the open-sky scenario. Although useful for testing algorithm capabilities quickly and cheaply, the results in this section confirm the importance of collecting real-world data in terms of producing more realistic results. Furthermore, BRAIM has shown an improvement from 0% for stand-alone GPS to 96.85% availability for GPS+WASP(Gaussian) data. This was further improved to 97.88% by implementing CP BRAIM. As shown in Tables 6.3 and 6.4, when Gaussianity for WASP is not assumed, p_{MI} values are larger by three orders of magnitude. As expected, this reflected negatively on the integrity availability. The best achieved correctly classified integrity availability of 63.3% was achieved for four cooperating users.

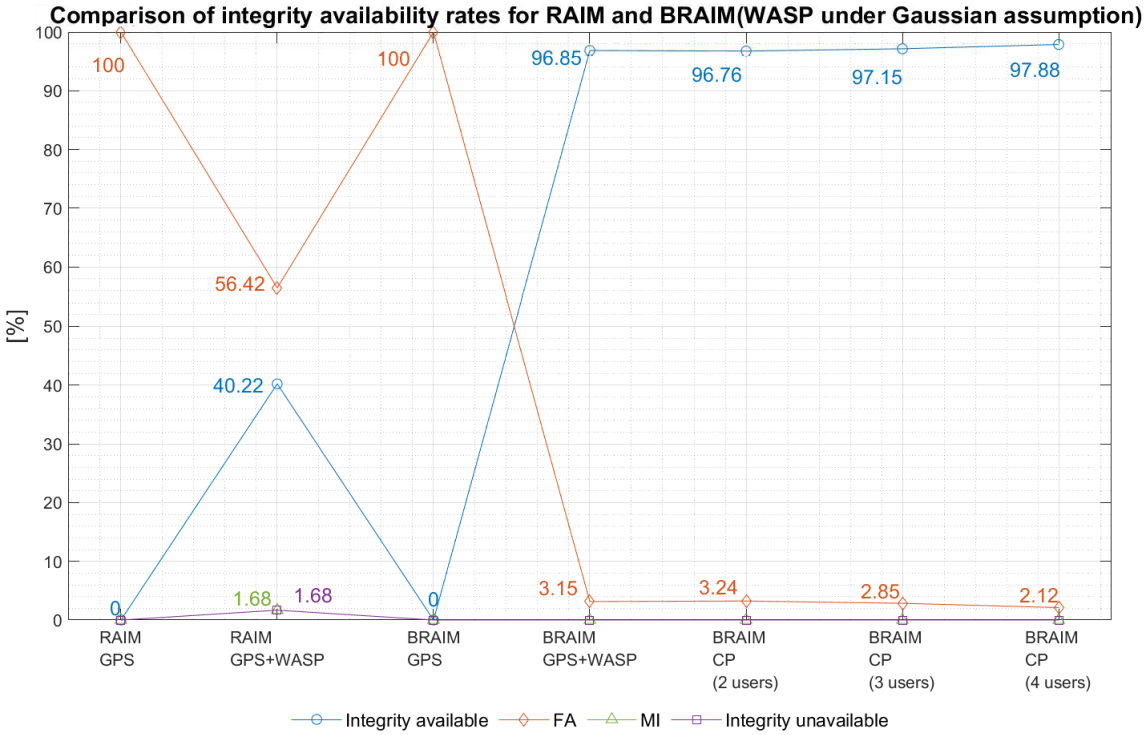


FIGURE 6.6: Comparison of RAIM and BRAIM integrity availability rates for road-level applications. Gaussian assumption is made for WASP error distribution.

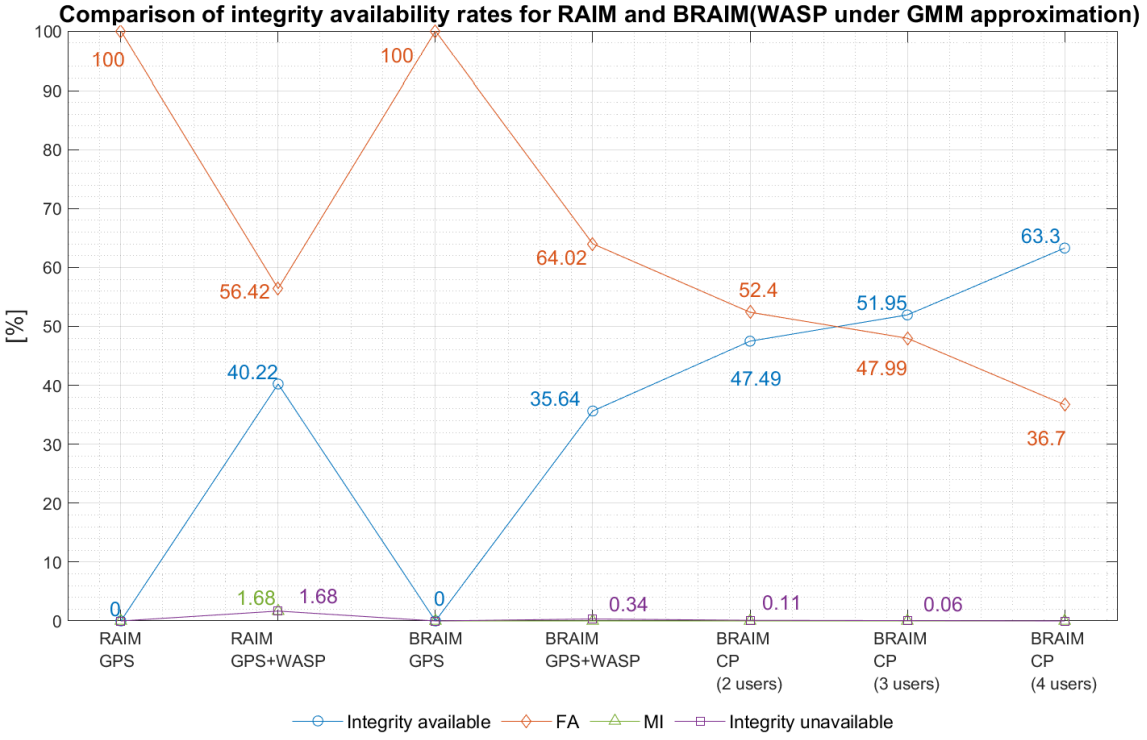


FIGURE 6.7: Comparison of RAIM and BRAIM integrity availability rates for road-level applications. WASP error distribution is approximated by the GMM.

The results of this section indicate the expected superiority of the BRAIM over the RAIM method, in terms of both the positioning and the integrity performance. However, discrepancies between the performance of integrity algorithms depending on the distribution

of the WASP measurements need to be addressed. This will be discussed in the following section.

6.3 Performance of the three novel algorithms

This section aims to present the performance of the three novel algorithms proposed in this research — FDE+BRAIM, SFC+BRAIM and FDE+SFC+BRAIM. Firstly, the positioning performance is discussed, which is followed by the integrity performance results. Lastly, a brief discussion is made on the integrity availability for the road- and lane-level ITS applications.

Since data used for initial algorithm validation were collected in the environment without any obstacles (as detailed in Section 3.4), some large errors were injected into the measurements. For timestamps 1-50 and 40-90, ranging errors of 25 m and 10 m for two different LPS nodes were injected, respectively. This created an overlap of 10 s (timestamps 40-50) where two large errors are injected into the measurement vector. In addition to injecting errors for two LPS nodes, errors for two satellites are injected. The two satellites with the lowest elevations (in this experiment, elevation for both is under 20°) were chosen. For timestamps between 80-120, a random error of size $3\sigma_S$ to $6\sigma_S$ (as seen in [113]) is injected for both of the satellites. For 10 s (timestamps 80-90), three large injected errors were present in the system. All experiment parameters used to produce the results are specified in Table 6.1.

6.3.1 Positioning performance

As expected, the implementation of different algorithms for integrity has resulted in different HPEs. Table 6.5 details all the average HPEs, the standard deviation of the HPEs and the maximum HPEs for GPS only, GPS+WASP and cooperative (WASP under Gaussian assumption and for GMM) data sets for every proposed algorithm. All values in the table are calculated based on all ten runs of each of the PFs.

Section 6.3 was first published in *Navigation, Journal of Institute of Navigation* in *Summer 2021* paper entitled *Case study of Bayesian RAIM algorithm integrated with Spatial Feature Constraint and Fault Detection and Exclusion algorithms for multi-sensor positioning* ([22] in the bibliography). Results regarding cooperative integrity performance are new and have not been published or submitted for publication yet. Consequently, the same is true for the discussion related to cooperative integrity results.

TABLE 6.5: Positioning performance results

Data	Algorithm	Avg HPE [m]	Std [m]	Max [m]
G	B	4.32	3.85	21.14
	FDE+B	2.96	1.41	19.26
	SFC+B (*map+1m*)	3.03	2.02	16.89
	SFC+B	2.91	1.80	15.83
	FDE+SFC+B (*map+1m*)	2.62	1.12	9.42
	FDE+SFC+B	2.63	1.19	9.44
G+W *Gaussian*	B	0.25	0.17	1.74
	FDE+B	0.25	0.17	1.49
	SFC+B (*map+1m*)	0.24	0.14	0.91
	SFC+B	0.27	0.15	1.52
	FDE+SFC+B (*map+1m*)	0.25	0.16	1.18
	FDE+SFC+B	0.28	0.17	1.60
G+W *GMM*	B	0.26	0.28	4.31
	FDE+B	0.31	0.44	5.46
	SFC+B (*map+1m*)	0.24	0.20	3.43
	SFC+B	0.26	0.26	4.68
	FDE+SFC+B (*map+1m*)	0.29	0.35	5.33
	FDE+SFC+B	0.31	0.42	5.99
CP *Gaussian*	B	0.25	0.18	1.82
	FDE+B	0.27	0.18	1.28
	SFC+B (*map+1m*)	0.24	0.14	0.83
	SFC+B	0.27	0.17	1.44
	FDE+SFC+B (*map+1m*)	0.25	0.16	1.06
	FDE+SFC+B	0.27	0.18	1.24
CP *GMM*	B	0.25	0.20	1.92
	SFC+B (*map+1m*)	0.31	0.42	3.60
	SFC+B	0.40	0.65	4.72

For GPS data, an improvement of the average HPE can be observed with the implementation of all novel algorithms. The average HPE for BRAIM is 4.32 m, which is due to the injected errors. The best performance is observed for the multi-sensor and cooperative FDE+SFC+BRAIM algorithm (with the 'perfect map' and a map with a buffer). Here, map error did not affect the positioning performance. The average HPE for the FDE+SFC+BRAIM algorithm is comparable to the performance of PF in Section 4.3.2

for the same GPS data when no errors were injected. In the case of GPS+WASP and CP data (when Gaussianity of WASP data is assumed and when GMM is used), the average HPE drops to ~ 0.30 m and does not change significantly depending on the algorithm. On average, in this instance, different integrity algorithms did not significantly impact positioning performance. As it was shown in Chapter 4, the proposed positioning systems based on the multi-sensor and cooperative fusion of GPS and WASP data is capable of achieving positioning accuracy required for the road- and lane-level applications [10]. Standard deviations and maximum errors of the GPS+WASP when the WASP actual error distribution is approximated by a GMM are larger than the ones when Gaussianity is assumed. It is not clear why this happens. One of the reasons may be due to the GMM assigning particles that have a larger error with a higher probability (Equation 4.1). This may also be due to large errors injected into data as described. Nevertheless, more research into this is necessary in the future.

6.3.2 Integrity performance

This section presents the integrity results for the required $HAL = 5$ m. The integrity results will be presented in terms of change of estimated p_{MI} (i.e., integrity estimate) depending on the used algorithm for GPS only, GPS+WASP and CP multi-sensor data. The performances of GPS+WASP and CP data are tested under the Gaussian assumption and for GMM approximation for WASP measurements. Even though a three-component GMM (Equation 4.1) with parameters in Table 4.1 was shown to be a better approximation to the WASP error distribution, it is valuable to see how p_{MI} is affected by this commonly made assumption of Gaussianity.

Table 6.6 presents the integrity results for $HAL = 5$ m. The median value was chosen as a metric of change of the estimated p_{MI} since it provides a better idea of the typical integrity value. This is demonstrated in Table 6.6 where a difference of two to six orders of magnitude is observed between the average and median p_{MI} for GPS+WASP data. In these cases, the average value is skewed by high values of p_{MI} (e.g., maximum p_{MI} column).

The results presented for GPS data show improvement of the median estimated p_{MI} with the implementation of different methods. The best result is, as expected, shown for FDE+SFC+BRAIM algorithm. However, it cannot be said that the improvement is significant, and it does not satisfy the required IR of $1 \cdot 10^{-7}$. As expected, the values

TABLE 6.6: Estimated integrity for $AL = 5\ m$

Data	Algorithm	Med p_{MI}	Avg p_{MI}	Max p_{MI}
G	B*	2.59e-01	3.18e-01	0.92
	FDE+B	2.53e-01	3.05e-01	0.71
	SFC+B (*map+1m*)	1.26e-01	1.64e-01	0.76
	SFC+B	1.09e-01	1.47e-01	0.68
	FDE+SFC+B (*map+1m*)	1.23e-01	1.55e-01	0.56
	FDE+SFC+B	1.06e-01	1.34e-01	0.58
G+W *Gaussian*	B	3.31e-10	5.24e-05	8.26e-03
	FDE+B	2.68e-10	2.81e-08	1.84e-06
	SFC+B (*map+1m*)	5.71e-12	4.89e-06	1.22e-03
	SFC+B	1.325e-12	5.07e-06	4.49e-03
	FDE+SFC+B (*map+1m*)	5.48e-12	9.06e-10	2.97e-07
	FDE+SFC+B	1.326e-12	1.86e-09	1.52e-06
G+W *GMM*	B	6.97e-07	1.08e-03	0.15
	FDE+B	9.67e-07	3.90e-03	0.98
	SFC+B (*map+1m*)	5.81e-08	2.05e-04	0.10
	SFC+B	2.94e-08	4.29e-04	0.37
	FDE+SFC+B (*map+1m*)	9.68e-08	8.94e-04	0.20
	FDE+SFC+B	3.39e-08	7.40e-04	0.21
CP *Gaussian*	B	4.55e-11	3.33e-05	3.07e-03
	FDE+B	2.22e-15	1.96e-10	3.51e-08
	SFC+B (*map+1m*)	1.70e-12	4.28e-06	7.29e-04
	SFC+B	2.74e-13	5.34e-06	9.52e-04
	FDE+SFC+B (*map+1m*)	0	1.89e-14	2.79e-12
	FDE+SFC+B	0	6.99e-15	7.02e-13
CP *GMM*	B	6.00e-08	1.01e-04	0.01
	SFC+B (*map+1m*)	9.04e-09	4.33e-04	0.05
	SFC+B	5.84e-09	6.20e-04	0.06

shown in Table 6.6, indicate that the implementation of proposed methods with GPS only is not feasible for any ITS application.

The performance of GPS+WASP and CP data (under Gaussian assumption) is shown in Figure 6.8. The left y-axis shows the change of median integrity estimate p_{MI} (blue circle marker) depending on the implemented algorithm, which is always shown on the

x-axis. With the fusion of GPS and WASP data, the required level of integrity (i.e., p_{MI}) is achieved. Implementation of different methods has resulted in notable improvement of the integrity estimate. Median p_{MI} for BRAIM is $3.31 \cdot 10^{-10}$ which improves to $1.33 \cdot 10^{-12}$ when both FDE and SFC are implemented with the BRAIM algorithm (i.e., FDE+SFC+BRAIM). Notably, FDE algorithms have not significantly affected the median p_{MI}. The SFC algorithm shows the biggest impact on the estimated p_{MI}. As expected, p_{MI} increases when a map with a buffer is used. However, the impact of accounting for map error was not significant in this experiment. Once the CP solution is used, the integrity performance of the BRAIM estimate improves by an order of the magnitude. Unlike the multi-sensor solution, the biggest impact on the median integrity is visible with the implementation of FDE in addition to the BRAIM. Again, the best median estimate of p_{MI} was achieved for FDE+SFC+BRAIM algorithm. However, in case of CP data, p_{MI} was equal to 0 (not shown in Figure 6.8, see Table 6.6).

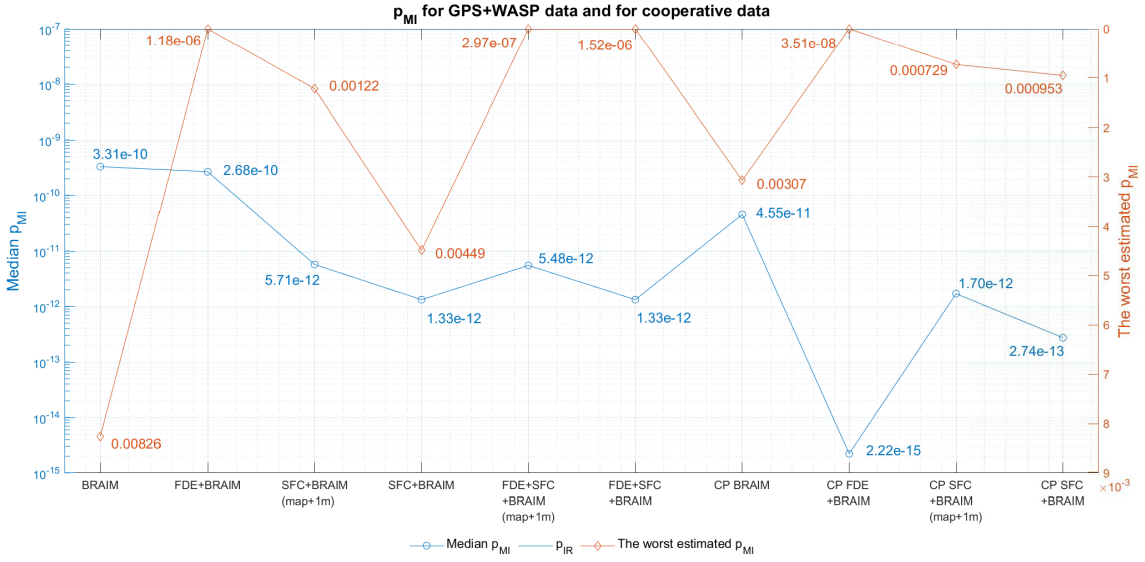


FIGURE 6.8: Integrity estimation for GPS+WASP data depending on the applied integrity algorithm.

The right y-axis of the Figure 6.8 shows the worst estimated integrity (orange diamond marker) which is also shown in the maximum p_{MI} column of Table 6.6. This value is important as it shows the capability of proposed algorithms to mitigate the effect of measurement outliers (i.e., FDE) and capability to improve integrity by improving the weights of particles within the map feature (i.e., SFC) (as discussed in Section 5.4.2). The worst estimated p_{MI} for GPS+WASP data is $8.26 \cdot 10^{-3}$ for the BRAIM algorithm. With the implementation of FDE, this is improved to $1.84 \cdot 10^{-6}$, which is further reduced to $2.97 \cdot 10^{-7}$ and $1.52 \cdot 10^{-6}$ once SFC was added (i.e., for FDE+SFC+BRAIM). The worst estimate of

p_{MI} for cooperative BRAIM is similar to the multi-sensor counterpart (i.e., $3.07 \cdot 10^{-3}$). In terms of reducing the worst estimated p_{MI}, SFC+BRAIM was more successful for CP (by an order of the magnitude). However, the FDE+BRAIM and FDE+SFC+BRAIM showed further reduction of the worst estimate by two and six orders of magnitude for CP data, respectively.

Figure 6.9 shows the integrity result for the multi-sensor and CP solution where WASP ranging errors are distributed with three-component GMM (noted with GPS+ WASP(GMM) and CP(GMM)). Although the average HPE of these positioning solutions is comparable with the one where Gaussianity is assumed, the integrity estimation is not. Compared to the results generated for the WASP data under the Gaussian assumption, the integrity estimate is worse by three to four orders of magnitude. The assumption is that due to the three-component GMM distribution, the measurements with larger errors have higher probability and the particles that are further away from the estimated position have larger weights than in the case of Gaussian assumption. This is important for BRAIM methods since only weights of particles bounded by HAL are used for p_{MI} estimation (see Figure 5.2). To confirm this assumption, a study of the *a posteriori* distribution is necessary in the future. Initial analysis has supported the assumption.

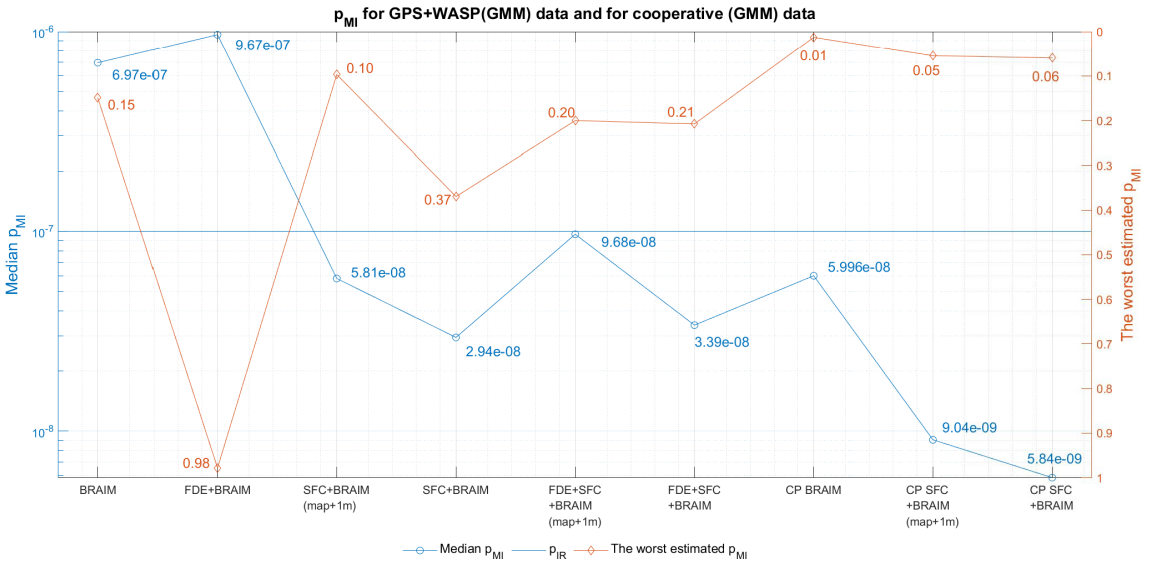


FIGURE 6.9: Integrity estimation for GPS+WASP(GMM) data for road-level positioning depending on the applied algorithm.

The best median p_{MI} for multi-sensor solution (with GMM approximation) is estimated for the SFC+BRAIM algorithm (with a 'perfect map') where $2.94 \cdot 10^{-8}$ was achieved. The worst estimates of p_{MI} are significantly larger than the ones for the Gaussian counterpart. Unlike the previous results where the implementation of FDE has improved (slightly)

the median p_{MI} and significantly reduced the worst p_{MI}, here, the opposite happens for FDE+BRAIM. The way to rectify this may be to implement an FDE method designed for PF and hence, without assumptions of error distributions made in the current FDE method. Once the cooperative WASP ranges were added to the multi-sensor solution (i.e., CP solution), further improvement of the median p_{MI} was observed. The median p_{MI} for CP BRAIM showed an improvement of one order of magnitude compared to the multi-sensor solution (i.e., from $6.97 \cdot 10^{-7}$ to $5.996 \cdot 10^{-8}$). That is comparable with the multi-sensor SFC+BRAIM. CP SFC+BRAIM implementation further reduced the median p_{MI} by an order of the magnitude. When it comes to the worst estimated integrity, an improvement of one order of the magnitude was observed. It is to be noted that, for the CP solution, novel FDE+BRAIM and FDE+SFC+BRAIM were not tested. The same issues noticed for multi-sensor FDE+BRAIM and FDE+SFC+BRAIM occur for the CP. As shown in Section 2.5, development of appropriate FDE methods is a large research area related to the problem of IM. Much of the current work for IM deals exactly with FDE methods. Development of the appropriate FDE method is out of the scope of this research and will be dealt with in the future.

The literature review in Section 2.5 indicated that unless, RTK or PPP GPS measurements are used, lane-level integrity (i.e., $HAL = 1.1\ m$ as in [10]) cannot be achieved. Nevertheless, this was experimentally demonstrated here for the multi-sensor positioning solution. Through that, the same can be implied for the CP. The performance of the proposed methods for $HAL = 1.1\ m$ is shown in Table 6.7. The best achieved median p_{MI}, when Gaussianity of WASP ranges is assumed, is $2.86 \cdot 10^{-2}$ for FDE+SFC+BRAIM algorithm. When Gaussianity of WASP ranges is not assumed, the best achieved median p_{MI} is $3.80 \cdot 10^{-3}$. It should be noted that the differences between median integrity estimates for different algorithms are not as large as they were for road-level integrity (Table 6.6). The results in Table 6.7 demonstrate that current implementation of the BRAIM and proposed algorithms are not appropriate for lane-level applications. This is probably due to actual error behaviour being worse than necessary to achieve $HAL = 1.1\ m$. As noted before, to achieve this level of integrity, other studies have used PPP (e.g., [58]) or RTK (e.g., [61]). Additional data such as IMU data may be necessary as both of these methods have fused GPS with it.

TABLE 6.7: Estimated integrity for $AL = 1.1\ m$

Data	Algorithm	Med p_{MI}	Avg p_{MI}	Max p_{MI}
G+W *Gaussian*	B	4.08e-02	7.09e-02	0.78
	FDE+B	3.94e-02	6.31e-02	0.65
	SFC+B (*map+1m*)	4.03e-02	6.91e-02	0.73
	SFC+B	2.95e-02	4.82e-02	0.70
	FDE+SFC+B (*map+1m*)	3.96e-02	6.19e-02	0.28
	FDE+SFC+B	2.86e-02	4.34e-02	0.9999998
G+W *GMM*	B	5.40e-03	4.02e-02	0.999995
	FDE+B	5.73e-03	4.48e-02	0.9993
	SFC+B (*map+1m*)	4.71e-03	3.51e-02	0.99995
	SFC+B	3.40e-03	2.57e-02	0.99
	FDE+SFC+B (*map+1m*)	5.79e-03	4.03e-02	0.998
	FDE+SFC+B	3.80e-03	3.41e-02	1.00

6.3.3 Discussion on availability

So far, the estimated probability of misleading information has been presented and discussed for four different algorithms, three different positioning solutions, different measurement error distributions and for two different generalised applications (road- and lane-level). As such, the previous section has referred to the position integrity results. This section will demonstrate and discuss the availability rates of integrity as defined in Section 5.5. Since the integrity availability will not be based on the BRAIM method only but for BRAIM paired with FDE and SFC, it can be said that this discussion refers to the IM.

As shown in the previous section, the effect of different p_{MI} estimations needs to be viewed in terms of integrity availability from a point of view of ITS applications. Although the goal is to provide the initial assessment of the proposed algorithms, integrity availability rates are an important metric that needs to be considered. According to [61], to ensure reliable positioning, the integrity availability rate should exceed 99%. However, this rate depends on the application. For autonomous vehicles, it would likely have to be higher than 99%.

Given the results of IM for GPS only for road-level requirements, and the results for GPS+WASP for lane-level requirements, the false alarm rate for both exceeds 99%. As

mentioned earlier, this is likely due to the measurement error behaviour being worse than necessary to satisfy the application requirements. Integration with different sensors, or use of PPP or RTK, may be beneficial to the integrity estimates. This was demonstrated for road-level requirements where p_{MI} improved significantly when GPS data was integrated with WASP data.

Figure 6.10 shows the integrity availability assessments for GPS+WASP and CP data with the assumption of Gaussianity for required $HAL = 5\ m$. As shown in Section 5.5, the four outcomes of IM when compared to HPE are — integrity available, integrity not available, false alarm (false negative) and false positive. The integrity unavailability and false positive rates are 0% and are not shown in Figure 6.10.

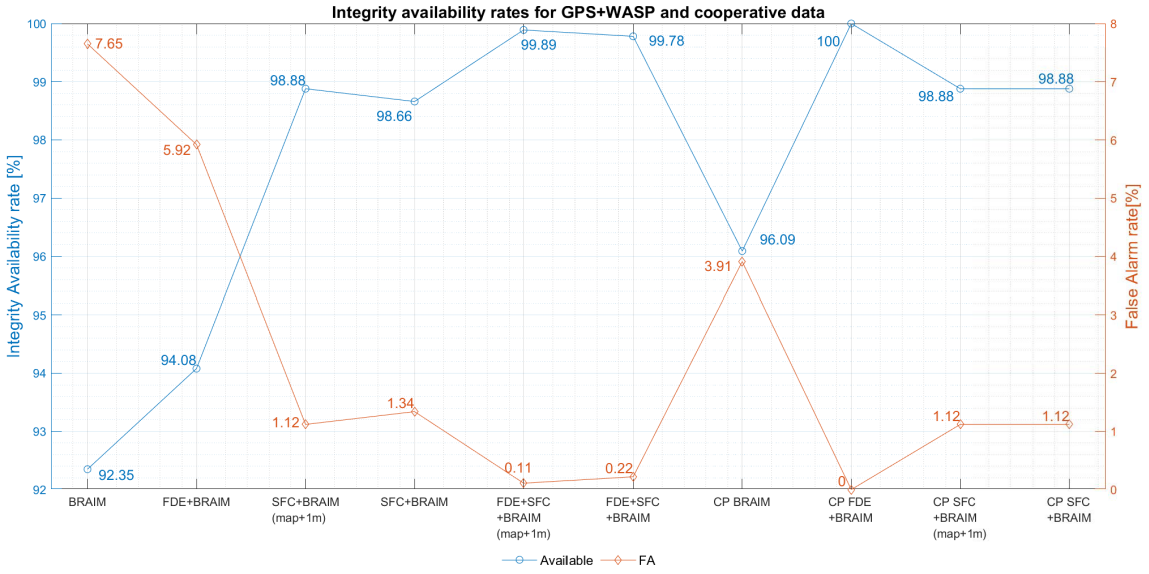


FIGURE 6.10: Integrity availability assessment for GPS+WASP data set for road-level positioning depending on the applied IM algorithm.

Integrity availability rate for GPS+WASP data is shown to increase with every new algorithm implementation. When comparing FDE+BRAIM and SFC+BRAIM algorithms in Figures 6.8 and 6.10, it is clear that SFC affects BRAIM more than FDE. Implementation of the FDE algorithm has improved integrity availability of BRAIM for 1.73%, while $\sim 6.4\%$ improvement was shown when SFC was implemented with BRAIM. An integrity availability exceeding 99% (i.e., 99.89%) was achieved once FDE+SFC+BRAIM was implemented (with the use of buffered map). This means that for FDE+SFC+BRAIM, 99.83% of the time integrity is correctly classified as available due to HPE being lower than the HAL and estimated integrity p_{MI} being better than the IR p_{IR}. The rest of the time, integrity is incorrectly classified as unavailable (i.e., false alarm). As shown in Table 6.5, HPE never exceeds the HAL. However, the integrity estimate exceeds IR in

some cases (as shown in Table 6.6). False alarm rates decrease when the FDE and SFC algorithms are integrated with BRAIM due to their effect on the magnitude of the estimated integrity. With the integration of cooperative WASP data, availability of 96.09% was achieved for BRAIM only, which is 3.74% improvement compared to the multi-sensor BRAIM. With the implementation of FDE, 100% availability was achieved for CP solution. Nevertheless, testing on more data collected in various environments would be required to provide further validation of the proposed method.

The integrity availability assessment for GPS+WASP and CP where WASP error distribution is approximated by a GMM is shown in Figure 6.11. Due to the lower p_{MI} estimates shown in Table 6.6, integrity availability is significantly reduced when GMM is used as the WASP range error distribution. The best integrity availability for multi-sensor data is 64.58% and the lowest false alarm rate is 35.42%. This is achieved for the SFC+BRAIM algorithm. It should be noted that integrity is correctly classified as unavailable for one (0.06%) and two (1.11%) time instants when multi-sensor FDE+SFC+BRAIM is used with the map with buffer and the 'perfect map', respectively. Due to its magnitude, it is not shown in the figure. CP BRAIM achieved 54.19% availability. This is an improvement of 29.16%, compared to the multi-sensor BRAIM. With the implementation of SFC, the availability improves to approximately 70%.

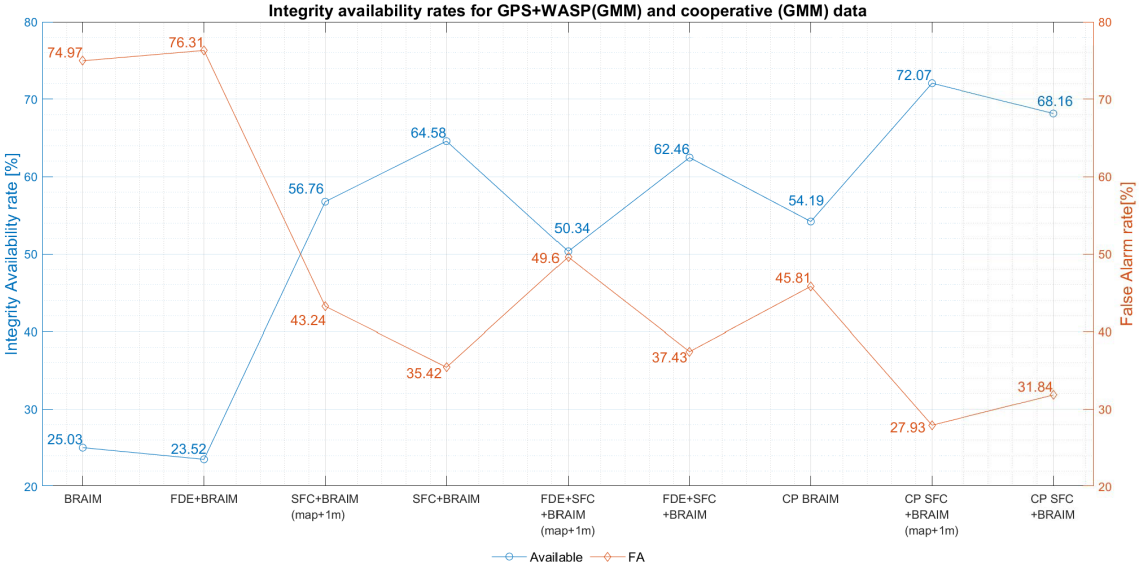


FIGURE 6.11: Integrity availability assessment for GPS+WASP(GMM) data for road-level positioning depending on the applied algorithm.

Results presented in this section and the one before could suggest that the multi-sensor and CP solutions under the Gaussian assumption have outperformed those solutions when

WASP measurement distribution is approximated by a GMM. However, if made, this conclusion would be invalid since GMM is a better fit to the actual WASP error distribution (Section 4.2). The GMM distribution should represent large rare-event errors more appropriately, which is exactly what every integrity algorithm should aim for. Therefore, it is fair to conclude that the multi-sensor and CP integrity assessment based on the GMM distribution of WASP, is a better approximation of the actual integrity and is safer to use because of that. In a case of large rare-event error, if Gaussianity is assumed, the algorithm may be overconfident and suggest integrity availability when it is not [70].

6.4 Utility of proposed SFC approach

Unlike GNSS and FDE, which can be used globally on any solution, the SFC method requires map data to aid the integrity algorithm. It can be said that the use of SFC is limited in terms of global application. The main goal of this section is to demonstrate what mapping requirements might be in order to utilise the proposed SFC approach.

In most of the research that is using spatial features in Positioning, Navigation and Timing (PNT) applications, spatial features are coming from maps and data sets that are created specifically for those studies, in either real or simulated environments. In this research, a map created specifically for the test area with the added buffer area to account for the assumed 1 m mapping error was used to produce a proof-of-concept (see Section 3.4). Maps like these are often biased since the researchers know exactly what data they need for spatial features, and the collected data might be over-fitted to their specific study (e.g., road lanes, curbs and traffic lights might be captured more accurately and, in more detail, than usual). Although such an approach is good for localised studies and model validation, it is unrealistic to expect it to provide a globally applicable solution because such spatial data sets might not available. In this section, the capabilities of SFC+BRAIM in conjunction with the OpenStreetMap (OSM) will be investigated.

The OSM[2] is a freely available global map data set as a source of spatial features. It is one of the most prominent Volunteered Geographic Information (VGI) projects in existence. As the term VGI [125] suggests, the OSM data is collected and maintained by a community

Section 6.4 was first published a conference paper *Robust vehicle localization and integrity monitoring based on spatial feature constrained PF* published as part of the *2020 IEEE/ION PLANS* conference proceedings ([118] in the bibliography) in *April 2020.* Minor changes have been made to terminology, some text adapted to the thesis.

[2]https://www.openstreetmap.org/

of volunteers that do not have to be geospatial scientists and covers most of the globe with high levels of data completeness - especially in urban environments. Because of that, this map data set was used for extracting the road feature data necessary for SFC.

This study aims to assess the performance of the implementation of SFC+ BRAIM, where the road network data are extracted from the OSM. In order to obtain a realistic insight into the achievable performance of the proposed method data used in the previous sections of this chapter could not have been used. A case study is performed in different environments for real-world Global Positioning System (GPS) data collected in Melbourne, Australia as described previously in Section 3.3.1. These environments represent the typical driving scenarios — driving on a highway, driving in the city (i.e., urban canyon), and driving on the road where the horizon is mostly clear. Although the use of the OSM means that the proposed method can be applied globally, because road features in the OSM are generally represented with the centerline and the number of lanes is stored as a spatial data attribute, the road extents are not readily available. An additional step is needed where the areas of road need to be generated from the available metadata.

This work is significant since it shows the realistically achievable performance of the proposed integrity algorithm (i.e., SFC+BRAIM) on real-world data and for currently available map data. As an alternative, an IM method that utilises the visual data to estimate integrity and maps the environment at the same time could be used. An example of the SLAM-based IM is proposed in [54].

6.4.1 Experimental setup

This section[1] defines the road features using the OSM. The road feature data used in the SFC part of the proposed method have been extracted from the OSM data set for Melbourne. In OSM, roads are represented as linear features (i.e., road centerlines). The number of lanes is stored as a numerical attribute, which means that the road extents are not readily available.

To obtain the road polygons (i.e., spatial features) that are showing the surface area of each road, several steps were performed in this study. First, roads were extracted from the downloaded OSM data set by selecting all linear features for which the *highway* attribute has a value different than *NULL*. Then, the *lanes* and *oneway* attributes of the selected

[1]Table 6.8 and Figures 6.12, 6.13a and 6.13b have been created in collaboration with Ivan Majic, the co-author of [118]. As such, the original paper was cited as the source.

features were analysed to determine the number of lanes for each selected road (Table 6.8). When the value for the *lanes* attribute is missing (i.e., value is *NULL*), the number of lanes is implied by the value of the *oneway* attribute. If both attributes are missing values, in this study it implies that the OSM contributor has mapped a regular two way road with one lane in each direction. This will then imply that the total width of the road is 7 m, since the standard width of the road lane in this study is set to be 3.5 m (i.e., this decision is based on the AustRoads report [10]). If the value for *lanes* is missing, but the value for *oneway* is *yes*, then it is implied that the road is a one-way road with only one lane and the total width of 3.5 m. In all other cases, the total width of the road is calculated by multiplying the width of a lane with the number of *lanes*, and the value of *oneway* is not considered.

TABLE 6.8: Values of the *lanes* and *oneway* attributes of OSM road features, and the implied numbers of lanes and road widths [118].

key: lanes	***key: oneway***	***implied lanes***	***implied road width***
NULL	NULL	2	7 m
NULL	yes	1	3.5 m
1	-	1	3.5 m
2	-	2	7 m
3	-	3	10.5 m
4	-	4	14 m

Finally, to obtain the road polygons, the road centerlines are buffered out by the distance necessary to create a polygon whose width is equal to the total width of the road. Three such polygons were obtained, one for the highway environment trajectory (Figure 6.12), one for the open-sky environment trajectory (Figure 6.13a), and one for the urban canyon environment trajectory (Figure 6.13b). These polygons were then used in SFC+BRAIM as the areas inside which the vehicle is always presumed to be.

6.4.2 Results and discussion

The results are presented individually for each of the three environments and compared to results obtained using only BRAIM. This will be done for only multi-sensor data and under the assumption of Gaussianity for WASP data.

The user's initial state is randomly drawn from the standard normal distribution for N_p particles. Pseudoranges in these experiments are assumed to be normally distributed with the variance estimated based on the satellite elevation as shown in [126]. In cases when

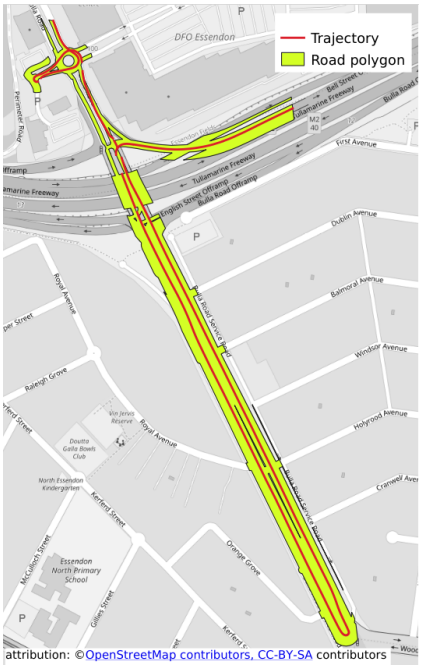
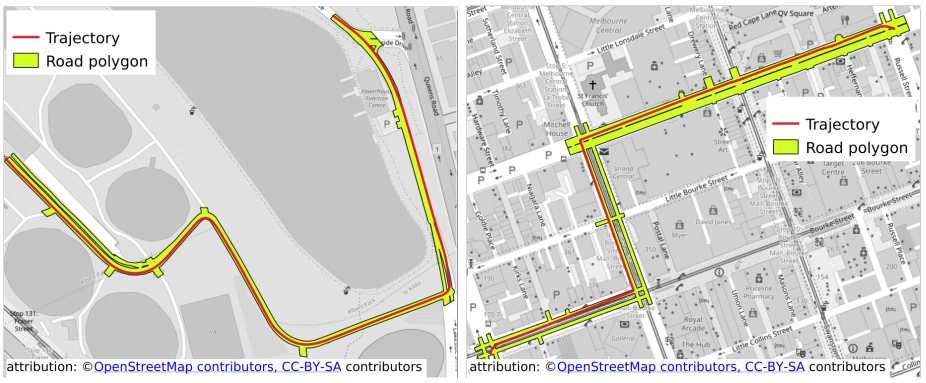


FIGURE 6.12: Trajectory and the road polygon for the highway environment [118].



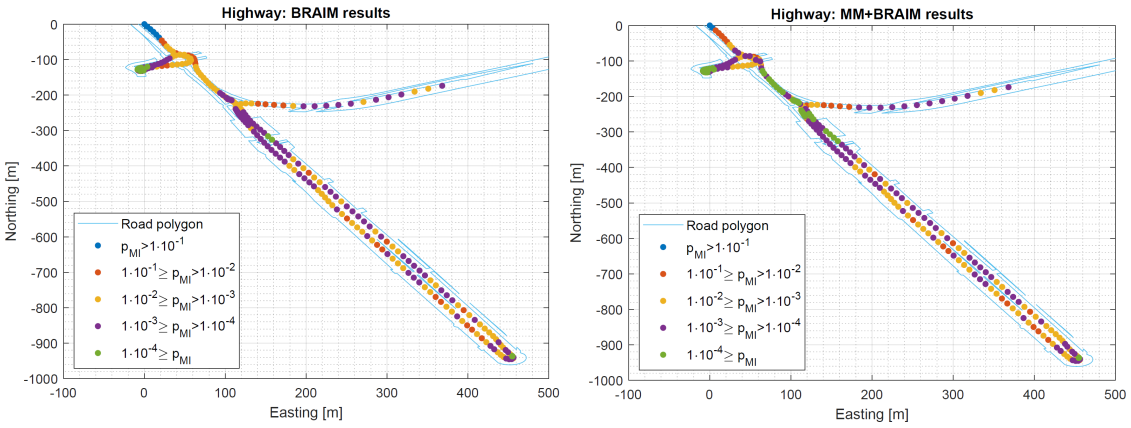
(A) (B)

FIGURE 6.13: Trajectory and the road polygon for the: a) open-sky environment, b) urban canyon. [118]

the elevation information is unavailable (i.e., only in the urban canyon), the variance of $(5.1\ m)^2$ is used. Process noise variances for all particles are randomly drawn from the standard normal distribution at every new timestamp. Every PF was run ten times for 300,000 particles. The experiment parameters used to produce the results are specified in Table 6.1. The results are presented in the local 2D coordinate system. Consequently, HPEs are estimated, and the integrity probability is estimated for road-level HAL (i.e., HAL of 5 m).

Figure 6.14 shows the results of BRAIM and SFC+BRAIM for **highway data**. Each point on the graph represents one point of the vehicle's trajectory at a certain time, with its coordinates shown in a local coordinate system (coordinates are ground truth coordinates).

The value of the position integrity (p_{MI}), i.e., the probability of misleading information, is shown. The colours indicate different levels of estimated integrity which are shown in the legends.



(A) (B)

FIGURE 6.14: Average integrity estimates for each point of the trajectory in the highway environment for: a) BRAIM, b) SFC+BRAIM.

It should be noted that the estimated integrity at each point was calculated as an average of all integrity estimates at that point (i.e., over ten PF iterations that were run). To improve the clarity of the graphs, and due to having multiple sets of estimated positions, graphs were made using ground truth coordinates.

Comparison of Figure 6.14a (BRAIM) and 6.14b (SFC+BRAIM) indicates an overall improvement in the integrity estimate (i.e., the integrity estimate is considered to be improved if the p_{MI} is reduced). This is confirmed in Table 6.9, where median integrity, calculated over all points and for all PF runs, has improved with the SFC+BRAIM algorithm. Median achieved integrity is $2.56 \cdot 10^{-4}$. The best estimate of integrity, or in other words, the smallest probability of misleading information has improved by two orders of magnitude when SFC+BRAIM was used, compared to the BRAIM solution.

TABLE 6.9: Positioning and integrity results for the highway environment

	HPE[m]			p_{MI}		
Alg.	***Average***	***St. dev.***	***Max***	***Median***	***St. dev.***	***Best est.***
BRAIM	0.98	0.72	10.66	$8.68 \cdot 10^{-4}$	0.046	$4.23 \cdot 10^{-5}$
SFC+B	1.30	1.06	10.58	$2.56 \cdot 10^{-4}$	0.034	$7.22 \cdot 10^{-7}$

Figure 6.15 shows the part of the highway trajectory where the vehicle goes through the roundabout, drives south, and upon return from the southeast direction turns right onto

the highway entrance ramp. Please note that these data were collected in Australia, where the traffic is on the left-hand side. The figure shows one of the issues that can occur when real map data are used.As the vehicle is turning onto the ramp, it seems as though the ground truth data has gone off-road. This occurs due to incorrect map data, where the value of the lanes attribute for the road is missing (see Table 6.8). This particular road is attributed as one-way. Since there is no value for the lanes attribute, the algorithm has assumed that there exists only one lane in total. However, since this road is approaching an intersection, in reality, it consists of three lanes - one turning left, one going straight, and one turning right which was taken by the vehicle in this experiment. This is just one example of the issues that can occur when real map data are used for MM or SFC approaches, which surely affects the performance.

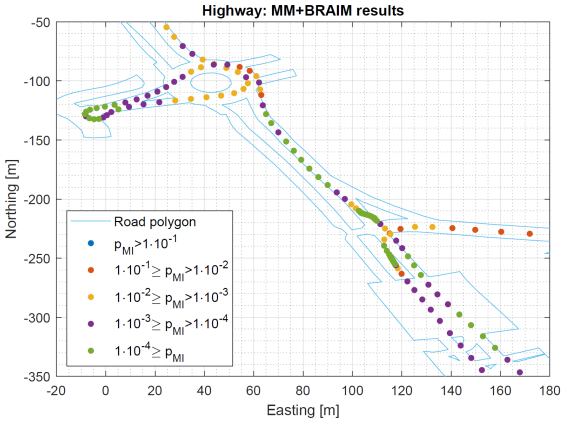
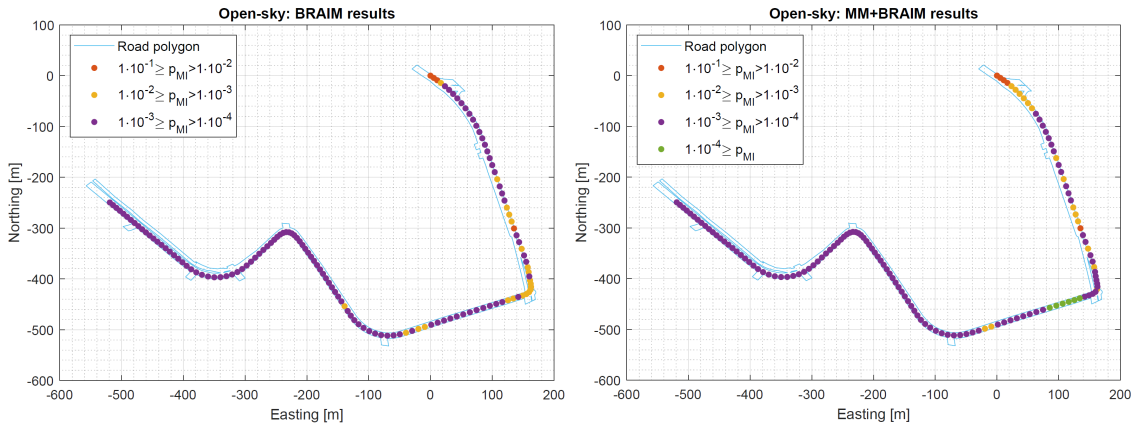


FIGURE 6.15: An example of the error in map data due to incompleteness of attribute data. Only one lane is assumed on a road where three lanes exist.

The performance of BRAIM and SFC+BRAIM for **open-sky environment** is shown in Figure 6.16. Similarly to the highway the data, an overall improvement in integrity can be noticed when comparing the average estimated integrity for all points in Figure 6.16a and 6.16b.

Table 6.10 shows that over all integrity estimates, the median p_{MI} improved slightly and insignificant improvement is visible for the best estimated integrity. It could be concluded that in the case of the open-sky environment, SFC+BRAIM performed similarly to BRAIM.

In the final experiment, performance of data collected in Melbourne's CBD (i.e., **urban canyon**) was tested. As expected, due to the lower quality and availability of measurements (Section 3.3), this data has performed the worst in terms of positioning, and in terms of integrity. Figure 6.17 shows the achieved levels of integrity for each point of

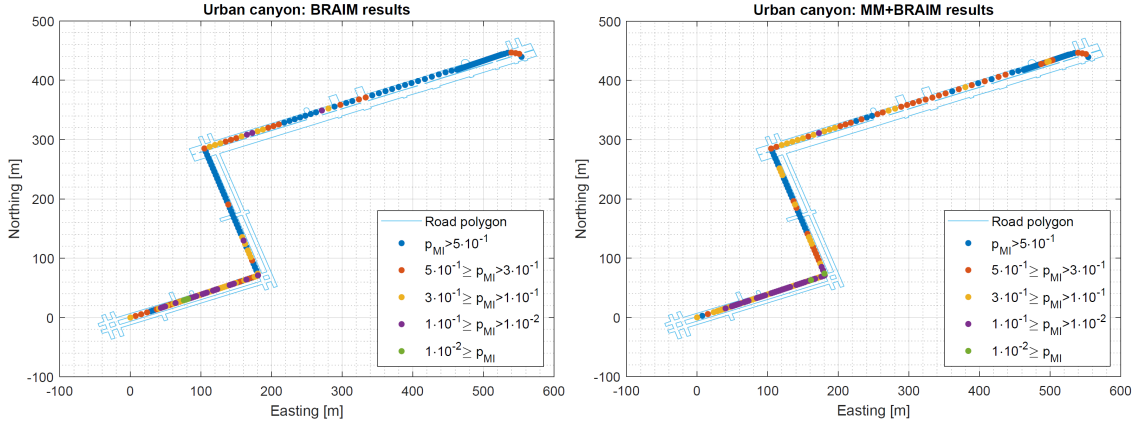


(A) (B)

FIGURE 6.16: Average integrity estimates for each point of the trajectory of open-sky data for: a) BRAIM, b) SFC+BRAIM.

TABLE 6.10: Positioning and integrity results for open-sky environment

	HPE[m]			p_{MI}		
Alg.	***Average***	***St. dev.***	***Max***	***Median***	***St. dev.***	***Best est.***
BRAIM	2.36	0.40	5.05	$5.84 \cdot 10^{-4}$	0.004	$1.63 \cdot 10^{-5}$
SFC+BRAIM	2.35	0.48	6.47	$4.97 \cdot 10^{-4}$	0.008	$1.50 \cdot 10^{-5}$



(A) (B)

FIGURE 6.17: Average integrity estimates for each point of the trajectory of urban canyon data for: a) BRAIM, b) SFC+BRAIM.

trajectory in CBD. Please note that the colours here denote different levels of integrity than before, as there was a need to present lower levels of integrity with more intervals.

Table 6.11 shows that the median integrity has improved slightly, and the best estimated integrity improved by one order of magnitude when SFC+BRAIM was used. However, the average HPE remained around 22 m. Figure 6.18a shows one of the trajectories where, although the estimated positions are not always on the road, the positions generally are

TABLE 6.11: Positioning and integrity results for urban canyon environment

	HPE[m]			p_{MI}		
Alg.	***Average***	***St. dev.***	***Max***	***Median***	***St. dev.***	***Best est.***
BRAIM	22.21	16.53	68.15	$5.48 \cdot 10^{-1}$	0.315	$3.00 \cdot 10^{-3}$
SFC+BRAIM	22.68	17.21	68.41	$3.73 \cdot 10^{-1}$	0.284	$6.68 \cdot 10^{-4}$

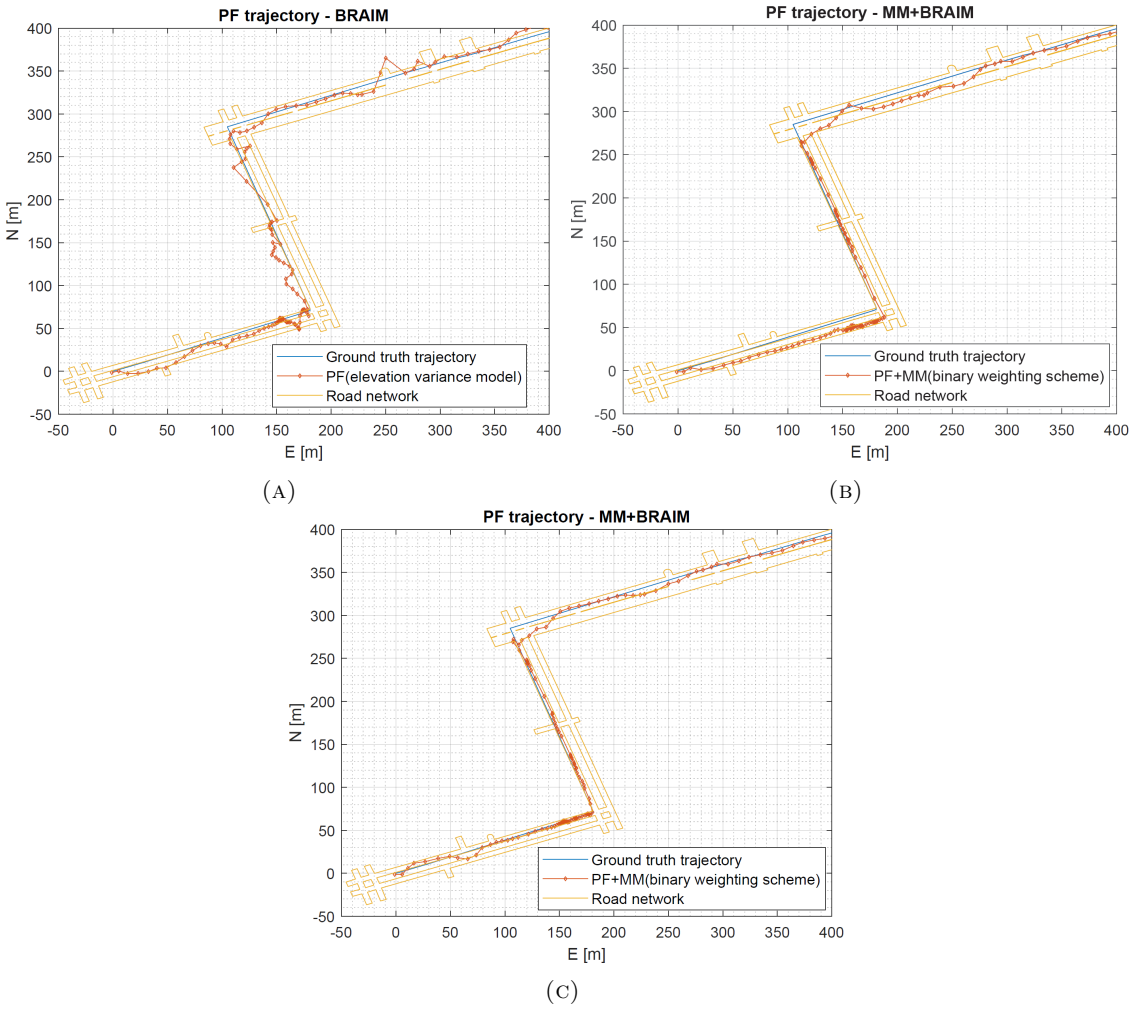


FIGURE 6.18: Examples of the estimated trajectory in urban environment estimated using: a) PF, b) SFC+PF when SFC has taken the vehicle into the wrong direction, and c) SFC+PF when SFC has correctly identified that vehicle is driving in W-E direction.

closer to the left side. This makes sense since, in this case, the vehicle is driving from West to East. However, once SFC is used, due to uncertainty of measurements and the error in the road polygon (two road directions do not meet for a long time at the beginning of the trajectory), the vehicle is sometimes positioned on the wrong side of the road (see Figure 6.18b), and sometimes it is positioned well (see Figure 6.18c). This has affected the HPE, and had the road been mapped better and assigned with correct attributes, the performance would have probably been better. This indicates another issue. As previously

stated, BRAIM summarises weights of all particles within the HAL from the estimated position. SFC increases the weights of the particles that are within the road polygon. If the road is not mapped out well, and the vehicle is positioned within that road, SFC increases the weight of the particles within road boundaries and inadvertently increases the weight of some particles that are not bounded by HAL. Consequently, integrity could be improved when the vehicle is driving in the wrong direction.

6.5 Conclusions

This chapter demonstrated the positioning and integrity performance of the proposed integrity algorithms. Firstly, RAIM and BRAIM algorithms were compared. The improvement of the integrity estimate was observed as the positioning solution became more advanced. The best performance was observed for CP BRAIM for which probabilities of misleading information of $1.75 \cdot 10^{-11}$ (Gaussian assumption) and $3.24 \cdot 10^{-8}$ (GMM) were achieved, for the required HAL of 5 m and IR of $1 \cdot 10^{-7}$.

After the comparison of the RAIM and BRAIM, the performance of the proposed novel FDE+BRAIM, SFC+BRAIM and FDE+SFC+BRAIM algorithms had to be tested. To do this, large errors were injected into the data. When all the measurement error distributions are assumed to be Gaussian, the best median p_{MI} for the CP solution has been observed using the FDE+SFC+BRAIM algorithm, and it was zero. Integrity availability of 100% was achieved in that case. When the Gaussian assumption is not made for WASP ranges, the best median p_{MI} was observed for CP SFC+BRAIM ant that was $5.84 \cdot 10^{-9}$. This is an improvement of one order of magnitude compared to the previously best achieved p_{MI} of $3.24 \cdot 10^{-8}$ for CP solution (even with large injected errors). Compared to the previously best achieved integrity availability of 63.30% for CP BRAIM (no injected errors), CP SFC+BRAIM (with injected errors) achieved 72.07% availability rate.

This analysis pointed to multiple challenges. For example, the FDE method as defined in Section 5.4, seems to not be appropriate for use when a GMM is used for WASP range error distribution. The theoretical background indicates that integrity estimates under the Gaussian assumption for WASP error distribution may be too optimistic. These challenges will be further discussed in the following chapter.

Lastly, this section aimed to demonstrate the utility of the proposed SFC approach. This was done for a different data set than previously used. The results have shown that in good conditions (i.e., good measurements availability and quality), using SFC+BRAIM approach with only GPS data, p_{MI} can be reduced to $2.56 \cdot 10^{-4}$. According to Table 2.5, p_{MI} of $1 \cdot 10^{-4}$ would satisfy the requirements of PCA where the required HAL is looser. These results provide a realistic insight into the issues of using real maps (e.g., missing attribute data, mapping errors) and how these issues can affect the positioning and integrity estimation.

7

Conclusions

This thesis has outlined and demonstrated a systematic process of the distributed cooperative integrity algorithm design for Intelligent Transport Systems (ITS).

The overall research question of this thesis was: "How can the positioning and integrity solution for ITS applications in the urban environment be improved?" That question is answered throughout the thesis by tackling different challenges of integrity monitoring in the urban environment.

First, in Chapter 2, a detailed review of integrity monitoring in the urban environment is given from the perspective of the selected positioning system. The majority of state-of-the-art solutions are based on multi-sensor positioning approaches. There is a consensus amongst researchers that GNSS only solutions are not sufficient for integrity monitoring in the urban environment. Recently, cooperative integrity techniques have gained traction. However, there is still no cooperative integrity method in the literature that provided integrity estimate for all the measurements involved in the cooperative system. This thesis has filled that gap.

For the purposes of this thesis and in accordance with the literature review, the overall research question was broken down into four research questions that have been addressed.

The first research question:**"What positioning system and algorithm will be the basis of the proposed integrity algorithm?"** has been addressed in Chapters 3 and 4. The majority of the available methods are based on the integration of GNSS with IMU, Dead Reckoning sensors or integration with SBAS. However, with the ongoing development of good and low-cost sensors, there are many opportunities for integration with different and non-traditional sensors. Signals of opportunity, such as Wi-Fi, have been receiving much attention in recent years. With the development of technological concepts such as smart cities and the internet of things [127], it is reasonable to assume that signals of opportunity will be widely available in the near future. This thesis has focused on multi-sensor integration of GNSS (more specifically, GPS) and a Local Positioning System that is based on terrestrial ranging to infrastructure. This is expanded to a cooperative solution by adding terrestrial ranging between multiple vehicles in the network. Section 3.2 tests the theoretically best achievable performance of such positioning systems by analysing the Posterior Cramér Rao Bounds (PCRB). With both the average position error and the standard deviation, as well as the PCRBs being under 0.2 m, it was confirmed that the proposed systems (i.e., multi-sensor and cooperative), with the Extended Kalman Filter (EKF) as the position estimator, are capable of achieving a sufficient level of accuracy (under 0.5 m) for road-level and lane-level applications as specified in [10].

Having defined the positioning system to be used in this thesis, the second part of the first question refers to the positioning algorithm (i.e., estimator). The EKF is the most commonly used method of fusing data. If EKF is used as the position estimator, a Gaussian assumption has to be made for measurement error distributions, and if non-linear, the measurement model needs to be linearised. Chapter 4 questions these assumptions and approximations and shows the superior performance of the Particle Filter (PF) (i.e., a non-linear non-Gaussian position estimator used in this thesis). To test the Gaussian assumption, the actual error distribution of the real-world terrestrial ranges measured by Wireless Ad hoc System for Positioning (WASP) units (more in Section 3.4) was fitted with the three-component Gaussian Mixture Model (GMM). GPS pseudorange error distribution was assumed to be Gaussian. Use of the PF showed an improvement of position estimation of 75%. The average position error for multi-sensor PF improved to ~ 0.2 m, which is comparable to the results of PCRB analysis.

Based on the first question, the multi-sensor and cooperative PF was chosen as the underlying positioning systems and the estimator of the integrity algorithms proposed in this thesis. This analysis and the proposed algorithms were the first major contribution of this thesis.

The second research question: **"What level of integrity is achievable with an existing integrity method for stand-alone GNSS and multi-sensor solution?"** has been addressed in Section 3.3. The scale of the integrity problem in the urban environment was investigated from the experimental point of view. The performance of the classical integrity method - Receiver Autonomous Integrity Monitoring (RAIM) was tested for stand-alone GPS data collected on a highway, in the open-sky area, in the suburban area and the urban canyon. Multiple problems have been identified in relation to classical RAIM methods. Firstly, by default, a position integrity estimate was unavailable in the urban canyon almost 50% of the time due to unavailability of redundant measurements. When there are more than four satellites available, integrity could be estimated, but it was classified as unavailable most of the time. Simulated ranges to LPS were integrated with real-world GPS in order to improve the integrity estimate availability (i.e., Can the integrity be estimated in the first place?) and the availability of integrity (i.e., If integrity can be estimated, is it successfully bounded by the integrity requirements?). This showed that the multi-sensor solution successfully mitigates the effect of the urban environment on the GPS measurement availability by ensuring sufficient measurement redundancy required by RAIM. Secondly, because of a rapidly changing environment and, consequently, satellite/user geometry, an integrity method where its bounding of integrity does not depend on the quality of the satellite/user or LPS/user geometry is necessary for the urban environment. Lastly, given the challenges of estimating integrity in the urban environments with methods that depend on the number of measurements, it is necessary to find a method whereby the integrity estimate does not depend on the number of measurements.

These three problems have been used as the guide in designing the novel integrity algorithms. This analysis and use of a multi-sensor solution to mitigate the environmental impact on the integrity estimator was the second major contribution of this thesis.

The third research question: **"Given the identified problems of the existing integrity algorithm in the urban environment, what algorithm can be proposed?"** has been addressed in Chapter 5, and an initial proof-of-concept was provided in Chapter 6.

Given the choice of the position estimator, an integrity method based on the PF had to be used. Bayesian RAIM (BRAIM) proposed in [18] was chosen. However, BRAIM was originally tested on simulated GPS data. In this thesis, that has been expanded to multi-sensor and cooperative positioning solutions and tested on real-world data. Unlike classical RAIM, the BRAIM integrity estimate does not require sufficient measurement redundancy since the integrity is estimated in the position domain based on the *a posteriori* distribution of the estimated position. For the same reason, it does not depend on satellite/user or LPS/user geometry. It also does not require any measurements as the position estimate is always available. However, those integrity estimates would then be based on the *a priori* distribution which would affect the trustworthiness of such estimates.

One of the most important characteristics of BRAIM and similar methods based on a PF is their robustness arising from the use of multiple hypotheses. If every particle is seen as one hypothesis with the assigned weight based on the measurement likelihood, integrity can be estimated by summing the weights of multiple hypotheses since the integrity risk is distributed across many particles. With this, a robust estimate of integrity is provided. Compared to the BRAIM method, the RAIM, in effect, tests a single hypothesis with respect to the presence of faulty measurements.

In addition to the decreased satellite visibility and geometry quality, an important factor making the urban environment challenging for GNSS, are large biases caused by errors such as multipath. A combination of BRAIM and the Fault Detection and Exclusion (FDE) algorithm was proposed to deal with large biases. This FDE+BRAIM is the first novel algorithm proposed in this thesis. The main role of FDE was to minimise the instances of misleading information that can happen due to the large errors. The results indicate that this method was successful in doing that and in improving the overall integrity estimate. The second proposed algorithm in this section was SFC+BRAIM, where BRAIM was paired with Spatial Feature Constraint algorithm. This was implemented to further remove the effect of faulty measurements and to decrease the integrity risk (explained in detail in Section 5.4.2). The SFC method eliminates the particles (i.e., hypotheses) that are not within the spatial feature and by doing that, eliminates the integrity risk associated with those particles. The results also show that this method successfully improved the integrity estimate for both the Gaussian assumptions and the GMM for WASP measurements. The third proposed algorithm was the combination of the previous two — FDE+SFC+BRAIM aiming to further improve the integrity.

Three novel integrity algorithms have been proposed, and initial algorithm validation was carried out. With that, the third major contribution of this research was made. The fourth major contribution is the implementation of the first fully connected, distributed cooperative integrity method. Unlike other methods, the integrity performance was quantified, and the integrity estimate is based on all the measurements from the cooperative positioning system.

Lastly, the fourth research question: **"What is the best achievable integrity for multi-sensor and cooperative system based on Particle Filter?"** was addressed in Chapter 6. Although cooperative FDE+SFC+BRAIM (Gaussianity assumed for WASP data) achieved the best performance in terms of the numerically smallest estimated probability of misleading information, that cannot be considered the best achieved performance. This is an important conclusion as it directly refers to the trustworthiness of the integrity estimate. Since GMM (fitted for WASP data) is a better fit than the Gaussian distribution, it should represent random errors more appropriately, which is exactly what every integrity algorithm should aim for. According to [70], in a case of large rare-event error, if Gaussianity is assumed, the algorithm may be overconfident and suggest integrity availability when it is not. Hence, it could be said that the results related to the Gaussian assumption are too optimistic and may lead to hazardously misleading information. The best performance was achieved for cooperative SFC+BRAIM when GMM is used as the distribution of the WASP measurement errors. That method achieved the median probability of misleading information of $5.84 \cdot 10^{-9}/epoch$ for the horizontal alarm limit of 5 m and integrity risk of $1 \cdot 10^{-7}/epoch$. That is one order of magnitude of median integrity improvement, compared to the cooperative BRAIM where the median probability of misleading information of $5.996 \cdot 10^{-8}/epoch$ was achieved. A similar improvement was observed when compared with the best performance of the multi-sensor solution (i.e., multi-sensor FDE+SFC+BRAIM).

7.1 Future work

Integrity algorithms and integrity monitoring algorithms are complex, and they have to account for many factors relating to the urban environment. A complete solution to the integrity problem of the ITS has not been proposed yet. This thesis has addressed multiple issues of integrity in the urban environment. However, some challenges remain to be solved in future research that would make integrity monitoring practical and useful

for ITS. The main areas of improvement are the development of more robust positioning systems based on various sensors, improving distributed cooperative integrity methods and designing algorithms capable of overcoming limits of integrity performance relative to the theoretical bounds. Additionally, the vertical integrity component needs to be developed for the integrity methods proposed in this thesis. The availability of 3D integrity will be a key requirement when traffic in cities becomes three dimensional[1] and 3D city maps become more prominent.

Firstly, given their availability on the vehicle, IMU and dead reckoning data will be utilised to improve the positioning and integrity performance. Multi-GNSS data should be utilised as well. Literature has shown that use of multi-GNSS improves integrity estimates. As indicated in Section 6.4, a method like Simultaneous Localisation And Mapping (SLAM) could be utilised to avoid the issue of erroneous or incomplete maps.

As mentioned throughout this thesis, the goal was to achieve road-level integrity. Because of this focus, only code pseudorange GPS measurements were used. The literature (see Chapter 2) indicates that it is necessary to use (N)RTK or PPP GNSS methods in order to achieve higher levels of integrity — lane-level and where-in-the-lane. Consequently, future improvements to the proposed algorithms will also include the use of more precise GNSS measurements such as NRTK or PPP.

FDE has been discussed in this thesis. When Gaussianity was assumed, a simple FDE method was successful in improving integrity estimate. However, when it came to the GMM used for WASP data, the FDE method was not appropriate as it required the Gaussian assumption. Solving this issue is out of the scope of this thesis as it would require substantial additional research. As demonstrated in the literature review, development of the FDE methods for the purpose of integrity monitoring is a field of research in itself. When it comes to algorithmic improvements, the biggest improvement to the methods proposed in this thesis would be to develop an FDE method tailored for non-linear non-Gaussian measurements.

The proposed algorithms have the potential to be run in real-time. However, they would have to be optimised for speed and/or use higher performance processing hardware.

The algorithms proposed in this thesis have been validated on real data. However, to fully understand an integrity algorithm, it would need to be validated on millions of data and

[1] https://www.abc.net.au/news/2020-02-28/uber-air-plans-for-1000-strong-melbourne-helicopter-fleet/12007092

for real-life scenarios in traffic. This would potentially bring out additional issues and aid the robustness of the proposed methods. The collection of additional data would also aid further error modelling and enable improved evaluation of the performance.

Bibliography

[1] A Auer, F Feese, and S Lockwood. History of Intelligent Transportation Systems. Technical Report FHWA-JPO-16-329, U.S. Department of Transportation, 2016. URL https://www.its.dot.gov/history/offline/download.pdf.

[2] SAE International. Taxonomy and definitions for terms related to driving automation systems for on-road motor vehicles. Technical report, 2016. doi: 10.4271/J3016_201806.

[3] WY Ochieng, K Sauer, D Walsh, G Brodin, S Griffin, and M Denney. GPS integrity and potential impact on aviation safety. *Journal of Navigation*, 56(1):51—-65, 2003. doi: 10.1017/S0373463302002096.

[4] European GNSS Agency. Report on the performance and level of integrity for safety and liability critical multi-applications. Technical report, 2015. URL https://www.gsa.europa.eu/sites/default/files/calls_for_proposals/Annex%202.pdf.

[5] D Imparato, A El-Mowafy, and C Rizos. Integrity monitoring: From airborne to land applications. In RB Rustamov and AM Hashimov, editors, *Multifunctional Operation and Application of GPS*, chapter 2, pages 23–43. IntechOpen, 2018. doi: 10.5772/intechopen.75777.

[6] European GNSS Agency. GSA GNSS Market Report, Issue 6. Technical report, 2018. doi: 10.2878/031762.

[7] T Li, H Zhang, X Niu, and Z Gao. Tightly-coupled integration of multi-GNSS single-frequency RTK and MEMS-IMU for enhanced positioning performance. *Sensors*, 17 (11):2462, October 2017. doi: 10.3390/s17112462.

[8] T Li, H Zhang, Z Gao, Q Chen, and X Niu. High-accuracy positioning in urban environments using single-frequency multi-GNSS RTK/MEMS-IMU integration. *Remote Sensing*, 10(2):205, January 2018. doi: 10.3390/rs10020205.

[9] N Alam and AG Dempster. Cooperative positioning for vehicular networks: Facts and future. *IEEE Transactions on Intelligent Transportation Systems*, 14(4):1708–1717, December 2013. doi: 10.1109/TITS.2013.2266339.

[10] ARRB Project Team. Vehicle positioning for C-ITS in Australia (background document). Technical Report Austroads Publication AP-R431-13, Austroads, 2013. URL https://austroads.com.au/publications/connected-and-automated-vehicles/ap-r431-13.

[11] E Smith, JW Cheong, and A Dempster. Integrity monitoring methods for cooperative Intelligent Transport Systems. In *Proceedings of the International Global Navigation Satellite Systems Association IGNSS Symposium 2016*, Sydney, NSW, Australia, December 2016. URL http://www.ignss2016.unsw.edu.au/sites/ignss2016/files/u80/Papers/non-reviewed/IGNSS2016_paper_30.pdf.

[12] DA Grejner-Brzezinska, CK Toth, T Moore, JF Raquet, MM Miller, and A Kealy. Multisensor navigation systems: A remedy for GNSS vulnerabilities? *Proceedings of the IEEE*, 104(6):1339–1353, June 2016. doi: 10.1109/JPROC.2016.2528538.

[13] G Retscher, A Kealy, J Gabela, Y Li, S Goel, CK Toth, A Masiero, W Błaszczak-Bak, V Gikas, H Perakis, Z Koppanyi, and DA Grejner-Brzezinska. A benchmarking measurement campaign in GNSS-denied/challenged indoor/outdoor and transitional environments. *Journal of Applied Geodesy*, 14(2):215–229, 2020. doi: 10.1515/jag-2019-0031.

[14] P Schwarzbach, A Michler, P Tauscher, and O Michler. An empirical study on V2X enhanced low-cost GNSS cooperative positioning in urban environments. *Sensors*, 19(23):5201, November 2019. doi: 10.3390/s19235201.

[15] D Salós, A Martineau, C Macabiau, B Bonhoure, and D Kubrak. Receiver Autonomous Integrity Monitoring of GNSS Signals for electronic toll collection. *IEEE Transactions on Intelligent Transportation Systems*, 15(1):94–103, February 2014. doi: 10.1109/TITS.2013.2273829.

[16] B Hofmann-Wellenhof, H Lichtenegger, and J Collins. *Global Positioning System: Theory and practice*. Springer-Verlag Wien, 2001. ISBN 978-3-211-83534-0.

[17] N Zhu, J Marais, D Bétaille, and M Berbineau. GNSS position integrity in urban environments: A review of literature. *IEEE Transactions on Intelligent Transportation Systems*, 19(9):2762–2778, January 2018. doi: 10.1109/TITS.2017.2766768.

[18] H Pesonen. A framework for Bayesian Receiver Autonomous Integrity Monitoring in urban navigation. *Navigation: Journal of The Institute of Navigation*, 58(3): 229–240, Fall 2011. doi: 10.1002/j.2161-4296.2011.tb02583.x.

[19] AK Brown. Civil aviation integrity requirements for the Global Positioning System. *Navigation, Journal of The Institute of Navigation*, 35(1):23–40, Spring 1988. doi: 10.1002/j.2161-4296.1988.tb00938.x.

[20] Imparato, D. *GNSS-based Receiver Autonomous Integrity Monitoring for aircraft navigation*. PhD thesis, Technische Universiteit Delft, Delft, Netherlands, April 2016. URL https://repository.tudelft.nl/islandora/object/uuid%3Aa5e5f5be-b1a6-42c2-b285-a4ff01e5bfd2.

[21] R Grover Brown. A baseline GPS RAIM scheme and a note on the equivalence of three RAIM methods. *Navigation, Journal of The Institute of Navigation*, 39(3): 301–316, Fall 1992. doi: 10.1002/j.2161-4296.1992.tb02278.x.

[22] J Gabela, A Kealy, M Hedley, and W Moran. Case study of Bayesian RAIM algorithm integrated with Spatial Feature Constraint and Fault Detection and Exclusion algorithms for multi-sensor positioning. *Navigation, Journal of Institute of Navigation*, 68(2):333–351, Summer 2021. doi: 10.1002/navi.433.

[23] B Roturier, E Chatre, and J Ventura-Traveset. The SBAS integrity concept standardised by ICAO. Application to EGNOS. In *Proceedings of the GNSS 2001*, Sevilla, Spain, May 2001.

[24] C Milner, C Macabiau, and P Thevenon. Bayesian inference of GNSS failures. *Journal of Navigation*, 69(2):277—-294, March 2016. doi: 10.1017/S0373463315000697.

[25] Australian Government. Civil Aviation Safety Authority. Global Navigation Satellite Systems (GNSS). In *CNS/ATM Resource guide*, chapter 3, pages 24–41. 2017. ISBN 978-1-921475-46-7.

[26] Y Jiang and J Wang. A new approach to calculate the Vertical Protection Level in A-RAIM. *Journal of Navigation*, 67(4):711—725, 2014. doi: 10.1017/S0373463314000204.

[27] BS Pervan. *Navigation integrity for aircraft precision landing using the Global Positioning System* . PhD thesis, Stanford University, Stanford, CA, USA, March 1996. URL https://trove.nla.gov.au/work/32958146.

[28] J Chang, X Zhan, and Y Zhai. Real-time integrity monitoring for civil aviation with improved navigation performance. In Z Jing, editor, *Proceedings of the International Conference on Aerospace System Science and Engineering 2019. ICASSE 2019. Lecture Notes in Electrical Engineering*, volume 622, pages 107–127. Springer, Singapore, March 2020. doi: 10.1007/978-981-15-1773-0_9.

[29] L Vidarsson, S Pullen, G Green, and P Enge. Satellite Autonomous Integrity Monitoring and its role in enhancing GPS user performance. In *Proceedings of ION GPS*, pages 690–702, Salt Lake City, UT, USA, September 2001.

[30] I Rodríguez, C Garc'ia, C Catal'an, A Mozo, P Tavella, L Galleani, P Rochat, Q Wang, and F Amarillo. Satellite Autonomous Integrity Monitoring (SAIM) for GNSS systems. In *Proceedings of the 22nd International Technical Meeting of the Satellite Division of The Institute of Navigation (ION GNSS 2009)*, pages 1330–1342, Savannah, GA, USA, September 2009.

[31] International Maritime Organization. Revised maritime policy and requirements for a future Global Navigation Satellite System (GNSS). Technical Report Resolution A.915(22), 2001. URL https://wwwcdn.imo.org/localresources/en/KnowledgeCentre/IndexofIMOResolutions/AssemblyDocuments/A.915(22).pdf.

[32] Acil Allen consulting. Precise positioning services in the maritime sector: An estimate of the economic and social benefits of the use of augmented positioning services in the maritime sector). Technical report, 2013. URL http://www.ignss.org/LinkClick.aspx?fileticket=b%2F3x6KEaFS4%3D&tabid=56.

[33] J Beugin, F Aleš, J Marais, and M Berbineau. Galileo for railway operations: question about the positioning performances analogy with the RAMS requirements allocated to safety applications. *European Transport Research Review*, 2:93–102, May 2010. doi: 10.1007/s12544-010-0032-3.

[34] P Brocard, O Julien, and M Mabilleau. Autonomous integrity monitoring proposal for critical rail applications. In *Proceedings of the 28th International Technical Meeting of the Satellite Division of The Institute of Navigation (ION GNSS+ 2015)*, pages 706–734, Tampa, FL, USA, September 2015.

[35] A Filip, J Taufer, H Mocek, L Baant, and V Maixner. The high integrity GNSS/INS based train position locator. *WIT Transactions on the Built Environment*, 74:497–506, 2004. doi: 10.2495/CR040511.

[36] ASTRAIL Consortium. Proposed GNSS minimum performance requirements. Technical Report Resolution A.915(22), 2019. URL https://projects.shift2rail.org/download.aspx?id=2795b653-8301-43ed-a563-b5334d194d53.

[37] DC Bruckner. *On the treatment of noise and conspiring bias in dual-frequency differential Global Navigation Satellite Systems.* the School of Electrical Engineering and Computer Science and the Russ College of Engineering and Technology of Ohio University, Athens, OH, USA, March 2010. Ph.D. Thesis.

[38] A Martineau. *Performance of Receiver Autonomous Integrity Monitoring (RAIM) for vertically guided approaches.* PhD thesis, National Polytechnic Institute of Toulouse, Toulouse, France, November 2008. URL https://tel.archives-ouvertes.fr/tel-02064255.

[39] CD Salós Andrés. *Integrity monitoring applied to the reception of GNSS signals in urban environments.* PhD thesis, National Polytechnic Institute of Toulouse, Toulouse, France, July 2012. URL https://tel.archives-ouvertes.fr/tel-02064255.

[40] SM Kay. *Fundamentals of statistical processing, Volume I: Estimation theory.* Prentice-Hall, Inc., 1993. doi: 10.5555/151045.

[41] P Zabalegui, G De Miguel, A Pérez, J Mendizabal, J Goya, and I Adin. A review of the evolution of the integrity methods applied in GNSS. *IEEE Access*, 8:45813–45824, March 2020. doi: 10.1109/ACCESS.2020.2977455.

[42] N Zhu, D Betaille, J Marais, and M Berbineau. GNSS integrity enhancement for urban transport applications by error characterization and Fault Detection and Exclusion (FDE). In *Proceedings of the Géolocalisation et Navigation dans l'Espace et le Temps, Journées Scientifiques 2018 de l'URSI*, Paris, France, March 2018.

[43] T Binjammaz. *Context-aware GPS integrity monitoring for Intelligent Transport Systems.* PhD thesis, De Montfort University, Leicester, United Kingdom, Spring 2015. URL https://dora.dmu.ac.uk/handle/2086/11397.

[44] TA Binjammaz, AH Al-Bayatti, and AH Al-Hargan. Context-aware GPS integrity monitoring for Intelligent Transport Systems. *Journal of Traffic and Transportation Engineering (English Edition)*, 3(1):1–15, 2016. doi: 10.1016/j.jtte.2015.09.002.

[45] NR Velaga, MA Quddus, AL Bristow, and Y Zheng. Map-aided integrity monitoring of a land vehicle navigation system. *IEEE Transactions on Intelligent Transportation Systems*, 13(2):848–858, March 2012. doi: 10.1109/TITS.2012.2187196.

[46] J Santa, B Ubeda, R Toledo, and AFG Skarmeta. Monitoring the position integrity in road transport Localization Based Services. In *Proceedings of the IEEE Vehicular Technology Conference*, Montreal, Que., Canada, Sept 2006. doi: 10.1109/VTCF.2006.575.

[47] NA Tmazirte, MEE Najjar, C Smaili, and D Pomorski. Multi-sensor data fusion based on information theory. Application to GNSS positioning and integrity monitoring. In *Proceedings of the 2012 15th International Conference on Information Fusion*, pages 743–749, July 2012.

[48] E Wang, T Pang, Z Zhang, and P Qu. GPS Receiver Autonomous Integrity Monitoring algorithm based on Improved Particle Filter. *Journal of Computers*, 9(9): 2066–2074, September 2014. doi: 10.4304/jcp.9.9.2066-2074.

[49] A Angrisano, S Gaglione, and C Gioia. RAIM algorithms for aided GNSS in urban scenario. In *Proceedings of the 2012 Ubiquitous Positioning, Indoor Navigation, and Location Based Service (UPINLBS)*, pages 1–9, Helsinki, Finland, October 2012. doi: 10.1109/UPINLBS.2012.6409786.

[50] Y Yang and J Xu. GNSS receiver autonomous integrity monitoring (RAIM) algorithm based on robust estimation. *Geodesy and Geodynamics*, 7(2):117–123, March 2016. doi: 10.1016/j.geog.2016.04.004.

[51] R. Toledo-Moreo, M. A. Zamora-Izquierdo, B. Ubeda-Minarro, and A. F. Gomez-Skarmeta. High-integrity imm-ekf-based road vehicle navigation with low-cost gps/sbas/ins. *IEEE Transactions on Intelligent Transportation Systems*, 8(3):491–511, September 2007. doi: 10.1109/TITS.2007.902642.

[52] M Maaref, J Khalife, and ZM Kassas. Integrity monitoring of LTE signals of opportunity-based navigation for autonomous ground vehicles. In *Proceedings of the 31st International Technical Meeting of the Satellite Division of The Institute of Navigation (ION GNSS+ 2018)*, pages 2456–2466, Miami, FL, USA, September 2018.

[53] M Maaref and ZM Kassas. Autonomous integrity monitoring for vehicular navigation with cellular signals of opportunity and an IMU. *IEEE Transactions on Intelligent*

Transportation Systems, 2020. URL http://kassas.eng.uci.edu/papers/Kassas_Autonomous_integrity_monitoring_for_vehicular_navigation_with_cellular_signals_of_opportunity_and_an_IMU.pdf. Submitted for publication. Currently available as non-refereed publication.

[54] S Bhamidipati and GX Gao. Integrity monitoring of Graph-SLAM using GPS and fish-eye camera. *Navigation: Journal of The Institute of Navigation*, 67(3):583–600, Fall 2020. doi: 10.1002/navi.381.

[55] E Shytermeja, A Garcia-Pena, and O Julien. Proposed architecture for integrity monitoring of a GNSS/MEMS system with a Fisheye camera in urban environment. In *Proceedings of the International Conference on Localization and GNSS 2014 (ICL-GNSS 2014)*, pages 1–6, June 2014. doi: 10.1109/ICL-GNSS.2014.6934179.

[56] S Gupta and GX Gao. Particle RAIM for integrity monitoring. In *Proceedings of the 32nd International Technical Meeting of the Satellite Division of The Institute of Navigation (ION GNSS+ 2019)*, pages 811–826, Miami, FL, USA, September 2019. doi: 10.33012/2019.16939.

[57] R Toledo-Moreo, D Betaille, and F Peyret. Lane-level integrity provision for navigation and Map Matching with GNSS, dead reckoning, and enhanced maps. *IEEE Transactions on Intelligent Transportation Systems*, 11(1):100–112, October 2010. doi: 10.1109/TITS.2009.2031625.

[58] K Gunning, J Blanch, T Walter, L de Groot, and L Norman. Integrity for tightly coupled PPP and IMU. In *Proceedings of the 32nd International Technical Meeting of the Satellite Division of The Institute of Navigation (ION GNSS+ 2019)*, pages 3066–3078, Miami, FL, USA, September 2019. doi: 10.33012/2019.17011.

[59] C Tanil, S Khanafseh, M Joerger, B Kujur, B Kruger, L de Groot, and B Pervan. Optimal INS/GNSS coupling for autonomous car positioning integrity. In *Proceedings of the 32nd International Technical Meeting of the Satellite Division of The Institute of Navigation (ION GNSS+ 2019)*, pages 3123–3140, Miami, FL, USA, September 2019.

[60] L Norman, E Infante, and L de Groot. Integrity performance for precise positioning in automotive. In *Proceedings of the 32nd International Technical Meeting of the Satellite Division of The Institute of Navigation (ION GNSS+ 2019)*, pages 1653–1663, Miami, FL, USA, September 2019.

[61] A El-Mowafy and N Kubo. Integrity monitoring of vehicle positioning in urban environment using RTK-GNSS, IMU and speedometer. *Measurement Science and Technology*, 28(5):055102, March 2017. doi: 10.1088/1361-6501/aa5c66.

[62] A El-Mowafy and N Kubo. Integrity monitoring for positioning of Intelligent Transport Systems using integrated RTK-GNSS, IMU and vehicle odometer. *IET Intelligent Transport Systems*, 12(8):901–908, September 2018. doi: 10.1049/iet-its.2018.0106.

[63] J Xiong, JW Cheong, Z Xiong, AG Dempster, S Tian, and R Wang. Integrity for multi-sensor cooperative positioning. *IEEE Transactions on Intelligent Transportation Systems*, pages 1–16, December 2019. doi: 10.1109/TITS.2019.2956936. Early Access.

[64] J Xiong, JW Cheong, AG Dempster, and Z Xiong. An integrity monitoring method for multi-sensor collaborative navigation. In *Proceedings of the 2020 IEEE/ION Position, Location and Navigation Symposium (PLANS*, pages 461–468, Portland, OR, USA, April 2020.

[65] J Liu, C Rizos, and BG Cai. Integrity monitoring of vehicle positioning using cooperative measurements under connected vehicles environments. In *Proceedings of the International Global Navigation Satellite Systems Association IGNSS Symposium 2018*, Sydney, NSW, Australia, February 2018. URL http://www.ignss2018.unsw.edu.au/sites/ignss2018/files/u80/Papers/IGNSS2018_paper_31.pdf.

[66] J Liu, B Cai, J Wang, and D Lu. Error bound estimation of cooperative vehicle localization using an integrity concept. In *Proceedings of the2015 International Conference on Connected Vehicles and Expo (ICCVE)*, pages 220–225, Shenzhen, China, October 2015. doi: 10.1109/ICCVE.2015.11.

[67] J Liu, X Wu, and B Cai. An improved GNSS Receiver Autonomous Integrity Monitoring method using Vehicle-to-Vehicle communication. In *Proceedings of the Second International Conference on Internet of Vehicles - Safe and Intelligent Mobility - Volume 9502*, pages 249—-260. Springer-Verlag, December 2015. doi: 10.1007/978-3-319-27293-1_22.

[68] J Liu, M Wang, B Cai, D Lu, and J Wang. A local integrity modeling method for GNSS under cooperative environments. In *Proceedings of the 2017 Chinese*

Automation Congress (CAC), pages 6290–6295, Jinan, China, October 2017. doi: 10.1109/CAC.2017.8243911.

[69] J Liu and B Cai. Cooperative integrity monitoring for vehicle localization: A GNSS/DSRC integrated approach. In C Gao, G Zhao, and H Fourati, editors, *Cooperative Localization and Navigation: Theory, Research, and Practice*, chapter 21, pages 425–436. Taylor & Francis Group, August 2019. doi: 10.1201/9780429507229-21.

[70] J Liu, C Rizos, and B Cai. A hybrid integrity monitoring method using vehicular wireless communication in difficult environments for GNSS. *Vehicular Communications*, 23:100229, June 2020. doi: 10.1016/j.vehcom.2019.100229.

[71] C Zhuang, H Zhao, S Hu, C Sun, and W Feng. Integrity monitoring algorithm for GNSS-based cooperative positioning applications. In *Proceedings of the 32nd International Technical Meeting of the Satellite Division of The Institute of Navigation (ION GNSS+ 2019)*, pages 2008–2022, Miami, FL, USA, September 2019. doi: 10.33012/2019.16881.

[72] S Bhamidipati and GX Gao. Distributed cooperative SLAM-based integrity monitoring via a network of receivers. In *Proceedings of the 32nd International Technical Meeting of the Satellite Division of The Institute of Navigation (ION GNSS+ 2019)*, pages 2023–2034, Miami, FL, USA, September 2019. doi: 10.33012/2019.16882.

[73] D Margaria, E Falletti, and T Acarman. The need for GNSS position integrity and authentication in ITS: Conceptual and practical limitations in urban contexts. In *Proceedings of the 2014 IEEE Intelligent Vehicles Symposium Proceedings*, pages 1384–1389, Dearborn, MI, USA, June 2014. doi: 10.1109/IVS.2014.6856485.

[74] J Gabela, S Goel, A Kealy, M Hedley, W Moran, and S Williams. Cramér Rao Bound analysis for cooperative positioning in Intelligent Transportation Systems. In *Proceedings of the International Global Navigation Satellite Systems Association IGNSS Symposium 2018*, Sydney, NSW, Australia, February 2018. URL http://www.ignss2018.unsw.edu.au/sites/ignss2018/files/u80/Papers/IGNSS2018_paper_21.pdf.

[75] SE Shladover and SK Tan. Analysis of vehicle positioning accuracy requirements for communication-based cooperative collision warning. *Journal of Intelligent Transportation Systems: Technology, Planning, and Operations*, 10(3):131–140, 2006. doi: 10.1080/15472450600793610.

[76] S Goel, A Kealy, and B Lohani. Cooperative UAS localization using low cost sensors. In *Proceedings of the ISPRS Annals of Photogrammetry, Remote Sensing and Spatial Information Sciences*, volume III-1, pages 183–190, Prague, Czech Republic, June 2016. doi: 10.5194/isprs-annals-III-1-183-2016.

[77] F Sottile, H Wymeersch, MA Caceres, and MA Spirito. Hybrid GNSS-terrestrial cooperative positioning based on Particle Filter. In *Proceedings of the 2011 IEEE Global Telecommunications Conference - GLOBECOM 2011*, pages 1–5, Houston, TX, USA, December 2011. doi: 10.1109/GLOCOM.2011.6134002.

[78] MR Gholami, S Gezici, and EG Ström. Improved position estimation using hybrid TW-TOA and TDOA in cooperative networks. *IEEE Transactions on Signal Processing*, 60(7):3770–3785, April 2012. doi: 10.1109/TSP.2012.2194705.

[79] EG Larsson. Cramér–Rao Bound analysis of distributed positioning in sensor networks. *IEEE Signal Processing Letters*, 11(3):334–337, April 2004. doi: 10.1109/LSP.2003.822899.

[80] F Penna, MA Caceres, and H Wymeersch. Cramér–Rao Bound for hybrid GNSS-terrestrial cooperative positioning. *IEEE Communications Letters*, 14(11):1005–1007, September 2010. doi: 10.1109/LCOMM.2010.091310.101060.

[81] JH Taylor. The Cramér–Rao estimation error lower bound computation for deterministic nonlinear systems. *IEEE Transactions on Automatic Control*, 24(2):343–344, April 1979. doi: 10.1109/TAC.1979.1101979.

[82] DC Popescu, M Hedley, and T Sathyan. Posterior Cramér–Rao Bound for anchorless tracking. *IEEE Signal Processing Letters*, 20(12):1183–1186, October 2013. doi: 10.1109/LSP.2013.2284598.

[83] T Baybura, İ Tiryakioğlu, MA Uğur, Hİ Solak, and Ş Şafak. Examining the accuracy of Network RTK and Long Base RTK methods with repetitive measurements. *Journal of Sensors*, 2019, November 2019. doi: 10.1155/2019/3572605.

[84] J Gabela, A Kealy, X Bachelet, W Moran, and M Hedley. Evaluation of integrity availability based on classic RAIM in different urban environments for stand-alone GPS and multi-sensor solutions. In *Proceedings of the International Global Navigation Satellite Systems Association IGNSS Symposium 2020*, Sydney, NSW, Australia, February 2020. URL http://www.ignss2020.unsw.edu.au/sites/ignss2020/files/uploads/proceedings/papers/paper_20.pdf.

[85] HT Tran and L Lo Presti. Kalman filter-based ARAIM algorithm for integrity monitoring in urban environment. *Information & Communications Technology Express*, 5(1):65–71, March 2019. doi: 10.1016/j.icte.2018.05.002.

[86] Leica Geosystems AG. Leica Viva GS15 Data sheet. Technical report, 2015. URL https://w3.leica-geosystems.com/downloads123/zz/gpsgis/viva%20gs15/brochures-datasheet/leica_viva_gs15_ds_en.pdf.

[87] J Wang, N Knight, and X Lu. Impact of the GNSS time offsets on positioning reliability. *Journal of Global Positioning Systems*, 10:165–172, 2011. doi: 10.5081/JGPS.10.2.165.

[88] J Gabela, E Smith, S Li, A Kealy, M Hedley, W Ni, A Dempster, and JW Cheong. A measurement campaign for cooperative positioning architecture based on GNSS and local positioning system. In *Proceedings of the International Global Navigation Satellite Systems Association IGNSS Symposium 2020*, Sydney, NSW, Australia, February 2020. URL http://www.ignss2020.unsw.edu.au/sites/ignss2020/files/uploads/proceedings/papers/paper_29.pdf.

[89] E Domínguez, G Seco-Granados, J Salcedo, D Egea, E Aguado, D Lowe, D Naberezhnykh, F Dovis, JP Boyero, and I Fernandez. Characterization of GNSS integrity threats in terrestrial applications using real signal captures. In *Proceedings of the 27th International Technical Meeting of The Satellite Division of the Institute of Navigation (ION GNSS+ 2014)*, pages 954–966, Tampa, FL, USA, September 2014.

[90] T Sathyan, D Humphrey, and M Hedley. WASP: A system and algorithms for accurate radio localization using low-cost hardware. *IEEE Transactions on Systems, Man, and Cybernetics, Part C (Applications and Reviews)*, 41(2):211–222, March 2011. doi: 10.1109/TSMCC.2010.2051027.

[91] Decawave. Decawave product brief: MDEK1001. Technical report, 2017. URL https://www.decawave.com/mdek1001/productbrief/.

[92] J Gabela, A Kealy, S Li, M Hedley, W Moran, W Ni, and S Williams. The effect of linear approximation and Gaussian noise assumption in multi-sensor positioning through experimental evaluation. *IEEE Sensors Journal*, 19(22):10719–10727, November 2019. doi: 10.1109/JSEN.2019.2930822.

[93] A Fowler and PJ Van Leeuwen. Observation impact in data assimilation: the effect of non-Gaussian observation error. *Tellus A: Dynamic Meteorology and Oceanography*, 65(1):20035, June 2013. doi: 10.3402/tellusa.v65i0.20035.

[94] S Li, M Hedley, and IB Collings. New efficient indoor cooperative localization algorithm with empirical ranging error model. *IEEE Journal on Selected Areas in Communications*, 33(7):1407–1417, July 2015. doi: 10.1109/JSAC.2015.2430273.

[95] D Yu and L Deng. Gaussian Mixture Models. In *Automatic Speech Recognition: A deep learning approach*, chapter 2, pages 13–21. Springer, London, November 2014. doi: 10.1007/978-1-4471-5779-3_2.

[96] RE Kalman and RS Bucy. New results in linear filtering and prediction theory. *Journal of Basic Engineering Transactions ASME*, 83(1):95–108, March 1961. doi: doi:10.1115/1.3658902.

[97] Y Bar-Shalom, XR Li, and T Kirubarajan. State estimation for nonlinear dynamic systems. In *Estimation with applications to tracking and navigation*, chapter 10, pages 371–420. John Wiley & Sons, Inc., New York, USA, January 2002. doi: 10.1002/0471221279.ch10.

[98] WH Foy. Position-location solutions by Taylor-series estimation. *IEEE Transactions on Aerospace and Electronic Systems*, AES-12(2):187–194, March 1976. doi: 10.1109/TAES.1976.308294.

[99] Z Xue and H Schwartz. A comparison of several nonlinear filters for mobile robot pose estimation. In *Proceedings of the 2013 IEEE International Conference on Mechatronics and Automation*, pages 1087–1094, Takamatsu, Japan, August 2013. doi: 10.1109/ICMA.2013.6618066.

[100] NJ Gordon, DJ Salmond, and AFM Smith. Novel approach to nonlinear/non-Gaussian Bayesian state estimation. *IEE Proceedings F (Radar and Signal Processing)*, 140(2):107–113, April 1993. doi: 10.1049/ip-f-2.1993.0015.

[101] JH Kotecha and PM Djuric. Gaussian sum particle filtering. *IEEE Transactions on Signal Processing*, 51(10):2602–2612, October 2003. doi: 10.1109/TSP.2003.816754.

[102] H Alkhatib, I Neumann, H Neuner, and H Kutterer. Comparison of sequential Monte Carlo Filtering with Kalman Filtering for nonlinear state estimation. In *Proceedings of the 1st International Conference on Machine Control & Guidance 2008*, pages 273–283, Zurich, Switzerland, June 2008.

[103] MS Arulampalam, S Maskell, N Gordon, and T Clapp. A tutorial on particle filters for online nonlinear/non-Gaussian Bayesian tracking. *IEEE Transactions on Signal Processing*, 50(2):174–188, February 2002. doi: 10.1109/78.978374.

[104] Y Song and B Lian. GNSS P2P cooperative positioning system for multiple Search-and-Rescue robots. In *China Satellite Navigation Conference (CSNC) 2015 Proceedings: Volume III. Lecture Notes in Electrical Engineering*, volume 342, pages 571–581, April 2015. doi: 10.1007/978-3-662-46632-2_50.

[105] C Xu, J He, X Zhang, P Tseng, and S Duan. Toward near-ground localization: Modeling and applications for TOA ranging error. *IEEE Transactions on Antennas and Propagation*, 65(10):5658–5662, October 2017. doi: 10.1109/TAP.2017.2742551.

[106] Y Geng, J He, and K Pahlavan. Modeling the effect of human body on TOA based indoor human tracking. *International Journal of Wireless Information Networks*, 20 (4):306–317, September 2013. doi: 10.1007/s10776-013-0227-3.

[107] H Lu, S Zhang, Y Dong, and X Lin. A Wi-Fi/GPS integrated system for urban vehicle positioning. In *Proceedings of the 13th International IEEE Conference on Intelligent Transportation Systems*, pages 1663–1668, Funchal, Portugal, September 2010. doi: 10.1109/ITSC.2010.5625268.

[108] H Li, X Chen, L Huang, and D Yao. A GPS/Wi-Fi integrated system for positioning in cooperative vehicle and infrastructure system. In *Proceedings of the 2012 IEEE International Conference on Vehicular Electronics and Safety (ICVES 2012)*, pages 285–289, Istanbul,Turkey, July 2012. doi: 10.1109/ICVES.2012.6294265.

[109] R Conley, R Cosentino, CJ Hegarty, ED Kaplan, JL Leva, MU de Haag, and K Van Dyke. Performance of stand-alone GPS. In ED Kaplan and CJ Hegarty, editors, *Understanding GPS: Principles and applications*, chapter 7, pages 301–378. Artech house, Norwood, MA, USA, 2006.

[110] PW Ward, JW Betz, and CJ Hegarty. Interference, multipath, and scintillation. In ED Kaplan and CJ Hegarty, editors, *Understanding GPS: Principles and applications*, chapter 6. Artech house, Norwood, MA, USA, 2006.

[111] P Enge. Local area augmentation of GPS for the precision approach of aircraft. *Proceedings of the IEEE*, 87(1):111–132, January 1999. doi: 10.1109/5.736345.

[112] BS Pervan, SP Pullen, and JR Christie. A multiple hypothesis approach to satellite navigation integrity. *Navigation: Journal of The Institute of Navigation*, 45(1): 61–71, Spring 1998. doi: 10.1002/j.2161-4296.1998.tb02372.x.

[113] NL Knight and J Wang. A comparison of outlier detection procedures and robust estimation methods in GPS positioning. *Journal of Navigation*, 62(4):699—-709, 2009. doi: 10.1017/S0373463309990142.

[114] X Han, SA Kazim, NA Tmazirte, J Marais, and D Lu. GNSS/IMU tightly coupled scheme with weighting and FDE for rail applications. In *Proceedings of the 2020 International Technical Meeting (ION ITM 2020)*, pages 570–583, San Diego, CA, USA, January 2020.

[115] A El-Mowafy, B Xu, and LT Hsu. Integrity monitoring using multi-GNSS pseudorange observations in the urban environment combining ARAIM and 3D city models. *Journal of Spatial Science*, pages 1–20, March 2020. doi: 10.1080/14498596.2020.1734109.

[116] Z Jiang, PD Groves, WY Ochieng, S Feng, CD Milner, and PG Mattos. Multi-constellation GNSS multipath mitigation using consistency checking. In *Proceedings of the 24th International Technical Meeting of The Satellite Division of the Institute of Navigation (ION GNSS 2011)*, pages 3889–3902, Portland, OR, USA, September 2011.

[117] E Wang, C Jia, G Tong, P Qu, X Lan, and T Pang. Fault detection and isolation in GPS Receiver Autonomous Integrity Monitoring based on chaos particle swarm optimization-Particle Filter algorithm. *Advances in Space Research*, 61(5):1260–1272, March 2018. doi: 10.1016/j.asr.2017.12.016.

[118] J Gabela, I Majic, A Kealy, M Hedley, , and S Li. Robust vehicle localization and integrity monitoring based on spatial feature constrained PF. In *Proceedings of the 2020 IEEE/ION Position, Location and Navigation Symposium (PLANS)*, pages 661–669, Portland, OR, USA, April 2020.

[119] L Li, M Quddus, and L Zhao. High accuracy tightly-coupled integrity monitoring algorithm for Map-Matching. *Transportation Research Part C: Emerging Technologies*, 36:13–26, November 2013. doi: 10.1016/j.trc.2013.07.009.

[120] N Kbayer and M Sahmoudi. 3d-mapping-aided GNSS localization for integrity monitoring in urban environments. In *Proceedings of 2017 14th International Multi-Conference on Systems, Signals Devices (SSD)*, pages 591–596, Marrakech, Morocco, December 2017. doi: 10.1109/SSD.2017.8167014.

[121] TN Ray, Pierce JD, and DM Bevly. A comparison of particle propagation and weight update methods for indoor positioning systems. In *Proceedings of the 31st International Technical Meeting of the Satellite Division of The Institute of Navigation (ION GNSS+ 2018)*, pages 3398–3408, Miami, FL, USA, September 2018.

[122] Y Lee, K Van Dyke, B DeCleene, J Studenny, and M Beckmann. Summary of RTCA SC-159 GPS Integrity Working Group activities. *Navigation, Journal of The Institute of Navigation*, 43(3):307–362, Fall 1996. doi: 10.1002/j.2161-4296.1996.tb02579.x.

[123] U.S. Department of Defense. *Global Positioning System Standard Positioning Service Performance Standard*. 5 edition, 2020. URL https://www.gps.gov/technical/ps/2020-SPS-performance-standard.pdf.

[124] E Ndashimye, SK Ray, NI Sarkar, and JA Gutiérrez. Vehicle-to-infrastructure communication over multi-tier heterogeneous networks: A survey. *Computer Networks*, 112:144–166, 2017. doi: 10.1016/j.comnet.2016.11.008.

[125] MF Goodchild. Citizens as sensors: the world of volunteered geography. *GeoJournal*, 69(4):211—-221, August 2007. doi: 10.1007/s10708-007-9111-y.

[126] B Li, L Lou, and Y Shen. GNSS elevation-dependent stochastic modeling and its impacts on the statistic testing. *Journal of Surveying Engineering*, 142(2):04015012, December 2015.

[127] Ž Bačić, T Jogun, and I Majić. Integrated sensor systems for smart cities. *Tehnički vjesnik*, 25(1):277–284, 2018. doi: 10.17559/TV-20160620125732.